Alma Mater Studiorum – Università di Bologna

DOTTORATO DI RICERCA IN

Ingegneria Civile, Chimica, Ambientale e dei Materiali

Ciclo XXIX

Settore Concorsuale di afferenza: 08/B2

Settore Scientifico disciplinare: ICAR 08

Experimental investigation on masonry reinforced by bed joints structural repointing and plating system

Presentata da: **Susanna Casacci**

Coordinatore Dottorato	**Relatore**
Luca Vittuari	**Dott. Ing. Cristina Gentilini**
	Correlatore
	Prof. Angelo Di Tommaso

Esame finale anno 2017

To my parents

To Antonio

Contents

3

List of Figures

List of Tables

List of Symbols

a = constant

a^* = spectral acceleration

a_g = peak ground acceleration

A_b = average bond area between the structural mortar and the bar

A_{eff} = effective area

A_f = cross - sectional area of the reinforcing bar

A_{FRCM} = area of FRCM reinforcement by unit width in both directions (horizontal and vertical)

A_n = net area of the specimen

A_m = interface loading area between the steel shoe and the wall

b = constant

b_f = width of the fabric

c = cohesion

c_{ct} = corrective factor

c_0 = initial cohesion

C_s = parameter controlling the shear stress contribution to failure

d^* = spectral displacement

d_s = secant displacement

d_u^* = ultimate displacement capacity of the structure

D = diameter

$\boldsymbol{D}$ = stiffness matrix in the elastic regime

E = elastic modulus

E_b = elastic modulus for the brick

E_{BAR} = elastic modulus of the bar

E_f = elastic modulus of the fabric

E_{FRCM} = elastic modulus of the bar

E_m = elastic modulus for the mortar

E_M = elastic modulus for the masonry

E_s = elastic modulus for the steel

f_c = compressive strength

f_{cb} = compressive strength of the bricks

f_{cd} = design compressive strength

f_{cm} = compressive strength of the mortar

f_{dt} = diagonal tensile strength of the masonry

f_f = flexural strength

f_{fm} = flexural strength of the mortar

f_i = force carried by i-th reinforcing bar

f'_m = compressive strength of the masonry

f_t= tensile strength

$f_{t,BAR}$= tensile strength of the reinforcing bar

$f_{t,FRCM}$= tensile strength of the FRCM grid

f'_t = tensile strength of the masonry

f_y = yield strength

f_{yd}= design yielding strength

F'_{max} = maximum debonding force of the FRCM from the substrate with the presence of the connectors

F'_{omax} = maximum debonding force of the FRCM from the substrate without connectors

g = potential function

g' = vertical gage length

G_b = shear modulus for the brick

G_f = specific fracture energy

G_{fc} = compressive fracture energy

G_f^I = mode I fracture energy

G_f^{II} = shear-slip fracture energy

G_m = shear modulus for the mortar

h = height of the brick

H = height of the masonry panel

k_n = linear normal stiffness

k_p = plastic strain

k_s = linear tangential stiffness

L_a = length of each anchoring system used to test the bar

L_e = effective length of the reinforcing bar

L_{eff} = effective length of the FRCM

L_i = effective bond length of the i-th reinforcing bar

L_p = total length of the bar

L_u = effective length of the bar

M^* = participating mass during the mechanism

n = percentage of the gross area of the unit that is solid

n_{layer} = number of layer of fabric

N = number of storey of the structure

N_0 = maximum pull - out force of the connectors

P_{crack} = load at which the crack formation occurs

$p_{lim.,und}$ = limit pressure of the soil in undrained conditions

18

P_{max} = peak load

$\bar{P}_{max}$ = mean value of peak load

P_{max}^{R} = maximum load for the reinforced specimen

P_{max}^{UNR} = maximum load for the unreinforced specimen

q = behavior factor

R = radius of the reinforcing bar

S = soil coefficient

S_e = elastic spectrum

t = thickness of the brick

t_m = thickness of the mortar joints

t_f = thickness of the steel fabric or steel plate product

T = thickness of the masonry panel

T_s = secant period

u = horizontal displacement

v = vertical displacement

V_c = shear capacity due to toe crushing failure

V_{dt} = shear capacity due to diagonal tension failure

V_f = contribution of reinforcement to nominal shear capacity of the specimen

V_m = shear capacity of the unreinforced masonry wall

V_n = nominal shear capacity

V_{sf} = shear capacity due to shear friction failure

V_{ss} = shear capacity due to shear sliding failure

w = width of the brick

W = width of the masonry panel

γ = shear strain

γ_{el} = elastic shear strain

γ_m = material security factor

γ_y = shear strain at yield

γ_u = ultimate shear strain

γ_w = specific weight

δ = dilatancy shear slip degradation coefficient

$\delta_{x,k}$ = normalized horizontal virtual displacement of the control point

Δ_d = displacement demand of the earthquake

Δu = horizontal extension of the specimen

Δv = vertical shortening of the specimen

$\Delta\lambda_i$ = plastic strain increment

Δ_1 = structural enhancement achieved in terms of peak load by using the bars in the mortar joints

Δ_2 = structural enhancement achieved in terms of load at which propagation of crack occurs by using the bars in the mortar joints

ε = strain

ε_{cu} = ultimate strain in compression

ε_u = breaking elongation

θ = angle between horizontal and the main diagonal of the wall

μ = pseudo-ductility

μ_d = design friction coefficient

μ_m = modified coefficient of internal shear friction in mortar joints

μ_0 = coefficient of internal friction in the mortar joints

ν = Poisson's ratio

ρ_f = reinforcement ratio

σ_u = confining normal stress

σ_c = compressive strength

σ_{max} = maximum tensile stress

τ = shear stress

τ_b = average bond strength between the bar and the structural mortar

τ_d = design shear stress

τ_{el} = shear stress in the elastic branch

τ_0 = shear bond strength of mortar joints

$\tau_{0,m}$ = modified shear bond strength in mortar joints

ϕ = friction coefficient

ϕ_{BAR} = diameter of the bar

ϕ_r = residual friction coefficient

ϕ_0 = initial friction coefficient

ψ = dilatancy coefficient

List of Acronyms

ADRS: Acceleration Response Spectrum

AFRP: Aramid Fiber Reinforced Polymer

CFRP: Carbon Fiber Reinforced Polymer

COD: Crack Opening Displacement

CP: Control Point

EB: Externally Bonded

FC: Confidence Factor

FRCM: Fiber Reinforced Cementitious Matrix

FRP: Fiber Reinforced Polymer

GFRP: Glass Fiber Reinforced Polymer

IQM: Masonry Quality Index

LC: Large Crack

LC4: Large Crack, 4 bars

LC8: Large Crack, 8 bars

LMCP: latex modified cementitious paste

LVDT: Linear Variable Displacement Transducer

NC: No Crack

NC8: No Crack, 8 bars

NSM: Near Surface Mounted

PBO: phenylenecisbenzobisoxazole

PVW: Principle of Virtual Works

RR: Reinforced Repointing

RF-A: Reinforced FRCM Asymmetric

RF-L: Reinforced FRCM constructed by using mortar L

RF-S: Reinforced FRCM Symmetric

RF-WC: Reinforced FRCM with connector constructed by using mortar W

RR-A: Reinforced Repointing Asymmetric

RR-S: Reinforced Repointing Symmetric

SC: Small Crack

SC4: Small Crack, 4 bars

SDOF: Single Degree of Freedom System

SLD: Damage Limit State

SLS: Serviceability Limit State

SLV: Life Safety Limit State

SR: Structural Repointing

SRG: Steel Reinforced Grout

TRM: Textile Reinforce Mortar

TSNSM: twisted stainless steel near-surface mounted

ULS: Ultimate Limit State

UNR: Unreinforced

UNR-L: Unreinforced specimen constructed with mortar L

UNR-W: Unreinforced specimen constructed with mortar W

Abstract

Strengthening of damaged masonry walls is an important aspect during building retrofitting operations. Innovative materials, as textile composites e.g. FRP (Fiber Reinforced Polymer), FRCM (Fiber Reinforced Cementitious Matrix), SRG (Steel Reinforced Grout), TRM (Textile Reinforced Mortar) can be used, in order to repair and strengthen either modern and historic constructions. However, these materials cannot be applied to masonry façades or elements with facing bricks because violate the aesthetic and conservation requirements. A recent technology, called reinforced repointing technique, have been developed being minimally invasive and respectful of the aesthetic of the fair – faced masonry elements. It involves the application of materials having high tensile strength such as reinforcing steel bars, steel textile sheets or composite thin pultruded laminae with crack arrestor function, to reduce the vulnerability of masonry structures against in-plane actions. The main advantages of reinforced masonry are: compressive strength and ductility are increased, pseudo-vertical cracks are contrasted as well as the original aesthetic aspect of the masonry is saved being the strengthening materials embedded in the joints.

Many of the studies in literature deal with experimental and/or numerical investigations conducted on undamaged masonry specimens. Nevertheless, the assessment of the mechanical behavior of reinforced masonry structures in their on-site conditions is fundamental for understanding the role of the reinforcement.

In such a context, this work presents the results of an extended experimental campaign conducted on undamaged and damaged masonry specimens, strengthened by using reinforced repointing technique and FRCM system. Also numerical and analytical models have been used to support and foresee the experimental results.

1. Chapter 1: Introduction

1.1 General framework and motivation

The vulnerability of historical constructions has always been a challenge for the researchers, due to the vast amount of the correlated uncertainties. Masonry behavior is in fact highly non linear even in low stress conditions, and the related models constitute an hard task to be fulfilled. The mechanical features of masonry structures are not only influenced by the single element characterization (typically clay brick and mortar), but also by a set of vulnerabilities that are connected to the history of the construction and to the methods used in the construction procedures. In such a contest, strengthening of masonry constructions is an important aspect during building retrofitting operations having "conservation" goals.

Innovative materials, as textile composites (FRP, SRG, FRCM…) are often used, in specially, for external reinforcement to increase the in-plane shear capacity and to provide out-of-plane load-carrying capability to masonry walls. Moreover, FRP composites can be easily applied to the intrados or extrados surfaces of both flat and vaulted masonry structures in order to prevent or delay the main collapse mechanisms and, consequently, to increase the load bearing capacity even in case of seismic events. However, wet lay-up textiles cannot be applied to fair-faced masonry. Recently, a technology called reinforced repointing technique, has been developed being minimally invasive and respectful of the aesthetic of the masonry elements.

It involves the application of materials having high tensile strength such as reinforcing steel bars, steel textile sheets or composites thin pultruded laminae with cracks arrestors function, to reduce the vulnerability of masonry structures against in-plane actions.

Reinforcement steel bars or FRP or FRCM composites are embedded with suitable mortar in the bed joints of a wall previously grooved. The main advantages of reinforced masonry are: compressive strength and ductility are increased, pseudo-vertical cracks are contrasted, the long term deformation (creep effects) are attenuated and, at the same time, the original aesthetic of the masonry is saved being the strengthening materials embedded in the joints.

1.2 Objective of the thesis

The objective of the thesis is to study and understand the advantages and drawbacks of the repointing technique. Experimental tests on small and large masonry specimens were carried out together with analytical and numerical models. In particular, two different test configurations were investigated: the first one called splitting mode in which a compressive non uniform load was applied on the surface of the specimens, the second one called diagonal configuration in which the load was applied on the corner of the samples in order to study the shear behavior of the panels strengthened with this technique. In the splitting configuration, specimens with an initial crack in the middle were tested with the aim to investigate the crack arrestors function of the composite materials inserted in the mortar joints.

1.3 Outline of the thesis

The thesis is organized as follows: in Chapter 2 the state of the art about the strengthening interventions achieved by using different composite materials such as FRP, FRCM, SRG and TRM is reported, together with a presentation of reinforced repointing technique. In Chapter 3, an experimental campaign developed by the author on pre-cracked small masonry specimens, reinforced by using repointing technique in the mortar joints is described. In particular, both carbon wires and steel bar are used as reinforcement materials. In this chapter, the specimens were tested in a non uniform compressive way simulating the condition in which a real masonry wall is subjected when an excessive compressive load occurs. In Chapter 4, diagonal compression test were performed by the author in collaboration with the University of Minho, Portugal, on small masonry specimens reinforced by using both repointing technique and FRCM system. Furthermore, analytical and numerical models were used with the aim to improve comprehension and to foresee the behavior of small strengthened specimens. In Chapter 5, large scale masonry specimens strengthened by using an FRCM system applied on one or both sides, were tested in compression. In Chapter 6, a vulnerability analysis and strengthening design made by the author on two real case study, the Luciano Pavarotti Theatre and the San Barnaba Church both in Modena, is reported. In Chapter 7, some conclusions have been derived.

2. Chapter 2: Strengthening Technique

2.1 Introduction

The great majority of constructions in Europe are masonry built. It is well known that masonry materials suffer of several structural issues. Low tensile strength, low ductility, poor material properties as well as weak connections between structural elements are among the causes of the vulnerability against out-of-plane loads and of the fragile collapses of masonry structures (Boscato et al. 2014; Castellazzi et al. 2013).

Reinforcement of masonry structures is mainly based on conventional methods such as: (*i*) addition of new structural elements; (*ii*) injection of material to fill cracks; (*iii*) local replacement of damaged masonry bricks; (*iv*) improvement of the connections and (*v*) addition of confinement walls. However, these technologies show well-known drawbacks such as, among the others, addition of mass to the structure, reduction of the available space, and, in some cases, the appearance of the building is affected.

Innovative materials, as textile composites e.g. FRP (Fiber Reinforced Polymer), FRCM (Fiber Reinforced Cementitious Matrix), SRG (Steel Reinforced Grout), TRM (Textile Reinforced Mortar) have been helpful, regarding the above mentioned issues, in order to repair and strengthen either modern and historic constructions (Valluzzi et al. 2014). The composite materials are used to: (*i*) provide tensile strength to masonry elements, (*ii*) modify the structural behavior and the collapse mechanism of the structure, (*iii*) increase the displacement capacity of strengthened composite-to-masonry systems. However, these materials cannot be applied to masonry façades or elements with facing bricks because violate the aesthetic and conservation requirements. A recent technology, called Reinforced Repointing technique (RR), has been developed being minimally invasive and respectful of the aesthetic of the fair – faced masonry elements.

2.2 Composite materials

Composite materials are characterized by high tensile strength, high stiffness-to-weight ratio, high fatigue and corrosion resistance. These features, together with the progressive reduction in the manufacturing and distribution costs of these materials have enhanced their use for structural purposes, such as: (*i*) to increase the load-bearing capacity of structural members, (*ii*) to improve the seismic capacity of the whole building (ties, connections among components, strengthening), (*iii*) to counteract specific incipient or already developed damage (high compression, shear and/or flexural conditions), (*iv*) to thwart opening of cracks and (*v*) to repair local weaknesses (De Lorenzis et al. 2007; Foraboschi 2004; Shrive 2006; Valluzzi et al. 2002; Carozzi et al. 2015).

2.2.1. FRP

FRP (Fiber Reinforced Polymer) are non-metallic composites made of a polymer matrix reinforced with continuos fibers. On the 80s of the last century, FRP began to be used in civil engineering for the first time and, in the last few decades, have been widely studied, and some design codes/recommendations have been published for strengthening applications.

The pioneering experimental research in this area started in the Swiss Research Institute EMPA in Zurich under the direction of U. Meier (Meier 1995). Initially only cables made of carbon and aramid fibers were applied for the structural strengthening, but in the recent years, pretensioned CFRP (Carbon Fiber Reinforced Polymer) laminates have also been used. Nowadays, glass, aramid and carbon fibers are the most often used, but there are still attempts to use other types of fibers such as basalt and bamboo.

Polymer matrices are usually made of epoxy resins, sometimes polyester and vinylester resins. Epoxy resins, compared to other types of matrices, are characterized by better mechanical properties and higher durability. Matrices allow uniform distribution of the tension forces on all fibers and protect them against mechanical damages as well as adverse effects of the environment. The matrix has practically no effect on the tensile strength of the composite, while it determines the shear and compression capacity of the material. Due to its structure, composites are anisotropic materials that significantly affect the possibility of their use (Derkowski 2015).

The main drawbacks in the use of FRPs are brittle failure and their sensitivity to impact notching and environmental agents. The differences in physical properties compared with masonry (e.g. thermal coefficient, porosity) may alter both the mechanical and physical equilibrium of the substrate (expansion and transpirability, respectively). Moreover the effectiveness of the anchorage (chemical, by adhesion; mechanical, by proper connections and devices) all play crucial functional roles. Nor does an epoxy matrix allow proper transpiration of the masonry substrate and this may cause compatibility and removability problems, which must be taken into account when cultural heritage buildings are involved (De Lorenzis et al. 2004). Finally, protection from UV may be required, with selected materials or plaster covering.

An example of retrofitting intervention on historical building by using FRP is the one applied on the bell tower of S. Lucia Church affected by the Umbria-Marche earthquake (1997) (Figure 1a). It is a sac-masonry structure built during XV century, 32m tall and 1100tons weight, located at the centre of a little town of Serra S. Quirico that is a mid-age suburb near Ancona. The supervisor to the Architectural Heritage of Marche, Arch. Enrico Guglielmo, asked Professor Edoardo Cosenza consulting for a solution by innovative materials. A reticular system, made of horizontal and vertical carbon fibres, were gripped on the inner walls of the tower (Figure 1b). The FRP was installed without removing the original wood beams at floors; only wood panels were temporarily removed and restored at the end of the whole process. Horizontal short composite elements were spaced in the walls corners to improve the grip. From the structural point of view FRP design aimed to greatly improve seismic capacity of the tower. Usually structural engineering practice neglects masonry tension strength, while FRP ensure a monolithic behavior for high intensity earthquakes. A reinforced concrete slab, built as foundation for formerly proposed steel structure, was used for anchoring composites to the ground without overloading the original tower's foundation (Cosenza & Iervolino 1997).

<table>
<tr><td>(a)</td><td>(b)</td></tr>
</table>

Figure 1 a) Bell Tower of S. Lucia; b) detail of application of FRP in the inner wall (Cosenza & Iervolino 1997).

2.2.2. FRCM

To overcome some problems related to the use of FRP, the organic matrices may be replaced by inorganic matrices. Infact, cementitious matrix exhibits significant heat resistance, allows vapor permeability, and can be applied at low temperatures or on wet surfaces. Composite materials made of cementitious matrix and high strength fibers are usually referred to as FRCM (Fiber Reinforced Cementitious Matrix). The FRCM composites are a combinations of polymer-modified cementitious matrices and high-strength fibers namely carbon and glass fibers. Based on the evidence reported in the literature, since the debonding takes place within the composite, the substrate mechanical properties could be less significant than in FRP applications, while the matrix and consequently the matrix-fiber bonding properties will play the fundamental role (D'Antino et al. 2015).

In (D'Ambrisi et al. 2013), an application of FRCM is reported. A PBO-FRCM is applied on the intrados of the concrete barrel vaults of the railway bridge located on the Rome-Formia railway (Figure 2).

(a)   (b)

Figure 2 a) Vaults of railfay bridge on Roma-Formia railway; b) detail of PBO_FRCM application on the intrados of one vault (D'Ambrisi et al. 2013).

2.2.3. SRG

The composite system comprised of high strength steel cords embedded in mortar-based matrices called SRG (Steel Reinforced Grout), has been successfully used for strengthening masonry structures (Razavizadeh et al. 2014).

These materials have a relatively long-term record in structural engineering, especially in the development of thin section product, but when they contain continuous fibers they fail to ensure their efficient use. This weakness is the consequence of the mortar's granularity, which hinders penetration and impregnation of fiber sheets. Therefore, cement-based matrices lack the fundamental properties of binders (such as epoxies), which is the ability to penetrate and wet individual fibers.

2.2.4. TRM

TRM (Textile Reinforced Mortar) is a composite material used to strengthen masonry. This technology solution consists of bonding a high performance fibre grid to the structure's surface with a plaster based on an inorganic matrix. TRM is characterized by a good mechanical and chemical compatibility with the masonry substrate (Papanicolaou et al. 2007; Bernat et al. 2013; Tetta et al. 2015).

2.3 Strengthening of masonry with composites

In the historical context, critical evaluation of the effects of generalized interventions on masonry structures must be carefully analyzed (Binda et al. 2006; Modena et al. 2011). In this context, reinforcement with composites may be suggested in the following cases: (*i*) counteracting overall or partial overturning of structural elements, (*ii*) improving connections among structural elements, (*iii*) in-plane or out-of-plane strengthening, enhancing the load-bearing capacity and stiffness of the walls under shear and/or bending loads, (*iv*) confinement under vertical loads, improving the strength and/or ductility of columns and piers, (*v*) bonding support for curved shapes, increasing the load-bearing capacity of arches and vaults and reducing their lateral thrust, (*vi*) repairing cracks or limiting their opening.

2.3.1. Reinforced Repointing Technique

Reinforced Repointing Technique, also called NSM (Near Surface Mounted), is a recent technology that consists in placing in the mortar bed joints thin laminae or bars of high tensile strength materials such as carbon, glass (Tinazzi et al. 2000), steel (Ismail et al. 2011; Petersen et al. 2012) or basalt (Quagliarini et al. 2012), resulting completely hidden after the application. It is a suitable technique for fair-faced masonry structures that show a crack pattern due to excessive compressive load (Figure 3), unlike the techniques described before that should be applied on the external surface of the masonry building.

Figure 3 View of St. Giustina's bell tower, Padua, Italy and crack pattern (Valluzzi et al. 2005).

Repointing technique can be unreinforced or reinforced. Unreinforced repointing is applied when the deterioration is localized in the mortar only, since it involves the partial replacement of the missing mortar with a new one, characterized by a better mechanical performance. Reinforced repointing consists in the same procedure as before but also, reinforcement elements in the form of rods or strips made of different materials, are embedded in the joints, applied on one or both sides of the wall (for thick walls), eventually connected by ties crossing the wall in the transverse direction. The transverse connection contrasts the wall dilation and reduces tensile stresses; it is also useful to prevent the out-of-plane deformation of the external leaves of multi-leaves walls and to increase the ductility. Regular horizontal bed joints are required to apply reinforced repointing.

The main operative phases for a correct execution of the intervention (Figure 4) are: (1) check the masonry conditions, (2) make the slot, usually by means of a grinder, that should be at least 10 mm high and 50-80 mm deep, (3) place the first layer of an appropriate groove filler (typically structural mortar or epoxy paste), (4) insertion of the reinforcing material: steel bars or plates, FRP laminates, glass fibre-reinforced polymer (GFRP) bars, carbon wires, etc, (5) application of a second layer of groove filler to cover the reinforcing element, (6) application of a final layer of material to seal the joints and to restore the original appearance of the façade (Tinazzi et al. 2000; Valluzzi et al. 2005; Maragna et al. 2016).
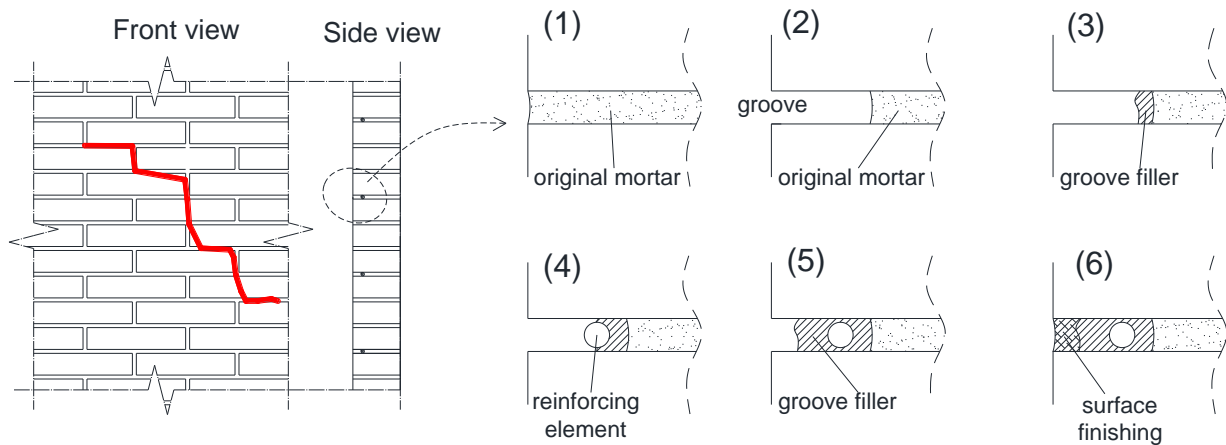
Figure 4 On the left, repointing intervention on a cracked fair-faced masonry wall and on the right, reinforced repointing intervention phases (Maragna et al. 2016)

2.3.2. Conservation issues for application to cultural heritage

The repair and structural strengthening of historical structures and the cultural heritage are subjected to a series of requirements and constraints aimed at ensuring their compliance with recognized conservation principles. Clearly, conservation must be combined with safety, especially in hazardous conditions, like those occurring in seismic areas, where the best solution which optimizes safety requirements with preservation criteria must be pursued. A brief mention of conservation principles is useful, to highlight the limitations of using composite materials for retrofitting purposes.

(*i*) *Respect for authenticity.* It is widely recognized that monuments do not only require preservation of their artistic or architectural features: their construction technologies and original structural conception should also be preserved, as a document of the past. Conversely, interventions should be distinguished from original parts.

(*ii*) *Minimum intervention*. Among the possible structural solutions, the one which has the least impact on the monument should be chosen; further interventions which are not necessary must be avoided, even if they result in a higher safety level.

(*iii*) *Compatibility*. The materials chosen for repairs should ensure chemical, physical and mechanical compatibility with the original materials. According to this principle, performances being equal, traditional materials and technique should be preferred over innovative ones, since their compatibility and absence of side-effects have been proven through the experience of centuries.

(*iv*) *Reversibility* or removability. To allow the strengthening system to be dismantled and if necessary replaced with a more efficient one, without causing severe damages or deteriorations to the original structure.

(*v*) *Durability*. The intervention should be designed to be durable according to the expected (long) life of the monument; in addition, any deterioration of strengthening materials should not affect the durability of the original parts (Petzet 1964).

All these criteria should be considered as guidelines in choosing the best strategies for repairing or strengthening historic structures and the cultural heritage According to this principles, composite materials in restoration works should be applied with particular caution when historical constructions are involved, so that their architectural and cultural value and their structural safety can be examined simultaneously. For instance,

textiles and bars, have the main advantage of neither increasing the load of the original structure nor affecting its stiffness properties; their use, if properly designed, can overcome specific weaknesses in masonry elements and avoid brittle failure of the components. A cautious approach should dominate, based on awareness of the fact that intervention cannot be presumed to be definitive, as further and more appropriate measures may emerge as more reliable in the future. So, it is important to take in account that the reinforcement may have to be removed and the structure must be repaired again, according to additional requirements and possible innovative techniques.

3. Chapter 3: Non uniform compressive test (splitting test) on small masonry specimens strengthened by Reinforced Repointing technique

3.1 Introduction

Masonry structures form a significant amount of architectural heritage all over the world, its conservation and exploitation is often a critical issue. It has been proven that massive structures as ancient towers, defensive walls, heavy piers may be in critical conditions under constant high dead loads even for stress values lower than the strength of the masonry. This condition, which is related to the long term behavior of masonry (creep), can entail a sudden collapse. Between the others, it is worth remembering the Civic Tower of Pavia. The collapse due to the long term behavior can occur even at 45-50% of the nominal strength value. An excessive state of deformation can be reached, and an unexpected collapse can eventually occur. Cracks appear very shortly before the failure, which happens suddenly without any other warning (such as large cracks or spalling). The only possible warning of the danger is made by the obsevation that all the cracks involve the bricks as the typical crack pattern occurring during compression test. Other causes, as thermal and hygroscopic strains and cyclic stresses caused by wind action or bell act in combination with the long term phenomena and contribute to worsen the damage. These results suggested that the evolution of the typical crack pattern, which can appear on the external walls of masonry buildings, should be carefully analysed. The development of the above described typical damage can be efficiently counteracted with the bed joints reinforcements technique. The first research, carried out in collaboration with the Politecnico of Milan and the University of Padua, concerned the use of small diameter steel bars, and allowed to perform some interventions on damaged historic structures (e.g. St. Sofia church in Padua, the bell tower of the Monza Cathedral). In the last years, the activity has been focused on CFRP as reinforcement, often used in combination with traditional mortars, to avoid compatibility problems. CFRP bars were chosen for their favorable mechanical and physical characteristics, such as high strength, low weight and corrosion immunity (Garbin et al. 2009; Valluzzi et al. 2005).

3.2 Experimental background

The bed joints reinforcement technique demonstrated his effectiveness in the dilation control following cracking phenomena more than to improve the mechanical characteristics of masonry. Infact, the main goal is to reduce the dilatancy of the wall in order to avoid cracks propagation into the bricks. This goal is achieved by the insertion of reinforcing bars into mortar bed joints in order to adsorb the tensile stresses otherwise carried out by the bricks and, consequently, to reduce the dilation of the wall. Nine double-brick masonry panels with nominal dimensions 1100 mm x 500 mm x 250 mm were built to be tested under monotonic compressive loads in strengthened and repaired conditions. Firstly, stainless steel rebars were embedded into horizontal mortar joints into a grooves about 60 mm deep, with suitable repointing mortar at every three bed joints. In order to check the effectiveness of the technique on each panel, the intervention was performed only

at one side of the walls, after preliminary compression of the specimens. Laboratory experimental tests simulating both monotonic and creep loads, carried out on strengthened and plain masonry panels, showed a significant reduction of the lateral dilation of about 37-39%. So it may be said that the bars are able to apply a confinement action to the masonry (Borri, Castori, et al. 2015). Moreover, a reduction of the crack pattern was also detected with vertical trend on the restored side. On the contrary, the cracks in the unrepaired side increased their opening and depth, and further spread of damage occurred, particularly located near the corners and in the middle portion of the prisms (Valluzzi et al. 2005).

A further development of the technique involved the use of CFRP rebars, instead of steel ones, and both lime-based and epoxy mortars. CFRP rebars were used in order to evaluate their effectiveness with compatible or high specific performance embedding products. Results pointed out that the better performances were obtained with symmetric applications and that the use of high strength epoxy resins as embedding material can be inappropriate due to the more brittle behavior both at local and global level (Garbin et al. 2009; Valluzzi et al. 2005).

3.3 Analytical investigation

3.3.1. Formulation of the problem

Reference is made to an ideal linear elastic model (Figure 5) made by superimposed blocks and interface elements, (Casacci et al. 2014). All the equations are developed in Appendix A.
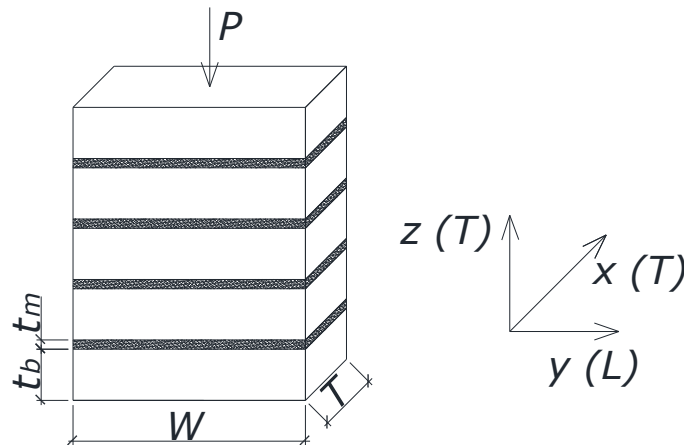
Figure 5 Geometrical model made by two isotropic materials.

3.3.1.1. Analytical formulation of an ideal model made by two different isotropic components

Blocks, namely the bricks, and interface elements, namely the joints, are considered isotropic. The following hypotheses hold: *i*) the stress - strain relations are written in terms of principal stresses, i.e. in the faces of the specimens identified by the normal directions *x*, *y* and *z* only normal stresses are present; *ii*) the model, restrained at the base, is loaded by a constant load, *P*, that produces a constant state of stress on the top and *iii*) tangential stresses on the interface elements are neglected (means interface element is attached to the other element only along its perimetric boundaries). Calling the two isotropic materials with pedex *b*, brick, and *j*, joint, the stress-strain relations become, Eq.(1) and Eq. (2)

$$
\begin{bmatrix} \varepsilon_{bx} \\ \varepsilon_{by} \\ \varepsilon_{bz} \end{bmatrix} =
\begin{bmatrix}
\dfrac{1}{E_b} & -\dfrac{\nu_b}{E_b} & -\dfrac{\nu_b}{E_b} \\
-\dfrac{\nu_b}{E_b} & \dfrac{1}{E_b} & -\dfrac{\nu_b}{E_b} \\
-\dfrac{\nu_b}{E_b} & -\dfrac{\nu_b}{E_b} & \dfrac{1}{E_b}
\end{bmatrix}
\begin{bmatrix} \sigma_{bx} \\ \sigma_{by} \\ \sigma_{bz} \end{bmatrix}
\tag{1}
$$

$$
\begin{bmatrix} \varepsilon_{jx} \\ \varepsilon_{jy} \\ \varepsilon_{jz} \end{bmatrix} =
\begin{bmatrix}
\dfrac{1}{E_j} & -\dfrac{\nu_j}{E_j} & -\dfrac{\nu_j}{E_j} \\
-\dfrac{\nu_j}{E_j} & \dfrac{1}{E_j} & -\dfrac{\nu_j}{E_j} \\
-\dfrac{\nu_j}{E_j} & -\dfrac{\nu_j}{E_j} & \dfrac{1}{E_j}
\end{bmatrix}
\begin{bmatrix} \sigma_{jx} \\ \sigma_{jy} \\ \sigma_{jz} \end{bmatrix}
\tag{2}
$$

By imposing the equilibrium along z direction, the following relation is obtained:

$$
\sigma_{bz} = \sigma_{jz} = \sigma_z
\tag{3}
$$

Calling t_b and t_j respectively the thickness of the two materials, by imposing the equilibrium along x and y directions, the following relations are obtained:

$$
\sigma_{bx} t_b + \sigma_{jx} t_j = 0 \rightarrow \sigma_{bx} = -\sigma_{jx} \frac{t_j}{t_b} = -\alpha \sigma_{jx}
$$
$$
\sigma_{by} t_b + \sigma_{jy} t_j = 0 \rightarrow \sigma_{by} = -\sigma_{jy} \frac{t_j}{t_b} = -\alpha \sigma_{jy}
\tag{4}
$$

with $\alpha = t_j/t_b$.

The compatibility along x and y directions is expressed by:

$$
\varepsilon_{bx} = \varepsilon_{jx} = \varepsilon_x
$$
$$
\varepsilon_{by} = \varepsilon_{jy} = \varepsilon_y
\tag{5}
$$

Substituting Eqs (4) and (5) in Eqs. (1) and (2), the stress - strain relations for the two materials can be written in a different manner. In particular, for the element b, the stress - strain relation becomes

$$
\begin{bmatrix} \varepsilon_x \\ \varepsilon_y \\ \varepsilon_{bz} \end{bmatrix} =
\begin{bmatrix}
\dfrac{1}{E_b} & -\dfrac{\nu_b}{E_b} & -\dfrac{\nu_b}{E_b} \\
-\dfrac{\nu_b}{E_b} & \dfrac{1}{E_b} & -\dfrac{\nu_b}{E_b} \\
-\dfrac{\nu_b}{E_b} & -\dfrac{\nu_b}{E_b} & \dfrac{1}{E_b}
\end{bmatrix}
\begin{bmatrix} -\alpha\phi_x \\ -\alpha\phi_y \\ 1 \end{bmatrix} \sigma_z
\tag{6}
$$

while for the element j, the stress - strain relation becomes

$$
\begin{bmatrix} \varepsilon_x \\ \varepsilon_y \\ \varepsilon_{jz} \end{bmatrix} =
\begin{bmatrix}
\dfrac{1}{E_j} & -\dfrac{\nu_j}{E_j} & -\dfrac{\nu_j}{E_j} \\
-\dfrac{\nu_j}{E_j} & \dfrac{1}{E_j} & -\dfrac{\nu_j}{E_j} \\
-\dfrac{\nu_j}{E_j} & -\dfrac{\nu_j}{E_j} & \dfrac{1}{E_j}
\end{bmatrix}
\begin{bmatrix} \phi_x \\ \phi_y \\ 1 \end{bmatrix} \sigma_z
\tag{7}
$$

with $\phi_x = \sigma_{jx}/\sigma_z$ and $\phi_y = \sigma_{jy}/\sigma_z$.

With this position, the stresses in the brick and in the joint, Eq. (4), can be written as:

$$\sigma_{bx} = -\alpha\sigma_{jx} = -\alpha\phi_x\sigma_z$$
$$\sigma_{by} = -\alpha\sigma_{jy} = -\alpha\phi_y\sigma_z$$
$$\sigma_{jx} = \phi_x\sigma_z$$
$$\sigma_{jy} = \phi_y\sigma_z$$

(8)

After some algebra, ϕ_x and ϕ_y are obtained and, in the case of isotropic materials, the two expressions are equivalent. In particular:

$$\phi = \phi_x = \phi_y = \frac{-\nu_j + \beta\nu_b}{\nu_j + \alpha\beta\nu_b - (1 + \alpha\beta)}$$

(9)

where ν_j and ν_b are the Poisson coefficient for the two materials and $\beta = E_j/E_b$ is the Young moduli ratio. Substituting Eq.(9) in Eq.(8), the stresses in the two materials are obtained:

$$\sigma_{bx} = \sigma_{by} = -\alpha\phi\sigma_z = -\alpha\frac{-\nu_j + \beta\nu_b}{\nu_j + \alpha\beta\nu_b - (1 + \alpha\beta)}\sigma_z$$

$$\sigma_{jx} = \sigma_{jy} = \phi\sigma_z = \frac{-\nu_j + \beta\nu_b}{\nu_j + \alpha\beta\nu_b - (1 + \alpha\beta)}\sigma_z$$

(10)

In the end, it is possible to evaluate the strains and the displacements of two materials along the three directions and, via equilibrium considerations, the mean values of the tangential stresses at the interface.

3.3.1.2 Analytical formulation of an ideal model made by one isotropic component and the other orthotropic

Reference is made to an ideal linear elastic model (Figure 5) made by superimposed bricks and joints. The bricks are considered isotropic, while the joints are orthotropic, simulating a reinforcing material made by fibers. Calling the two materials with pedex *b* and *o*, and assuming fibers located in the *y* direction:

$$E_{oy} = E_{oL}$$
$$E_{ox} = E_{oz} = E_{oT}$$
$$\nu_{xy} = \nu_{zy} = \nu_{oTL}$$
$$\nu_{xz} = \nu_{oTT}$$

(11)

being E_{oL}, E_{oT} the elastic moduli in the longitudinal and transversal direction, respectively, ν_{oTL} and ν_{oTT} are the Poisson coefficients.

The stress - strain relations for the brick is written in Eq.(1), while, for the orthotropic material, is:

$$\begin{bmatrix}\varepsilon_{ox}\\\varepsilon_{oy}\\\varepsilon_{oz}\end{bmatrix} = \begin{bmatrix}\dfrac{1}{E_{oT}} & -\dfrac{\nu_{oTL}}{E_{oT}} & -\dfrac{\nu_{oTT}}{E_{oT}}\\ -\dfrac{\nu_{oTL}}{E_{oT}} & \dfrac{1}{E_{oL}} & -\dfrac{\nu_{oTL}}{E_{oT}}\\ -\dfrac{\nu_{oTT}}{E_{oT}} & -\dfrac{\nu_{oTL}}{E_{oT}} & \dfrac{1}{E_{oT}}\end{bmatrix}\begin{bmatrix}\sigma_{ox}\\\sigma_{oy}\\\sigma_{oz}\end{bmatrix}$$

(12)

Calling t_b and t_o the thickness of the two materials, respectively, by imposing the equilibrium along x, y and z directions, the following relations are obtained:

$$\sigma_{bx}t_b + \sigma_{ox}t_o = 0 \rightarrow \sigma_{bx} = -\sigma_{ox}\frac{t_o}{t_b} = -\alpha\sigma_{ox} \qquad \textit{eq. along x}$$

$$\sigma_{by}t_b + \sigma_{oy}t_o = 0 \rightarrow \sigma_{by} = -\sigma_{oy}\frac{t_o}{t_b} = -\alpha\sigma_{oy} \qquad \textit{eq. along y} \tag{13}$$

$$\sigma_{bz} = \sigma_{oz} = \sigma_z \qquad \textit{eq. along z}$$

with $\alpha = t_o/t_b$.

The compatibility along x and y directions is expressed by:

$$\varepsilon_{bx} = \varepsilon_{ox} = \varepsilon_x$$
$$\varepsilon_{by} = \varepsilon_{oy} = \varepsilon_y \tag{14}$$

Substituting Eq.(13) and Eq.(14) in Eq.(1) and Eq.(12), the stress - strain relations for the two materials can be written in a different manner. In particular for the element b becomes:

$$\begin{bmatrix} \varepsilon_x \\ \varepsilon_y \\ \varepsilon_{bz} \end{bmatrix} = \begin{bmatrix} \dfrac{1}{E_b} & -\dfrac{\nu_b}{E_b} & -\dfrac{\nu_b}{E_b} \\ -\dfrac{\nu_b}{E_b} & \dfrac{1}{E_b} & -\dfrac{\nu_b}{E_b} \\ -\dfrac{\nu_b}{E_b} & -\dfrac{\nu_b}{E_b} & \dfrac{1}{E_b} \end{bmatrix} \begin{bmatrix} -\alpha\phi_x \\ -\alpha\phi_y \\ 1 \end{bmatrix} \sigma_z \tag{15}$$

while for the element o becomes:

$$\begin{bmatrix} \varepsilon_{ox} \\ \varepsilon_{oy} \\ \varepsilon_{oz} \end{bmatrix} = \begin{bmatrix} \dfrac{1}{E_{oT}} & -\dfrac{\nu_{oTL}}{E_{oT}} & -\dfrac{\nu_{oTT}}{E_{oT}} \\ -\dfrac{\nu_{oTL}}{E_{oT}} & \dfrac{1}{E_{oL}} & -\dfrac{\nu_{oTL}}{E_{oT}} \\ -\dfrac{\nu_{oTT}}{E_{oT}} & -\dfrac{\nu_{oTL}}{E_{oT}} & \dfrac{1}{E_{oT}} \end{bmatrix} \begin{bmatrix} \phi_x \\ \phi_y \\ 1 \end{bmatrix} \sigma_z \tag{16}$$

with $\phi_x = \sigma_{ox}/\sigma_z$ and $\phi_y = \sigma_{oy}/\sigma_z$.

Considering the definitions of ϕ_x and ϕ_y, the stresses in the isotropic element (Eq.(13)) and in the orthotropic one can be written:

$$\sigma_{bx} = -\alpha\sigma_{ox} = -\alpha\phi_x\sigma_z$$
$$\sigma_{by} = -\alpha\sigma_{oy} = -\alpha\phi_y\sigma_z$$
$$\sigma_{ox} = \phi_x\sigma_z \tag{17}$$
$$\sigma_{oy} = \phi_y\sigma_z$$

In the above equations, the only unknowns are the expressions of the two ratios ϕ_x and ϕ_y. After some algebra, the final expressions can be obtained:

$$\phi_x = \phi_T = \frac{(-\nu_b\beta_T + \nu_{oTT})\left(-\alpha\beta_T - \dfrac{\beta_T}{\beta_L}\right) - (-\nu_b\beta_T + \nu_{oTL})(\alpha\nu_b\beta_T + \nu_{oTL})}{(\alpha\nu_b\beta_T + \nu_{oTL})^2 - (-\alpha\beta_T - 1)\left(-\alpha\beta_T - \dfrac{\beta_T}{\beta_L}\right)} \tag{18}$$

$$\phi_y = \phi_L = \frac{(-\alpha\beta_T - 1)(-\nu_b\beta_T + \nu_{oTL}) - (-\nu_b\beta_T + \nu_{oTT})(\alpha\nu_b\beta_T + \nu_{oTL})}{(\alpha\nu_b\beta_T + \nu_{oTL})^2 - (-\alpha\beta_T - 1)\left(-\alpha\beta_T - \frac{\beta_T}{\beta_L}\right)} \tag{19}$$

where $\beta_L = E_{oL}/E_b \rightarrow E_{oL} = \beta_L E_b$ and $\beta_T = E_{oT}/E_b \rightarrow E_{oT} = \beta_T E_b$.

Substituting Eq.(18) and Eq.(19) in Eq.(17), the stresses in the two materials can be easily calculated. At the end, it is possible to evaluate the strains and the displacements of two materials along the three directions and, via equilibrium considerations, the mean values of the tangential stresses.

3.3.2. Numerical examples

The aim of this paragraph is to study the influence of different materials as interface elements after a uniform compression along z direction equal to 10 MPa ($\sigma_z = 10$ MPa).

3.3.2.1. Ideal model made by two different isotropic components: bricks and mortar, bricks and steel

The model is made by bricks and, as interface element, first with mortar, m, and second, by steel lamina, s.

3.3.2.1.1. Brick and mortar

Considering bricks with nominal dimensions equal to 250 x 120 x 55 mm³, elastic modulus, E_b, equal to 6400 MPa and Poisson ratio, ν_b, equal to 0.125, by using Eq.(1) the constitutive matrix can be written as

$$\begin{bmatrix} 15.625 & -1.953 & -1.953 \\ -1.953 & 15.625 & -1.953 \\ -1.953 & -1.953 & 15.625 \end{bmatrix} 10^{-5} \quad [MPa^{-1}] \tag{20}$$

Considering mortar with nominal dimensions equal to 250 x 120 x 10 mm³, elastic modulus, E_m, equal to 2100 MPa and Poisson ratio, ν_m, equal to 0.2, by using Eq.(2) the constitutive matrix becomes

$$\begin{bmatrix} 47.619 & -9.524 & -9.524 \\ -9.524 & 47.619 & -9.524 \\ -9.524 & -1.953 & 47.619 \end{bmatrix} 10^{-5} \quad [MPa^{-1}] \tag{21}$$

Calculating ϕ according to Eq.(9) and substituting the numerical values in Eq.(10), stresses in the brick and in the mortar are found:

$$\sigma_{bx} = \sigma_{by} = -\alpha\phi\sigma_z = -0.182(0.187)\sigma_z = -0.034\sigma_z$$
$$\sigma_{mx} = \sigma_{my} = \phi\sigma_z = 0.187\sigma_z = 0.187\sigma_z \tag{22}$$

By using relations (6) and (7), strains in the brick and in the mortar can be calculated:

$$\begin{bmatrix} \varepsilon_{bx} \\ \varepsilon_{by} \\ \varepsilon_{bz} \end{bmatrix} = \begin{bmatrix} 24.2 \\ 24.2 \\ -157.6 \end{bmatrix} 10^{-5}; \qquad \begin{bmatrix} \varepsilon_{mx} \\ \varepsilon_{my} \\ \varepsilon_{mz} \end{bmatrix} = \begin{bmatrix} 24.2 \\ 24.2 \\ -440.7 \end{bmatrix} 10^{-5}; \tag{23}$$

Multiplying the strains for the dimensions of the components, the values of the displacements on the external surfaces are obtained:

$$\begin{bmatrix} u_{bx} \\ u_{by} \\ u_{bz} \end{bmatrix} = \begin{bmatrix} 2.9 \\ 5.8 \\ -8.7 \end{bmatrix} 10^{-2} \, [mm]; \qquad \begin{bmatrix} u_{mx} \\ u_{my} \\ u_{mz} \end{bmatrix} = \begin{bmatrix} 2.9 \\ 5.8 \\ -4.4 \end{bmatrix} 10^{-2} \, [mm]; \tag{24}$$

In the end, it is possible to evaluate approximate mean values of the tangential stresses both in longitudinal and transversal direction (Figure 6):

$(\sigma_{Ib}Tt_b)/2$ $(\sigma_{Ib}Tt_b)/2$

$(\sigma_{Ib}Tt_b)/2$ $(\sigma_{Ib}Tt_b)/2$
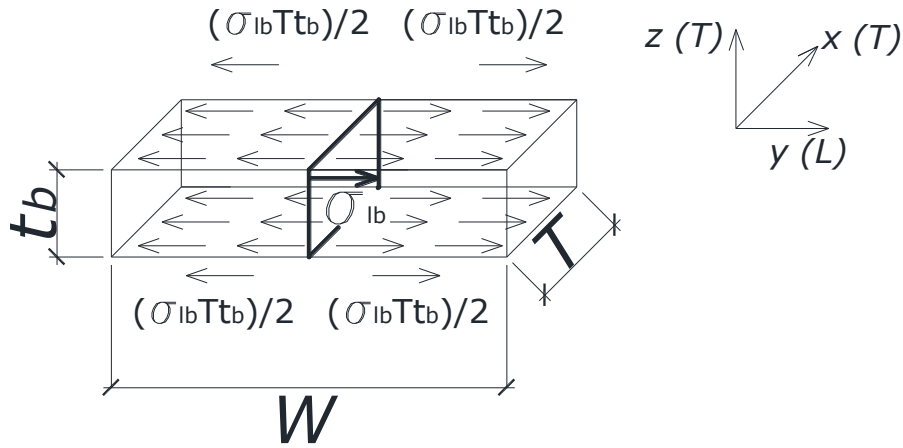
Figure 6 State of stress in the brick.

$$\tau_{by} = \frac{\sigma_{by}Tt_b}{2\frac{W}{2}T} = \frac{\sigma_{by}t_b}{W} = \frac{-0.034 \cdot (-10) \cdot 55}{250} = 0.075 \, MPa$$

$$\tau_{my} = \frac{\sigma_{my}Tt_m}{2\frac{W}{2}T} = \frac{\sigma_{my}t_m}{W} = \frac{0.187 \cdot (-10) \cdot 10}{250} = -0.075 \, MPa$$

$$\tau_{bx} = \frac{\sigma_{bx}Wt_b}{2W\frac{T}{2}} = \frac{\sigma_{bx}t_b}{T} = \frac{-0.034 \cdot (-10) \cdot 55}{120} = 0.155 \, MPa$$ (25)

$$\tau_{mx} = \frac{\sigma_{mx}Wt_m}{2W\frac{T}{2}} = \frac{\sigma_{mx}t_m}{T} = \frac{0.187 \cdot (-10) \cdot 10}{120} = -0.155 \, MPa$$

3.3.2.1.1. Brick and steel lamina

Using for brick the same characteristics as before and assuming a steel lamina with nominal dimensions equal to 250 x 120 x 1 mm³, elastic modulus, E_s, of 210000 MPa, Poisson ratio, v_s, equal to 0.30, by using the same procedure utilized for the latter case, the approximate mean values of tangential stresses in both directions are obtained:

$$\tau_{by} = -0.124 \, MPa$$
$$\tau_{sy} = 0.124 \, MPa$$
$$\tau_{bx} = -0.259 \, MPa$$ (26)
$$\tau_{sx} = 0.259 \, MPa$$

3.3.2.2. Ideal model made by two different components: bricks and Graphite - epoxy as interface element

The model is made by bricks and graphite - epoxy (Gr – EP(AS)) as interface material.

3.3.2.2.1. Brick and Gr – EP (AS)

Using for the brick the same characteristics as before and assuming a Gr – EP (AS) lamina with nominal dimensions equal to 250 x 120 x 1 mm³, elastic modulus in the longitudinal direction, E_{oL}, of 137895 MPa, elastic modulus in the transversal direction, E_{oT}, of 8963 MPa. For the Poisson ratio, the following values have been considered:

$$v_{oLT} = 0.30$$

$$\nu_{oTL} = \frac{0.30}{137895} = 0.019$$

$$\nu_{oTT} = 0.49$$

By using Eq.(17), the constitutive matrix becomes:

$$\begin{bmatrix} 11.116 & -0.212 & -5.467 \\ -0.212 & 0.725 & -0.212 \\ -5.467 & -0.212 & 11.116 \end{bmatrix} 10^{-5} \quad [MPa^{-1}] \tag{27}$$

Calculating ϕ_x and ϕ_y.according to Eq.(18) and Eq.(19), and substituting the numerical values in Eq.(17), the stresses in the brick and in the Gr – EP (AS) are obtained:

$$\sigma_{bx} = -\alpha\phi_x\sigma_z = -0.018(0.271)\sigma_z = -0.005\,\sigma_z$$

$$\sigma_{by} = -\alpha\phi_y\sigma_z = -0.018(-1.659)\sigma_z = -0.029\,\sigma_z$$

$$\sigma_{ox} = \phi_x\sigma_z = 0.271\,\sigma_z \tag{28}$$

$$\sigma_{oy} = \phi_y\sigma_z = -1.659\,\sigma_z$$

By using the relations (15) and (16), strains in the brick and Gr - EP (AS) can be calculated:

$$\begin{bmatrix} \varepsilon_{bx} \\ \varepsilon_{by} \\ \varepsilon_{bz} \end{bmatrix} = \begin{bmatrix} 20.9 \\ 14.7 \\ -155.8 \end{bmatrix} 10^{-5}; \qquad \begin{bmatrix} \varepsilon_{ox} \\ \varepsilon_{oy} \\ \varepsilon_{oz} \end{bmatrix} = \begin{bmatrix} 20.9 \\ 14.7 \\ -100.3 \end{bmatrix} 10^{-5}; \tag{29}$$

Multiplying the strains for the dimensions of the components, the values of the displacements on the external surfaces are obtained:

$$\begin{bmatrix} u_{bx} \\ u_{by} \\ u_{bz} \end{bmatrix} = \begin{bmatrix} 2.5 \\ 3.7 \\ -8.6 \end{bmatrix} 10^{-2} \, [mm]; \qquad \begin{bmatrix} u_{mx} \\ u_{my} \\ u_{mz} \end{bmatrix} = \begin{bmatrix} 2.5 \\ 3.7 \\ -0.1 \end{bmatrix} 10^{-2} \, [mm]; \tag{30}$$

In the end, it is possible to evaluate the approximate mean values of the tangential stresses both in the longitudinal and transversal directions:

$$\tau_{by} = -0.066 \, MPa$$

$$\tau_{oy} = 0.066 \, MPa$$

$$\tau_{bx} = 0.023 \, MPa \tag{31}$$

$$\tau_{ox} = -0.023 \, MPa$$

3.3.2.3. Summary and discussion of the results

In Table 1, the results for different models analyzed, are collected.

Table 1 Results of the different models analyzed

	Isotropic			Orthotropic
	Brick	Mortar	Steel	Gr-EP(AS)
t [mm]	55	10	1	1
E_y [MPa]	6400	2100	210000	137895
E_x [MPa]	6400	2100	210000	8963
ν_{yx}	0.125	0.2	0.3	0.30
ν_{xy}	0.125	0.2	0.3	0.019
ν_{xz}	0.125	0.2	0.3	0.49
ϕ_x	-	0.187	-3.111	0.271
Φ_y	-	0.187	-3.111	-1.659
$-\alpha\phi_x$	-	-0.034	0.056	-0.005
$-\alpha\phi_y$	-	-0.034	0.056	0.029
τ_y [MPa]	-	-0.075	0.124	0.066
τ_x [MPa]	-	-0.155	0.259	-0.023
$\varepsilon_x \times 10^{-5}$	-	24.2	11.8	20.9
$\varepsilon_y \times 10^{-5}$	-	24.2	11.8	14.7
$\varepsilon_{bz} \times 10^{-5}$	-	-157.6	-154.0	-155.8
$\varepsilon_{jz} \times 10^{-5}$	-	-440.7	-13.7	-100.3

The cases analyzed can be subdivided in two main groups: *i*) brick masonry with isotropic reinforcement such as mortar and steel and *ii*) brick masonry with orthotropic fibers reinforcement such as Graphite - epoxy. Several conclusions can be derived:

i) the ratio ϕ is strongly dependent on the ratio between the elastic moduli and on the Poisson coefficients of the two materials composing the sample; this is the reason of the inversion of the sign in the case of brick and steel with respect to the case of brick and mortar. In the case of Gr-EP(AS), ϕ is negative in the longitudinal direction where the elastic modulus is higher, and it is positive in the transversal direction where the elastic modulus is of the same order of magnitude with respect to the case of mortar;

ii) positive values of $-\alpha\phi$ produce positive values of tangential stresses when the sample is compressed, so the interface element produces confinement in the brick that results under compression (most favorable stress condition). Negative values of $-\alpha\phi$ mean that the interface element is in compression and the brick is in traction;

iii) the smaller are the values of the strains along *x* and *y* directions, the more favorable is the stress condition in the brick (compression);

iv) the use of Gr-EP(AS) produces benefits in the longitudinal direction but, in the transversal direction the behavior of the model is very close to the one made by brick and mortar; this means that this solution is expected to produce major benefits in the direction of the fibers.

3.4 Carbon bundles as repointing technique

3.4.1. Material characterization

3.4.1.1. Bricks and mortar

Commercial solid fired clay bricks (55 x 120 x 250 mm^3) were used to realize the specimens. From three bricks, seven cylindrical samples were cut from each brick: four perpendicular to bed (samples 1, 2, 3 and 4) and three parallel to bed (samples 5, 6 and 7), (Figure 7).
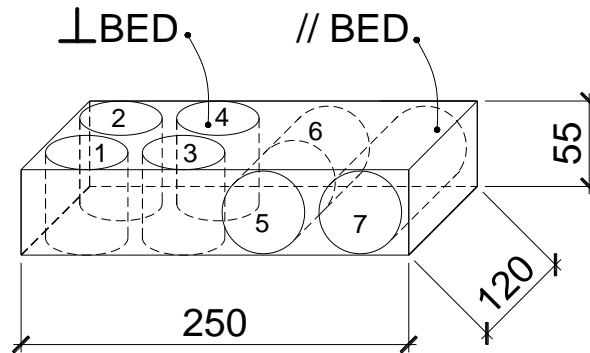
Figure 7 Samples extracted in order to determine brick mechanical properties (two orthogonal directions). Dimensions in mm.

Small cylinders (nominal size 50 x 50 mm^2) were tested in order to determine compressive strength (direction parallel and perpendicular to bed), while bigger cylinders (nominal size 50 x 120 mm^2) were tested to measure elastic modulus and Poisson's ratio, according to (EN 772-1 2010) and (EN 14580 2013).

In Table 2, the mechanical properties of the bricks used for realizing the specimens are reported (f_c = compressive strength, E = elastic modulus, ν = Poisson's ratio, ε_{cu} = ultimate strain in compression). All the values were obtained as the mean on three samples.

Table 2 Mechanical properties of the bricks used for the manufacturing of the specimens. Values averaged on three samples. Standard deviation in parentheses.

Material	f_c [MPa]		E [MPa]	ν [/]	ε_{cu} [%]
Brick	// to bed	20.25 (1.44)	7564 (1508)	0.12 (0.06)	0.35 (0.10)
	⊥ to bed	21.30 (1.31)			

For mortar preparation, a cement-based mortar was employed for both construction phase and repointing operations. Six 40 x 40 x 160 mm^3 prismatic samples were cast for determining compressive and flexural strength as well as elastic modulus and Poisson's ratio, according to (EN 196-1 2011). Curing of the mortar consisted in one month at T = 20 ± 2 °C and RH ≥ 90%.

In Table 3, the mechanical properties of the mortar used for realizing the specimens are reported (f_c = compressive strength, f_f = flexural strength, E = elastic modulus, ν = Poisson's ratio, ε_{cu} = ultimate strain in compression). All the values were obtained as the mean on three samples.

Table 3 Mechanical properties of the mortar used for the manufacturing of the specimens. Values averaged on three samples. Standard deviation in parentheses.

Materials	f_c [MPa]	f_f [MPa]	E [MPa]	ν [/]	ε_{cu} [%]
Mortar	13.57 (0.65)	0.73 (0.07)	11148 (574)	0.15 (0.03)	0.12 (0.02)

3.4.1.2. Carbon wires

The carbon wires (nominal diameter equal to 6 mm) were used to strengthen the specimens. A picture is given in Figure 8. A yellow sheath of aramid fabric is wrapped around the dry carbon yarn.

Figure 8 Carbon wire employed for reinforcing the specimens in the mortar joints.

The bundle tensile strength provided by the manufacturer resulted equal to 2200 MPa and the elastic modulus, E, equal to 240 GPa. Before the application, wires were impregnated by using a bi-component resin characterized by a flexural strength, f_f, higher than 5 MPa and an ultimate strain, ε_u, equal to 1.2 %.

3.4.2 Specimens

Each specimen was manufactured with five bricks and four 10 mm thick mortar layers and had a nominal total size equal to 250 x 315 x 120 mm^3. Bricks were previously immersed for 24 hours in water, to avoid the depletion of water from the fresh mortar. The curing conditions adopted for the masonry specimens consisted in one month at T = 20 ± 2 °C and RH ≥ 90%.

In order to realize the initial crack, some bricks were previously cut by means of a cylindrical saw: in this way, the depth of the crack is equal to the depth of the brick (120 mm). The initial crack, realized during the construction phase, was intended to simulate a structural condition in which masonry elements that have to be retrofitted can be found in situ. In particular, three types of specimens were constructed:

i) reference specimen with no crack, hereinafter denoted with NC – No Crack (Figure 9a and Figure 9b);

ii) specimens with a large crack crossing through the three central bricks and the two central mortar layers, hereinafter denoted with LC - Large Crack (Figure 9c and Figure 9d);

iii) specimens with a small crack passing through the central brick, hereinafter denoted with SC - Small Crack (Figure 9e and Figure 9f).

It should be noted that the repointing technique was realized during the manufacturing phase, by inserting the carbon bundles, of nominal length equal to 250 mm, in the mortar joints. In particular, NC and LC specimens

were reinforced inserting in each mortar joint two carbon bundles for a total of eight bundles, 30 mm from the edges, in a symmetric position, Figure 9b and Figure 9d, respectively. Before the insertion in the joints, the carbon bundles were impregnated with an epoxy resin and cured. SC specimens were reinforced, by inserting four carbon bundles, 30 mm from the edges, in the central mortar joints, Figure 9f. Specifically, the reinforced No Crack specimens are indicated hereinafter as NC8, the reinforced Large Crack specimens are indicated as LC8, while the reinforced Small Crack specimens are indicated hereinafter as SC4. Three specimens of each type were manufactured, for a total of eighteen specimens.

(a) NC specimen (b) NC8 specimen

(c) LC specimen (d) LC8 specimen

(e) SC specimen (f) SC4 specimen
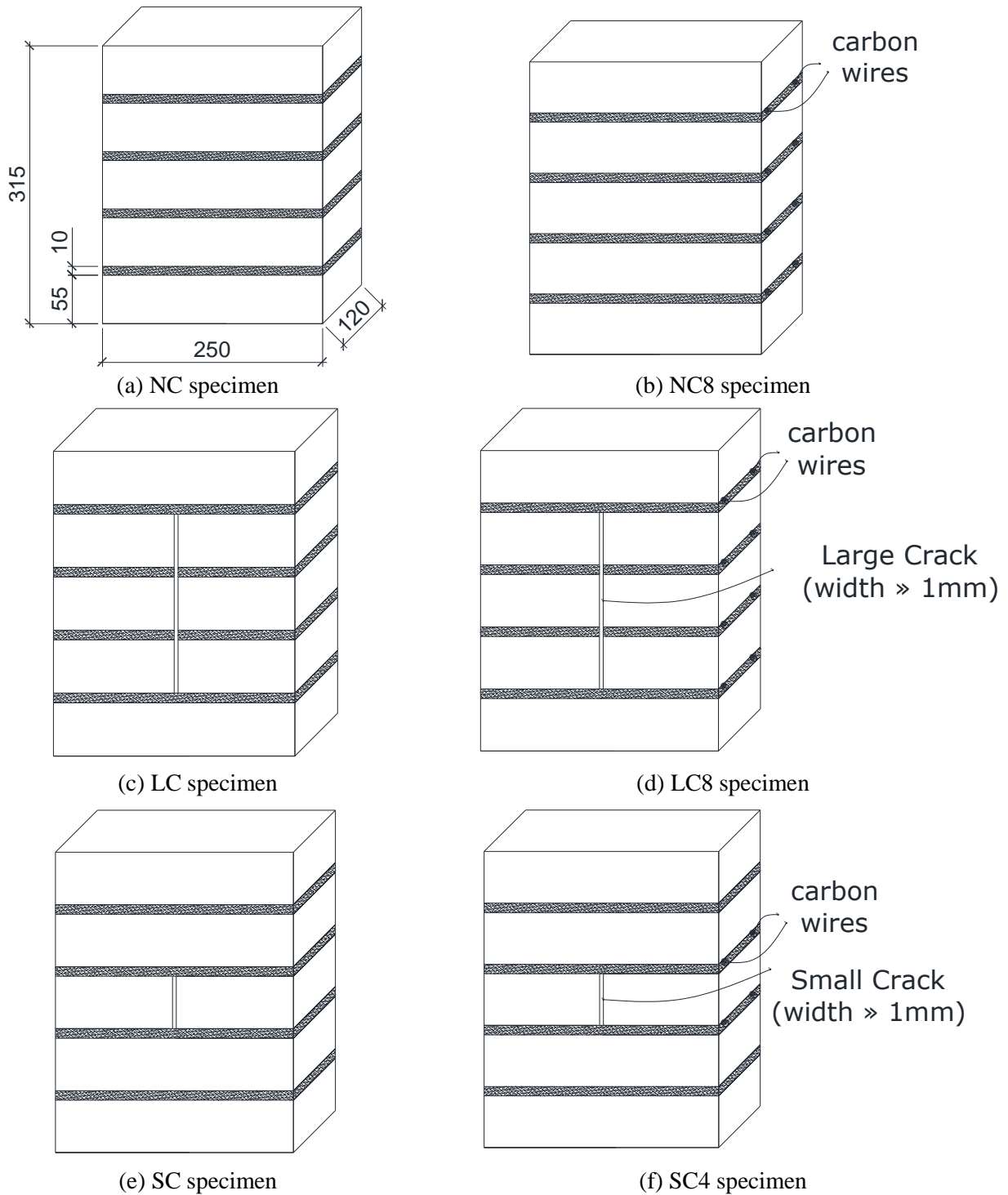
Figure 9 Specimens tested in the experimental program. Dimensions in mm.

In Table 4, the specimens description is summarized.

Table 4 Specimen label and description

Specimen label	Number of each specimens	Description
NC	3	Specimen without crack and without reinforcement (Figure 9a)
NC8	3	Specimen without crack and with 8 carbon bundles in the mortar joints (Figure 9b)
LC	3	Specimen with large crack and without reinforcement (Figure 9c)
LC8	3	Specimen with large crack and with 8 carbon bundles in the mortar joints (Figure 9d)
SC	3	Specimen with small crack and without reinforcement (Figure 9e)
SC4	3	Specimen with small crack and with 4 carbon bundles in the mortar joints (Figure 9f)

3.4.3. Test set up and instrumentation

After curing, all the specimens were subjected to an *ad hoc* designed splitting test. The specimen was positioned vertically on a 100 x 120 x 10 mm^3 steel plate resting on a cylindrical joint. A compression force was applied by means of a thick metallic plate placed above the upper specimen surface; a spherical joint was employed in order to compensate possible irregularities of the specimen geometry, (Figure 10).
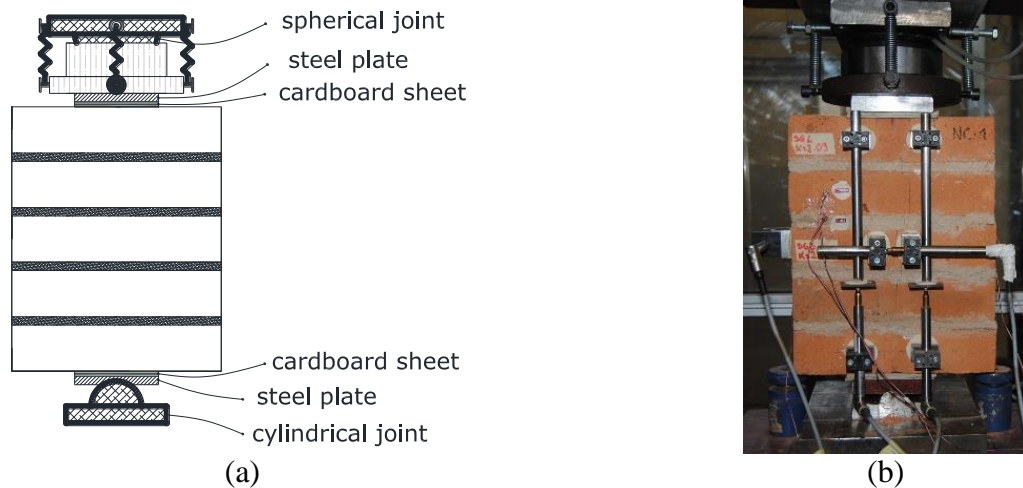
Figure 10 a) Test set-up and b) specimen positioned in the universal machine.

It should be noted that with such apparatus a splitting mode failure of the specimens is obtained. All the specimens were tested in a universal testing machine Metrocom 1000 kN operating in displacement control at a rate equal to 0.2 mm/min.

In Figure 11, the instrumentation of NC and NC8 specimens is described. In the following, the two 250 x 315 mm^2 faces of the specimens are labelled as front face and back face; the two 120 x 315 mm^2 side faces of the specimens are labelled as A-A face and B-B face.

(a) Front face   (b) Back face   (c) Side A-A   (d) Side B-B
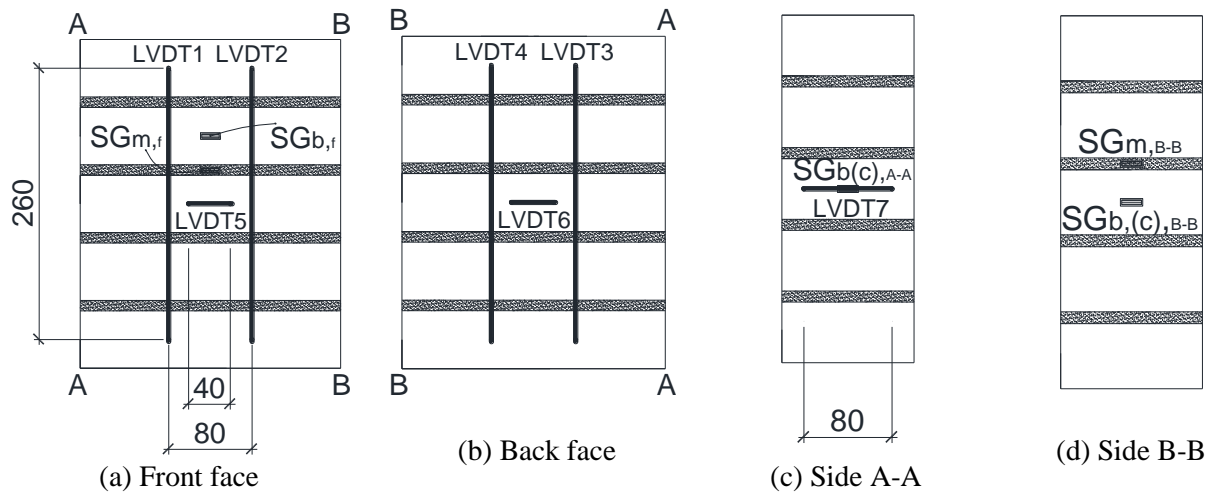
Figure 11 NC and NC8 specimens: instrumentation. Dimensions in mm.

In order to register the specimen displacements and strains during the test, Linear Variable Displacement Transducers (LVDTs) and strain gauges (SGs) were employed. In particular:

- four longitudinal LVDTs (hereinafter named as LVDT1, LVDT2, LVDT3, LVDT4 applied two on the front face and two on the back face of the specimen) with a displacement range 0 - 10 mm are used to evaluate the relative vertical displacements;

- two horizontal LVDTs (hereinafter named as LVDT5 and LVDT6 applied one on the front face and the other on the back face of the specimen) with a displacement range 0 - 10 mm are used to evaluate the Crack Opening Displacement (COD);

- one horizontal LVDT (hereinafter named as LVDT7 applied on A-A face of the specimen) with a displacement range 0 - 2 mm is used to measure the displacement of the central brick in the horizontal direction on the side face;

- two horizontal 10 mm length strain gauges are glued on the central brick on the side faces (hereinafter named as SGb(c),$_{A-A}$ and SGb(c),$_{B-B}$ applied on A-A face and B-B face, respectively);

- one horizontal 6 mm length strain gauge applied on a layer of mortar on B-B face (hereinafter named as SGm,$_{B-B}$);

- one horizontal 10 mm length strain gauge applied on a brick on the front face (hereinafter named as SGb,$_f$);

- one horizontal 6 mm length strain gauge applied on a layer of mortar on the front face (hereinafter named as SGm,$_f$).

The LVDTs are applied through metal bases on the surface of the specimens by using HBM X60 bi-component adhesive, suitable for porous materials. Strain gauges are glued with cyanoacrylate adhesive.

All the instruments were connected to a data acquisition system.

It should be noted that several preliminary tests were conducted in order to calibrate the set-up, the loading condition as well as the instrumentation. Once the results were considered reliable, the experimental tests have been carried out.

In order to collect more detailed information, the instrument set-up was slightly different from the previous one (NC and NC8). In Figure 12, the instrumentation of LC, LC8, SC and SC4 specimens is shown.

(a) Front face and B-B face   (b) Back face and A-A face
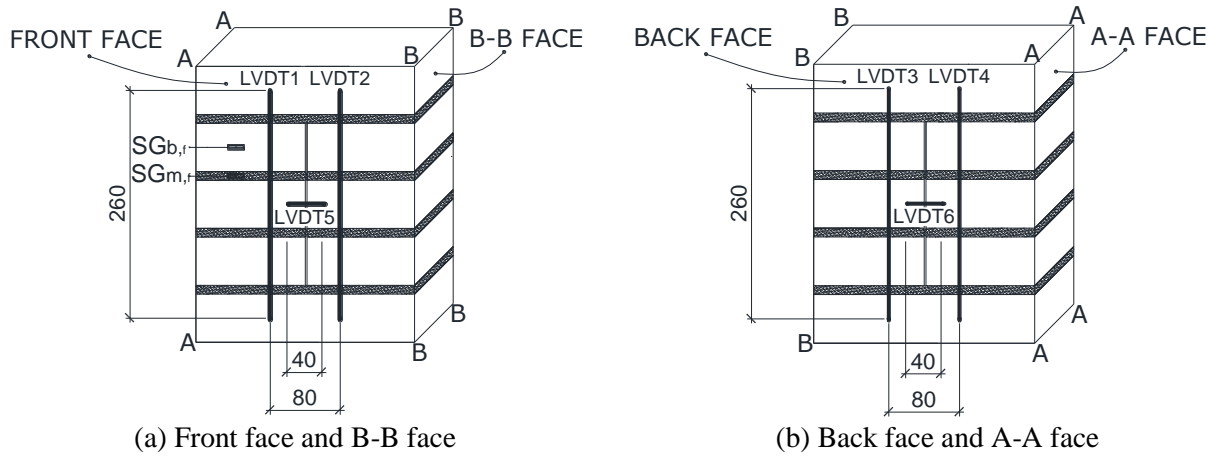
Figure 12 Instrumentation of LC, LC8, SC and SC4 specimens. Dimensions in mm.
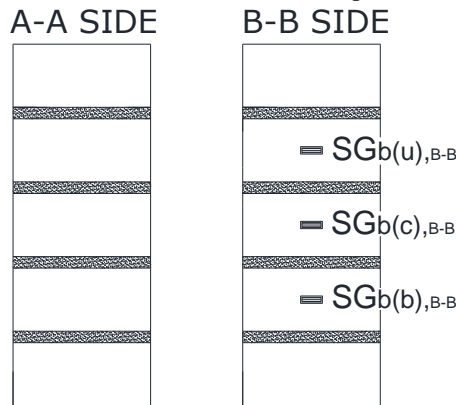
Figure 13 Instrumentation of the side faces of SC4 specimens.

In particular, the vertical displacements were registered by: LVDT1, LVDT2 (both applied on the front face), LVDT3 and LVDT4 (both applied on the back face).

The horizontal displacements at the centre of the specimens across the crack were registered by: LVDT5 (applied on the front face) and LVDT6 (applied on the back face).

With the aim of achieving information about the local deformation state of bricks and mortar, strain gauges were employed. For LC and LC8 specimens, in the front face, $SGb_{,f}$ and $SGm_{,f}$ were applied on the brick and on the mortar, respectively, while one specimen of the type SC4 was instrumented as shown in Figure 13. In particular, SC4 shows on the B-B face three horizontal strain gauges applied on the central bricks ($SGb(b)_{,B-B}$, $SGb(c)_{,B-B}$, $SGb(u)_{,B-B}$). All the instruments were connected to a data acquisition system.

In addition, one specimen per type (NC-3, NC8-3, LC-3, LC8-3, SC-3, SC4-3) on the back face, have been instrumented also with DIC, Digital Image Correlation (Ghiassi et al. 2013). Digital Image Correlation Measurement System, Vic 3D, is able to obtain deformations, ε, in a range of 0.005% ($\pm$ 50 $\mu\varepsilon$). and 2000% The system is made of two 5 Megapixel CCD digital cameras (resolution of 2452 x 2056 pixel) with Schneider lenses. The cameras are installed on a rigid bar to avoid vibrations and small relative displacements, Figure 14a. The bar is positioned on a tripod. For application of the DIC technique, a speckle pattern, produced by applying a thin coating of white matt followed by a spread distribution of black dots using spray paint, is applied to the specimens surfaces. Cameras are placed at 1 m from the specimen. For the data acquisition, Vic snap software is used. In Figure 14b, the adopted reference system, xy, for the specimens is shown.

(a) Instrumentation
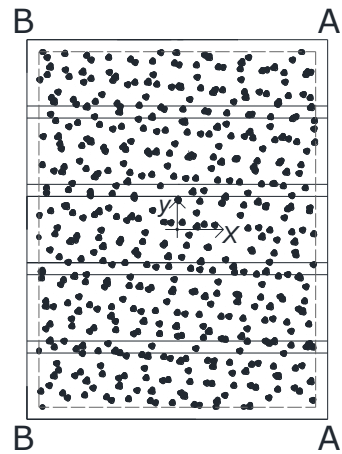
(b) Reference system *xy*

Figure 14 DIC

3.4.4. Test results

3.4.4.1. NC specimens

In the following, results obtained from the tests conducted on no crack specimens without reinforcement (NC-1, NC-2 and NC-3) are presented. In particular, results are given in terms of load versus vertical displacement (load - *v* curves), load versus horizontal displacement (load - *u* curves), load versus strains registered on the side faces (A-A and B-B) as well as load versus strains on the front face. In the following figures, grey curves are referred to NC specimens results, while black curves are relative to NC8 specimens whose results will be described in Section 10.1.4.2.

It is worth noting that positive signal of the LVDTs means shortening, while negative signal means elongation. The convention for the strain gauges is opposite to the LVDT one.

NC-1 specimen at three different stages during the splitting test is shown in Figure 15.

(a)

(b)

(c)

Figure 15 NC-1 specimen: a) at the beginning of the test; b) propagation of the crack for a load equal to 60 kN and c) specimen failure at the end of the test.

In order to check for the symmetry of the test set up, in Figure 16 all the load - *v* curves obtained from the four vertical LVDTs (from LVDT1 to LVDT4) applied on specimen NC-1 are shown. The bold grey curve (LVDTv mean) is obtained as the average of the signals from the four LVDTs. For clarity purposes, only the curves obtained from NC-1 specimen are presented, since the other not reinforced specimens show a similar behavior.
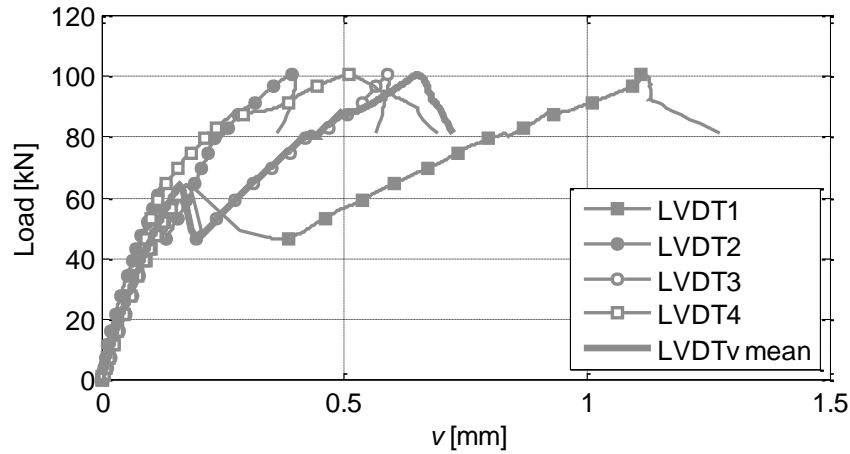
Figure 16 Load - *v* curves for NC-1 specimen from LVDT1, LVDT2, LVDT3 and LVDT4. Average curve is in grey continuous line.

Figure 16 shows that the symmetry during the tests is maintained. The four curves from the vertical LVDTs overlap in the elastic phase, and differences attain for higher values of load. It is worth noting, LVDT1 registers a greater displacement after the propagation of the crack due to a small rotation of the steel plate contrast of the LVDT itself.

Figure 17, collects the load - *u* curves obtained from the test on NC-1 specimen. As before, there are two curves related to the two horizontal LVDTs (LVDT5 and LVDT6), while the bold grey curve (LVDTu mean) is obtained as the average of the two curves.
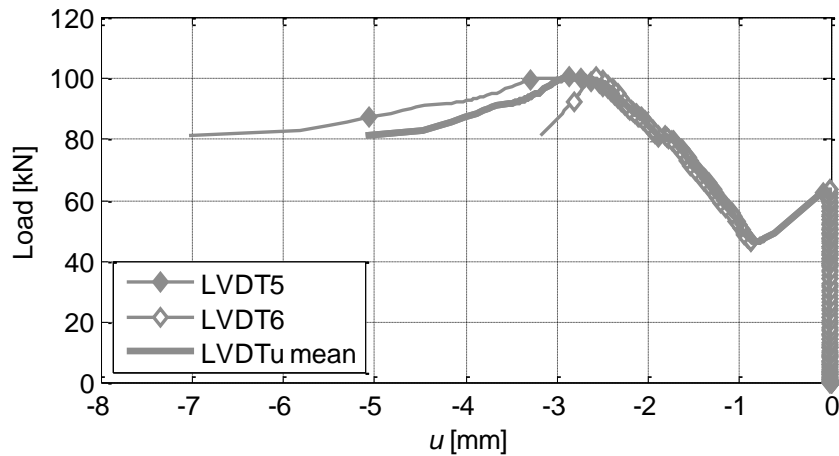
Figure 17 Load - *u* curves for NC-1 specimen from LVDT5 and LVDT6. Average curve is in grey continuous line.

Figure 17 confirms the good symmetry preserved during the test. In fact, the COD registered by the two opposite horizontal LVDTs overlap for the major part.

The load - *v* curves for all the NC specimens are reported in Figure 18a in grey color. The curves are calculated as the average of the four LVDTs on each specimen. In Figure 18b, a simplified schematization of the curves is reported.
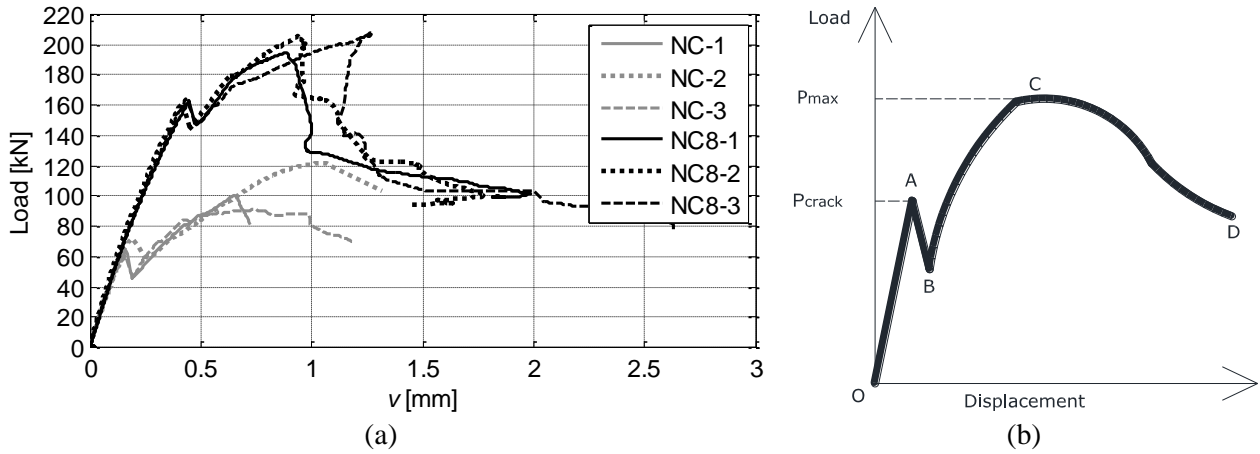
Figure 18 Load - *v* curves: a) for NC-1 (grey continuous line), NC-2 (grey dotted line), NC-3 (grey dashed line), NC8-1 (black continuous line), NC8-2 (black dotted line) and NC8-3 (black dashed line); b) simplified schematization.

Figure 19 collects all the average load - *u* curves in grey color for all the NC specimens.
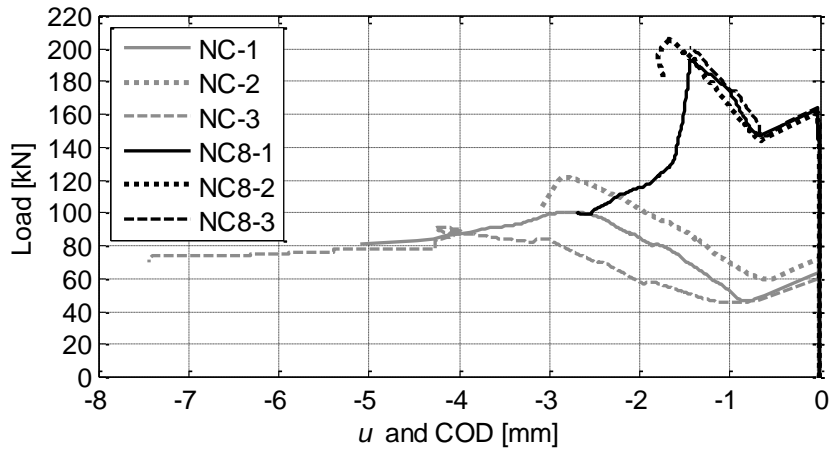
Figure 19 Load – *u* curves for NC-1 (grey continuous line), NC-2 (grey dotted line), NC-3 (grey dashed line), NC8-1 (black continuous line), NC8-2 (black dotted line), NC8-3 (black dashed line).

Figure 18a collects all the load-vertical displacement curves from all the tested NC specimens. In Figure 18b six main features can be distinguished: (*i*) pre-crack condition (from point O to point A); (*ii*) crack formation, P_{crack} (point A); (*iii*) load drop (from point A to point B); (*iv*) increasing load (from point B to point C); (*v*) peak load, P_{max} (point C) and (*vi*) post-peak softening (from point C to point D).

For all the specimens the pre-crack condition is characterized by an almost linear elastic branch until load attains a value around 60 kN. Afterwards, a drop of about 10 kN corresponding to the formation of a vertical crack in the middle of the specimen occurs. Then, the load starts to increase again corresponding to new sources of strength of the specimens, even if with a significant decrease in stiffness (the second ascending branch is less steep than the first one), until a peak load around 100 kN is reached. In the post-peak behavior, a softening branch can be detected before a brittle collapse occurs. The failure mechanism of the NC specimens is characterized by a brittle and sudden splitting of the specimen in two parts, Figure 15c. Besides, after the peak load is attained, horizontal cracks at the interface between mortar and brick start to propagate. These cracks are due to the particular stress state that characterizes the NC specimens during the test. At the beginning, the specimens are compressed, while after the propagation of the crack, the state of stress changes from a compression in the centre under the loading plate towards flexure. The flexure, starting from the external edges, creates tractions in the vertical direction resulting in the horizontal cracks.

Reference is made to the grey curves in Figure 19, where the load-horizontal displacement curves for NC-1, NC-2, and NC-3 specimens are reported. As long as the load is below 60 kN, the horizontal displacement is around zero. Once the load attains the P_{crack} value, a meaningful displacement is registered confirming that for this value of load a crack starts to open. In other words, below P_{crack} in the elastic phase, the strains can be still evaluated, while at P_{crack}, the crack opening displacement measure is adopted (Hillerborg 1991). Then, the specimens are able again to sustain load, even if with a lower value of stiffness and, correspondingly, a large increase in the horizontal displacement (COD) is verified.

Results obtained from LVDT7 and the three strain gauges ($SGb(c)_{,A-A}$, $SGb(c)_{,B-B}$ and $SGm_{,B-B}$) on the A-A and B-B faces of the NC-1, NC-2 and NC-3 specimens are presented in Figure 20a, Figure 20b, Figure 20c and Figure 20d, respectively. In order to compare results from LVDT7 and strain gauges, the sign of the curve obtained from transducer was changed (i.e. in Figure 20a, positive signal means elongation). In Figure 20e and Figure 20f, the load - strain curves obtained from strain gauges $SGb_{,f}$, applied on the brick, and $SGm_{,f}$ applied on the mortar, on the front face of the specimens are represented, respectively.

In Figure 20a, the horizontal strains on the middle brick (A-A face) of all the NC specimens calculated from the LVDT7 signal are reported. In general, for low load values, the strains are positive which correspond to an elongation of the central brick in the side face. Once the P_{crack} is attained, a discontinuity in the behavior is registered. For NC-3, the transducer reveals a negative deformation, means contraction, during the elastic phase.

The curves for $SGb(c)_{,A-A}$, that is applied under LVDT7, Figure 20b, show a good agreement with the ones obtained from LVDT7, Figure 20a. Generally, during the elastic phase, the strains are positive. Then, after the propagation of the crack, an inversion in the direction is observed and the strains become negative. This represents another indication of the change in the specimen stress state from compression to combined compression and bending that produces negative strains on the sides of the specimens.

Comparing the curves from $SGb(c)_{,A-A}$ with the ones obtained from $SGb(c)_{,B-B}$, Figure 20c, glued on the central brick, in a symmetric position one respect to the other, a good agreement is revealed, confirming the symmetry maintained during the test. Figure 20d shows the curves obtained from $SGm_{,B-B}$ applied in the mortar layer on A-A face. NC-1 and NC-3 curves are in agreement. However, for NC-2 specimen, $SGm_{,B-B}$ indicates during the elastic phase, a negative deformation possibly due to a defect in the application of the strain gauge on the mortar layer. A good agreement of the results in Figure 20e and Figure 20f for $SGb_{,f}$ on the brick and $SGm_{,f}$ on the mortar applied on the front face, respectively, is achieved before the propagation of the crack. After this phenomenon, due to a very small distance between the strain gauges and the vertical crack, the results may be not reliable. As expected, the strains in the horizontal direction on the front face are one order of magnitude bigger (around 0.1%) than the ones registered in the side faces (around 0.01%).
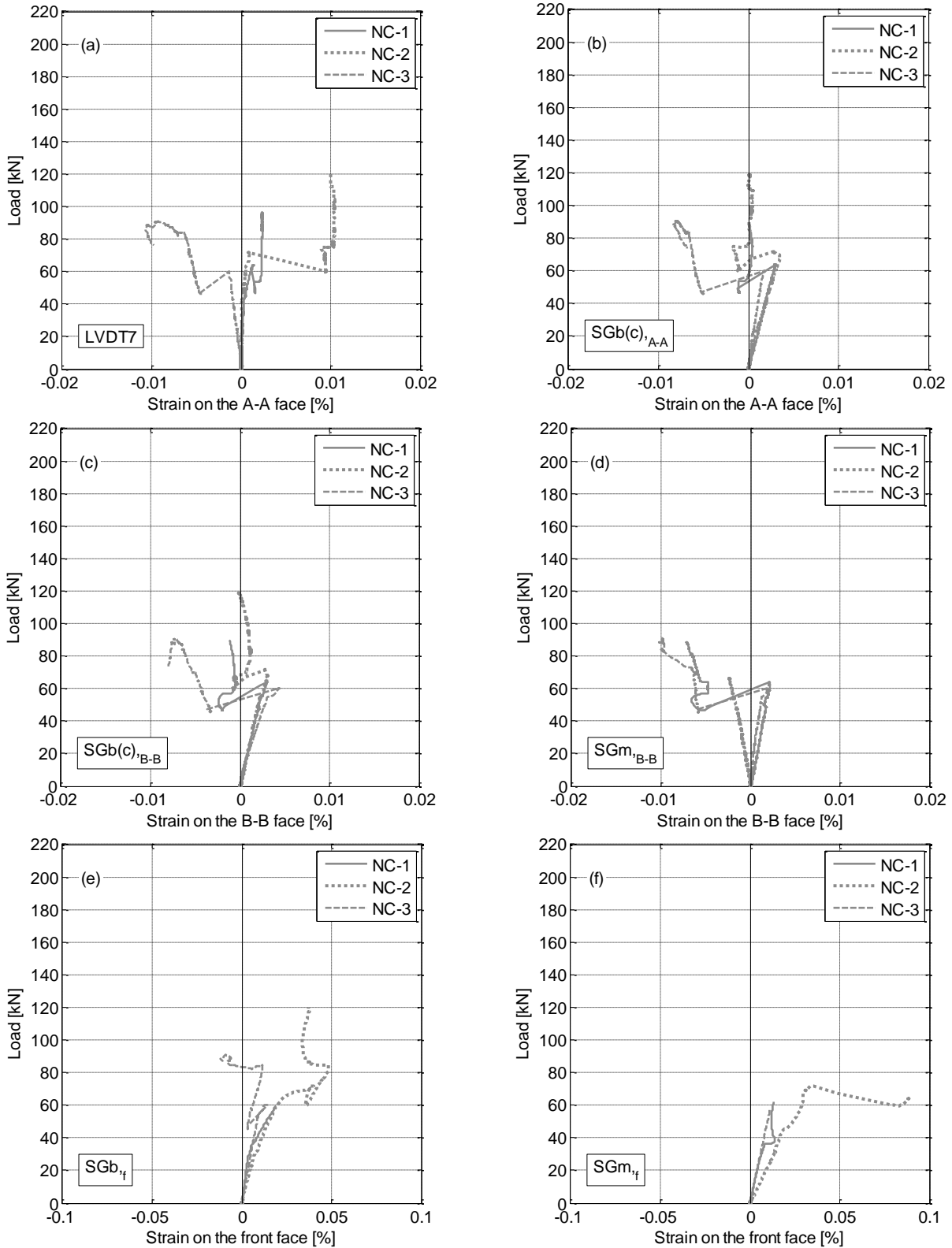
Figure 20 a) Load - strain in the brick obtained from LVDT7 (A-A face); b) load - strain in the brick obtained from SGb(c),$_{A-A}$ (A-A face); c) load - strain in the brick obtained from SGb(c),$_{B-B}$ (B-B face); d) load - strain in the mortar obtained from SGm,$_{B-B}$ (B-B face); e) load - strain in the brick obtained from SGb,$_f$ (front face); f) load - strain in the mortar obtained from SGm,$_f$ (front face). NC-1 (grey continuous line), NC-2 (grey dotted line), NC-3 (grey dashed line).

3.4.4.1.1. DIC

The color maps of the strains, ε_{xx}, in the horizontal direction at four levels of load are shown in Figure 21. The values of load chosen are: 15 kN (elastic branch), 59 kN (P_{crack}), 45 kN (load drop after P_{crack}) and 90 kN (P_{max}).

54
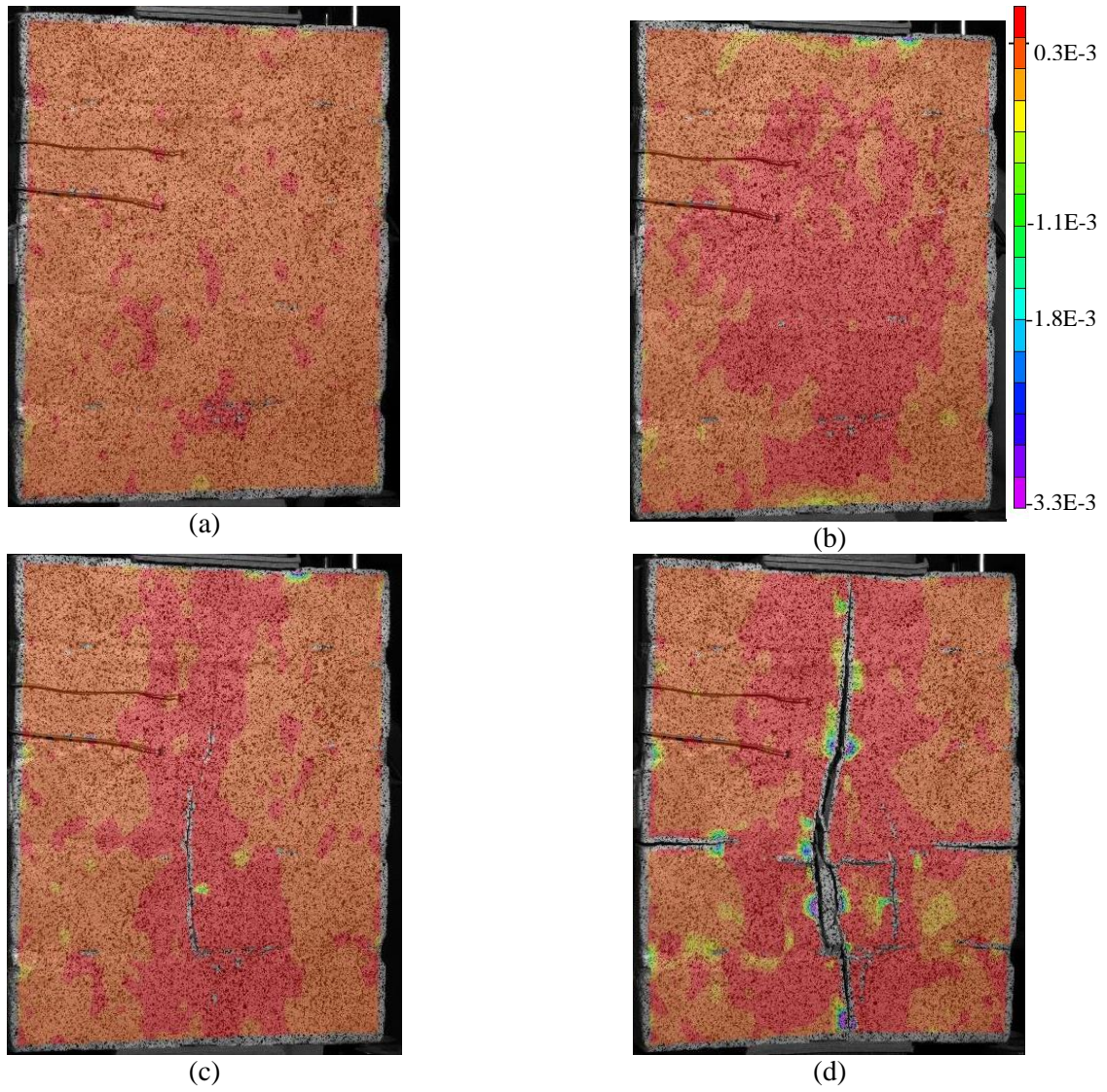
Figure 21 NC-3 specimen: color maps of the strains in the horizontal direction, ε_{xx}, for load levels equal to a) 15 kN (elastic branch); b) 59 kN (P_{crack}); c) 45 kN (load drop) and d) 90 kN (P_{max}).

The color maps of the strains, ε_{yy}, in the vertical direction at the same load levels are shown in Figure 22.
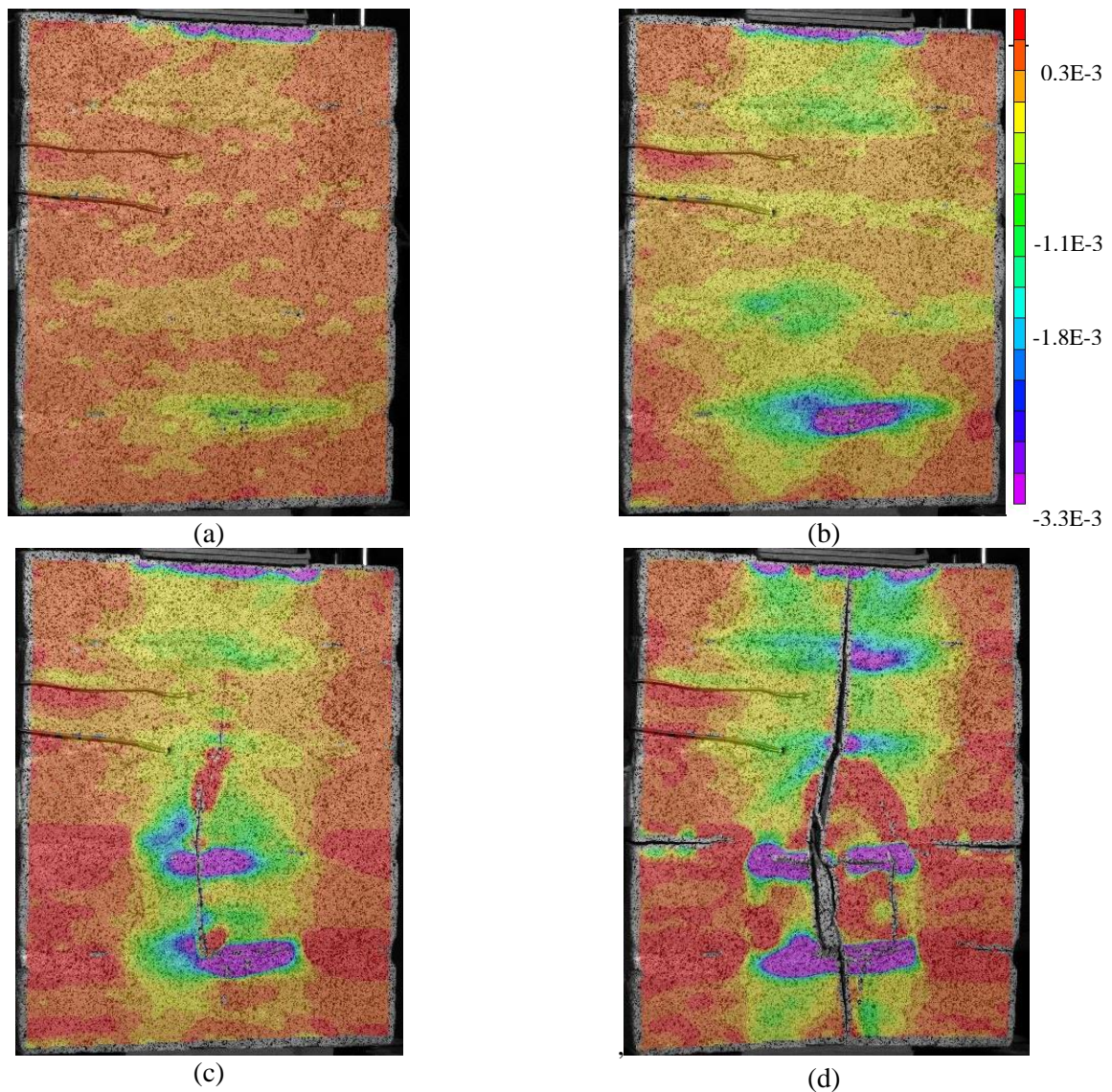
Figure 22 NC-3 specimen: color maps of the strains in the vertical direction, ε_{yy}, for load levels equal to a) 15 kN (elastic branch); b) 59 kN (P_{crack}); c) 45 kN (load drop) and d) 90 kN (P_{max}).

It should be noted that for comparison purposes the deformation scale for ε_{xx} and ε_{yy} has been kept the same for NC-3 and NC8-3.

The color maps of ε_{xx}, Figure 21, show that from a load of 15 kN (Figure 21a) to a load of 59 kN (Figure 21b), the deformation starts to increase towards the centre of the specimen (darker color in Figure 21b). At 45 kN, Figure 21c, the vertical crack has propagated and at P_{max}, Figure 21d, horizontal cracks at the brick/mortar interface are also visible.

In Figure 22, deformations in the vertical direction are concentrated in the area under the loading plate with negative values. Positive values attain at the edges of the specimen.

In order to investigate the behavior of the specimens in the vertical direction, five fictitious LVDTs have been chosen (1A, 1B, 1C, 1D, 1E), 260 mm long, i.e. the same length of the real longitudinal LVDTs, Figure 23a. It should be noted that 1A and 1E sections are outside the loading plate; 1B and 1D are under the corners of the load plate in the same positions of LVDT3 and LVDT4; while 1C section is in the middle of the specimen.

In order to investigate the behavior of the specimens in the horizontal direction, five sections in the middle of

the bricks have been chosen (2A, 2B, 2C, 2D, 2E), 40 mm long, i.e. the same length of the real horizontal LVDTs, Figure 23b.

(a)   (b)
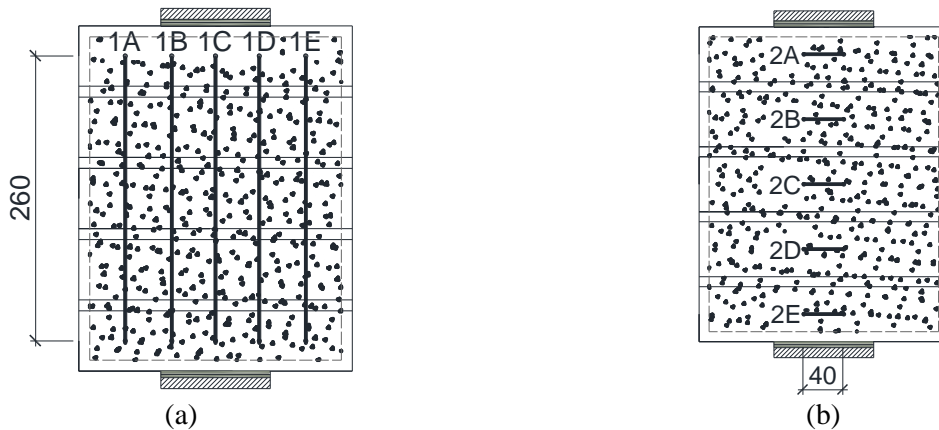
Figure 23 Fictitious a) vertical and b) horizontal LVDTs. Dimensions in mm.

In Figure 24a, the load - *v* curves obtained from fictitious LVDTs 1B and 1D symmetrically displayed with respect to real LVDTs 1 and 2 are reported. The load - *v* curves obtained from fictitious LVDTs 1A, 1C and 1E are depicted in Figure 24b.
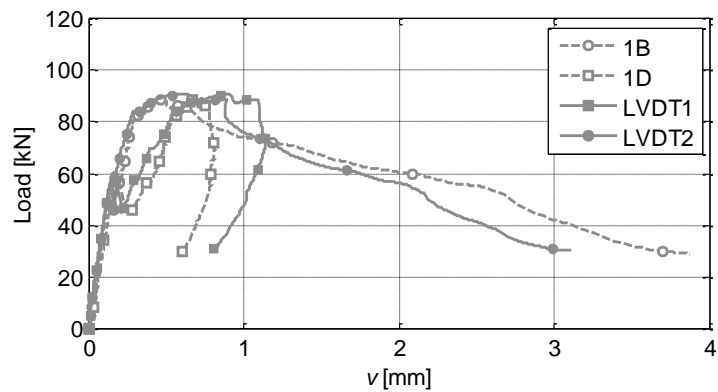
(a)
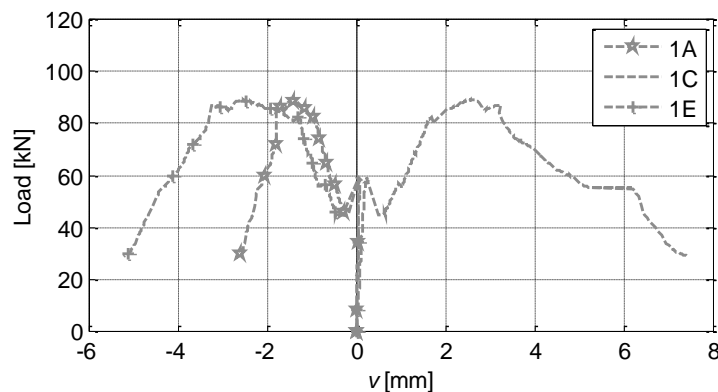
(b)

Figure 24 Load - *v* curves for NC-3 specimen: a) obtained from real LVDTs (LVDT1 and LVDT2 on the front face) and fictitious LVDTs (1B and 1D on the back face) and b) obtained from fictitious LVDTs (1A, 1C and 1E on the back face).

The curves in Figure 24 show that the fictitious LVDTs 1B, 1C and 1D, that are under the plate, remain in the positive part of the displacements. This confirms that under the plate the state of stress remains of compression showing a contraction in the vertical displacements.

On the contrary, the displacement registered by the outermost LVDTs (1A and 1E) is positive before P_{crack} is attained, then, with the propagation of the crack, become negative showing an elongation. This behavior confirms that a state of flexure is verified close to the specimen edges.

The load - u curves obtained from fictitious LVDTs, 2A, 2B, 2C, 2D and 2E are shown in Figure 25a, Figure 25b.

(a)

(b)
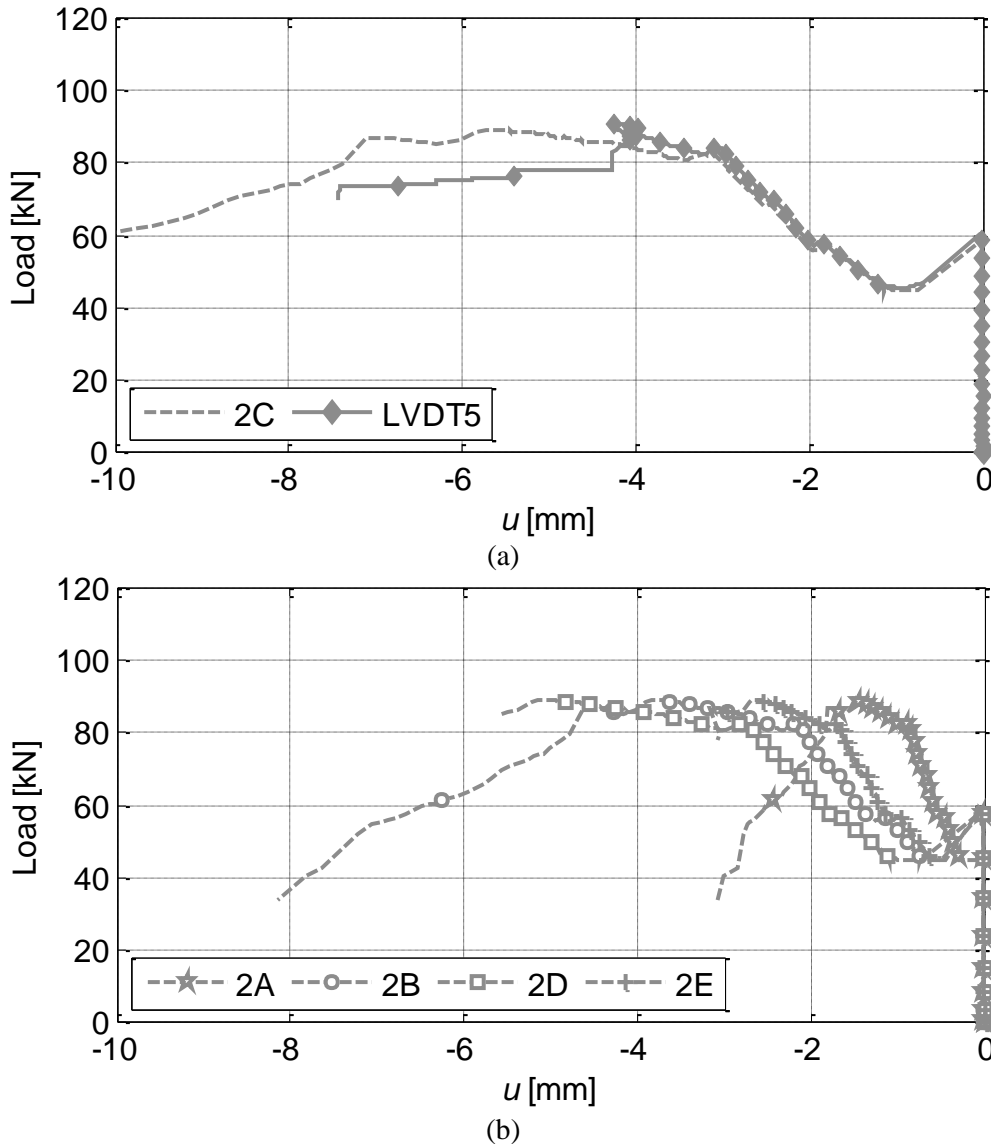
Figure 25 Load - u curves for NC-3 specimen: a) obtained from real LVDT (LVDT5 on the front face) and fictitious LVDT (2C on the back face) and b) obtained from fictitious LVDTs (2A, 2B, 2D and 2E on the back face).

The horizontal displacement curves registered in the five LVDTs, Figure 25, show that, as expected, the highest is the one registered at the centre of the specimen (2C). While in the top and bottom brick, close to the tips of the crack, the COD is smaller.

3.4.4.2. NC8 specimens

In the following, results obtained from the tests conducted on reinforced specimens (NC8-1, NC8-2 and NC8-3) are presented. In Figure 26, NC8-1 specimen during the test is shown.

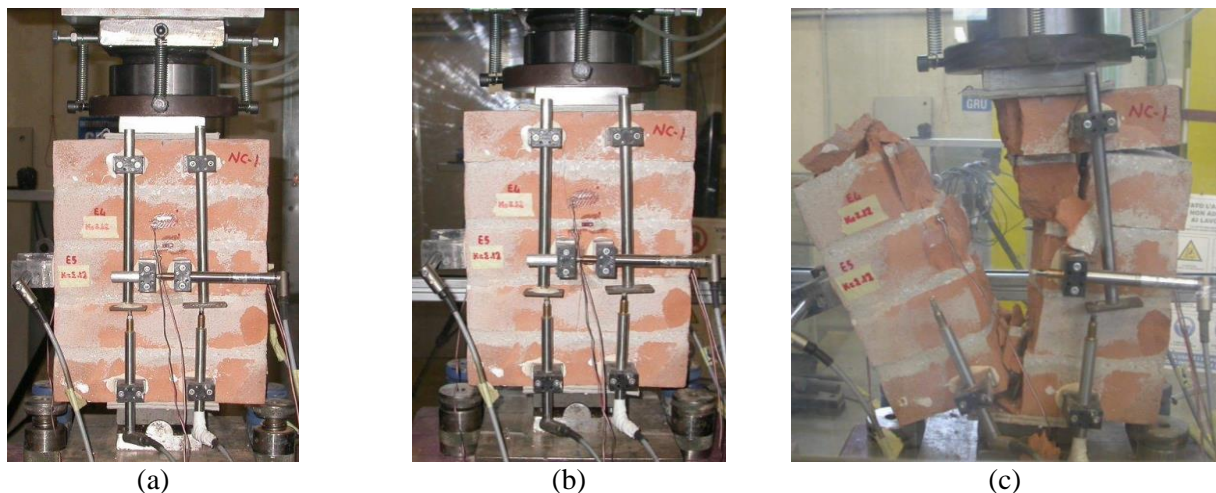|		
(a)	(b)	(c)
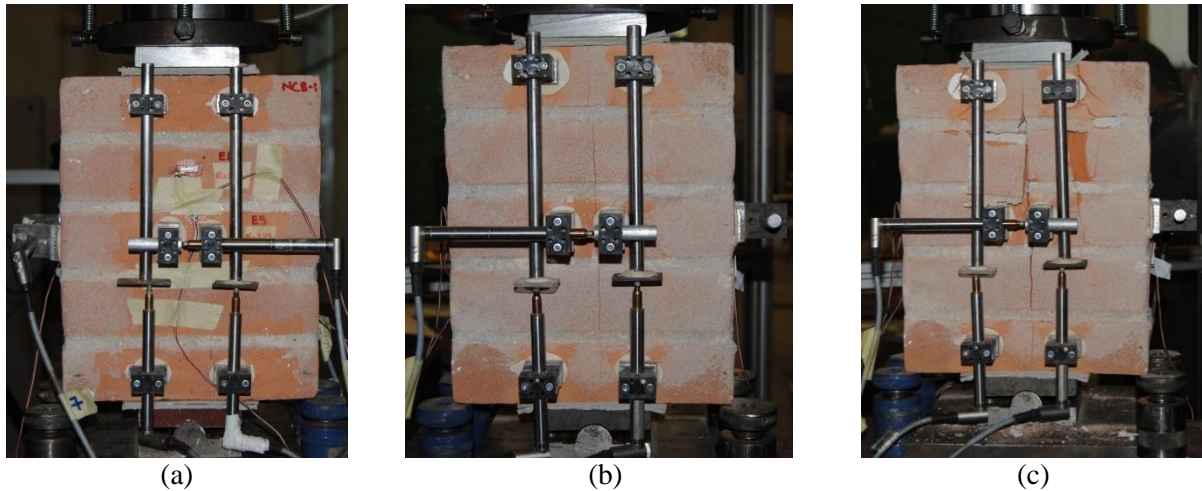
Figure 26 NC8-1 specimen: a) at the beginning of the test; b) propagation of the crack for a load equal to 160 kN and c) specimen failure at the end of the test.

The load - v curves and the load - u curves for all the reinforced specimens are reported in Figure 18a and Figure 19 in black color, respectively. Curves are obtained as the average of the corresponding LVDTs.

In the load - v curves for NC8-1, NC8-2 and NC8-3 specimens, Figure 18a black curves, the same six features detected in the NC specimens can be observed.

The first phase, representing a pre-crack condition, is characterized by a linear branch until a load equal to 160 kN (P_{crack}). Then, a drop of about 20 kN occurs due to the propagation of a vertical crack in the middle of the specimen. In the third phase, the specimens are still able to sustain increasing load with a decrease in stiffness (the slope of this branch of the curves is lower with respect to the slope of the first branch), until a peak load around 200 kN (P_{max}) is attained. It is worth noting that the confinement on the faces of the specimen along the horizontal direction due to the presence of carbon wires in the mortar joints, produces a lower stiffness reduction during the third phase with respect to the behavior showed by NC specimens. Indeed, the mean vertical displacement at which P_{max} is attained is around 1 mm as for NC specimens, but occurs for a level of load that is double compared to the not reinforced specimens. The failure mechanism of the reinforced specimens is mainly ductile and no sudden ruptures occur, since the wires work as arrestor against the propagation of the vertical crack. At the end of the test, the global failure of the specimens is due to the local failure of the brick under the loading plate that is interested by inclined cracks, Figure 26c. The stress state in the NC8 specimens remains mainly of compression during the test and no horizontal cracks occur at the brick/mortar interface.

In the load-horizontal displacement curves, Figure 19 black curves, after the first rigid, elastic branch until a load equal to P_{crack}, an increase in the horizontal displacement (smaller compared to the one reached for the not reinforced specimens) due to the opening of the crack is observed.

Results obtained from LVDT7 and the three strain gauges (SGb(c),$_{A-A}$, SGb(c),$_{B-B}$ and SGm,$_{B-B}$) on the A-A and B-B faces of the specimens are represented in Figure 27a, Figure 27b, Figure 27c and Figure 27d, respectively. In Figure 27e and Figure 27f, the load - strain curves obtained from strain gauges SGb,$_f$, applied on the brick, and SGm,$_f$, applied on the mortar, on the front face of the specimens are represented, respectively.
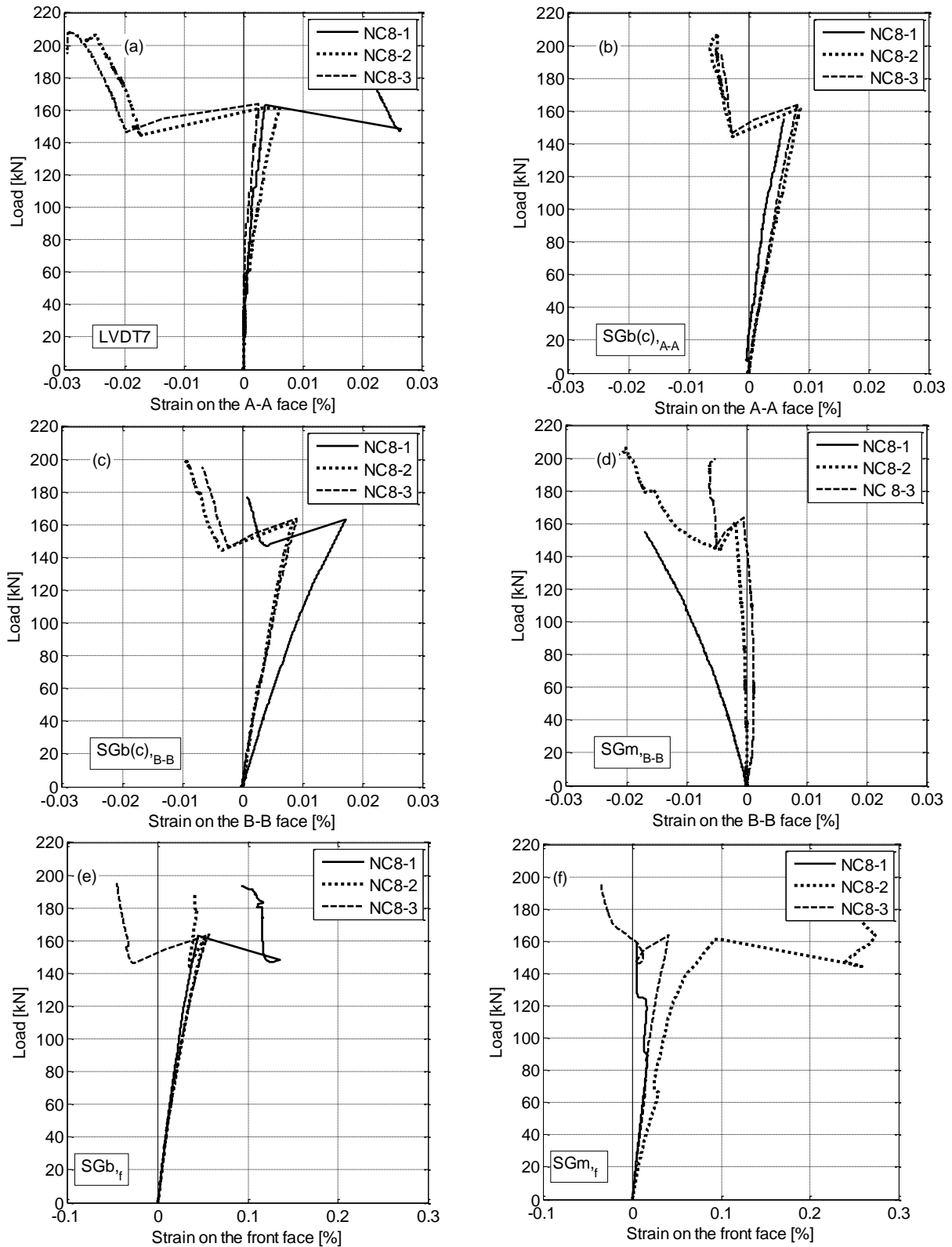
Figure 27 a) Load - strain in the brick obtained from LVDT7 (A-A face); b) load - strain in the brick obtained from SGb(c),A-A (A-A face); c) load - strain in the brick obtained from SGb(c),B-B (B-B face); d) load - strain in the mortar obtained from SGm,B-B (B-B face); e) load - strain in the brick obtained from SGb,f (front face); f) load - strain in the mortar obtained from SGm,f (front face). NC8-1 (black continuous line), NC8-2 (black dotted line), NC8-3 (black dashed line).

From Figure 27a to Figure 27d, the strains in the A-A and B-B faces of the specimens at P_{crack} are larger than the ones registered in the NC specimens, due to the higher and the orthogonal confinement exerted by the longitudinal carbon wires.

A good agreement is observed in Figure 27a and Figure 27b between the LVDT7 applied on the side face of the specimens and the corresponding strain gauge SGb(c)$_{,A-A}$, except for post-crack behavior of the specimen NC8-1 for which the LVDT registers positive deformations, while SGb(c)$_{,A-A}$ negative ones.

The signals of strain gauges SGb(c)$_{,A-A}$ and SGb(c)$_{,B-B}$, Figure 27b and Figure 27c, glued on the central brick, in a symmetric position one respect to the other, show a good agreement.

The deformations registered from strain gauge SGm$_{,B-B}$ applied in the mortar layer, Figure 27d, are more dispersed and specimen NC8-1 show negative values also in the elastic branch. The reasons of this behavior can be ascribed to a defect in the application of the strain gauge or to the possible formation of micro-cracks close to the strain gauge.

In Figure 27e and Figure 27f, the results derived from two horizontal strain gauges (SGb$_{,f}$ on the brick and SGm$_{,f}$ on the mortar) applied on the front face show a good agreement before the propagation of the crack. After, due to the very small distance between the strain gauges and the vertical crack, the results may be not reliable.

3.4.4.2.1. DIC

Four levels of load have been considered in order to plot the color maps of the strains ε_{xx} and ε_{yy} in the horizontal and vertical direction, Figure 28 and Figure 29, respectively. The values of load chosen are: 90 kN (P_{max} for NC specimens and elastic branch for NC8 specimens), 160 kN (P_{crack} for NC8 specimens), 143 kN (load drop after P_{crack} for NC8 specimens) and 204 kN (P_{max} for NC8 specimens).

(a)

(b)

(c)

(d)
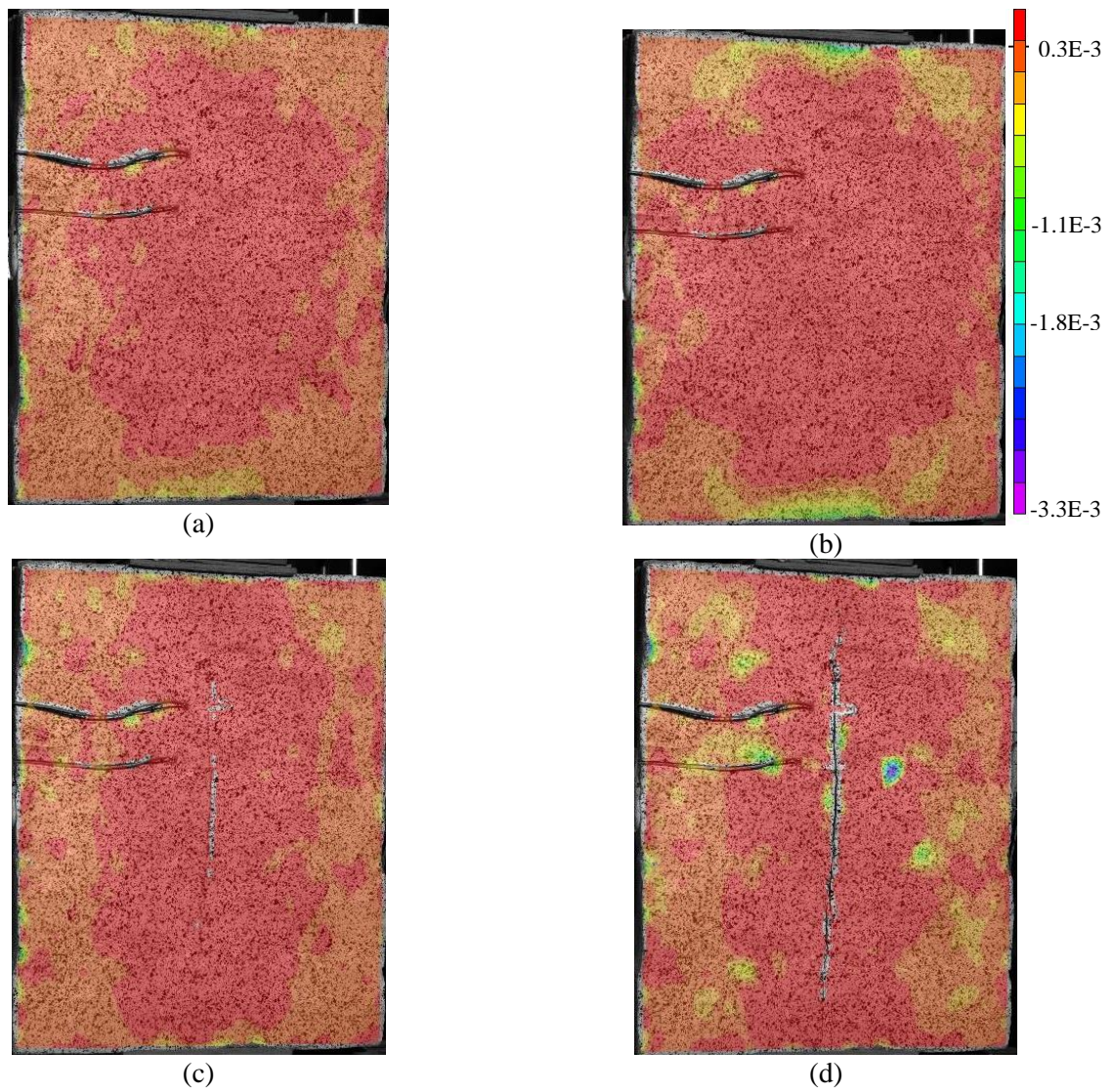
Figure 28 NC8-3 specimen: color maps of the strains in the horizontal direction, ε_{xx}, for load levels equal to a) 90 kN (elastic branch); b) 160 kN (P_{crack}); c) 143 kN (load drop) and d) 204 kN (P_{max}).
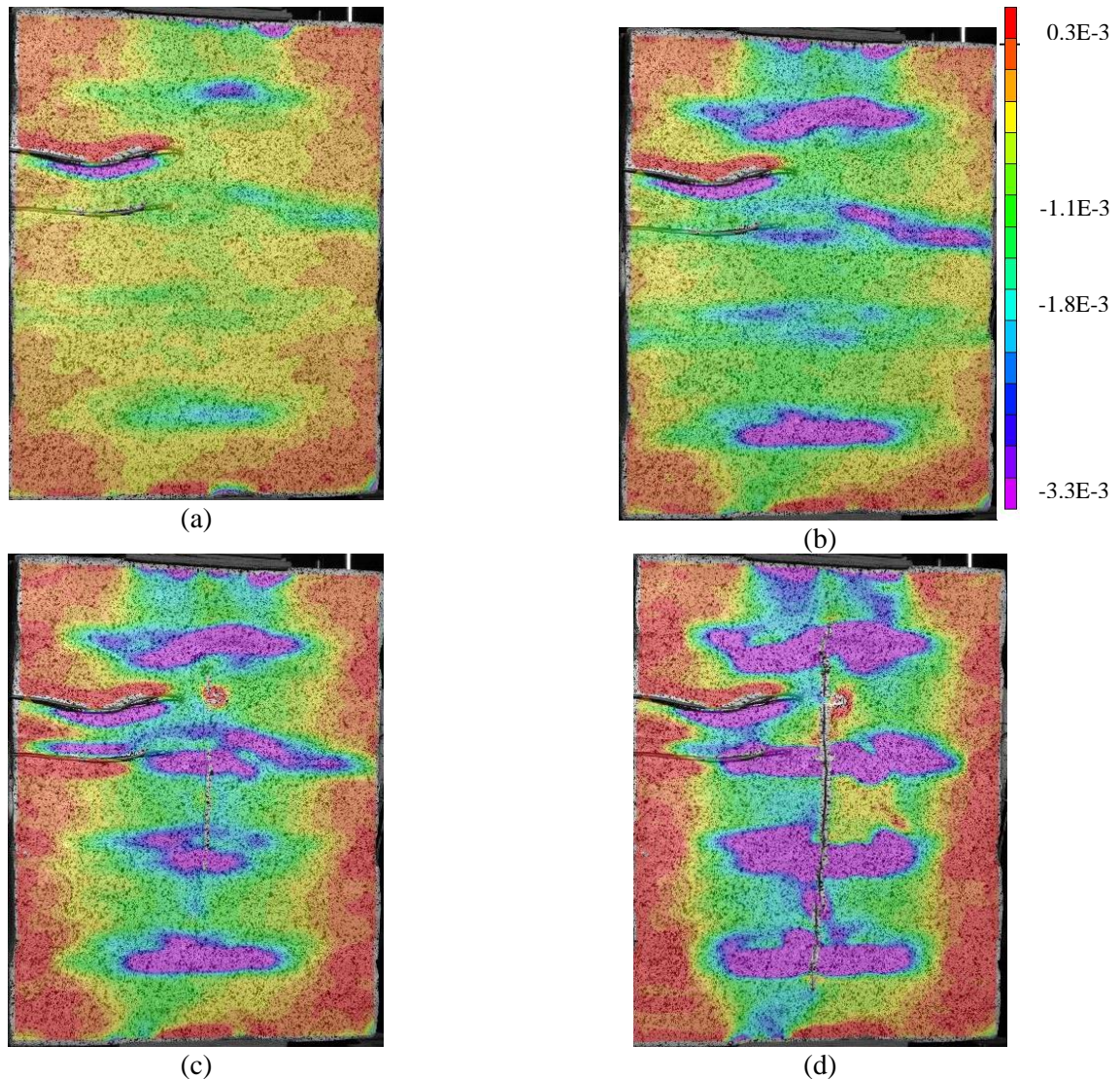
Figure 29 NC8-3 specimen: color maps of the strains in the vertical direction, ε_{yy}, for load levels equal to a) 90 kN (elastic branch); b) 160 kN (P_{crack}); c) 143 kN (load drop) and d) 204 kN (P_{max}).

The color maps for ε_{xx}, Figure 28, show that for a load equal to 90 kN, i.e. P_{max} for the NC specimens but is still in the elastic phase for NC8 specimens, horizontal strains are almost uniformly distributed all over the surface. A strain concentration starts to be visible at 160 kN which corresponds to the load at which the crack starts to propagate.

For what concerns ε_{yy}, Figure 29, the vertical deformations are negative in the greatest part of the specimen and the confinement effect of the presence of the carbon wires in the joints is evident.

The same vertical and horizontal fictitious LVDTs chosen for the NC specimens are considered for the NC8 specimens (Figure 23a and Figure 23b, respectively).

A comparison between load - v curves between real LVDTs (LVDT1 and LVDT2) and fictitious LVDTs (1B and 1D) is reported in Figure 30a, while results from the other fictitious LVDTs (1A, 1C and 1E) are depicted in Figure 30b.
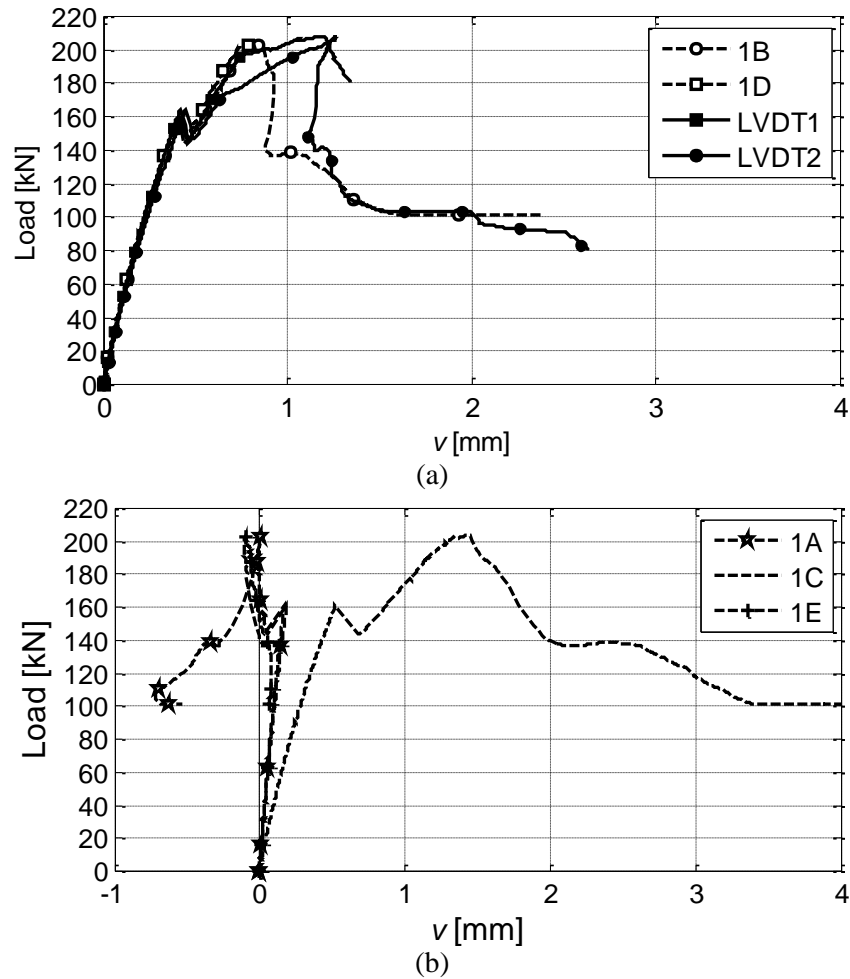
(a)

(b)

Figure 30 Load - *v* curves for NC8-3 specimen: a) obtained from real LVDTs (LVDT1 and LVDT2 on the front face) and fictitious LVDTs (1B and 1D on the back face) and b) obtained from fictitious LVDTs (1A, 1C and 1E on the back face).

The load - *v* curves in Figure 30, show that LVDTs 1B, 1C and 1D under the loading plate, register a positive displacement during the whole test, meaning a contraction of the specimen that remains compressed. The displacements registered by LVDTs 1A and 1E (outside the plate) are positive before P_{crack} is attained, then they become very close to zero. Only 1A registers negative displacements in the very end of the test. This confirms that the state of stress in the reinforced specimens is mainly of compression.

A comparison between load - *u* curves between real LVDT (LVDT5) and fictitious LVDT (2C) is reported in Figure 31a, while results from the other fictitious LVDTs (2A, 2B, 2D and 2E) are depicted in Figure 31b.

(a)

(b)
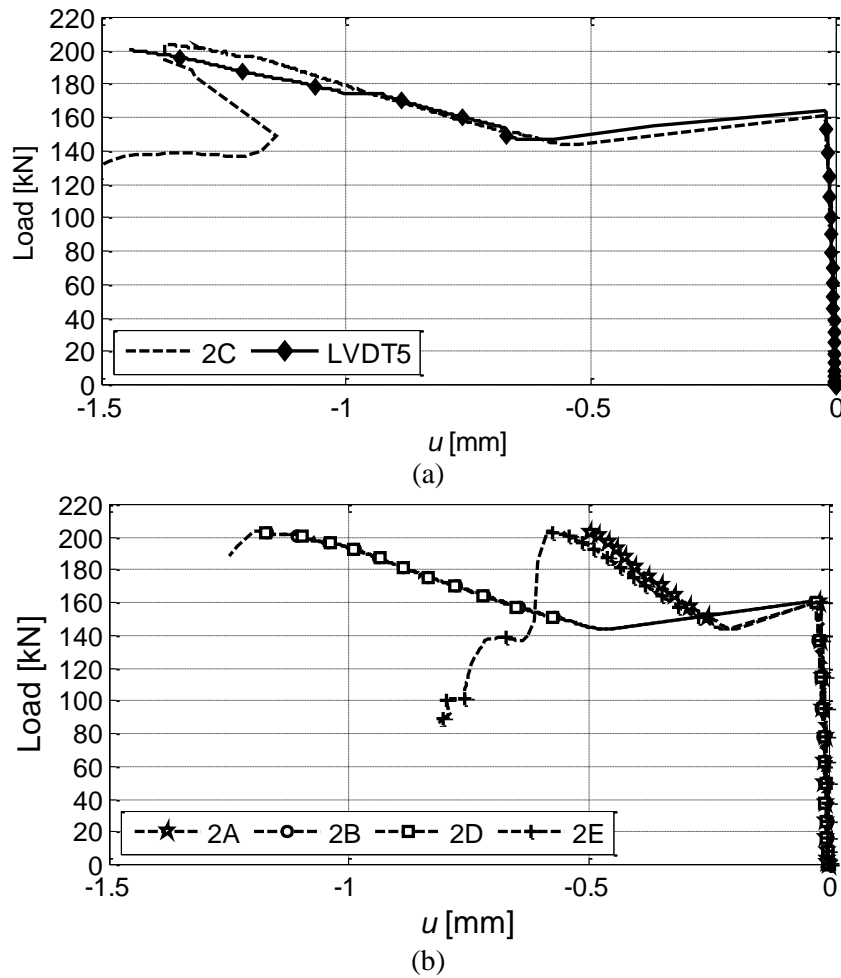
Figure 31 Load - *u* curves for NC8-3 specimen: a) obtained from real LVDT (LVDT5 on the front face) and fictitious LVDT (2C on the back face) and b) obtained from fictitious LVDTs (2A, 2B, 2D and 2E on the back face).

The horizontal displacement curves registered in the five fictitious LVDTs, Figure 31, show that, as before, the higher is the one registered at the centre of the specimen (2C), while in the top and bottom brick, close to the tips of the crack, the COD is smaller. The value of the COD in the five sections is always smaller than the corresponding one achieved by the plain sample.

3.4.4.3. LC and LC8 specimens

In Figure 32, LC and LC8 specimens at three different stages during the test are showed. Test results for the unreinforced and reinforced specimens with large crack are presented in terms of load versus vertical relative displacement (load - *v* curves), load versus horizontal relative displacement (load - *u* curves), as well as load versus strain on the front face. For clarity purpose, two curves (grey and black lines), one for each type (unreinforced and reinforced, respectively), are selected as representative of the structural behaviour of the specimens characterized by an initial crack of large dimensions.

65
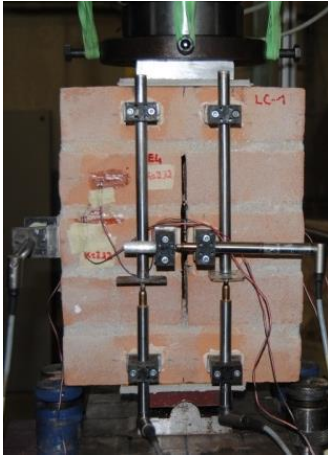
(a) LC specimen at the beginning of the test
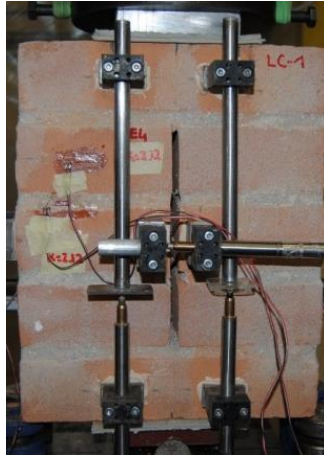
(b) propagation of the crack at P_{crack}
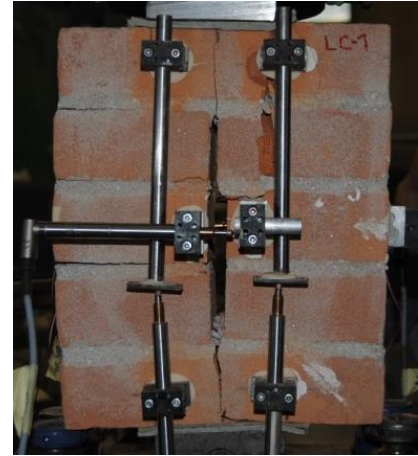
(c) failure of LC specimen at the end of the test

(d) LC8 specimen at the beginning of the test

(e) propagation of the crack at P_{crack}
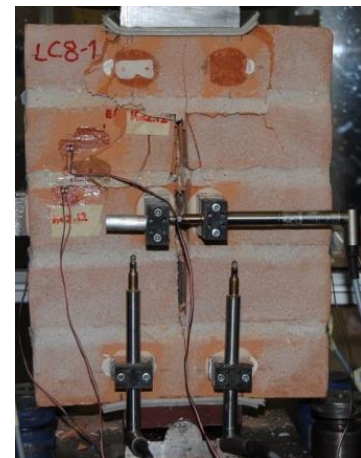
(f) failure of LC8 specimen at the end of the test

Figure 32 LC and LC8 specimens during the test.

In Figure 33a, for positive abscissa, the load - v curves for LC and LC8 specimens are represented. Each curve is obtained as the average of the signals from the four vertical LVDTs (LVDT1, LVDT2, LVDT3 and LVDT4, Figure 12). It should be noted that positive signal registered by the LVDTs means shortening, while negative signal means elongation. For negative abscissa, the load - u curves for LC and LC8 specimens are shown. Each curve is obtained as the average of the signals from the two horizontal LVDTs (LVDT5 and LVDT6, Figure 12). For clarity purpose, a magnification of the first part of the curves, in the interval indicated by the dashed rectangle in Figure 33a, is given in Figure 33b.
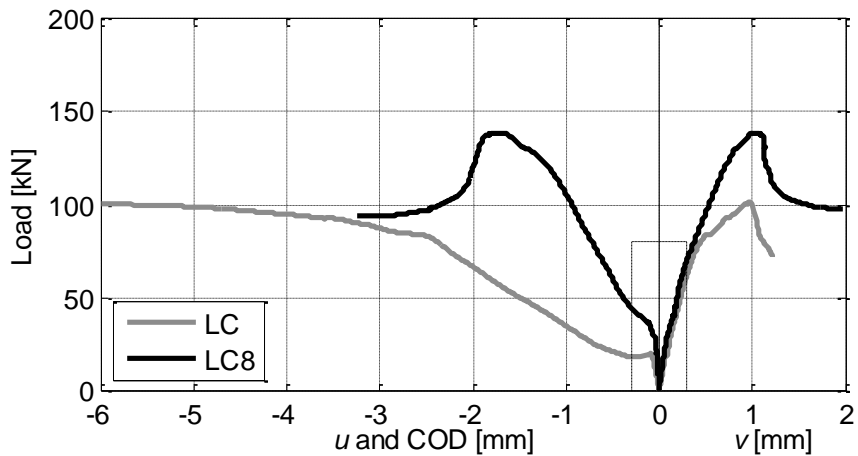
(a) Load - *v* and load - *u* curves for LC (grey line) and LC8 (black line)
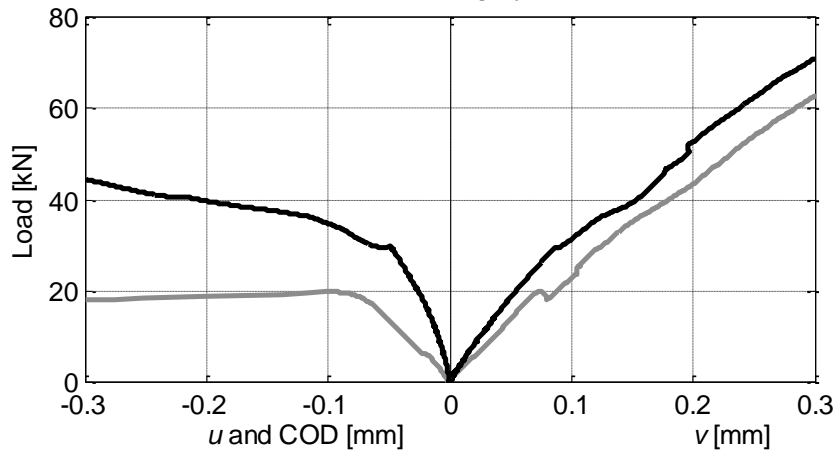
(b) Magnification of the same curves

Figure 33 LC and LC8 results.

Reference is made to the black load - *v* curve in Figure 33a and Figure 33b. Five main features can be distinguished: *i)* initial elastic behavior; *ii)* load at which the crack starts to propagate (P_{crack}); *iii)* load increase; *iv)* peak load (P_{max}) and *v)* post-peak softening and collapse.

LC specimen exhibits a linear behavior at the beginning of the test, Figure 33b. For a certain load value indicated as P_{crack} (around 20 kN), the pre-existent crack starts to propagate and the curve shows a very small load drop of few kilonewtons. Then, the specimen is able again to sustain load and a load increase is registered. However, this second ascending branch is less steep with respect to first one indicating a state of damage of the specimen. After the peak load is attained, Figure 33a, a short softening branch is registered. The specimen gets to collapse in a brittle way splitting in two parts and with the formation of horizontal cracks at the brick/mortar interface, Figure 32c.

Comparing the grey load - *v* curve related to the unreinforced specimen with the black one, it can be noted that in the initial part of the diagram, the two curves show a similar slope, though the stiffness of LC8 is a little higher than that of LC, Figure 33b. The load value P_{crack} is recognizable looking at the load - *u* curve that shows, around 30 kN, a slope change. As expected, reinforced specimen reaches a higher peak load (P_{max}) with respect to LC, Figure 33a, and after the peak load is attained, the softening branch is longer with respect to the unreinforced specimens, showing a more ductile behavior. At the end of the test, the collapse of LC8 specimen

is due to a severe cracking of the brick under the loading plate, while horizontal cracks and the splitting of the specimen are not verified, Figure 32f.

Considering the curves in the negative part of the abscissa, Figure 33a and Figure 33b, the horizontal displacements (*u*) across the pre-existent crack are registered. At the beginning of the test, for low load values, the curves are almost vertical meaning that the horizontal displacement is around zero. As soon as the load level attains the P_{crack} value, the horizontal displacement starts to increase. As stated before, from this load value the horizontal displacement is indicated as COD. For LC specimen, grey curve, the COD increases significantly for low load increments (semi-horizontal branch in Figure 33b). For LC8 specimen, after P_{crack} is attained, the COD increases for higher load increments.

In Figure 34a and Figure 34b, the load-strain curves obtained from strain gauges SGb,f, applied on the brick, and SGm,f, applied on the mortar, on the front face of the specimens are represented, respectively. It should be noted that the sign convention for the strain gauges is opposite to the LVDT one, i.e. positive signal means elongation.
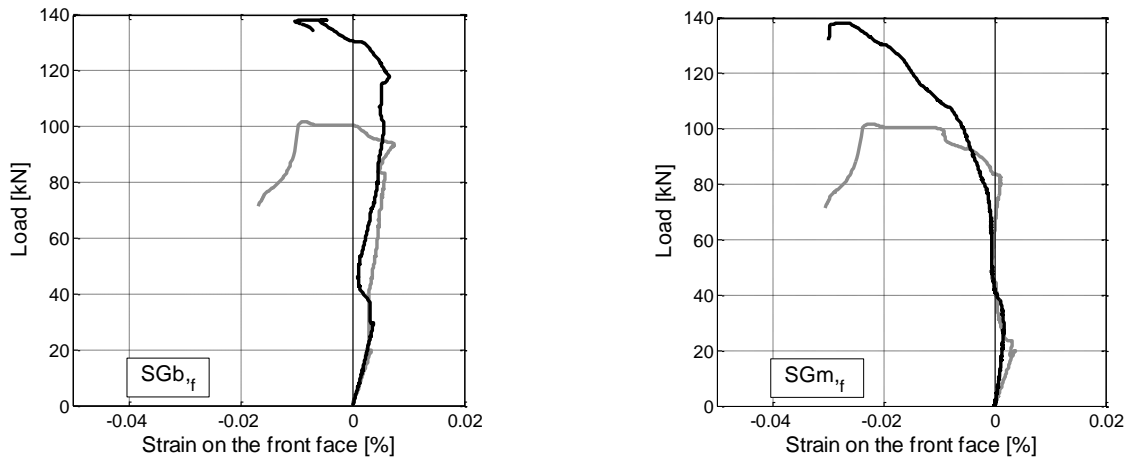
(a) Load – strain curves in the brick obtained from SGb,f (front face)   (b) Load – strain curves in the mortar obtained from SGm,f (front face)

Figure 34 Load – strain curves for LC (grey line) and LC8 (black line) specimens. For the labels refer to Figure 12.

From Figure 34a and Figure 34b, results derived from two horizontal strain gauges (SGb,f and SGm,f) applied on the front face of the specimens are reported. It can be noted that the strains are positive in the first part of the test for both LC and LC8 specimens, meaning a horizontal dilatation of the specimens as a consequence of the vertical compression load. Then, after the propagation of the crack, strains become negative. This represents an indication of the change in the specimen state of stress from compression to combined compression and bending.

3.4.4.3.1. DIC

The color maps of the strains ε_{yy} in the vertical direction at three levels of load for LC and LC8 specimens are shown in Figure 35. For unreinforced and reinforced specimens, a picture of the strains in the pre-crack propagation condition, at P_{crack} as well as at P_{max} is given.
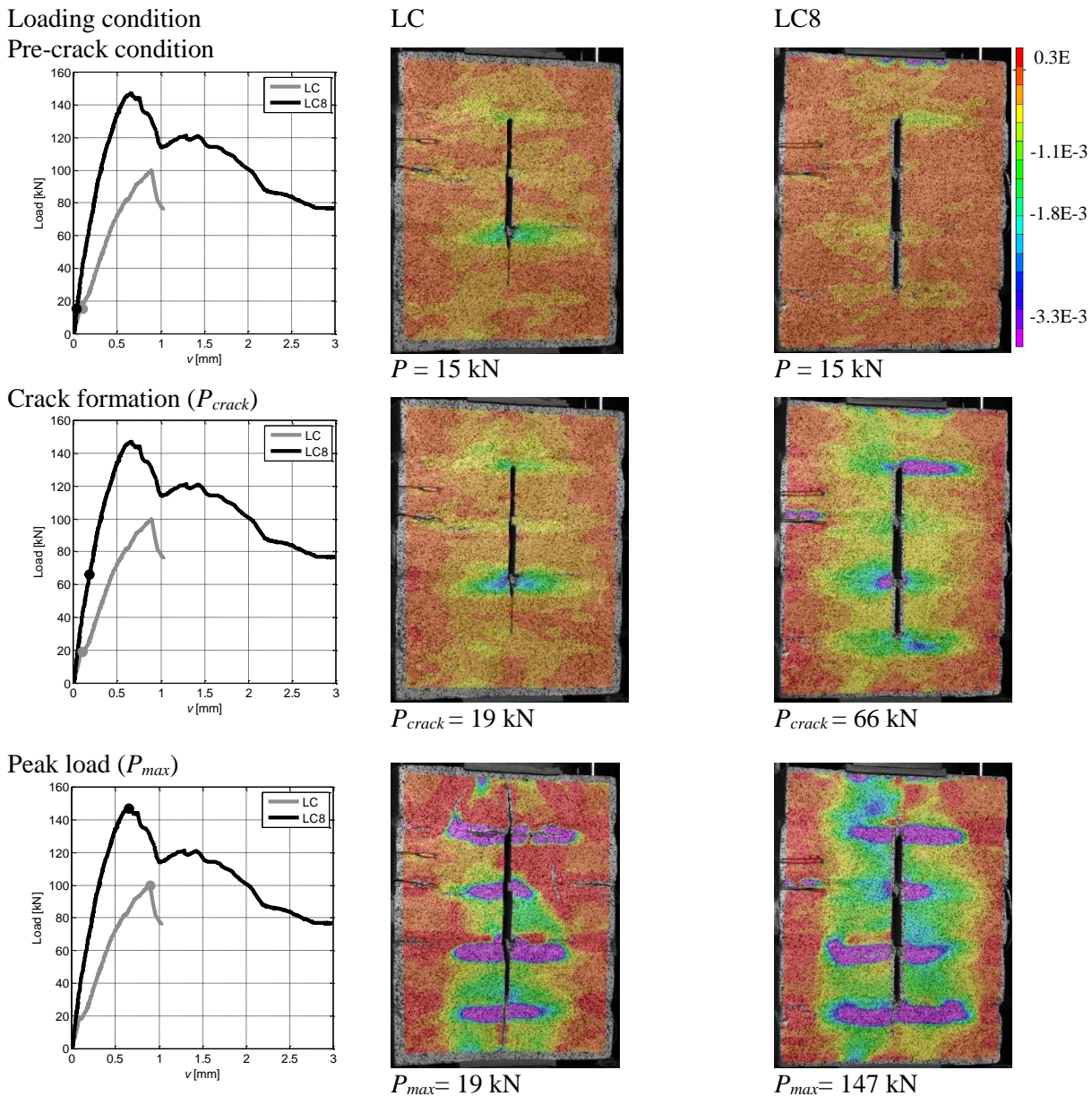
Figure 35 Color maps of the strains in the vertical direction, ε_{yy}, in the pre-crack condition, at P_{crack} and at P_{max} for LC and LC8 specimens. On the left, the grey and black dots track the load at which each color map is captured for LC and LC8 specimens, respectively.

In Figure 35, the color maps for both LC and LC8 specimens, reveal negative strains ε_{yy} in the vertical direction in the area under the loading plate that become positive near the edges of the specimen. At the peak load, in LC specimen the propagation of the crack in the top and bottom brick is evident, while in LC8 specimen this phenomenon is contrasted by the confinement effect due to the presence of carbon bundles in the joints.

In order to investigate for the displacements of the specimens in the vertical direction, five fictitious LVDTs have been chosen (1A, 1B, 1C, 1D, 1E), 260 mm long, i.e. the same length of the real longitudinal LVDTs, Figure 23a. It should be noted that 1A and 1E sections are outside the loading plate; 1B and 1D are under the corners of the loading plate in the same position of real LVDT3 and LVDT4; while 1C section is in the middle of the specimen. In the horizontal direction, five sections in the middle of the bricks have been chosen (2A, 2B, 2C, 2D and 2E), 40 mm long, i.e. the same length of the real horizontal LVDTs, Figure 23b.

For LC specimen, in Figure 36a and Figure 36b, the load - *v* and the load - *u* curves obtained from the vertical and horizontal fictitious LVDTs are plotted, respectively.
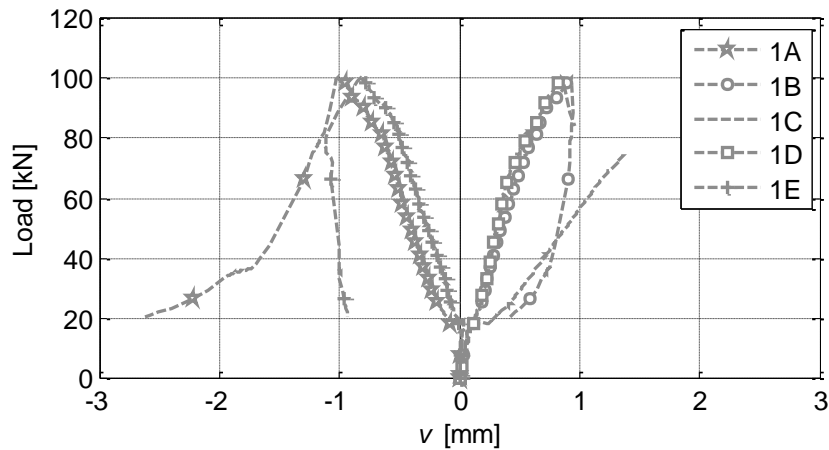
(a) Load - *v* curves for LC specimen obtained from fictitious LVDTs (1A, 1B, 1C, 1D and 1E)
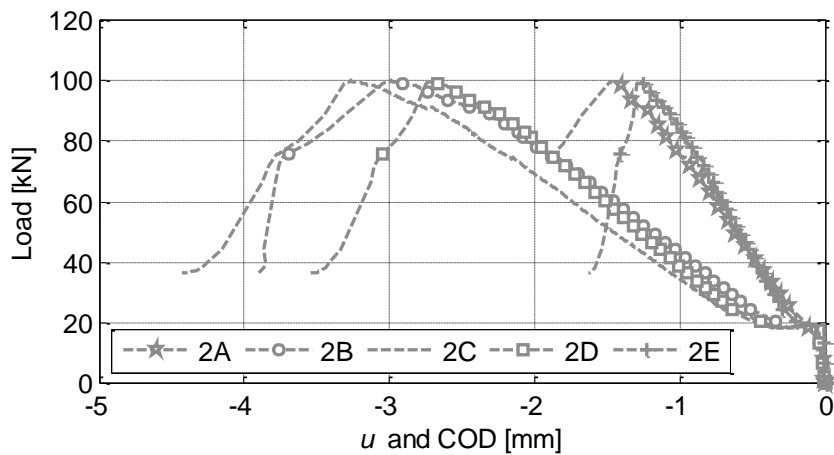
(b) Load - *u* curves for LC specimen obtained from the fictitious LVDTs (2A, 2B, 2C, 2D and 2E)

Figure 36 DIC results for LC specimen.

The curves in Figure 36a, referred to LC specimens, show that fictitious LVDTs 1B, 1C and 1D, that are under the loading plate, remain in the positive part of the displacements. This confirms that, under the plate, the state of stress remains of compression. On the contrary, the displacements registered by the outermost LVDTs (1A and 1E) are positive before P_{crack} is attained, then, when the crack propagates, become negative showing an elongation. This behavior confirms that a state of flexure is verified close to the specimen edges.

The load - *u* curves registered in the five LVDTs for LC specimens, Figure 36b, show that, as expected, the highest is the one registered at the centre of the specimen (2C). While in the top and bottom brick, close to the tips of the initial crack, the COD is smaller.

In Figure 37a and Figure 37b, the load-*v* and the load-*u* curves obtained from the vertical and horizontal fictitious LVDTs are plotted for LC8 specimen, respectively.
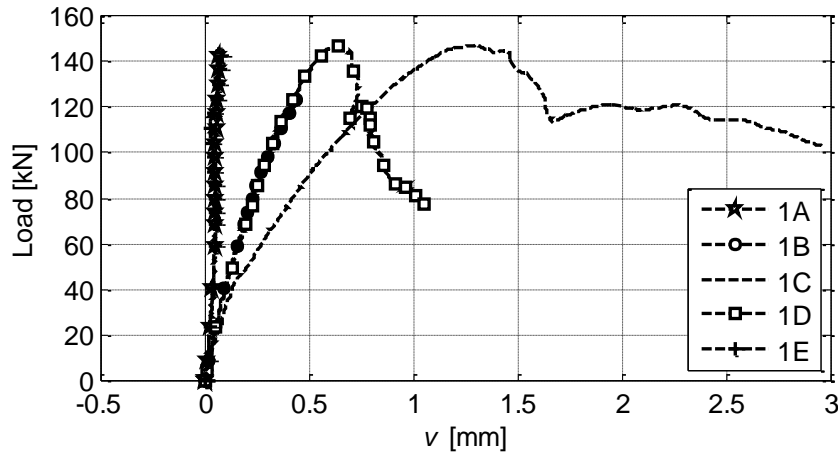
(a) Load - *v* curves for LC8 specimen obtained from fictitious LVDTs (1A, 1B, 1C, 1D and 1E)
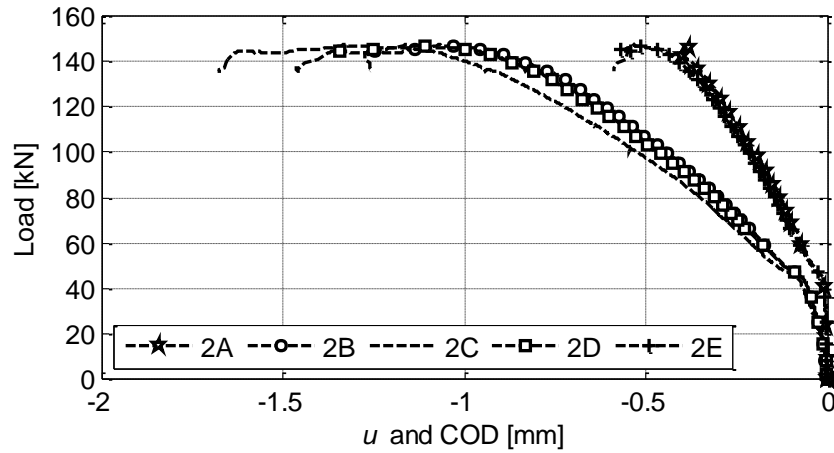
(b) Load - *u* curves for LC8 specimen obtained from the fictitious LVDTs (2A, 2B, 2C, 2D and 2E)

Figure 37 DIC results for LC8 specimen.

In Figure 37a, the vertical relative displacements remain in the positive part: this confirms a predominant compression state of stress in the LC8 reinforced specimens.

The load - *u* curves registered in the five LVDTs, Figure 37b, show that, as before, the highest is the one registered at the centre of the specimen (2C), while in the top and bottom brick, close to the tips of crack, the COD is smaller. The values of the COD in the five sections are always smaller than the corresponding ones achieved by the unreinforced specimen.

In order to make a comparison between fictitious and real LVDTs, in Figure 38a, a magnification of the curves obtained from one of the real vertical transducers, LVDT2, is compared to the signal registered by the corresponding fictitious LVDT 1D. In the same figure, the curve obtained from the real horizontal transducer LVDT5 is compared to the signal registered by the corresponding fictitious LVDT 2C. This comparison is made only for LC8 specimen for brevity sake. For clarity purposes, in Figure 38b, the displacements registered by fictitious and real LVDTs are reported at three different levels of load: in the pre-crack propagation condition, at P_{crack} as well as at P_{max}.

(a) Load - v and load - u curves for LC8 specimen obtained from fictitious and real LVDTs
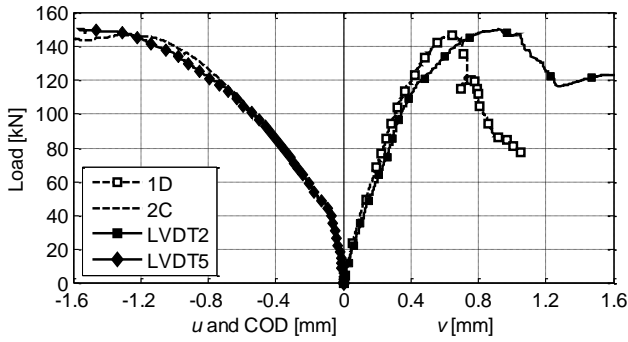
(b) Comparison in terms of numerical values between fictitious and real LVDTs

		$P =$ 15kN	$P_{crack} =$ 66 kN	$P_{max} =$ 154 kN
v [mm]	1D (fictitious)	0.04	0.18	0.65
	LVDT2 (real)	0.04	0.23	0.93
u & COD [mm]	2C (fictitious)	0.01	-0.25	-1.57
	LVDT5 (real)	0.01	-0.25	-1.57

Figure 38 LC8 specimen: comparison between real and fictitious LVDTs in terms of load - v and load - u curves and numerical values.

A good agreement between the real LVDTs and fictitious ones is shown in Figure 38a. It is worth noting that the load-displacement curves for LC8 specimen obtained from fictitious and corresponding real LVDTs have the same trend. The good accordance between real LVDTs and DIC results is also confirmed in Figure 38b, in which the numerical values of LVDT2 (real) versus LVDT 1D (fictitious) in the vertical direction, and LVDT5 (real) versus LVDT 2C (fictitious) in the horizontal direction are compared.

3.4.4.4. SC and SC4 specimens

In Figure 39, SC and SC4 specimens at three different stages during the test are reported.
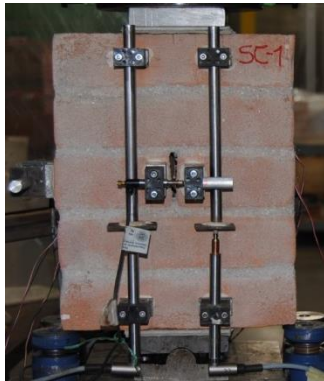
(a) SC specimen at the beginning of the test

(b) propagation of the crack at P_{crack}

(c) failure of LC specimen at the end of the test

(d) SC4 specimen at the beginning of the test

(e) propagation of the crack at P_{crack}

(f) failure of the specimen at the end of the test

Figure 39 SC and SC4 specimens during the test.

Also for SC specimens, two curves (grey and black lines), one for each type (unreinforced and reinforced, respectively), were selected as representative of the structural behaviour of the specimens characterized by an

initial crack of small dimensions. It should be noted that, in the following figures, the axes scale is kept the same of that employed for LC specimens for comparison purposes.

In Figure 40a, the load-v curves for SC and SC4 specimens are represented in the first quadrant. Each curve is obtained as the average of the signals from the four vertical LVDTs (LVDT1, LVDT2, LVDT3 and LVDT4, Figure 12). For negative abscissa, the load-u curves, obtained as the average of the signals from the two horizontal LVDTs (LVDT5 and LVDT6, Figure 12), for the SC and SC4 specimens are shown. A magnification of the first part of the curves, in the interval indicated by the dashed rectangle in Figure 40a, is given in Figure 40b.
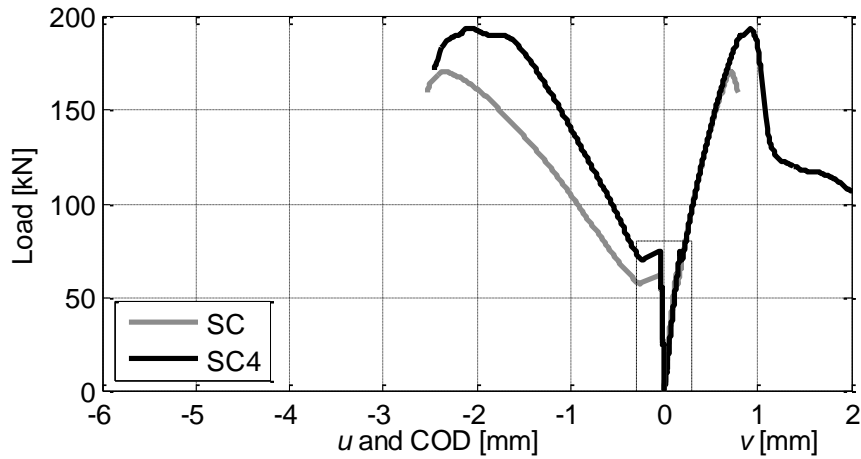
(a) Load - v and load - u curves for SC (grey line) and SC4 (black line)
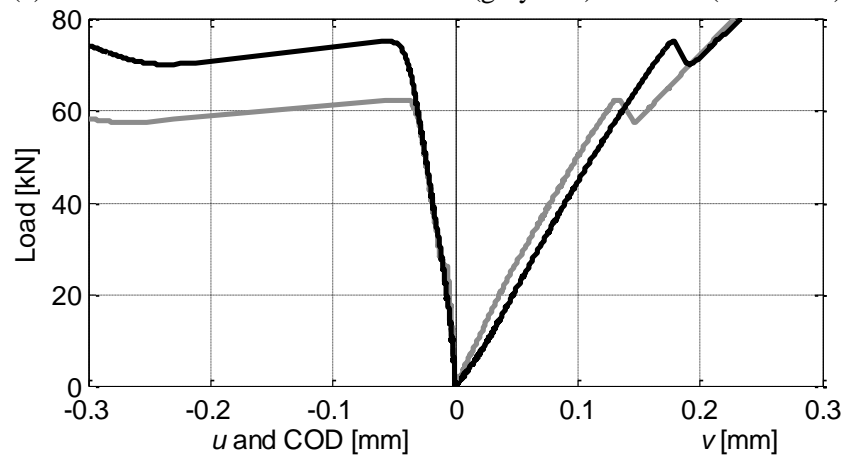
(b) Magnification of the same curves

Figure 40 SC and SC4 results.

Reference is made to Figure 40a and Figure 40b, where the load - v and load - u curves for SC and SC4 specimens are reported in grey and black color, respectively.

Differently from the behavior that characterizes the specimens with large crack, six main features can be distinguished: *i*) initial elastic behavior; *ii*) load at which the crack starts to propagate (P_{crack}); *iii*) load drop; *iv*) load increase; *v*) peak load (P_{max}) and *vi*) post-peak softening and collapse.

In the initial part of the diagrams, Figure 40b, grey and black curves show a similar behavior being linear and with the same slope. For a load around 60 kN, P_{crack}, a drop appears for SC specimen corresponding to the propagation of the vertical crack. Due to the presence of the bundles, the propagation of the crack for the reinforced specimen occurs for a greater load value (P_{crack} is around 75 kN for SC4). As expected, SC specimen

shows a smaller peak load, Figure 40a, around 160 kN, with respect to the reinforced specimen, whose P_{max} is around 190 kN. The softening branch for SC specimen is very short and after P_{max} is attained, a brittle collapse occurs. It is important to note that at failure, cracks due to tensile stresses on the corners of the specimen at the brick/mortar interface are present, Figure 39c. Conversely, SC4 specimen is characterized by a ductile collapse mechanism, Figure 39f, as shown by the softening branch in Figure 40a.

Looking at the load-u curves, the same slope of the two curves below P_{crack} shows that the bundles do not affect the behavior of the specimens for low load values. At P_{crack}, a meaningful horizontal displacement due to the opening of the crack is observed, Figure 40b. This behavior was observed also in the specimens with large crack. Then, SC specimen starts again to sustain load but with a lower value of stiffness with respect the first branch. The crack arrestor function of the bundles can be highlighted considering that for a certain load level greater than P_{crack}, the COD registered for SC specimen is greater than the COD of SC4 specimen. For higher load values, this difference increases.

Results obtained from strain gauges on the B-B face for SC4 specimen are reported in Figure 41.
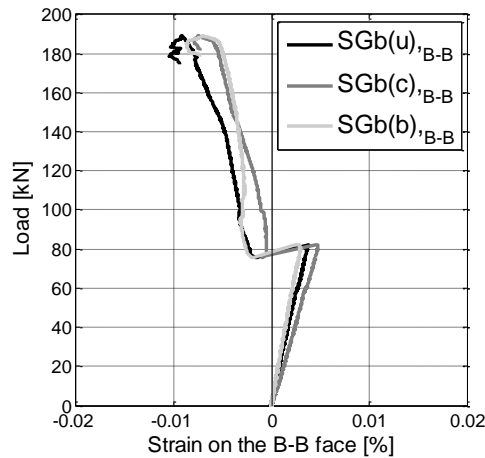
Figure 41 Load - strain curves for SC4 specimen (B-B face). For the labels refer to Figure 13.

The horizontal strains registered for the SC specimen on the B-B face, Figure 41, reveal an elongation during the elastic phase that is bigger for the central brick with respect to the lower and upper brick that are similar, as expected. In correspondence of P_{crack}, a behavior discontinuity is registered. A change in sign is detected and strains become negative. This is explained as a change in the state of stress from elongation of the specimen at the beginning of the test to a contraction after the propagation of crack.

3.4.4.4.1. DIC

The color maps of the strains ε_{yy} in the vertical direction at four levels of load for SC and SC4 specimens are shown in Figure 42. For the unreinforced and reinforced specimens, a picture of the strains in the pre-crack propagation condition, at P_{crack} as well as at P_{max} is given.
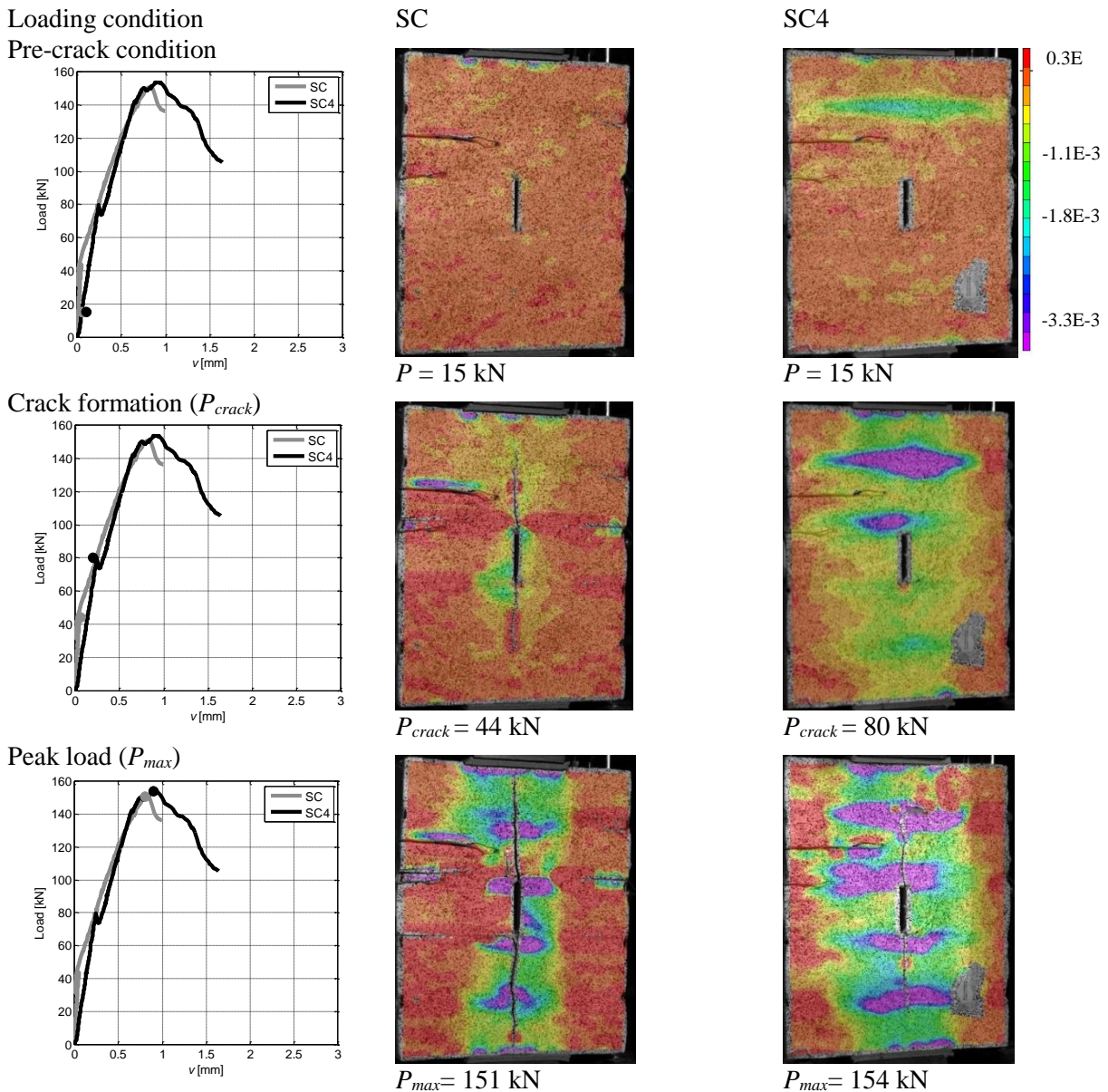
Figure 42 Color maps of the strains in the vertical direction, ε_{yy}, in the pre-crack condition, at P_{crack} and at P_{max} for SC and SC4 specimens. On the left, the grey and black dots track the load at which each color map is captured for SC and SC4 specimens, respectively.

The color maps of the strains ε_{yy} in the vertical direction, Figure 42, are negative in the area under the loading plate and become positive near the edges of the specimen. As before, the confinement effect due to the presence of carbon bundles in the mortar joints for SC4 specimen contrasts the opening of the crack that occurs in SC specimen.

In Figure 43a and Figure 43b, the load - v and the load - u curves obtained from the vertical and horizontal fictitious LVDTs are plotted for SC specimen, respectively.
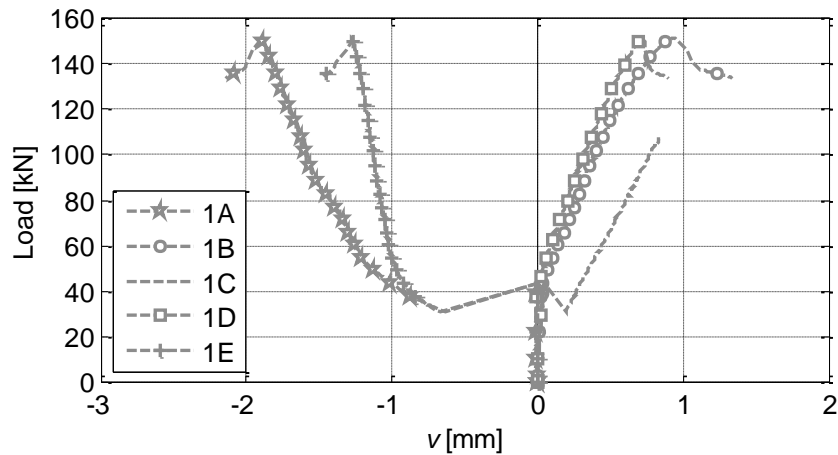
(a) Load - v curves for SC specimen obtained from fictitious LVDTs (1A, 1B, 1C, 1D and 1E)
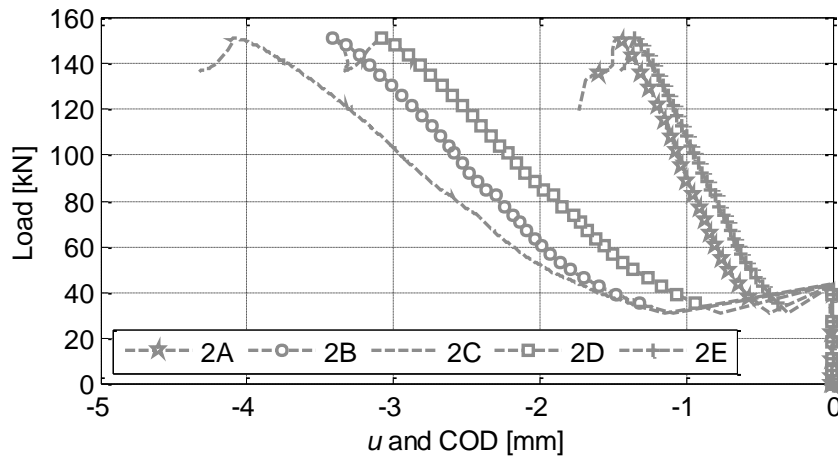
(b) Load - u curves for SC specimen obtained from the fictitious LVDTs (2A, 2B, 2C, 2D and 2E)

Figure 43 DIC results for SC specimen.

The curves in Figure 43a, referred to SC specimen, show that fictitious LVDTs 1B, 1C and 1D, that are under the loading plate, remain in the positive part of the displacements. This confirms that, under the plate, the state of stress remains of compression showing a contraction in the vertical direction. On the contrary, the displacements registered by the outermost LVDTs (1A and 1E) are positive before P_{crack} is attained, then, with the propagation of the crack, become negative showing an elongation. This behavior confirms that a state of flexure is verified close to the specimen edges.

The load-u curves registered in the five LVDTs for SC specimen, Figure 43b, show that, as expected, the highest is the one registered at the centre of the specimen (2C), while in the top and bottom brick, the COD is smaller.

In Figure 44a and Figure 44b, the load-v and the load-u curves obtained from the vertical and horizontal fictitious LVDTs are plotted for SC4 specimen, respectively.
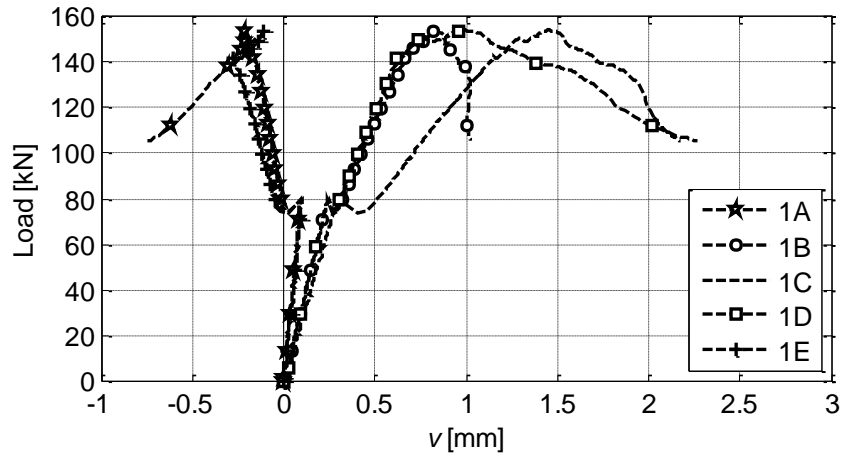
(a) Load - *v* curves for SC4 specimen obtained from fictitious LVDTs (1A, 1B, 1C, 1D and 1E)
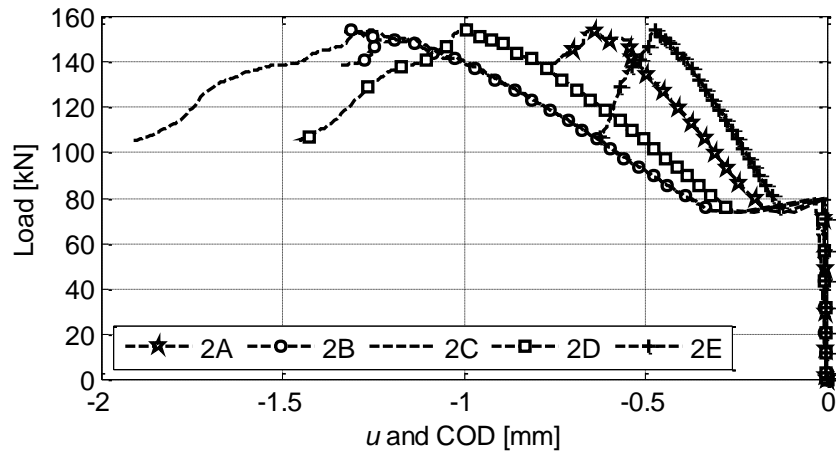
(b) Load - *u* curves for SC4 specimen obtained from the fictitious LVDTs (2A, 2B, 2C, 2D and 2E)

Figure 44 DIC results for SC4 specimen.

The load-*v* curves in Figure 44a, show that LVDTs 1B, 1C and 1D under the loading plate, register a positive displacement during the whole test, meaning a contraction of the specimen that remains compressed. The displacements registered by LVDTs 1A and 1E (outside the loading plate) are positive before P_{crack} is attained, then a change in sign occurs, but with negative values of relative displacements lower than those achieved by SC specimen. This confirms that the state of stress in the reinforced specimens is mainly of compression.

The load-*u* curves registered in the five LVDTs, Figure 44b, show that, as before, the highest is the one registered at the centre of the specimen (2C), while in the top and bottom brick, the COD is smaller. The value of the COD in the five sections is always smaller than the corresponding one achieved by the plain specimen. In order to make a comparison between fictitious and real LVDTs, in Figure 45a, a magnification of the curves obtained from one of the real vertical transducers LVDT2 is compared to the signal registered by the corresponding fictitious LVDT 1D. In the same figure, the curve obtained from the real horizontal transducer LVDT5 is compared to the signal registered by the corresponding fictitious LVDT 2C. This comparison is made only for SC4 specimen for brevity sake. For clarity purposes, in Figure 45b, the displacements registered by fictitious and real LVDTs are reported at three different levels of load: in the pre-crack propagation condition, at P_{crack} as well as at P_{max}.
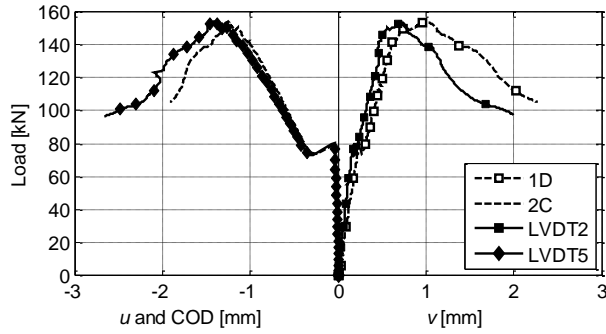
(a) Load - v and load - u curves for SC4 specimen obtained from fictitious and real LVDTs

		$P =$ 15kN	$P_{crack} =$ 80 kN	$P_{max} =$ 154 kN
v [mm]	1D (fictitious)	0.05	0.31	0.76
	LVDT2 (real)	0.03	0.18	0.58
u & COD [mm]	2C (fictitious)	0.00	-0.03	-1.15
	LVDT5 (real)	0.00	-0.04	-1.27

(b) Comparison in terms of numerical values between fictitious and real LVDTs

Figure 45 SC4 specimen: comparison between real and fictitious LVDTs in terms of load – v and load – u curves and numerical values.

As before, a good agreement between the real LVDTs and fictitious ones is shown in Figure 45a. It is worth noting that the load-displacement curves for SC4 specimen obtained from fictitious and corresponding real LVDTs have the same trend. The good accordance between real LVDTs and DIC results is also confirmed in Figure 45b, in which the numerical values of LVDT2 (real) versus LVDT 1D (fictitious) in the vertical direction, and LVDT5 (real) versus LVDT 2C (fictitious) in the horizontal direction are compared.

3.4.5. Summary

A summary of the relevant mechanical parameters obtained from the splitting tests for all the not reinforced and reinforced specimens is given in Table 5, in terms of maximum load, P_{max}, P_{crack}, vertical and horizontal displacements measured by LVDTs at P_{max}, Δ_1 and Δ_2. The parameters Δ_1 and Δ_2, represent the structural enhancement achieved in terms of P_{max} and P_{crack} by using the carbon wires and are calculated as follows:

$$\Delta_1 = [(\bar{P}_{max}^R - \bar{P}_{max}^{UNR})/(\bar{P}_{max}^{UNR})] \cdot 100 \tag{32}$$

where $\bar{P}_{max}^R$ and $\bar{P}_{max}^{UNR}$ are the mean maximum load for the reinforced specimens (NC8, LC8 and SC4) and unreinforced specimens (NC, LC and SC), respectively and

$$\Delta_2 = [(\bar{P}_{crack}^R - \bar{P}_{crack}^{UNR})/(\bar{P}_{crack}^{UNR})] \cdot 100 \tag{33}$$

where $\bar{P}_{crack}^R$ and $\bar{P}_{crack}^{UNR}$ are the mean load at which the propagation of the crack occurs for the reinforced specimens (NC8, LC8 and SC4) and unreinforced specimens (NC, LC and SC), respectively.

Table 5 Summary of the results of the experimental investigation. Standard deviation in parentheses.

Sample	P_{max} [kN]	P_{crack} [kN]	v at P_{max} [mm]	u at P_{max} [mm]	Δ_1 [%]	Δ_2 [%]
NC-1	100.47	62.3	0.65	2.73		
NC-2	121.87	71.7	0.70	3.00		
NC-3	90.89	60.4	0.74	4.26		
NC	104.41 (15.86)	64.80 (6.05)	0.70 (0.05)	3.33 (0.82)	-	-
NC8-1	194.88	161.6	0.89	1.47		
NC8-2	206.02	160.9	0.95	1.69		
NC8-3	208.02	163.3	1.27	1.44		
NC8	202.97 (7.08)	161.90 (1.23)	1.04 (0.20)	1.53 (0.14)	94.40	149.85
LC-1	122.68	10.47	0.63	2.18		
LC-2	93.55	5.99	0.90	3.28		
LC-3	101.78	6.09	0.98	5.00		
LC	106.00 (15.02)	7.52 (2.56)	0.84 (0.18)	3.49 (1.42)	-	-
LC8-1	138.34	29.48	1.01	1.69		
LC8-2	192.54	22.45	0.61	1.58		
LC8-3	150.13	19.24	0.95	1.57		
LC8	160.34 (28.50)	23.72 (5.24)	0.86 (0.21)	1.61 (0.07)	51.26	215.42
SC-1	103.73	40.35	0.90	-		
SC-2	170.76	62.38	0.72	2.37		
SC-3	154.09	44.79	2.17	4.93		
SC	142.86 (34.90)	49.17 (11.65)	1.26 (0.79)	3.65 (1.81)	-	-
SC4-1	188.96	82.11	0.85	1.66		
SC4-2	193.77	74.95	0.93	2.07		
SC4-3	153.87	80.31	0.69	1.42		
SC4	178.86 (21.78)	79.12 (3.72)	0.82 (0.12)	1.72 (0.33)	25.20	60.91

Comparing the test results for NC and NC8 specimens in Table 5, it can be noted that the peak loads are almost doubled for NC8 with respect to NC ($\Delta_1\sim94\%$). Correspondingly, the crack opening displacement (COD) for NC8 is the half of the one for NC at the peak load. As stated before, the carbon wires work as crack arrestor. Besides, P_{crack} is three times for NC8 with respect to NC ($\Delta_2\sim150\%$), showing clearly the effects of the carbon wires in increasing the load for which the crack starts to propagate. In general, the peak load values are reached for greater displacements in the case of NC8, highlighting a greater ductility for these last specimens. Also the displacements reached at the P_{crack} are greater for NC8 with respect to NC specimens.

From Table 5, comparing the results for LC and LC8 specimens in terms of peak load the increment is around 50% ($\Delta_1 = 51.26\%$) for LC8 with respect to LC. The mean value of the COD that corresponds to the peak load is the half for LC8 (1.61 mm) specimens compared to the one of LC (3.49 mm). Moving from LC to LC8, the propagation of crack occurs for a level of load that is three times higher ($\Delta_2 = 215.42\%$).

Comparing the results for SC and SC4 specimens, as reported in Table 5, the mean value of the peak load for SC specimens is 142.86 kN, while for SC4 is 178.86 kN, so the increment Δ_1 is about 25%. As for LC and

LC8 specimens, the mean value of the COD for SC4 specimens is the half of the one of SC specimens. Furthermore, the increment in the load at which crack starts to propagate,Δ_2, passing from SC to SC4 is 60.91%.

Consequently, two advantages of using carbon bundles can be derived: 1) crack arrestor function and 2) crack propagates at a higher load level.

3.5 Steel bars as repointing technique

3.5.1. Material characterization

3.5.1.1. Bricks and mortar

Bricks used in the construction phase are the same presented before in paragraph 3.4.1.1.

Two different types of mortar were used in the specimens: a cement-based mortar (Mortar A) to realize the joints and a structural mortar (Mortar B) for repointing. In Table 6, the mechanical properties of the mortar, provided by the manufacturer according to (EN 1015-11 2007; EN 196-1 2011) are reported (f_c = compressive strength, f_f = flexural strength).

Table 6 Mechanical properties of the mortars employed for the manufacturing of the specimens.

Material	f_c [MPa]	f_f [MPa]
Mortar A (cement-based mortar)	5.89	1.85
Mortar B (structural mortar)	>15	>5

3.5.1.2. Twisted steel bars

The twisted steel bars (nominal diameter equal to 6 mm and nominal cross sectional area equal to 8 mm^2) are used to strengthen the specimens, Figure 46.

Figure 46 Twisted steel bar.

In order to check the mechanical properties of the steel bars, direct tensile tests were performed. Following the procedure proposed in (Quagliarini et al. 2012), an anchorage system consisting of a steel pipe filled with a thixotropic epoxy resin has been employed. Based on preliminary tests, it was determined that 100 mm anchor length could offer adequate restraint. The dimension of the specimens has been obtained according to (BS EN ISO 6892-1:2009 2015). The specimens, with a total length (L_p) of 500 mm, are provided with two anchoring systems (one for every end), with a length (L_a) of 100 mm, leaving an effective length (L_u) of 300 mm.

A universal testing machine, Galdabini 100 kN, has been used for the tests. The top end of the specimen has been first fixed on the top jaw of the machine, and then also the bottom end has been fixed before applying the load. The load has been applied through a constant speed of 2 mm/min until the failure of the specimen. It is notably that specimens rupture occurred at a time between one and ten minutes, according to (BS EN 845-1:2013 2003; BS EN 846-7:2012 2015). Each specimen was provided by a deformometer placed in a central position in the bar to record for the elongation. A LVDT (linear variable displacement transducer) measured the displacement of the machine head (Figure 47). To check if the anchoring system could affect the test, also the position on the sample where the break occurs has been recorded. In particular, as suggested by (Ismail & Ingham 2012), if the distance between rupture point and anchoring steel pipe was greater than two times the diameter of the sample, the failure mode was considered satisfactory and the test was accepted.

| (a) | (b) |

Figure 47 Tensile test on the steel bar: a) specimen at the beginning of the test; b) specimen at the end of the test.

Results in terms of breaking force (P_{max}), maximum tensile stress (σ_{max}), breaking elongation (ε_u) as well as elastic modulus are collected in Table 7. The values were obtained as the mean on three samples. In Figure 48, σ - ε curve for one steel bar is reported.

Table 7 Mechanical properties of the steel bars. Values averaged on five samples. Standard deviation in parentheses.

Material	E [MPa]	P_{max} [kN]	σ_{max} [MPa]	ε_u [%]
Bar 1	147694	9.38	1172.95	-
Bar 2	130356	9.66	1207.66	3.67
Bar 3	139734	9.60	1200.16	2.33
Mean	139261.33 (8678)	9.55 (0.14)	1193.59 (18.26)	3.00
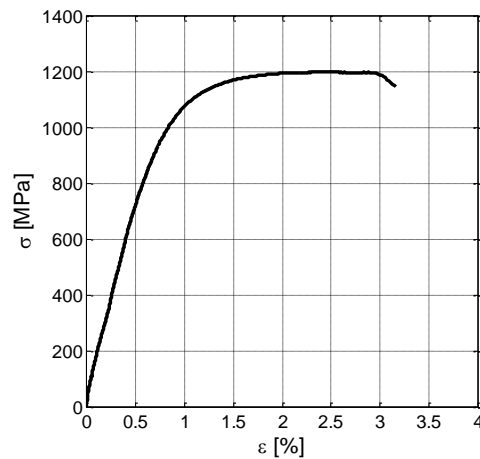
Figure 48 Stress-strain curve for steel bar.

3.5.2. Specimens

Each specimen was built with five bricks and four 10 mm thick mortar layers and had a nominal total size equal to 250 x 315 x 120 mm³.

In particular, three types of specimens were constructed:

i) specimens without crack hereinafter denoted with NC – No Crack, Figure 49;
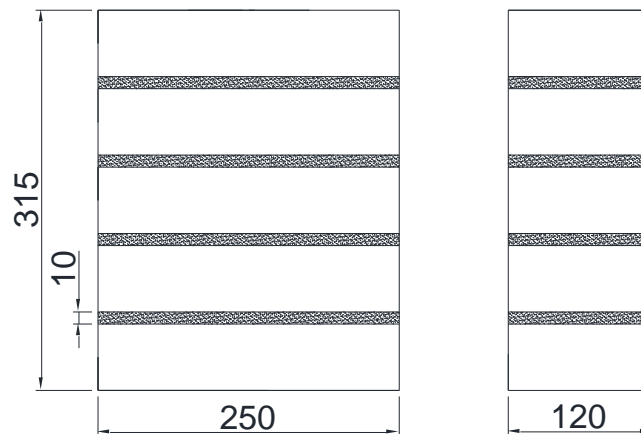
Figure 49 NC specimens. Dimensions in mm.

ii) specimens with a large crack through the three central bricks, hereinafter denoted with LC - Large Crack (Figure 50a);

iii) specimens with a small crack through the central brick, hereinafter denoted with SC – Small Crack (Figure 51a).

The specimens were strengthened, after the maturation of 28 days, by using repointing technique, achieved by inserting in the mortar joints, at a depth of 30 mm from the edges, the steel bars.

LC specimens were reinforced by using two different configurations:

i) LC4: inserting in the top and bottom joints two steel bars for a total of four bars, in a symmetric position (Figure 50b);

ii) LC8: inserting in each mortar joint two steel bars for a total of eight bars, in a symmetric position (Figure 50c).

(a)   (b)   (c)
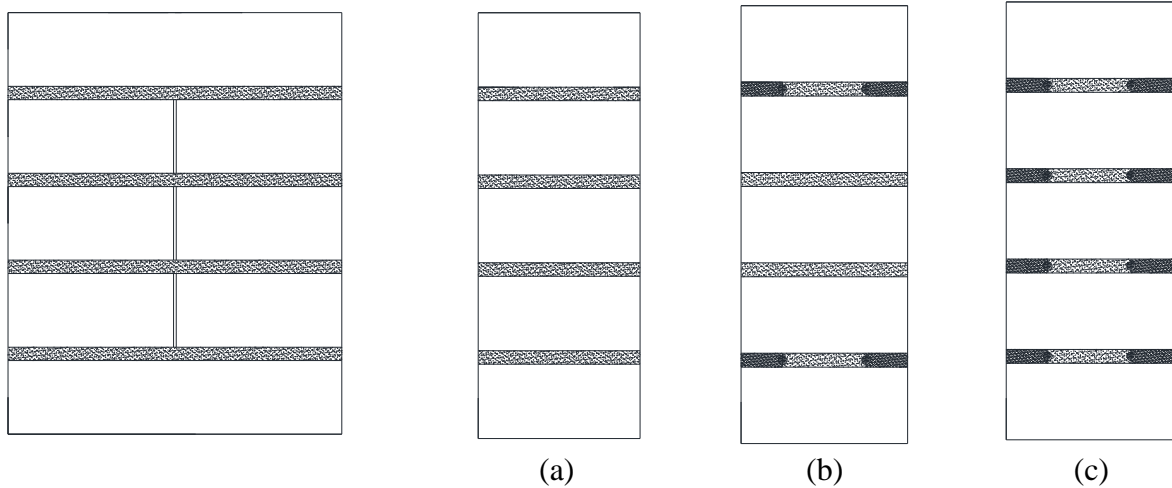
Figure 50 LC specimens: a) LC, b) LC4 and c) LC8.

SC specimens were reinforced by inserting four steel bars, in the central mortar joints, indicated hereinafter as SC4 (Figure 51b).

(a)   (b)
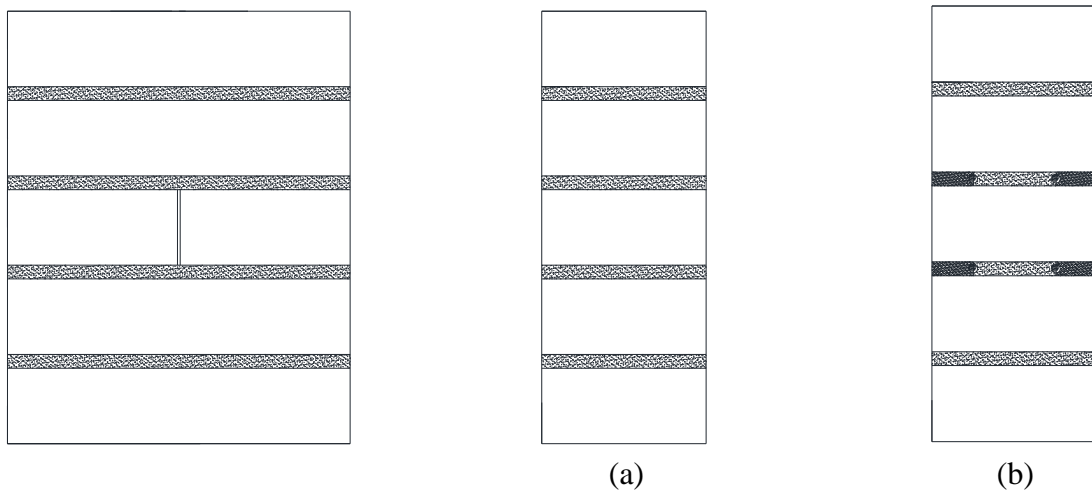
Figure 51 SC specimens: a) SC and b) SC4.

In Table 8, the tested specimens are summarized.

Table 8 Tested specimens: labels and description.

Specimen label	Number of each specimens	Description
NC	4	Specimen without crack and without reinforcement (Figure 49)
LC	4	Specimen with large crack and without reinforcement (Figure 50a)
LC4	4	Specimen with large crack and 4 steel bars in the mortar joints (Figure 50b)
LC8	4	Specimen with large crack and 8 steel bars in the mortar joints (Figure 50c)
SC	4	Specimen with small crack and without reinforcement (Figure 51a)
SC4	4	Specimen with small crack and 4 steel bars in the mortar joints (Figure 51b)

3.5.3. Test set up and instrumentation

After curing, all the specimens were subjected to the purposely designed splitting test presented before.

In Figure 52, the instrumentation of the specimens is shown. In particular, the vertical displacements were registered by: LVDT1, LVDT2 (both applied on the front face), LVDT3 and LVDT4 (both applied on the back face).

The horizontal displacements at the centre of the specimens across the crack were registered by: LVDT5 (applied on the front face) and LVDT6 (applied on the back face).

(a) Specimen front face   (b) Specimen back face
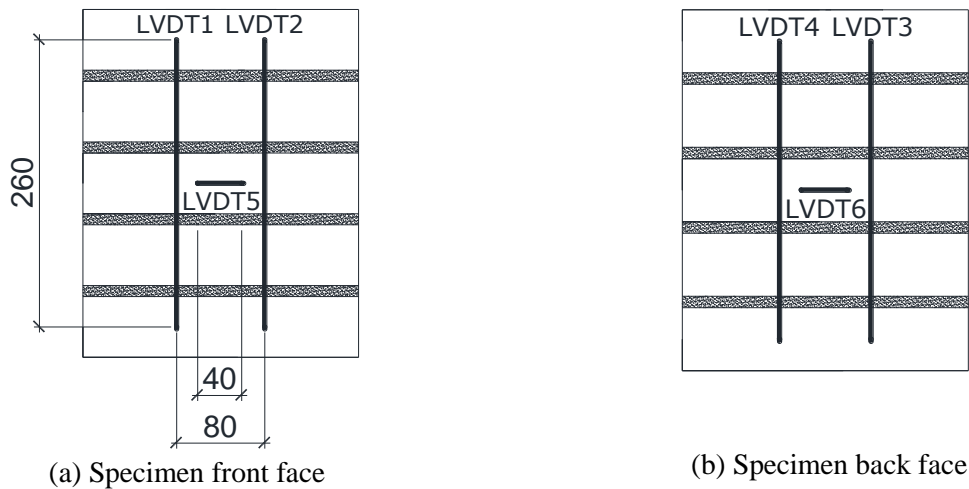
Figure 52 Instrumentation of the specimens. Dimensions in mm.

3.5.4. Results

Results are given in terms of load versus vertical displacement (load - *v* curves) and load versus horizontal displacement (load - *u* curves). Light grey curves are referred to not reinforced specimens, dashed dark grey are referred to specimens reinforced with four steel bars and black curves are referred to specimens strengthened with eight bars. It is worth noting that positive signal of the LVDTs means shortening, while negative signal means elongation. For clarity purposes, only the results of one specimens per type are reported in the figures.

3.5.4.1. NC specimens

In Figure 53, NC specimen at two different stages during the splitting test is reported.

(a)   (b)
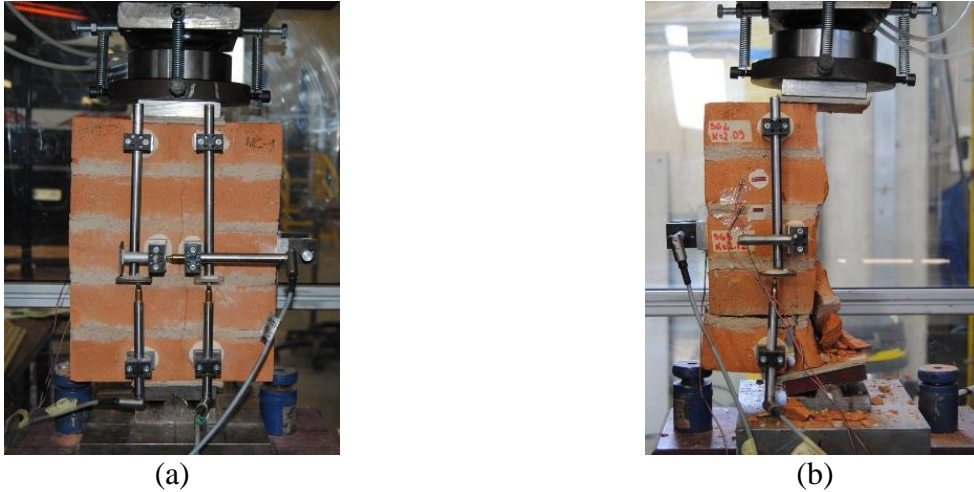
Figure 53 NC specimen: a) propagation of the crack for a load equal to 110 kN and b) specimen failure at the end of the test.

In Figure 54, for positive abscissa, the load - v curve for NC sample is represented. The curve is obtained as the average of the signals from the four vertical LVDTs (LVDT1, LVDT2, LVDT3 and LVDT4). For negative abscissa, the load - u curve for NC sample is shown. The curve is obtained as the average of the signals from the two horizontal LVDTs (LVDT5 and LVDT6). It should be noted that the acronym COD, reported on the abscissa, stands for Crack Opening Displacement (Hillerborg 1991). Following Hillerborg 1991, before the crack begins to propagate, strains can be calculated and the horizontal displacement across the crack is indicated with u. Once the initial crack propagates, the horizontal displacement measured by LVDTs becomes Crack Opening Displacement.

For all the specimens, in the load - v curve, six main features can be distinguished: (*i*) pre-crack condition, (*ii*) crack formation, P_{crack}, (*iii*) load drop, (*iv*) increasing load, (*v*) peak load, P_{max} and (*vi*) post-peak softening. Once the initial crack propagates, the horizontal displacement measured by the LVDTs becomes the Crack Opening Displacement.
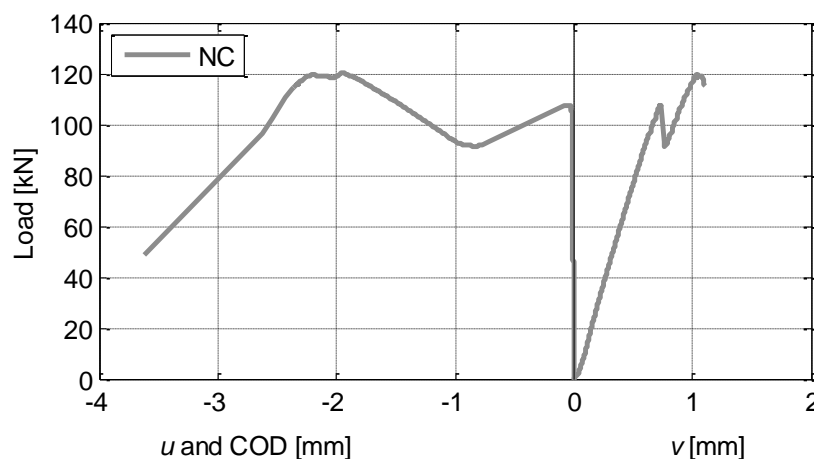
Figure 54 Load - v and load - u curves for NC specimens.

The pre-crack condition is characterized by an almost linear elastic branch until load attains a value around 110 kN, (P_{max}). Afterwards, a drop of about 20 kN corresponding to the formation of a vertical crack in the middle of the specimen occurs (Figure 53a). After, the load starts to increase again corresponding to new sources of strength of the specimens, even if with a significant decrease in stiffness (the second ascending

branch is less steep than the first one), until a peak load around 120 kN, (P_{max}) is reached. In the post-peak behaviour, a softening branch can be detected before a brittle collapse occurs. The failure mechanism of the NC specimens is characterized by a brittle and sudden splitting of the specimen in two parts, (Figure 53b). Besides, after the peak load is attained, horizontal cracks at the interface between mortar and brick start to propagate. These cracks are due to the particular stress state that characterizes the specimens during the test. At the beginning, the specimens are compressed, while after the propagation of the crack, the state of stress changes toward an eccentric compression. The flexure creates tractions at the external edges in the vertical direction resulting in the occurrence of horizontal cracks.

As long as the load is below 110 kN, the horizontal displacement (u) is around zero. Once the load attains the P_{crack} value, a meaningful displacement is registered confirming that for this load value a crack starts to open. In other words, below P_{crack} in the elastic phase, the strains can be still evaluated, while at P_{crack}, the crack opening displacement measure is adopted. Afterward, the specimens are able again to sustain load, even if with a lower value of stiffness and, correspondingly, a large increase in the horizontal displacement (COD) is verified.

3.5.4.2. LC, LC4 and LC8 specimens

In Figure 55, the failure modes for LC, LC4 and LC8 specimens are reported.

| (a) | (b) | (c) |
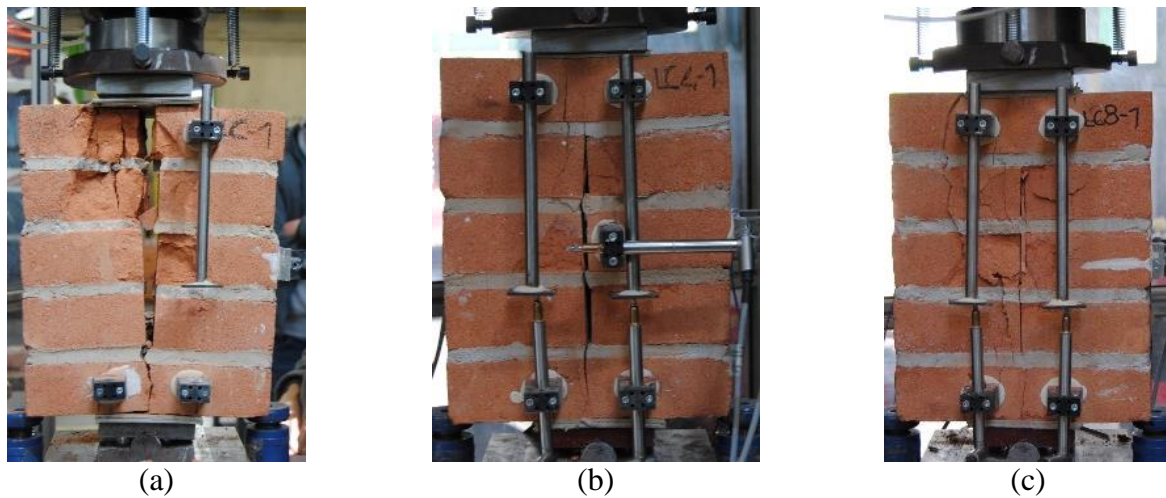
Figure 55 Failure modes: a) LC, b) LC4 and c) LC8.

In Figure 56, the results of the LC specimens without and with reinforcement are shown.
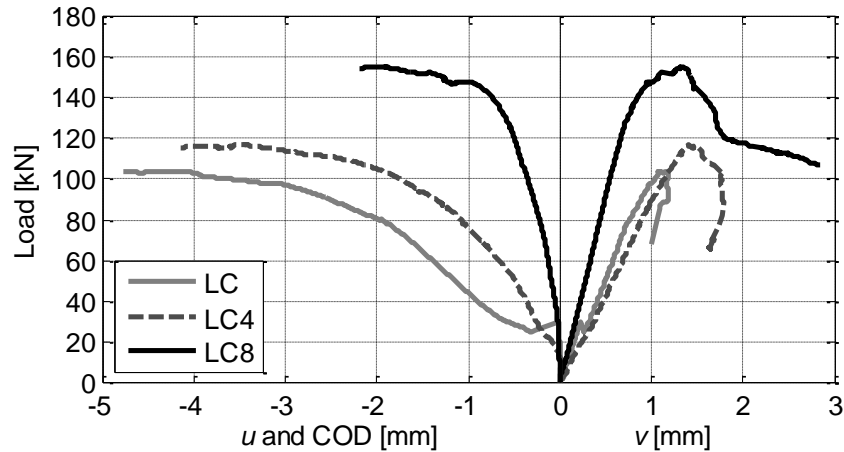
Figure 56 Load - *v* and load - *u* curves for LC, LC4 and LC8 specimens.

LC specimen, grey curve, exhibits a linear behaviour at the beginning of the test. For a certain load value indicated as P_{crack} (around 30 kN), the pre-existent crack starts to propagate and the curves show a very small load drop of few kilonewtons. Then, the specimen is able again to sustain load and a load increase is registered. However, this second ascending branch is less steep with respect to first one indicating a state of damage of the specimen. After the peak load is attained, a short softening branch is registered. The specimen gets to collapse in a brittle way splitting in two parts and with the formation of horizontal cracks at the brick/mortar interface (Figure 55a).

Comparing the light grey curve related to the unreinforced specimen with the dashed dark grey and black ones referred to reinforced specimens, it can be noted that in the initial part of the diagram, the three curves show a similar slope. The load value P_{crack} is recognizable looking at the load - *u* curve that shows, around 30 kN, a slight slope change. As expected, reinforced specimens reach a higher peak load (P_{max}) with respect to LC, and after the peak load is attained, the softening branch is longer with respect to the unreinforced specimen, showing a more ductile behaviour. At the end of the test, the collapse of LC4 and LC8 specimens is due to a cracking of the brick under the loading plate, while horizontal cracks and the splitting of the specimen do not occur, (Figure 55b and Figure 55c).

Considering the curves in the negative part of the abscissa, the horizontal displacements (*u*) across the pre-existent crack are registered. At the beginning of the test, for low load values, the curves are almost vertical meaning that the horizontal displacement is around zero. As soon as the load level attains the P_{crack} value, the horizontal displacement starts to increase. As stated before, from this load value the horizontal displacement is indicated as Crack Opening Displacement (COD). For LC specimen the COD increases significantly for low load increments. For LC4 and LC8 specimens, after P_{crack} is attained, the COD increases for higher load increments.

3.5.4.3. SC and SC4 specimens

In Figure 57, the failure modes for SC and SC4 specimens are reported.

(a) (b)
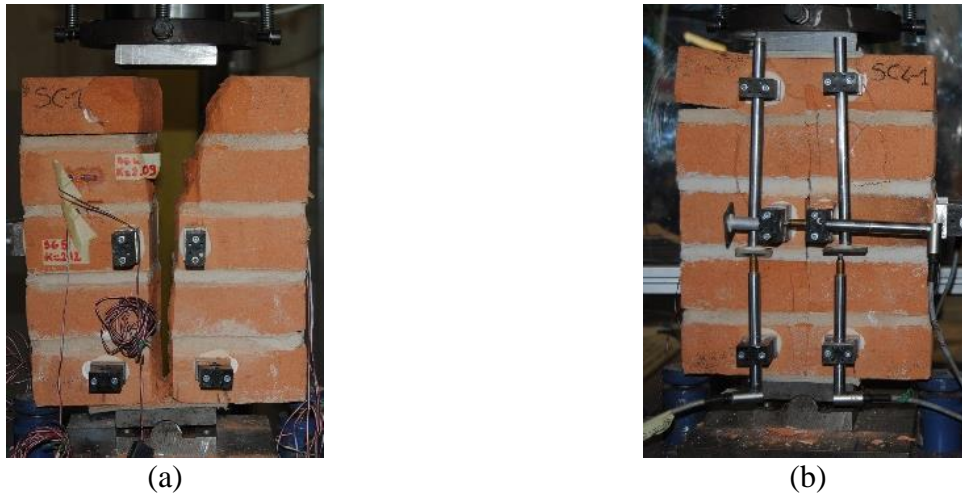
Figure 57 Failure modes: a) SC and b) SC4.

In Figure 58, the results of the SC specimens without and with reinforcement are shown.
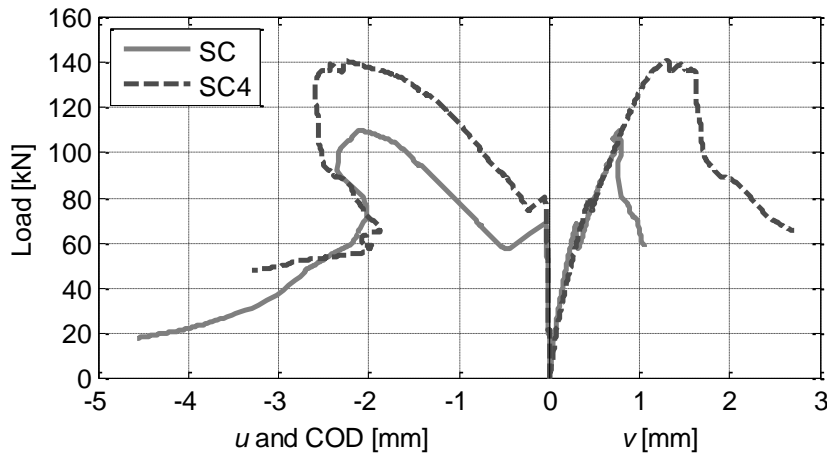
Figure 58 Load - *v* and load - *u* curves for SC and SC4 specimens.

In the initial part of the load - *v* graph, the two curves show a similar behavior being linear and with the same slope. For a load around 70 kN, P_{crack}, a drop appears for SC specimen corresponding to the propagation of the vertical crack. Due to the presence of the steel bars, the propagation of the crack for the reinforced specimen occurs for a higher load value (P_{crack} is around 80 kN). As expected, SC specimen shows a smaller peak load, around 110 kN, with respect to the reinforced specimen, whose P_{max} is around 140 kN. The softening branch for SC specimen is very short and after P_{max} is attained, a brittle collapse occurs (Figure 57a). It is important to note that at failure, cracks due to tensile stresses on the corners of the specimen at the brick/mortar interface are present. Conversely, SC4 specimen is characterized by a ductile collapse mechanism, (Figure 57b), as shown by the softening branch in Figure 58.

Looking at the load - *u* curves, the same slope of the two curves below P_{crack} shows that the bars do not affect the behavior of the specimens for low load values. At P_{crack}, a meaningful horizontal displacement due to the opening of the crack is observed. This behavior was observed also in the specimens without crack and with large crack. Then, SC specimen starts again to sustain load but with a lower value of stiffness with respect to the first branch. The crack arrestor function of the bars can be highlighted considering that for a certain load level higher than P_{crack}, the COD registered for SC specimen is greater than the COD of SC4 specimen. For higher load values this difference increases.

88

3.5.5. Summary

All the results are collected in Table 9 in terms of maximum load, P_{max}, load at which the propagation of crack occurs, P_{crack}, vertical and horizontal displacements measured by LVDTs at P_{max}, Δ_1 and Δ_2 evaluated using Eq.(32) and Eq.(33).

Table 9 Summary of the results of the experimental investigation. Standard deviation in parentheses.

Sample	P_{max} [kN]	P_{crack} [kN]	v at P_{max} [mm]	u at P_{max} [mm]	Δ_1 [%]	Δ_2 [%]
NC-1	120.49	107.51	1.04	1.95		
NC-2	116.69	89.46	0.88	2.85		
NC	118.59 (2.69)	98.49 (12.76)	0.96 (0.11)	2.40 (0.64)	-	-
LC-1	104.04	29.75	1.08	4.20		
LC-2	96.59	20.38	0.76	2.87		
LC-3	121.50	30.42	1.40	3.83		
LC-4	89.70	20.08	0.83	3.49		
LC-5	121.60	20.32	0.91	3.15		
LC	102.96 (14.49)	24.19 (5.39)	0.99 (0.26)	3.51 (0.53)	-	-
LC4-1	116.64	-	1.42	3.50		
LC4-2	115.64	-	1.42	2.82		
LC4-3	133.46	-	1.10	2.47		
LC4-4	133.34	-	1.32	4.47		
LC4	121.91 (9.97)	-	1.31 (0.15)	3.31 (0.88)	18.40	-
LC8-1	155.18	-	1.34	1.97		
LC8-2	169.46	-	0.91	0.82		
LC8-3	151.06	-	1.33	1.96		
LC8	158.57 (9.66)	-	1.19 (0.24)	1.58 (0.66)	54.01	-
SC-1	109.70	68.21	0.79	2.10		
SC-2	124.14	79.81	1.12	2.98		
SC-3	117.78	43.51	1.22	4.40		
SC	117.21 (7.24)	63.84 (18.54)	1.04 (0.22)	3.16 (1.16)	-	-
SC4-1	140.80	80.38	1.32	2.30		
SC4-2	142.54	61.18	1.36	1.90		
SC4-3	152.51	79.01	1.18	2.33		
SC4	145.28 (6.32)	73.52 (10.71)	1.29 (0.09)	2.18 (0.24)	23.95	15.16

From Table 9, comparing the results for LC and LC4 specimens in terms of peak load the increment is around 20% (Δ_1=18.40%) for LC4 with respect to LC, and is around 50% (Δ_1=54.01%) for LC8 with respect to LC. However, due to the presence of a large crack on the specimens, it was difficult to obtain the value at which the propagation of crack occurred, P_{crack}; this is the reason why Δ_2 is not calculated. The mean value of the COD that corresponds to the peak load is the half for LC8 (1.58 mm) specimens compared to the one of LC (3.51 mm), and for LC4 is 3.31 mm.

Comparing the results for SC and SC4 specimens, as reported in Table 9, the mean value of the peak load for SC specimens is 117.21 kN, while for SC4 is 145.28 kN, so the increment Δ_1 is about 25%. Moreover, the mean value of crack load for SC specimens is 63.84 kN, while for SC4 is 73.52 kN, so the increment Δ_2 is about 15%. As for LC and LC8 specimens, the mean value of the COD for SC4 specimens is close to the half of the SC specimen ones.

3.6 Conclusions

The results of an experimental campaign conducted on small masonry specimens without and with an initial crack were discussed in detail (Casacci et al. 2016). The initial crack, realized during the construction phase, was intended to simulate a structural condition in which masonry elements that have to be retrofitted can be found in situ. For comparison purposes, not reinforced specimens were also tested. Specimens were reinforced inserting in the mortar joints high strength carbon bundles impregnated with an epoxy resin or steel stainless helifix bar. An *ad hoc* splitting test was employed to induce in the specimens the propagation of the main crack. DIC was employed to investigate for the state of stress and deformation of the specimens during the test.

The results showed that:

i) the initial slope of the load - *v* curves is similar for reinforced and unreinforced specimens, meaning that the carbon bundles and the steel bars do not affect the elastic phase of the specimens;

ii) the peak load is always greater for reinforced specimens;

iii) the presence of the bars modifies the collapse mechanism from brittle to ductile preventing the formation of horizontal cracks at brick/mortar interface;

iv) for a certain load level, the crack starts to propagate: in NC a load drop of several kN is achieved, in LC and LC4 specimens a small load drop of few kN is registered, for LC8 specimens only a change in the curve slope is verified, while for SC and SC4 specimens a load drop of several kN occurs;

v) the COD for reinforced specimens, considering the same load level, is always smaller with respect to the COD for unreinforced specimens, highlighting the crack arrestor function of the bars;

vi) from DIC results, it can be noted that for unreinforced specimens in the load - *v* curves registered close to the edges and outside the loading plate, after P_{crack} is attained, the displacements move from positive to negative, revealing a combined state of compression and bending close to the edges. This results in the formation of horizontal cracks at the brick/mortar interface that leads to the collapse of the specimens;

vii) the maximum load, $\bar{P}_{max}$, increases as reinforcement ratio, ω_f, increases;

$$\omega_f = \frac{A_{reinf}}{A_n} \frac{E_{reinf}}{E_m} = \rho_f \frac{E_{reinf}}{E_m} \tag{34}$$

where A_{reinf} is the bar or FRCM area, A_n is the net area of the specimen, while E_{reinf}, E_m are the moduli of elasticity of bars or FRCM and masonry, respectively (all the calculations are reported in Appendix B);

viii) the employed testing set-up has been proved to be effective in highlighting the phenomenon of localized crack propagation in compression. In fact, the reduced lateral confinement of the specimens (in comparison to

that of real masonries) allows to reach a splitting mode of collapse. Thus, the function of reinforcement in the joints resulted evident.

4. Chapter 4: Diagonal compression test on small masonry specimens

4.1 Introduction

A large part of existing buildings and architectural heritage in Europe and all over the world are made of bricks and stones masonry that suffers from several structural weaknesses including low tensile strength and flexural resistance as well as low ductility (Gentilini et al. 2012; Franzoni et al. 2014; Valluzzi et al. 2014; Franzoni et al. 2015). For these reasons, masonry buildings are particularly prone to seismic damage (Magenes & Calvi 1997; Castellazzi et al. 2013). Strengthening interventions are necessary to improve the mechanical performance of masonry structures (Ghiassi et al. 2013; Gattesco & Boem 2015).

In general, reinforcement techniques can be classified in two groups: traditional and modern techniques. Traditional techniques are mainly based on conventional methods such as, among the others, addition of new structural elements, injection of material to fill cracks, local replacement of damaged masonry bricks, improvement of the connections and addition of confinement walls. However, as it is well known, these strengthening solutions show drawbacks such as addition of mass to the structure, reduction of the available space and modification of the appearance of the building. Modern techniques mainly consist in the application of innovative materials such as composites, made of carbon, glass, aramid, steel, basalt etc. Composites can be externally bonded, in the form of textiles, to the masonry structure (wet lay-up) or internally inserted in the joints, in the form of bars or strips (structural repointing). In (Valluzzi et al. 2014), the main advantages and constraints related to the strengthening intervention of externally bonded composites to masonry are highlighted.

In this study, the main focus is on reinforced repointing technique that involves the application of materials having high tensile strength such as reinforcing steel bars, carbon wires, steel textile sheets or composites thin pultruded laminae to reduce the vulnerability of masonry structures against in-plane actions and long terms high level dead loads (Bednarz et al. 2014; Casacci et al. 2015). The technology is also called near surface mounted (NSM) reinforcement, because the reinforcing material is embedded with structural mortar or epoxy paste in the mortar bed joints of a wall previously grooved for few centimetres by means of a grinder, (Valluzzi et al. 2005; Borri et al. 2011; Akhaveissy & Milani 2013). If it is required, after the insertion of the strengthening material, the joints are covered with a mortar whose colour and formulation is similar to the original one, resulting completely hidden after application. NSM reinforcement technique is particularly suitable for fair-faced masonry buildings whose aesthetic appearance has to be preserved as well as for historic monuments and artefacts.

Starting from the 1950s, this strengthening method has been applied to reinforced concrete structures. Fibre Reinforced Polymer (FRP) reinforcement in the form of bars was applied to concrete elements by means of epoxy paste or cement grout to reduce corrosion risk (De Lorenzis & Nanni 2001; De Lorenzis & Teng 2007). The application of this technique to masonry is more recent and has attracted considerable attention from researchers in the last decades (Oliveira et al. 2012).

4.1.1. Diagonal compression test on masonry elements

Diagonal compression test is normalized by (ASTM E 519 2002) and (RILEM 1991) standards. This test is adopted to determine the diagonal tensile strength of masonry, f_{dt}. (ASTM E 519 2002) it provides that the nominal size of each specimen shall not be less than 1200 mm x 1200 mm in order to be representative of a full size masonry assemblage. To provide statistically significant results, at least three specimens should be tested. (RILEM 1991) standard does not provide specific dimensions for the specimen to be tested; only defines the shape of the finished specimen which should be as square as possible and should be made of a minimum of four units wide. To provide results statistically significant, at least five specimens must be tested. (ASTM E 519 2002) standard gives the formula to compute, for the tested specimen, the values of shear strain, shear elastic modulus and shear stress, while the (RILEM 1991) standard gives indication only about the estimation of the shear strength.

The diagonal compression test can be performed both on site and in laboratory; it is a destructive test due to the fact that leads to failure the masonry panel. Nevertheless, this test can be applied to different types of masonry and, in laboratory, can be performed by using two different configurations as illustrated in Figure 59b and Figure 59c: standard and modified.
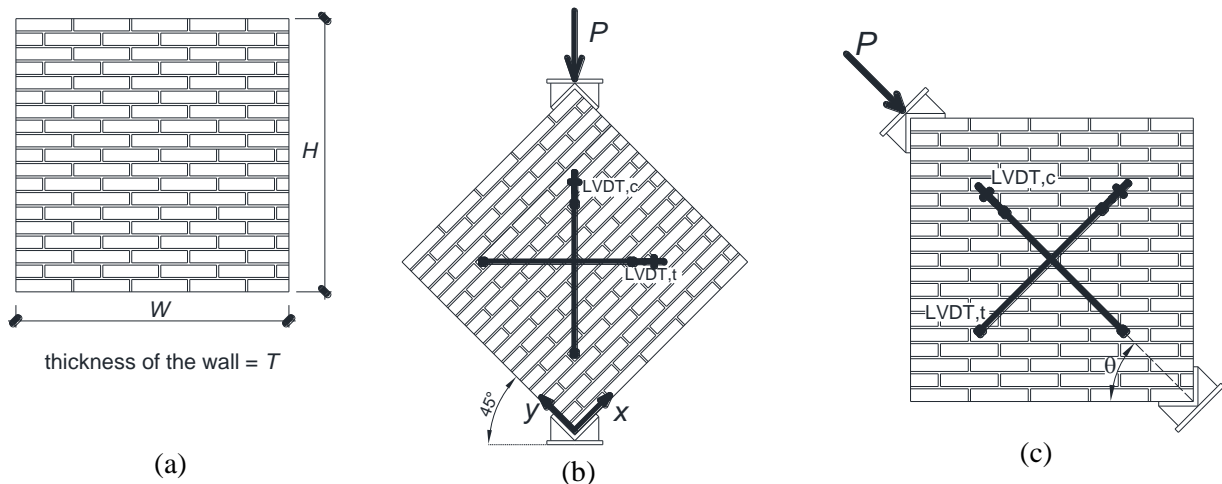
Figure 59 a) Dimensions of the wall specimen; b) standard and c) modified diagonal compression test set-up configuration.

Both the available standards (ASTM E 519 2002; RILEM 1991) give indications only about the standard configuration. The need to adopt the modified configuration appears in presence of heavy and fragile specimens, for which the rotation procedure necessary to set them in the testing machine could be dangerous and may compromise the integrity of the specimens. The load is applied through two steel plates (shoes) placed on the corners of the masonry panel. During the test, the values of the applied load and the diagonal displacements, that can be measured by four Linear Variable Displacement Transducers (LVDTs), two on each side (LVDT,c and LVDT,t in Figure 59b) are recorded. The load cell is used to measure the force along the loaded diagonal, while the LVDTs are placed on each face of the wall: one oriented along the force line to measure the wall shortening, and the other perpendicular to the force line to record the crack opening.

Considering (Figure 59), a panel subjected only to a diagonal compressive load and zero axial load, the elastic solution on the hypothesis of homogeneous, isotropic continuum provides (Brignola et al. 2008; Calderini et al. 2010; Almeida et al. 2015) the following state of stress at the centre of the panel:

$$\sigma_x = \sigma_y \cong -\frac{0.56P}{A_n} \tag{35}$$

$$\tau_{xy} = \frac{1.05P}{A_n} \tag{36}$$

The principal stresses in tension and compression result:

$$\sigma_I \cong -\frac{0.5P}{A_n} \tag{37}$$

$$\sigma_{II} \cong -\frac{1.62P}{A_n} \tag{38}$$

where, being A_n the net area of the panel, P the applied load and the loading direction angle being 45°. In (ASTM E 519 2002)standard, it is assumed that the diagonal compression test produces a uniform shear stress field τ_{xy} at the centre of the panel and, as consequence, the principal stresses result: $\sigma_I = \sigma_{II} = \tau_{xy}$.

4.2 Experimental background

In the following, a literature review on the diagonal compression test performed on masonry specimens reinforced by using structural repointing is reported. The tests, have been performed both in situ or in laboratory, were carried out on wall panels made of clay units or concrete blocks, reinforced using different materials such as steel, glass, polyethylene in the form of bars, strips, cords, laminates or grids.

In (Li et al. 2005), the authors performed diagonal compression tests on walls built by using concrete blocks in a running bond pattern with overall dimensions 1625 mm x 1625 mm x 152 mm. They used blocks of 406 mm x 203 mm x 152 mm, with a net area of 35400 mm² and an average net area compressive strength of concrete masonry prisms equal to 16.8 MPa. Moreover, the average compressive strength of the employed mortar was 5.67 MPa. Different strengthening techniques were applied on the specimens: GFRP laminates installed by manual wet lay-up, GFRP bars and stainless steel bars installed by using repointing technique, and internal steel wires. In Table 10, the mechanical properties of reinforcing materials are reported (f_t = tensile strength and E = elastic modulus).

Table 10 Mechanical properties of the reinforcing materials (Li et al. 2005).

Material	Cross-sectional area [mm²]	f_t [MPa]	E [GPa]
GFRP laminates	8.9	1687	83.1
GFRP bars	33.2	824	50.2
Stainless steel bars	9.4	939	118.9
Internal steel wire-ladders	44.5	625	204.4

For the repointing operations, two types of embedding materials were used: the first was an epoxy paste and the other was a latex modified cementitious paste (LMCP). The 28-day splitting tensile strengths of epoxy paste and LMCP were 18.5 MPa and 5.6 MPa, respectively. One of the aspects investigated in this work was

the effect of the eccentricity derived from the application of the reinforcing material on one face of the specimens.

In Table 11, the results of the experimental campaign are reported in terms of amount of reinforcement (ρ_f) calculated by using Eq.(39), maximum force (P_{max}), parameter Δ_1 calculated by using Eq.(32), and pseudo-ductility (μ), calculated by using Eq.(40)

$$\rho_f = A_{reinf}/A_{wall} \tag{39}$$

$$\mu = \gamma_u/\gamma_y \tag{40}$$

where γ_u is the ultimate shear strain and γ_y is the shear strain corresponding to the bend-point of the in-plane load versus shear strain curve.

It should be noted that, from here onwards, the symbol (*) in the tables means that the calculations are made by the present author. Differently, where the symbol is not reported, the parameters in the tables are taken from literature.

Table 11 Summary results (Li et al. 2005)

Masonry texture and panel dimensions (*W*, *H*, *T*) [cm]	Type of repair	$\rho_f \cdot 10^{-3}$ (*)	P_{max} [kN]	Δ_1 [%](*)	μ
Concrete masonry (162.5x162.5x15.2)	UNR	-	76.5	-	1.00
	$7\phi6.4$ GFRP bars (every Horiz. joint on one side)	0.941	141.5	84.97	13.10
	$7\phi6.4$ GFRP bars (every Horiz. joint alternately on both side)	0.941	137.9	80.26	20.20
	$7\phi7.1$ wire ladder (every Horiz. joint on one side)	1.261	149.9	95.95	22.30
	$4\phi6.4$ GFRP bars + $3\phi7.1$ wire ladder (every Horiz. joint alternately GFRP bars and internal steel wires on one side)	1.078	113.4	48.23	3.00
	$7\phi3.6$ stainless steel bars (every Horiz. joint on one side)	0.266	89.9	17.52	2.50
	$7\phi3.6$ stainless steel bars; cement-based paste (every Horiz. joint on one side)	0.266	155.2	102.88	-
	$7\phi6.4$ GFRP bars; cement-based paste (every Horiz. joint on one side)	0.941	130.3	70.33	20.90
	$7\phi6.4$ GFRP bars + 4 GFRP layup strips (every Horiz. joint on one side + 4 vertical strips at 406mm on centers on one side)	1.085	134.8	76.21	5.10
	$7\phi6.4$ GFRP bars (every Horiz. joint on one side)	0.941	170.4	122.74	17.10
	$4\phi6.4$ GFRP bars (every second Horiz. joint on one side)	0.538	98.3	28.50	5.00
	$3\phi6.4$ GFRP bars (every second Horiz. joint on one side)	0.403	134.8	76.21	9.30

From the experimental results, by using the FRP strengthening technique, an increment of both in-plane strength and ductility of the walls compared to the unreinforced ones was achieved. Furthermore, reinforced walls showed a more stable behaviour after failure with respect to the unstrengthened specimens. The mechanical response depended on the amount, but not on the type of reinforcements, due to the fact that failure did not involve the strengthening material but the interfacial mechanical interlock between the cords and the mortar joints. Due to reinforcement eccentricity, cracks mainly occurred on the unstrengthened face and, at the same time, the wall tilted toward the reinforced side. An improvement in both stability and ductility was achieved by using symmetrically distributed reinforcements.

In (Turco et al. 2006), walls characterized by nominal dimensions of 1600 mm x 1600 mm x 150 mm were tested in diagonal compression without and with reinforcements. The specimens were made of concrete masonry units, characterized by a compressive strength around 10 MPa, and mortar with compressive strength equal to 7.6 MPa. As reinforcement, smooth and sand coated GFRP bars were applied as repointing in the mortar joints by using, as structural mortar, latex modified cementitious paste and epoxy paste. The average values of maximum stress and elastic modulus of GFRP reinforcements were close to 824 MPa and 50 GPa, respectively, while the splitting tensile strength after 28 days was 5.59 MPa in the case of latex modified paste and 18.54 MPa in the case of epoxy based paste. Three different reinforcement layouts were analyzed: (*i*) bars placed in every horizontal joint on one side of the wall, (*ii*) bars placed in every second horizontal joint on one side of the wall, (*iii*) bars placed in every second horizontal joint on both sides of the wall.

In Table 12, the results of the experimental tests are summarized in terms of amount of reinforcement calculated by using Eq.(39), ρ_f, maximum force, P_{max}, parameter Δ_1 calculated by using Eq.(32), and pseudo-ductility, μ, calculated by using Eq.(40).

As expected, the failure of the unreinforced walls was brittle, governed by bonding between masonry units and mortar. Looking at reinforced specimens, the failure was divided in two phases: in-plane, characterized by a diagonal crack along the mortar joints; and out-of-plane phase, only for the walls strengthened by using epoxy paste. Cementitious paste was better than epoxy for shear strengthening because allowed sliding and, consequently, a redistribution of stresses in the system.

Table 12 Summary results (Turco et al. 2006)

Masonry texture and panel dimensions (*W*, *H*, *T*) [cm]	Type of repair	$\rho_f \cdot 10^{-3}$ (*)	P_{max} [kN]	Δ_1 [%](*)	μ
Concrete masonry (160x160x15)	UNR	-	108	-	1
	Sand-coated GFRP bars (every horizontal joint on one side, embedded with epoxy paste)	0.824	198.9	84.17	13.10
	Smooth GFRP bars (every horizontal joint on one side, embedded with epoxy paste)	0.572	241.1	123.24	nd
	Sand-coated GFRP bars (every horizontal joint on one side, embedded with cementitious paste)	0.824	184.1	70.46	21.60
	Sand-coated GFRP bars (every second horizontal joint on one side, embedded with epoxy paste)	0.353	195	80.56	20.20
	Smooth GFRP bars (every second horizontal joint on one side, embedded with epoxy paste)	0.245	190.4	76.30	nd
	Sand-coated GFRP bars (every second horizontal joint on both side, embedded with epoxy paste)	0.707	189	75.00	5.00

In (Corradi et al. 2008), diagonal compression tests were performed on site on walls with dimensions of 1200 mm x 1200 mm and variable thickness. Two repair techniques were adopted in this experimental campaign: deep repointing (deep because the depth of the groove was about 70-80 mm) and deep repointing with injections. The grout used for the injections was a ready mix hydraulic lime, and the structural mortar used during the repointing operations was lime-cement based. The panels were tested before and after strengthening interventions. In Table 13, the mechanical properties of grout and structural mortar were reported (f_f = flexural strength and f_c = compressive strength).

Table 13 Mechanical properties of grout and structural mortar (Corradi et al. 2008).

Material	f_f [MPa]	f_c [MPa]
Grout for injection	3	7
Structural mortar	3.55	10.75

In Table 14, the results of the experimental program are reported in terms of maximum force, P_{max}, structural enhancement (Δ_1) calculated by using Eq.(32), shear stiffness (G) calculated by using Eq.(41), as well as shear strength (τ_{max}) calculated by using Eq.(42) substituting P with P_{max}, according to (ASTM E 519 2002)

$$G = \frac{\tau_{1/3} - \tau_i}{\gamma_{1/3}}$$

(41)

where $\tau_{1/3}$ is the shear stress at 1/3 of the maximum load, $\gamma_{1/3}$ is the corresponding angular strain and τ_i the initial shear stress ($\tau_i = 0.002$ MPa) due to the application of a pre-load.

$$\tau = \frac{P cos\theta}{A_n}$$

(42)

Table 14 Summary results (Corradi et al. 2008).

Masonry texture	Type of repair	Panel dim. (W, H, T) [cm]	P_{max} [kN]	Δ_1 [%](*)	G [MPa]	τ_{max} [MPa]
Double-leaf roughly cut stone masonry	UNR	120x120x48	48.06	-	37	0.059
	Repointing + grout injection	120x120x48	127.89	166	731	0.157
	UNR	120x120x67	51.17	-	80	0.045
	Repointing	120x120x67	61.41	20.01	232	0.054

From the experimental outcomes, an increment of shear stiffness was achieved by using deep repointing, but to obtain also an improvement of shear strength, injections were necessary.

In (Ismail et al. 2011), the in-plane shear behaviour of masonry walls was studied. The specimens were classified in two series: Series 1 (single-leaf modern masonry construction) and Series 2 (two-leaf historical masonry construction). The specimens in both series were subjected to diagonal compression test. Series 1 included two UNR specimens and eight strengthened ones of nominal dimensions 1200 mm x 1200 mm x 110 mm. New solid clay bricks, with nominal dimensions of 230 mm x 110 mm x 75 mm, and 10 mm thick mortar joints were used. The compressive and tensile strength of masonry were 32.1 MPa and 0.4 MPa, respectively. Series 2 included one UNR specimen and six strengthened ones of nominal dimensions 1200 mm x 1200 mm x 220 mm. Salvaged solid clay bricks, with nominal dimensions 220 mm x 105 mm x 90 mm, and roughly 15 mm thick mortar joints were employed. The compressive and tensile strength of masonry were 10.7 MPa and 0.2 MPa, respectively. As bond pattern, the masonry was laid in one header course after every three stretcher-courses. The specimens in both test series were strengthened using the same type of high strength twisted stainless steel bars. Two different sized bars were used: 6 mm outside diameter (Series 1 and 2) and 10 mm outside diameter (Series 1 only). In Table 15, the mechanical properties of the twisted steel bars are reported (D = diameter, f_t = ultimate tensile strength, E = elastic modulus).

Table 15 Mechanical properties of twisted steel bars (Ismail et al. 2011).

Material	D [mm]	Cross-sectional area [mm²]	f_t [MPa]	E [GPa]
Stainless steel twisted bars	6	7.14	1168	110-180
	10	14.8	1108	-

The twisted stainless steel near surface mounted (TSNSM) reinforcements were bonded using an injectable cementitious grout, and inserted in the slots cut into the surface of the masonry. Differently from other experimental programs in literature dealing with repointing technique in masonry, in this case, the reinforcing bars were applied not only in the mortar bed joints, but also in vertical slots. The vertical slots were either located in the brick units, midway between mortar head joints, or through alternating brick units and mortar head joints. The reinforcements were applied on both faces of the Series 1 specimens, whereas for Series 2 specimens the strengthening system was applied only on one side. Two different test setups were used for each test series. Specimens of Series 1 were tested following the standard configuration (Figure 59b) in accordance with (ASTM E 519 2002), while samples of Series 2, that were heavier and with lower mechanical characteristics, were tested in the modified configuration (Figure 59c).

In Table 16, the results of the experimental tests are reported in terms of amount of reinforcement (ρ_f) calculated by using Eq.(39), maximum force (P_{max}), structural enhancement (Δ_1) calculated by using Eq.(32), shear modulus, G, shear strength calculated by using Eq.(42) and pseudo-ductility, μ.

The shear modulus was defined as the secant modulus between $0.05\tau_{max}$ and $0.75\tau_{max}$ of the shear stress-shear strain plots. The pseudo-ductility was calculated as

$$\mu = \delta_u/\delta_y$$

$$(43)$$

where δ_u is the drift at failure corresponding to $0.8\ \tau_{max}$ and δ_y is the drift at yield.

The UNR control specimens exhibited an approximately linear behaviour until the first cracks and then failed suddenly along a diagonal step joint when they reached their maximum diagonal tensile strength. The specimens strengthened only in the horizontal direction showed diagonal cracks when the peak load was reached, and, after that, larger deformation was achieved without a relevant increase in shear strength. For the strengthened specimens with vertical and grid reinforcement schemes, diagonal cracks initiated close to peak load as before, but were restrained by the steel bars, resulting in a more ductile mode of failure than those observed for both the UNR control specimens and the ones strengthened only in the mortar bed joints (horizontal scheme). In several cases, the value of the ductility was very high, due to the considerable variability in the calculation of yield drift, δ_y. These large variations in δ_y were attributed to a redistribution of stresses and deformations throughout the heterogeneous material during the pre-peak loading phase.

Table 16 Summary results (Ismail et al. 2011).

Masonry texture and panel dimensions (*W*, *H*, *T*) [cm]	Type of repair	$\rho_f \cdot 10^{-3}$ (*)	P_{max} [kN]	Δ_1 [%] (*)	G [MPa]	τ_{max} [MPa]	μ
Single-leaf modern masonry (120x120x11)	UNR	-	157.0	-	2800	0.84	1.00
	UNR	-	129.0	-	3500	0.69	1.00
	4 slots on both faces equally spaced with 1TSNSMφ6 bar in each slot (Vert.)	0.433	193.0	34.97	2600	1.03	2.00
	4 slots on both faces equally spaced with 1TSNSMφ6 in each slot (Vert.)	0.433	212.0	48.25	3800	1.14	3.00
	4 slots on both faces equally spaced with 2TSNSMφ6 in each slot (Vert.)	0.865	212.0	48.25	3800	1.14	6.00
	4 slots on both faces equally spaced with 2TSNSMφ6 in each slot (Vert.)	0.865	192.0	34.27	1300	1.03	2.00
	4 slots on both faces equally spaced with 2TSNSMφ10 in each slot (Vert.)	1.794	163.0	13.99	8700	0.87	26.00
	4 slots on both faces equally spaced with 2TSNSMφ10 in each slot (Vert.)	1.794	209.0	46.15	11200	1.12	198.00
	4 slots on one face and 3 on the other with 1TSNSMφ6 (Horiz.)	3.786	105.0	-26.57	5600	0.56	8.00
	4 slots on one face and 3 on the other with 1TSNSMφ6 (Horiz.)	3.786	124.0	-13.29	2200	0.66	4.00
Double-leaf historical masonry (120x120x22)	UNR	-	51.0	-	1000	0.14	7.00
	2 slots on one face equally spaced with 1TSNSMφ6 in each slot (Vert.)	0.0541	87.0	70.59	700	0.23	6.00
	3 slots on one face equally spaced with 1TSNSMφ6 in each slot (Vert.)	0.0811	93.4	83.14	1200	0.25	18.00
	4 slots on one face equally spaced with 1TSNSMφ6 in each slot (Vert.)	0.108	94.0	84.31	1300	0.25	46.00
	5 slots on one face equally spaced with 1TSNSMφ6 in each slot (Vert.)	0.135	94.6	85.49	2500	0.25	112.00
	4 slots on one face with 1TSNSMφ6 in each slot (Grid)	0.108	96.2	88.63	700	0.26	9
	2 slots on one face equally spaced with 1TSNSMφ6 in each slot (Horiz.)	0.0541	71.6	40.39	800	0.19	29

In (Borri et al. 2011), diagonal compression tests were carried out in situ on unreinforced and reinforced stone masonry panels. This type of masonry was mainly used in Central Italy and, particularly in Umbria and Abruzzo regions, areas in which the seismic risk is relevant. Different repair techniques were applied on the panels. Between traditional ones, deep repointing in the mortar joints and application of FRP on the surface of the panels by using both GFRP laminates and GFRP mesh were used. Moreover, a strengthening technique

called "Reticolatus" was proposed by the authors. The main phases of application were: (*i*) make a first layer of repointing, (*ii*) embed a continuous mesh of steel cords in the mortar joints, (*iii*) fix the mesh to the wall by using transversal metal bars, (*iv*) make the second layer of repointing. The mechanical properties of the strengthening materials were reported in Table 17.

Table 17 Mechanical properties of strengthening materials (Borri et al. 2011).

Material		f_t [MPa]	E [MPa]
GFRP laminates		407	87616
GFRP mesh		24	400-450
Reticolatus	Steel cords	2875	215
	Polyethylene cords	637	116

In Table 18, the results of the in situ test are summarized in terms of maximum force (P_{max}), structural enhancement (Δ_1) calculated by using Eq.(32), apparent shear modulus of the panel (G), tensile strength of the masonry (f_t'), shear strength (τ_{max}).

The apparent shear modulus G was defined as the secant stiffness of the linear elastic branch until the occurrence of the first cracks and computed as:

$$G = \frac{\tau_{el} - \tau_i}{\gamma_{el} - \gamma_i}$$

(44)

where τ_i is equal to 0.015 MPa, τ_{el} corresponds to the point on the curve where the first cracks occur in the panel, while γ_i and γ_{el} are the corresponding values of the shear strain. The tensile strength, f_t', was computed as

$$f_t' = 0.5 \frac{P_{max}}{A_n}$$

(45)

where A_n is the net area of the specimen calculated by using the Eq.(46)

$$A_n = \left(\frac{W + H}{2}\right) Tn$$

(46)

with W, H and T the width, the height and the thickness of the wall, respectively and n the percentage of the gross area of the unit that is solid, expressed as a decimal.

The shear strength was defined as:

$$\tau_{max} = \frac{f_t'}{1.5}$$

(47)

Table 18 Summary results (Borri et al. 2011)

Masonry texture	Type of repair	Panel dim. (*W*, *H*, *T*) [cm]	P_{max} [kN]	Δ_1 [%] (*)	G [MPa]	f_t' [MPa]	τ_{max} [MPa]
Triple-leaf roughly cut stone masonry (pink calcareous stone)	UNR	120x120x45	30.6	-	51	0.030	0.019
	FRP jacketing (unidirectional GFRP strips)	120x120x45	126.4	313.07	169	0.123	0.078
	FRP jacketing (unidirectional GFRP strips)	115x110x45	68.6	124.18	142	0.070	0.044
Double-leaf roughly cut stone masonry (white calcareous stone)	URM	125x110x52	21	-	55	0.016	0.011
	Reticolatus (steel cords)	125x110x52	56.5	169.05	198	0.044	0.029
	Deep repointing	120x120x52	35.3	68.09	147	0.027	0.018
Double-leaf roughly cut stone masonry (pink calcareous stone)	UNR	120x120x67	37.6	-	30	0.035	0.023
	UNR	120x120x67	50.3	-	39	0.030	0.020
	FRP jacketing (unidirectional GFRP strips)	124x124x67	112	154.83	151	0.070	0.047
	Deep repointing	124x124x67	63	43.34	98	0.038	0.026
	FRP jacketing (GFRP mesh)	120x120x67	104.2	137.09	245	0.063	0.042
Triple-leaf roughly cut stone masonry (pink calcareous stone)	UNR	120x120x62	40.9	-	24	0.027	0.018
	UNR	120x120x70	55	-	62	0.033	0.022
	UNR	120x120x70	33.5	-	34	0.020	0.013
	UNR	120x125x62	58.8	-	81	0.039	0.026
	UNR	125x130x81	68.1	-	102	0.033	0.022
	UNR	120x125x67	49.1	-	43	0.030	0.020
	Reticolatus (steel cords)	125x130x61	137.9	170.92	294	0.089	0.059
Triple-leaf roughly cut stone masonry (white calcareous stone)	UNR	125x121x62	51.6	-	79	0.033	0.022
	Reticolatus (polyethylene cords)	134x123x60	122.5	137.40	345	0.076	0.051

The behaviour of unstrengthened masonry panels was linear until the first masonry cracks appeared at low values of load, then non linear behaviour occurred until the peak load; after that, the response was ductile characterized by lower strength and more spread damages. From the results, the authors observed that the deep repointing technique was effective when used as a repair technique, instead of applied on undamaged masonry. The "Reticolatus" provided advantages in terms of shear strength than FRP jacketing. The better performances achieved by using reticolatus were independent from the type of cords used.

4.3 Material characterization

Standard tests were performed to characterize the mechanical properties of the materials used in the experimental campaign.

4.3.1. Brick

Portuguese solid clay bricks having nominal size 50 x 100 x 200 mm^3 were used for manufacturing the specimens. Brick compressive strength in flatwise direction was obtained according to (EN 772-1 2010) on six 40 mm cubic specimens. In Table 19, the mechanical properties of the bricks are reported in terms of elastic modulus E and brick compressive strength f_{cb}.

Table 19 Mechanical properties of the bricks used for the manufacturing of the specimens

Materials	E [MPa]	f_{cb} [MPa]
Portuguese clay brick	9500	14.3

4.3.2. Mortar

Two different types of commercial pre-mixed mortar were used for realizing the specimens. A cement-based mortar (Mortar A) was used to construct the specimens, and a structural mortar (Mortar B) was used for the strengthening operations. Mortar compressive and flexural strengths were obtained according to (EN 196-1 2011).

In Table 20, the mechanical properties of mortars are reported in terms of elastic modulus E, mortar compressive and flexural strength, f_{cm} and f_{fm}, respectively.

Table 20 Mechanical properties of the mortars used for the manufacturing of the specimens. Coefficient of variation in parentheses.

Materials	E [MPa]	f_{cm} [MPa]	f_{fm} [MPa]
Mortar A (cement-based mortar)	4527	8.82 (1.29)	2.59 (0.63)
Mortar B (structural mortar)	8000	10.77 (0.03)	-

4.3.3. Basalt bars

Basalt bars (nominal diameter equal to 5 mm) were used to strengthen the specimens. In order to verify for the mechanical properties of the basalt bars, direct tensile tests were performed. Following the procedure proposed in (Quagliarini et al. 2012), an anchorage system consisting of a steel pipe filled with a thixotropic epoxy resin has been employed. The dimension of the specimens has been derived according to (ASTM D 7205 2011). The test piece was of adequate length to give an effective length between terminations set by this standard. The specimens, with a total length of 1000 mm, were provided with two anchoring systems (one for every end), with a length of 250 mm, leaving an effective length of 500 mm.

A universal testing machine, Galdabini 100 kN, has been used for the tests. The top end of the specimen has been first fixed on the top jaw of the machine, and then also the bottom end has been fixed before applying the load. The load has been applied at a constant speed of 2 mm/min until the failure of the specimen. Each specimen was provided by a deformometer placed in a central position in the bar to record for the elongation. A LVDT (linear variable displacement transducer) was employed to measure the displacement of the head

machine. To check if the anchoring system could affect the test, also the place on the sample where the break occurs has been recorded.

Results in terms of elastic modulus E_{BAR}, tensile strength $f_{t,BAR}$ and breaking elongation ε_u are collected in Table 21. The values are obtained as the mean on five samples.

Table 21 Mechanical properties of the basalt bars.

Materials	E_{BAR} [MPa]	$f_{t,BAR}$ [MPa]	ε_u [%]
Basalt bar	>45000(*)	>1000(*)	/

4.3.4. FRCM

FRCM composite used to strengthen the specimens consisted of a glass fibre square mesh, characterized by a 25 x 25 mm^2 mesh size, tensile strength, $f_{t,FRCM}$, equal to 45 kN/m, modulus of elasticity, E_{FRCM}, equal to 72000 MPa, equivalent thickness of dry fabric equal to 0.035 mm and elongation at failure ε_u, equal to 1.8%. Furthermore, from experimental tests, the average value of the tensile strength of the dry fibers is 830 MPa.

4.4 Specimens

Each specimen was built with nine courses of bricks and eight 10 mm thick mortar layers, and had a nominal total size equal to 520 x 530 x 100 mm3 (Figure 60a).

In particular, five types of specimens were constructed:

i) reference specimens hereinafter denoted with UNR – Unreinforced, Figure 60b;

ii) specimens with asymmetric structural repointing obtained inserting one basalt bar in the third and one in the sixth mortar joint for a total of two bars, hereinafter denoted with RR-A - Reinforced Repointing Asymmetric, Figure 60c;

iii) specimens with symmetric structural repointing obtained inserting two basalt bars in the third and two in the sixth mortar joint for a total of four bars, hereinafter denoted with RR-S - Reinforced Repointing Symmetric, Figure 60d;

iv) specimens with asymmetric FRCM obtained applying a 1-ply glass-based grid mesh on one side of the specimen, hereinafter denoted with RF-A - Reinforced FRCM Asymmetric, Figure 60e;

v) specimens with symmetric FRCM obtained applying a 1-ply glass-based grid mesh on both sides of the specimen, hereinafter denoted with RF-S - Reinforced FRCM Symmetric, Figure 60f.

The specimens were strengthened after the maturation of 28 days.

As repointing technique, the main phases of the intervention were: preparation of a groove in the mortar joints for a depth around 20 mm from the edges, partial filling of the joints with structural mortar (Mortar B), positioning of the basalt bars, filling the void and restoring the original appearance by a second layer of structural mortar (Mortar B).

As FRCM system, the main phases of the application were: spray the structural mortar (Mortar B) on the surface to increase its roughness and consequently the adhesion between the surface of the wall and the mortar

layer used to apply FRCM, application of the first layer of structural mortar with a thickness of 5 mm, positioning of the glass fiber mesh, application of a second layer of structural mortar.

In Table 22, the tested specimens are summarized. A total of three specimens for type has been tested.
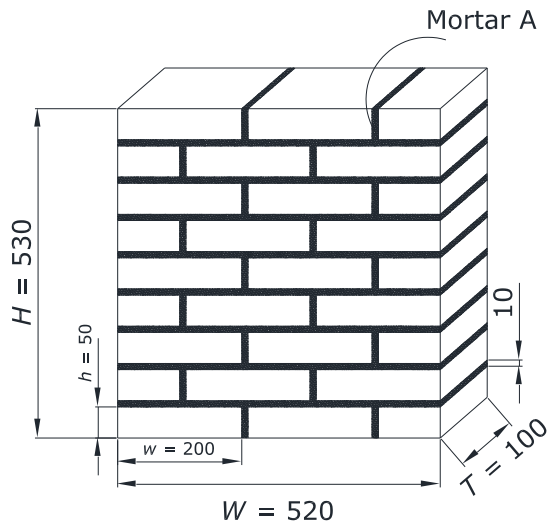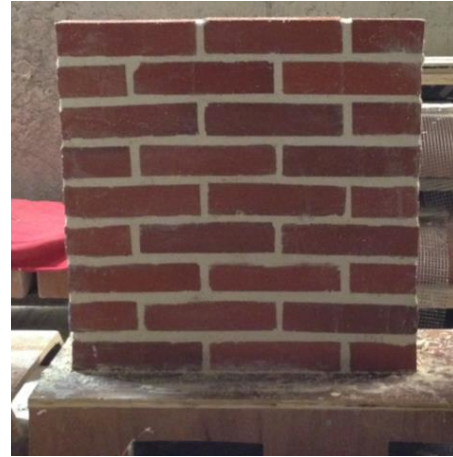
(a) UNR specimen

(b) UNR specimen
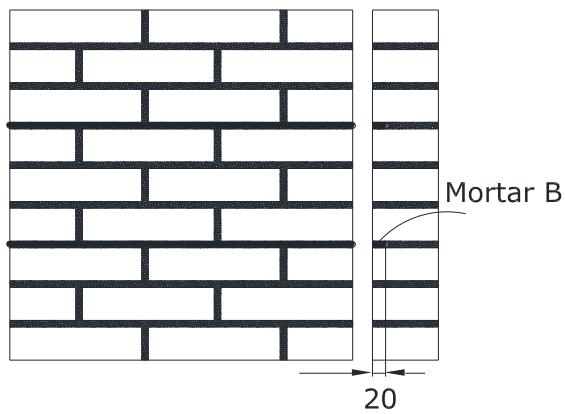
(c) RR-A specimen
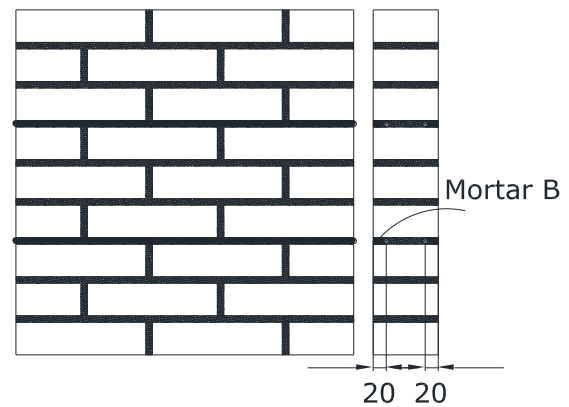
(d) RR-S specimen
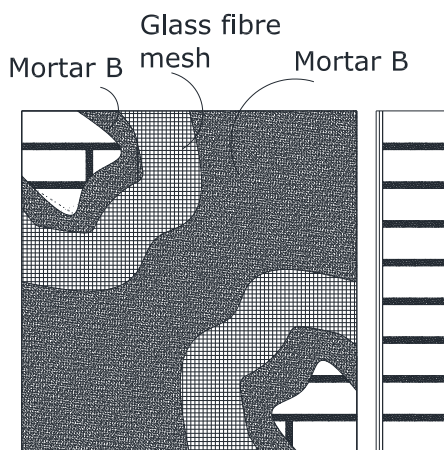
(e) RF-A specimen
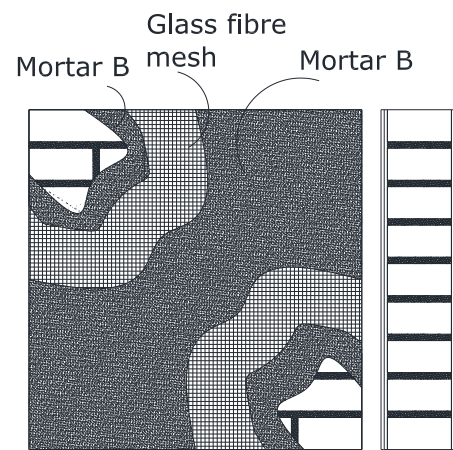
(f) RF-S specimen

Figure 60 Specimens tested in the experimental program. Dimensions in mm.

Table 22 Specimen label and description.

Specimen label	Number of each specimens	Description
UNR	3	Specimen without reinforcement (Figure 60a)
RR-A	3	Specimen with reinforcement: 2 basalt bars inserted asymmetrically in the mortar joints (Figure 60c)
RR-S	3	Specimen with reinforcement: 4 basalt bars inserted symmetrically in the mortar joints (Figure 60d)
RF-A	3	Specimen with reinforcement: 1-ply glass-based FRCM composite applied asymmetrically on one side of the specimen (Figure 60e)
RF-S	3	Specimen with reinforcement: 1-ply glass-based FRCM composite applied symmetrically on both sides of the specimen (Figure 60f)

4.5 Test set up and instrumentation

After curing, all the specimens were subjected to a diagonal compression test in a standard configuration normalised by (ASTM E 519 2002) and (RILEM 1991), Figure 61. The load is applied through a steel shoe with dimensions 115 x 115 x 15 mm^3 placed at the top corner. All the specimens were tested in a universal testing machine Sentur2 500 kN operating in displacement control at a rate equal to 0.002 mm/s.

Figure 61 Test set-up.

In Figure 62, the instrumentation of the specimens is shown. During the test, the values of the applied load and the diagonal displacements were recorded (Mojsilovic & Salmanpour 2016). The displacements were measured by four linear variable displacement transducers: two on the front face (LVDTc,f and LVDTt,f), and two on the back face, (LVDTc,b and LVDTt,b). In particular, LVDTc,f and LVDTc,b were vertically oriented

along the force line to measure the wall shortening, while LVDTt,f and LVDTt,b were placed horizontally, perpendicular to the force line to record the crack opening. A load cell was used to measure the force along the loaded diagonal.

(a) Specimen front face   b) Specimen back face

Figure 62 Instrumentation of the specimens.

4.6 Results

In the following, results obtained from the tests conducted on the specimens are presented. In particular, results are given in terms of load versus vertical displacement (load - v curves) and load versus horizontal displacement (load – u curves). For clarity purpose, only one curve for each type (unreinforced, reinforced with asymmetric and symmetric repointing, reinforced with asymmetric and symmetric FRCM system), was selected as representative of the structural behaviour of the specimens. It is worth noting that negative signal of the LVDTs means shortening, while positive signal means elongation.

4.6.1. UNR specimens

In Figure 63, for negative abscissa, the load - v curves for a selected UNR specimen are represented. The mean curve (bold black line) is obtained as the average of the signals from the two vertical LVDTc (LVDTc,f and LVDTc,b in Figure 62). For positive abscissa, the load - u curves for UNR specimen are shown and the mean one (bold black line) is obtained as the average of the signals from the two horizontal LVDTt (LVDTt,f and LVDTt,b in Figure 62).

In Figure 64, pictures of a selected unreinforced specimen at the end of the test are reported.
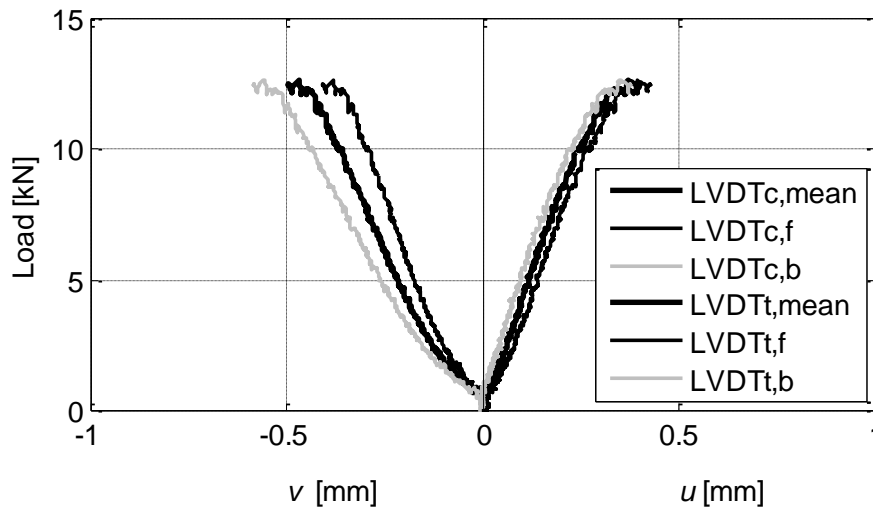
Figure 63 Load-vertical and load-horizontal displacement curves for a selected UNR specimen.

(a) UNR specimen: front face

(b) UNR specimen: detail of the mortar joints

Figure 64 UNR specimen: failure mode.

Referring to load - v curve and load - u curve in Figure 63, UNR specimen exhibited a linear behavior until the end of the test. After the peak load (P_{max}) is reached (around 12 kN) corresponding to a vertical shortening equal to 0.5 mm and a horizontal elongation equal to 0.4 mm, the specimen collapsed in a brittle way in which a main crack developed within the mortar joints, Figure 64a. After that, sliding due to detachment at the brick/mortar interface occurred, Figure 64b.

4.6.2. RR-A and RR-S specimens

In Figure 65, for negative abscissa, the load - v curves (grey lines) for two selected specimens reinforced by repointing (RR specimens) are represented. Each curve is obtained as the average of the signals from the two vertical LVDTc (LVDTc,f and LVDTc,b in Figure 62). For positive abscissa, the corresponding load - u curves for the RR specimens are shown. Each curve is obtained as the average of the signals from the two horizontal

LVDTt (LVDTt,f and LVDTt,b in Figure 62). For comparison purposes, the curves (black lines) of the UNR specimen are reported on the same figure.

In Figure 66a and Figure 66b, RR-A and RR-S specimens at the end of the test are shown, respectively.
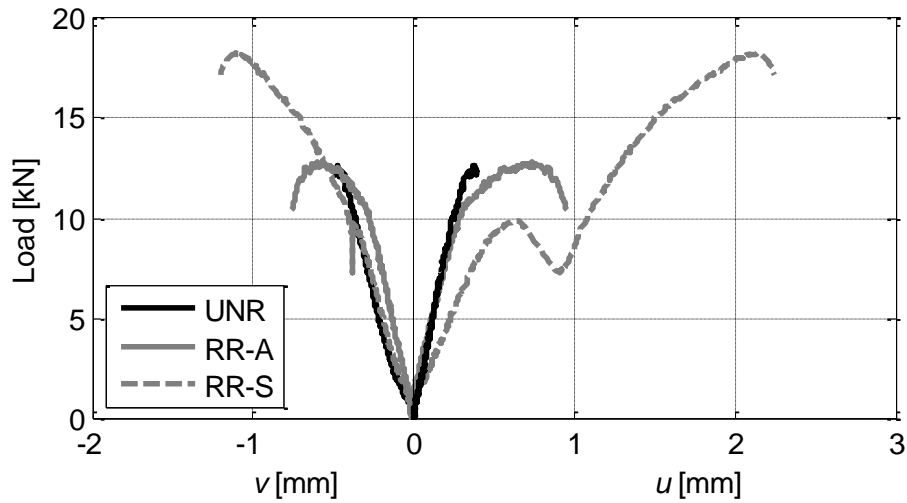
Figure 65 Load-vertical and load-horizontal displacement curves for RR-A (continuous grey line) and RR-S (dashed grey line) specimens.

| (a) RR-A specimen | (b) RR-S specimen |

Figure 66 RR specimen: (a) failure mode of RR-A specimen and (b) failure mode of RR-S specimen.

Referring to load - v curves, RR specimens exhibited a linear behavior at the beginning of the test, Figure 65. For a certain load value (around 10 kN for RR-A and 13 kN for RR-S), the curves changed slope and the second ascending branches, that are less steep with respect to first ones, indicate a state of damage of the specimens. After the peak load is attained (around 12 kN with a vertical displacement of 0.8 mm for RR-A and 17 kN with a vertical displacement of 1.2 mm for RR-S), a brittle behavior due to sliding is registered.

Comparing the load - v black curve related to the unreinforced specimen with the grey ones of RR specimens, it could be noted that in the initial part of the diagram, the curves showed a similar slope, while the stiffness of RR-A was a little higher than that of UNR. As expected, reinforced specimens reached a higher peak load (P_{max}) with respect to UNR with also an increment in displacement capacity.

Considering the curves in the positive part of the abscissa, Figure 65, the behavior of the reinforced specimens is linear at the beginning of the test. Then, after first cracks occurred, a change in a slope is registered and crack openings started to increase until P_{max}.

Notwithstanding the presence of the bars, the failure of the retrofitted specimens was brittle, such that a crack developed within the mortar joints that were not strengthened with basalt bars, Figure 66a and Figure 66b.

4.6.3 RF-A and RF-S specimens

In Figure 67, for negative abscissa, the load - v curves (grey lines) for two selected specimens retrofitted with FRCM system (RF specimens) are represented. Each curve is obtained as the average of the signals from the two vertical LVDTc (LVDTc,f and LVDTc,b in Figure 62). For positive abscissa, the corresponding load - u curves for the RF specimens are shown. Each curve is obtained as the average of the signals from the two horizontal LVDTt (LVDTt,f and LVDTt,b in Figure 62). For comparison purposes, the curves of the UNR specimen are reported on the same figure.

In Figure 68 and Figure 69, selected RF-A and RF-S specimens at the end of the test are shown, respectively.
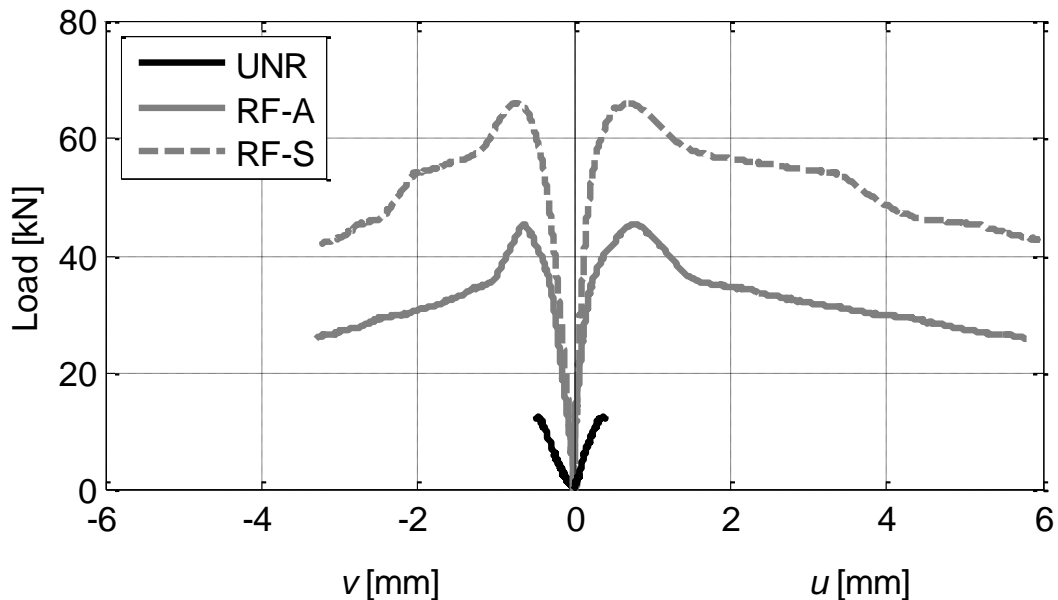
Figure 67 Load-vertical and load-horizontal displacement curves for RF-A (continuous grey line) and RF-S (dashed grey line) specimens.

(a) RF-A specimen: front face

(b) RF-A specimen: back face

Figure 68 RF-A specimen: failure mode.

(a) RF-S specimen

(b) RF-S specimen: debonding on the front face

Figure 69 RF-S specimen: failure mode.

Referring to load - v curves, RF specimens exhibited a linear behavior at the beginning of the test, Figure 67. For a certain load value (around 30 kN for RF-A and 50 kN for RF-S), the curves change slope and the second ascending branches, that are less steep with respect to first ones, indicate a state of damage of the specimens. After the peak load is attained (around 45 kN for RF-A and 65 kN for RF-S with a vertical shortening of 3.8 mm for both specimens), a softening branch is registered.

Comparing the load - v black curve related to the unreinforced specimen with the grey ones of RF specimens, it could be noted that from the initial part of the diagram, the stiffness of RF is higher than that of UNR. As expected, reinforced specimens reach a higher peak load (P_{max}) with respect to UNR, and after the peak load

is attained, the softening branch is longer with respect to the unreinforced specimen, showing a more ductile behavior.

Referring to the failure mode of RF-A specimens, Figure 68, after having reached the peak load, vertical cracks started to appear in the mid area of the specimen body, involving both the bed joints and the bricks. As the cracking pattern developed and the cracks got wider, the specimen started to tilt towards the reinforced side. The cracks kept evolving in the mid vertical position, between the two loading shoes, leaving the outer corners unaffected. FRCM debonded from the masonry substrate to which it was applied. The specimens failed due to diagonal tension.

Referring to the failure mode of RF-S specimen, Figure 69, after having reached the peak value of the compression load, vertical cracks started to appear in the mid part of the specimen body. The cracking pattern developed within the two loading shoes, leaving the outer corners unaffected, and a diagonal tension failure occurred in the specimen. On both sides, the FRCM layers began to debond from the masonry underneath, eventually detaching from the upper corner.

4.7 Summary

A summary of the relevant mechanical parameters obtained from the diagonal compression test for all the specimens in terms of mean values and standard deviations is given in Table 23. The average peak load values ($\bar{P}_{max}$) are listed. Parameter Δ, representing the structural enhancement achieved in terms of $\bar{P}_{max}$ by using reinforcements, is calculated by using Eq.(32).

The maximum shear stress (τ_{max}) is computed following (ASTM E 519 2002) by using Eq.(42), assuming that the shear stress τ is equal to both tensile and compressive principal stresses, representing a pure shear stress state in masonry (Brignola et al. 2008; Calderini et al. 2010).

The elastic shear modulus is derived by using Eq.(48):

$$G = \frac{\tau_{el}}{\gamma_{el}} \tag{48}$$

where τ_{el} is the shear stress in the elastic branch and γ_{el} is the corresponding shear strain (in mm/mm) calculated as:

$$\gamma_{el} = \frac{\Delta v_{el} + \Delta u_{el}}{g'} \tag{49}$$

where Δv_{el} is the mean vertical shortening (in mm) measured in the elastic branch by LVDTc, Figure 62, Δu_{el} is the mean horizontal extension (in mm) measured in the elastic branch by LVDTt, Figure 62, and g' is the vertical gage length (in mm). In this study, the value of g' is equal to 500 mm.

The evaluation of a μ parameter allowed to quantify the benefit in terms of ductility of the considered retrofitting solutions. This coefficient is evaluated as:

$$\mu = \min\left(\frac{\Delta u_u}{\Delta u_{max}}; \frac{\Delta v_u}{\Delta v_{max}}\right) \tag{50}$$

where Δu_{max} and Δv_{max} are the horizontal and vertical displacements corresponding to the maximum load, respectively, while Δu_u and Δv_u are the horizontal and vertical displacements corresponding to the ultimate

conditions, respectively. In particular, in the case of repointing strengthening, the ultimate displacements are taken at failure, whereas for the FRCM strengthening, the collapse is considered to occur when the load reached the 80% of its maximum, after the peak has been reached.

Finally, in order to compare the two retrofitting solutions, a parameter ω_f representing the calibrated reinforcement ratio (Babaeidarabad et al. 2014), is defined by using Eq..

Table 23 Summary of the results of the experimental investigation. Standard deviation in parentheses.

Specimen label	$\bar{P}_{max}$ [kN]	Δ_1 [%]	$\bar{\tau}_{max}$ [MPa]	$\bar{G}$ [MPa]	μ	ω_f [%]	Failure mode
UNR	13.54 (5.31)	-	0.18 (0.07)	186.38	-	-	sliding
RR-A	14.62 (3.63)	7.99	0.20 (0.05)	253.02	1.21 (0.07)	0.49	sliding
RR-S	19.48 (1.88)	43.95	0.26 (0.03)	403.92	1.09 (0.07)	0.99	sliding
RF-A	43.96 (4.35)	224.81	0.59 (0.06)	672.78	2.09 (0.74)	0.37	diagonal tension
RF-S	64.45 (6.34)	376.20	0.87 (0.09)	2050.25	2.82 (0.49)	0.74	diagonal tension

4.8 Discussion of the results

From Table 23, comparing the results for UNR and RR-A specimens in terms of peak load, the increment is around 8% $\Delta_1 = 7.99\%$), whereas between UNR and RR-S the load capacity increment is around 44% ($\Delta_1 = 43.95\%$). Moreover, an increment in the shear modulus, $\bar{G}$, is registered moving from UNR specimens to RR. In terms of ductility, it is worth noting that μ parameter is lower for RR-S with respect to RR-A. This is due to the fact that the failure of the reinforced specimens with repointing was brittle, so it was difficult to determine the values of displacements at ultimate conditions, Eq.(67). The presence of the bars did not change the failure mode with respect to UNR specimens, only avoided sliding of the joints that were strengthened.

Comparing the results for UNR and RF-A specimens in terms of $\bar{P}_{max}$, the increment is double ($\Delta_1 = 224.81\%$), whereas between UNR and RF-S, the increment is equal to 376% ($\Delta_1 = 376.20\%$). An increment in shear modulus, $\bar{G}$, is achieved moving from UNR to RF specimens. In terms of ductility, μ is double compared to the one obtained for the reinforced specimens with repointing technique. The presence of FRCM modifies the mode of failure from sliding (UNR specimens) to diagonal tension (RF specimens).

Furthermore, the maximum load, $\bar{P}_{max}$, increases as reinforcement ratio, ω_f, increases.

In summary, an increment in displacement capacity is highlighted in the specimens retrofitted with the bars. While, the structural enhancements achieved by using FRCM system are: *i*) increment in shear capacity, *ii*) increment in displacement capacity, *iii*) more stable behavior compared to the specimens reinforced with repointing and *iv*) change in failure mode.

4.9 Analytical investigation

In this section, the analytical procedure presented in the code (ACI 549.4R-13 2013), to predict the nominal shear capacities of masonry walls is followed and finally compared to the ones obtained from the experimental tests.

Considering a masonry panel of width equal to W, height equal to H and thickness equal to T, subjected to a compression load equal to P, it is possible to compute the nominal shear capacity of the specimen, V_n, as the sum of two contributions:

$$V_n = V_m + V_f \qquad (51)$$

where V_m and V_f are the contributions of the masonry wall and the reinforcement, respectively.

4.9.1. UNR specimens

In a diagonal compression test, four types of failure mechanisms have been identified, depending on physical and mechanical properties of the wall, Figure 70.

| (a) sliding and friction failure | (b) diagonal tension failure | (c) toe crushing failure |
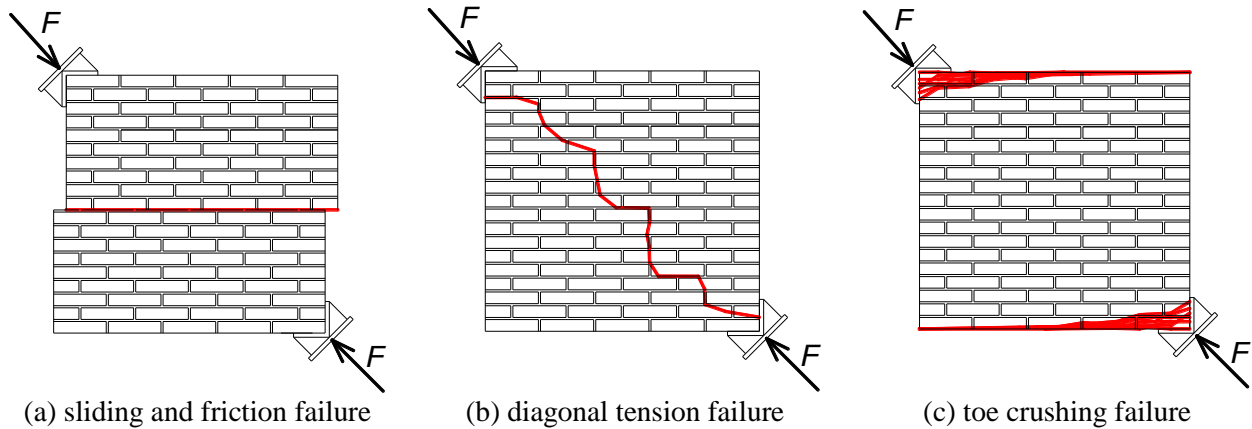
Figure 70 Shear failure mechanism, (Maragna et al. 2016).

The specimen fails when the shear load reaches the minimum shear capacity, V_m:

$$V_m = min\{V_{ss}, V_{sf}, V_{dt}, V_c\} \qquad (52)$$

4.9.1.1. Shear capacity due to shear sliding failure, V_{ss}, Figure 70a:

$$V_{ss} = \frac{\tau_0}{1 - \mu_0 tg\theta} A_n \qquad (53)$$

where τ_0 is the shear bond strength between mortar and bricks, μ_0 is the coefficient of internal shear friction in mortar joints, θ is the angle between horizontal and main diagonal of the wall and A_n is the net area of the specimen calculated by using Eq.(46).

4.9.1.2. Shear capacity due to shear friction failure, V_{sf}, Figure 70a:

$$V_{Sf} = \frac{\tau_{0,m}}{1 - \mu_m tg\theta} A_n \qquad (54)$$

where $\tau_{0,m}$ and μ_m are the modified shear bond strength in the mortar joints and the modified coefficient of internal shear friction in the mortar joints, respectively, calculated as

$$\tau_{0,m} = \frac{\tau_0}{1 + 1.5\,\mu_0\,\dfrac{h}{w}} \tag{55}$$

and

$$\mu_m = \frac{\mu_0}{1 + 1.5\,\mu_0\,\dfrac{h}{w}} \tag{56}$$

with w and h the width and height of the brick.

4.9.1.3. Shear capacity due to the diagonal tension failure, V_{dt}, Figure 70b:

$$V_{dt} = \frac{tg\theta + \sqrt{21.26 + tg^2\theta}}{10.58} f_t'\, A_n \tag{57}$$

where the tensile strength of the masonry f_t' is considered equal to $0.67\sqrt{f_m'}$ for clay bricks, with f_m' being the compressive strength of the masonry.

4.9.1.4. Shear capacity due to toe crushing failure at the loading end, V_c, Figure 70c:

$$V_c = \frac{2wf_m'}{3h + 2wtg\theta} A_m \tag{58}$$

where A_m is the interface loading area between the steel shoe and the wall along the horizontal direction (Babaeidarabad et al. 2014).

4.9.2. RR-A and RR-S specimens

In order to calculate the V_f contribution given by the bars, a modified version of the approach presented by (Li et al. 2005) is followed. In (Li et al. 2005), a perfect bond between the bar and the epoxy paste was considered, and, as a consequence, the shear resistance of reinforcing bars was limited by bond failure between epoxy paste and the surrounding original mortar.

In this study, the shear resistance of the bars is controlled by bond failure between structural mortar and the bar itself. The effective length of the bar is the minimum length at which the maximum stress of the bar is achieved.
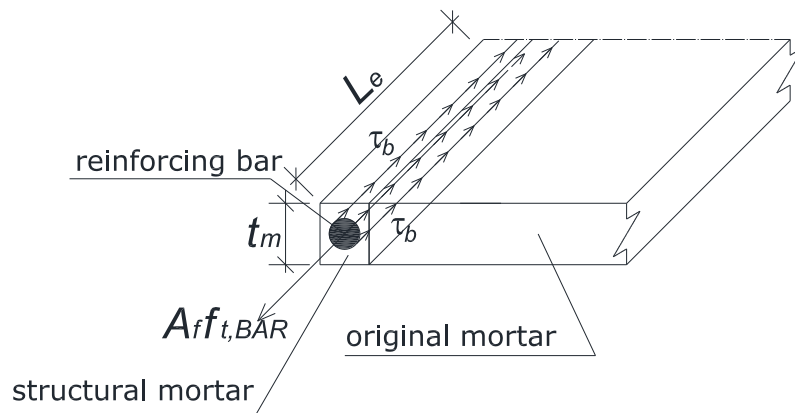
Figure 71 Distribution of the stresses along a bar embedded in the mortar joint.

In the analysis, the bond stress between structural mortar and the bar is assumed to be uniform along the effective length of the bar at ultimate, Figure 71. For equilibrium, the tensile force developed in the bar should be equal to the bond strength between structural mortar and the bar:

$$\tau_b A_b = f_{t,BAR} A_f \tag{59}$$

where τ_b is the average bond strength between the bar and the structural mortar, A_b is the average bond area between the bar and the structural mortar, $f_{t,BAR}$ is the maximum tensile stress of the near surface mounted bar and A_f is the cross-sectional area of the bar. Thus,

$$A_b = 2\pi R L_e \tag{60}$$

where R is the radius of the bar and L_e is the effective length of the bars in masonry.

Substituting Eq.(78) in Eq.(59), the effective length results

$$L_e = \frac{f_{t,BAR} R}{2\tau_b} \tag{61}$$

To calculate the resistance of bars related to the bond controlled shear failure, a shear crack with a constant inclination angle of 45 degrees is assumed in the model. Thus, each bar intersected by the crack is divided into two parts at the two sides of the crack. The shear resistance provided by the bars, V_f, is computed as the sum of the forces resisted by the bars intersecting the diagonal crack. The force carried by each bar is calculated as the product of the average bond strength and the surface area of the bond between bar and structural mortar according to the effective bond length of the bar, which is the shortest part of the bar intersected by the diagonal crack.

Therefore

$$V_f = \sum_{i=1}^{N} A_{fi} f_i = \tau_b 2\pi R \sum_{i=1}^{n} L_i \qquad L_i \leq L_e \tag{62}$$

where f_i is the force carried by i-th reinforcing bar, N is the total number of bars intersected by the diagonal crack and L_i is the effective bond length of the i-th bar intersecting the diagonal crack.

4.9.3. RF-A and RF-S specimens

The contribution of FRCM is calculated following (ACI 549.4R-13 2013) as:

$$V_f = 2n_{layer} A_{FRCM} W f_{t,FRCM} \tag{63}$$

where n_{layer} is the number of layers of fabrics, A_{FRCM} is the area of fabric reinforcement by unit width in both horizontal and vertical directions, $f_{t,FRCM}$ is the tensile strength in the FRCM reinforcement calculated as:

$$f_{t,FRCM} = E_{FRCM} \varepsilon_u \tag{64}$$

where E_{FRCM} and ε_u are the tensile modulus of elasticity of the cracked FRCM and the ultimate tensile strain of FRCM reinforcement, respectively.

4.9.4. Summary

All the calculations are given in Appendix C for determining the shear capacities of the unreinforced and reinforced walls tested in this research program.

In Table 24, a comparison between the experimental and the analytical results is reported in terms of nominal shear capacity. A ratio between the results is also calculated.

Table 24 Comparison between experimental and analytical results.

	UNR	RR-A	RR-S	RF-A	RF-S
	[kN]	[kN]	[kN]	[kN]	[kN]
Experimental	$V_n =$ $P_{max}cos(\theta)$	$V_n =$ $P_{max}cos(\theta)$	$V_n =$ $P_{max}cos(\theta)$	$V_n =$ $P_{max}cos(\theta)$	$V_n =$ $P_{max}cos(\theta)$
	7.11	7.68	10.23	23.09	33.85
Analytical	$V_n = V_m$	$V_n = V_m + V_f$	$V_n = V_m + V_f$	$V_n = V_m + V_f$	$V_n = V_m + V_f$
	11.9	16.71	21.32	22.9	33.9
Ratio experimental/analytical	0.60	0.46	0.48	1.01	0.99

4.9.5. Discussion of the results

From Table 24, it is possible to observe that analytical results give a good prediction of the shear capacity for the case of FRCM system reinforcement. While, for the specimens reinforced on one or both sides with repointing technique, analytical results overestimate the shear capacity. This aspect shows that the analytical model employed to calculate the contribution of the bar reinforcement should be improved.

4.10 Numerical modeling

4.10.1. Modeling masonry: micro and macro modeling

Masonry is a material which exhibits different directional properties due to the mortar joints which act as planes of weakness. In general, the approach towards its numerical representation can focus on the micro-modeling of the individual components (unit and mortar), or the macro-modeling of a masonry as a composite (Lourenço 1996). Depending on the level of accuracy and the simplicity desired, considering a masonry sample represented in Figure 72a, four different modeling strategies can be adopted:

i) detailed micro-modeling: units and mortar are represented using continuum elements, while the unit/mortar interface is represented by discontinuous elements (Figure 72b);

ii) simplified micro-modeling: expanded units are represented using continuum elements, while the behavior of the mortar joints and unit/mortar interface is lumped in discontinuous elements (Figure 72c);

iii) macro-modeling: units, mortar and unit/mortar interface are smeared out in the continuum (Figure 72d).

(a) masonry sample

(b) detailed micro-modeling

(c) simplified micro-modeling
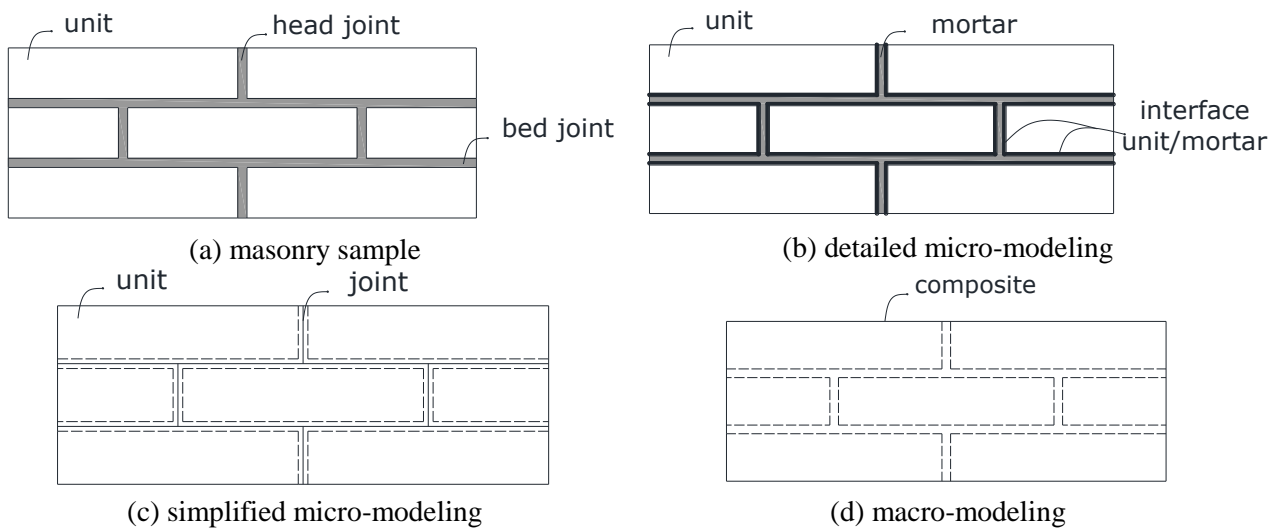
(d) macro-modeling

Figure 72 Modeling strategies for masonry structures.

In the detailed micro-modeling, Young's modulus, E, Poisson's ratio, v, and inelastic properties of both unit and mortar are taken into account. The interface represents a potential crack/slip plane with initial dummy stiffness to avoid interpenetration on the continuum.

In the simplified micro-modeling, each joint, consisting of mortar and the two unit/mortar interfaces, is lumped into an "average" interface while the units are expanded in order to keep the geometry unchanged. Masonry is considered as a set of elastic blocks bonded by potential fracture/slip lines at the joints. Accuracy is lost since Poisson's effect of the mortar is not included.

The macro-modeling approach does not make a distinction between units and joints but considers masonry as a homogeneous anisotropic continuum.

4.10.2. Modeling strategy for UNR specimens

A simplified micro-modeling approach is selected to model unreinforced specimens in order to have a better understanding about the local behavior of masonry.

The modeling approach used is based on the concentration of all the damage in the relatively weak joints and, if necessary, in potential pure tensile cracks in the units placed vertically in the middle of each unit (Figure 73). The units, that were expanded in both directions by the mortar thickness, were modeled with continuum elements. Mortar joints and potential cracks in the units were modeled with zero-thickness interface elements.
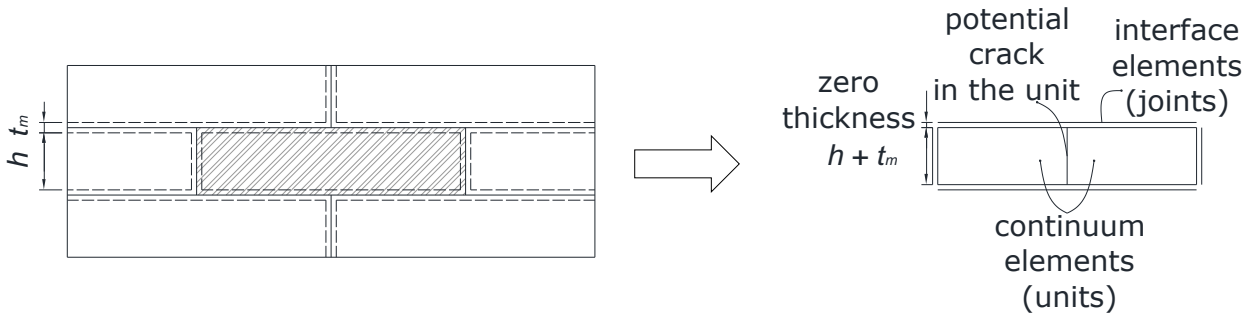
Figure 73 Modeling strategy adopted for UNR specimens.

4.10.2.1. Adopted non linear interface model: Combined cracking-shearing-crushing

In order to take into account a non linear behavior of the joints, a combined cracking-shearing-crushing model have been used (Lourenco & Rots 1997; Van Zijl 2000). It is appropriate to simulate fracture, frictional slip as well as crushing along interfaces, for instance at joints in masonry. The plane stress interface model (Figure 74) is based on multi-surface plasticity, comprising a Coulomb friction model combined with a tension cut-off and an elliptical compression cap.
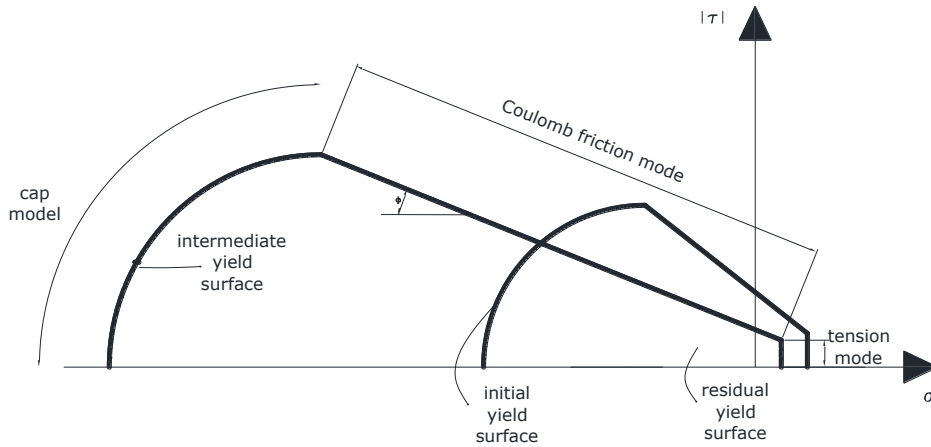
Figure 74 Two-dimensional interface model.

Softening acts in all three modes and is preceded by hardening in the case of the cap model. The interface model is derived in terms of the generalized stress and strains vectors Eq.(65):

$$\underline{\sigma} = \begin{cases} \sigma \\ \tau \end{cases}$$
$$\underline{\varepsilon} = \begin{cases} u \\ v \end{cases} \tag{65}$$

with σ and u the stress and relative displacement respectively in the interface normal direction and τ and v the shear stress and relative displacement respectively.

In the elastic state the constitutive behavior is described by Eq. (66)

$$\underline{\sigma} = \boldsymbol{D}\underline{\varepsilon} \tag{66}$$

with the stiffness matrix

$$\boldsymbol{D} = diag[k_n \; k_s] \tag{67}$$

the components of the elastic stiffness matrix $\boldsymbol{D}$ are defined as:

$$k_n = \frac{E_b E_m}{t_m(E_b - E_m)} \tag{68}$$

$$k_s = \frac{G_b G_m}{t_m (G_b - G_m)}$$

where E_b and E_m are the Young's moduli, G_b and G_m are the shear moduli, respectively, for brick and mortar and t_m the thickness of the joint.

4.10.2.1.1. Shear slipping

A Coulomb friction yield/crack initiation criterion

$$f = |t| + \sigma \phi - c \tag{69}$$

describes the shear-slipping, with ϕ the friction coefficient equal to $tg\phi$, the friction angle and c the cohesion. Both cohesion softening and friction softening are captured.

The adhesion softening is described by

$$c(\sigma, k) = c_0 e^{-\frac{c_0}{G_f^{II}} k} \tag{70}$$

where c_0 is the initial adhesion of the brick/mortar interface and G_f^{II} the shear-slip fracture energy.

The friction softening is coupled to the adhesion softening via

$$\phi(\sigma, k) = \phi_0 + (\phi_r - \phi_0) \frac{c_0 - c}{c_0} \tag{71}$$

where ϕ_0 the initial and ϕ_r the residual friction coefficient.

The adhesion and friction parameters are found by linear regression of the micro-shear experimental data, while the fracture energy is determined by the appropriate integration of the stress-crack width response that produces the total energy dissipated by both the adhesion and the friction softening

$$G_f^{II*} = G_f^{II} \left(1 + \frac{\sigma}{c_0} (\phi_r - \phi_0) \right) \tag{72}$$

The experimentally linear relation between the fracture energy and the normal confining stress is

$$G_f^{II} = \begin{cases} a\sigma + b & if \ \sigma < 0 \\ b & if \ \sigma \geq 0 \end{cases} \tag{73}$$

with a and b constants to be determined by linear regression of the experimental data.

4.10.2.1.2. Dilatancy

The flow rule

$$\dot{\varepsilon}_p = \begin{pmatrix} \dot{u}_p \\ \dot{v}_p \end{pmatrix} = \lambda \frac{\partial g}{\partial \underline{\sigma}} \tag{74}$$

is used to describe the dilatancy, choosing a suitable potential function

$$\frac{\partial g}{\partial \underline{\sigma}} = \begin{pmatrix} \psi \\ sign(\tau) \end{pmatrix} \tag{75}$$

with ψ equal to $tg\psi$ being the dilatancy coefficient. Following directly from the flow rule

$$\psi = \frac{\dot{u}_p}{\dot{v}_p} sign(\tau) \tag{76}$$

By integration the shear-slip induced normal uplift is found to be

$$u_p = \int \psi \, d|\Delta v_p| \tag{77}$$

There is experimental evidence that dilatancy depends on both the confining stress and the shear-slip. A dilatancy formulation of separate variables is

$$\psi = \psi_1(\sigma)\,\psi_2(v_p)$$
(78)

simplifies curve fitting and ensures convexity of the potential function g

$$g = \int \left(\frac{\partial g}{\partial \underline{\sigma}}\right)^T d\underline{\sigma} = |\tau| + \psi_2(v_p)\int \psi_1(\sigma)d\sigma$$
(79)

Therefore, a description of the normal uplift upon shear-slipping is chosen as

$$u_p = \begin{cases} 0 & \text{if } \sigma < \sigma_u \\ \frac{\psi_0}{\delta}\left(1 - \frac{\sigma}{\sigma_u}\right)(1 - e^{-\delta v_p}) & \text{if } \sigma_u \le \sigma < 0 \\ \frac{\psi_0}{\delta}(1 - e^{-\delta v_p}) & \text{if } \sigma \ge 0 \end{cases}$$
(80)

which yields after differentiation

$$\psi = \begin{cases} 0 & \text{if } \sigma < \sigma_u \\ \frac{\psi_0}{\delta}\left(1 - \frac{\sigma}{\sigma_u}\right)e^{-\delta v_p} & \text{if } \sigma_u \le \sigma < 0 \\ \frac{\psi_0}{\delta}e^{-\delta v_p} & \text{if } \sigma \ge 0 \end{cases}$$
(81)

The dilatancy ψ_0 at zero normal confining stress and shear slip, the confining (compressive) stress σ_u at which the dilatancy becomes zero, and the dilatancy shear slip degradation coefficient δ, are material parameter to be obtained by, for instance, a least square fit of Eq.(80) to experimental test data. Note that for tensile stress, a stress independent dilatancy coefficient is assumed.

4.10.2.1.3. Softening

A strain softening hypothesis is employed, where the softening is governed by shear-slipping, yielding

$$\Delta k = |\Delta v_p| = \Delta \lambda$$
(82)

upon substitution of Eq.(74) and Eq.(75).

4.10.2.1.4. Tension cut off

The yield function for the tension cut off-is

$$f_2 = \sigma - \sigma_t$$
(83)

with σ_t the tensile, or brick-mortar bond strength. The strength is assumed to soften exponentially

$$\sigma_t = f_t e^{-\frac{f_t}{G_f^I}k_2}$$
(84)

with f_t the bond strength and G_f^I the mode I fracture energy. The softening is governed by a strain softening hypothesis.

$$\Delta k_2 = |\Delta u_p|$$
(85)

which upon consideration of an associated flow rule

$$\Delta \varepsilon_p = \Delta \lambda_2 \frac{\partial f_2}{\partial \underline{\sigma}}$$
(86)

reduces to

$$\Delta k_2 = \Delta \lambda_2 \tag{87}$$

4.10.2.1.5. Compression cap

The yield function for the compression cap, is

$$f_3 = \sigma^2 + C_s \tau^2 - \sigma_c^2 \tag{88}$$

with C_s a parameter controlling the shear stress contribution to failure and σ_c the compressive strength. The latter is assumed to evolve according to the strain hardening hypothesis.

$$\Delta k_3 = \sqrt{\Delta \varepsilon_p^T \Delta \varepsilon_p} \tag{89}$$

which, upon consideration of an associated flow rule

$$\Delta \varepsilon_p = \Delta \lambda_3 \frac{\partial f_3}{\partial \underline{\sigma}} \tag{90}$$

becomes

$$\Delta k_3 = 2\Delta \lambda_3 \sqrt{\sigma^2 + (C_s \tau^2)} \tag{91}$$

The yield surface hardens, as described by a parabolic hardening rule, followed by parabolic/exponential softening, Figure 75. The peak strength f_{cx} is reached at a plastic strain k_p. Subsequently, the softening branch is entered, governed by the fracture energy G_{fc}.
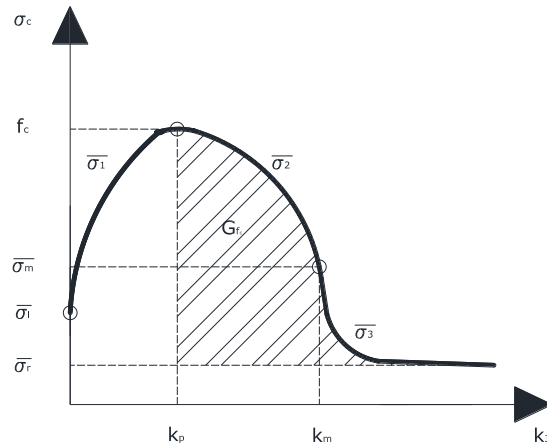
Figure 75 Hardening-softening law for interface compression cap.

For practical reasons, all stress values are related to peak strength f_c as follows:

$$\overline{\sigma_i} = \frac{1}{3} f_c$$

$$\overline{\sigma_m} = \frac{1}{2} f_c \tag{92}$$

$$\overline{\sigma_r} = \frac{1}{7} f_c$$

The three regions of this hardening-softening rule are given by

$$\overline{\sigma_1}(k_3) = \overline{\sigma_i} + (f_c - \overline{\sigma_i})\sqrt{\frac{2k_3}{k_p} - \frac{k_3^2}{k_p^2}}$$

$$\overline{\sigma_2}(k_3) = f_c + (\overline{\sigma_m} - f_c)\left(\frac{k_3 - k_p}{k_m - k_p}\right)^2 \tag{93}$$

$$\overline{\sigma_3}(k_3) = \overline{\sigma_r} + (\overline{\sigma_m} - \overline{\sigma_r})exp\left(2\left(\frac{\overline{\sigma_m} - f_c}{k_m - k_p}\right)\left(\frac{k_3 - k_m}{\overline{\sigma_m} - \overline{\sigma_r}}\right)\right)$$

4.10.2.1.6. Corners

At each of the intersections of the Coulomb friction criterion with the tension cut-off and the compression cap the plastic strains increment is given by

$$\Delta\varepsilon_p = \Delta\lambda_1 \frac{\partial g_1}{\partial\underline{\sigma}} + \Delta\lambda_1 \frac{\partial g_i}{\partial\underline{\sigma}} \tag{94}$$

where the subscript 1 refers to the shear criterion and *i* refers to tension cut-off (*i=2*) and to compression cap (*i=3*).

4.10.2.2. Models and numerical results

4.10.2.2.1. Finite element and constitutive behavior

A 2D finite element model was developed using Midas FX+ for DIANA.

Bricks

Bricks were modeled by using 2D plane stress CQ16M elements (mesh size 15 x 15 mm) characterized by a linear elastic behavior with an elastic modulus, E_b, equal to 9500 MPa and a Poisson's ratio, *v*, of 0.15, Figure 76a.

Cracks

Cracks were modeled by using a 2D line interface L8IF elements (zero thickness), in the middle of each brick. From the experimental results, no cracks were observed in the middle of the brick, therefore a linear elastic behavior with dummy stiffness, k_n and k_s, have chosen equal to $10^6 \ N/mm^3$, Figure 76b.

Joints

Joints were modeled by using a 2D line interface L8IF elements (zero thickness), Figure 76b, to simulate head and bed mortar layers. From the experimental results, failure of the specimen occurred due to sliding along the second and third mortar joints. The combined cracking-shearing crushing model was used to capture this failure mechanism.
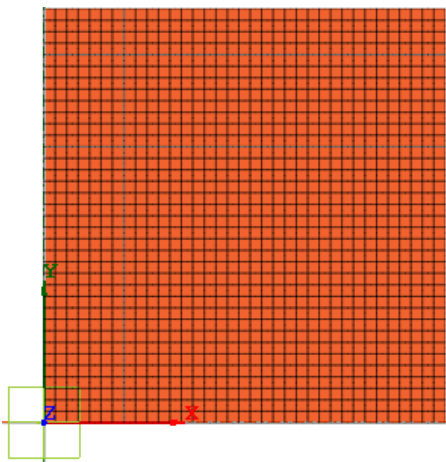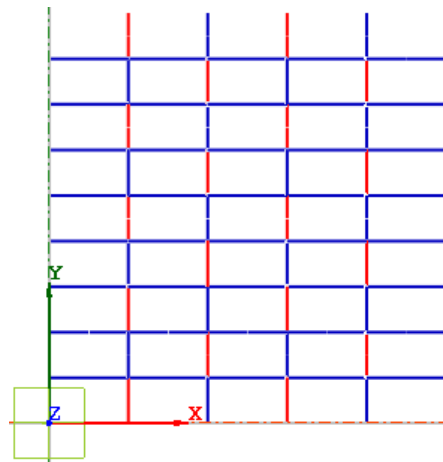
| (a) bricks | (b) potential cracks (red line) and mortar joints (blue line) |

Figure 76 Finite element model.

Load

One vertical and one horizontal displacements have been applied on the top corner of the specimen. In order to simulate the steel plate used in laboratory, a rigid link has been applied on 7 nodes in the horizontal direction and 7 nodes in the vertical direction, Figure 77a.

Boundary conditions

In the bottom corner, 7 nodes in the horizontal direction and 7 nodes in the vertical direction, have been fixed, Figure 77b.

(a) imposed displacement and rigid link   (b) boundary conditions

Figure 77 Applied load and boundary conditions.

4.10.2.2.2. Calibration of the model

In Table 25, all the parameters used in the model are reported.

Table 25 Numerical values for the combined cracking-shearing-crushing model.

	Linear material properties			
Masonry	Young's modulus	E	9500	MPa
	Poisson's ratio	ν	0.15	-
	Linear material properties			
Cracks	Linear normal stiffness	k_n	$1 \cdot 10^6$	N/mm^3
	Linear tangential stiffness	k_s	$1 \cdot 10^6$	N/mm^3
	Linear material properties			
	Linear normal stiffness	k_n	5 (calibrated)	N/mm^3
	Linear tangential stiffness	k_s	3(calibrated)	N/mm^3
	Cracking			
	Tensile strength	f_t	0.12(calibrated)	MPa
	Fracture energy	G_f	0.0001	N/mm
	Shearing			
	Cohesion	c	0.1	N/mm^2
	Tangent of friction angle	$tg\phi$	0.75	-
	Tangent of dilatancy angle	$tg\psi$	0.001	-
Joint	Tangent of residual friction angle	$tg\phi_r$	0.75	-
	Confining normal stress	σ_u	-0.001	MPa
	Exponential degradation coefficient	δ	5	-
	Mode II fracture energy			
	Factor a	a	0	-
	Factor b	b	0.04	-
	Crushing			
	Compressive strength	f_c	0.7 (calibrated)	MPa
	Factor	C_s	9 (calibrated)	-
	Compressive inelastic law			
	Compressive fracture energy	G_{fc}	1.6	N/mm
	Equivalent plastic relative displacement	k_p	0.003	mm

With the aim to calibrate the tensile strength of the joints, f_t, it is worth remembering the condition imposed by the Mohr-Coulomb criterion, Eq.(115):

$$f_t = \frac{1}{8} \div \frac{1}{10} f_c$$

$$f_t \leq \frac{c}{tg\phi}$$

(95)

From (Lourenço 1996), the following parameters have been suggested:

$G_f = 0.012 \ N/mm$ fracture energy for mode I

$c = 1.5 \cdot f_t$

$tg\phi = 0.75$

$G_{f_c} = d \cdot f_c$ compressive fracture energy

It is worth noting that in order to reproduce the results achieved from the experimental campaign, low values of mechanical parameter for the mortar joints compared to the ones achieved from the materials characterization must be used.

The numerical model has been considered "calibrated" when the fictitious LVDTs along the loaded diagonal, evaluated on the numerical model (continuous black line), perfectly matched the experimental one (dashed black line) in the same positions, (Figure 78).

Figure 78 Experimental LVDT vs. numerical LVDT.

4.10.2.2.3. Analysis

A preliminary linear analysis have been done to check the mesh. After that, a structural non linear analysis have been run. In particular, a Regular Newton-Raphson iterative scheme together with an energy norm criterion (convergence tolerance 10^{-3}) were adopted to solve the non linear equations. Regarding the incremental part of the solution procedures, a spherical arc-length control method was used.

4.10.2.2.4. Results

The results are presented in terms of displacement and principal stress in all the model, and tangential stress only along the joints.

In particular, in Figure 79a, a color map of the global displacement at the end of the test is reported, while in Figure 79b, a load versus displacement curve of the corner in which the load is applied, is presented.
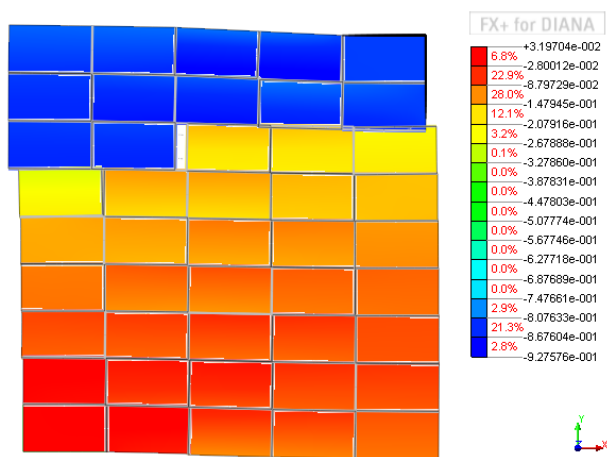
(a) Contour plot of the displacement at the end of the test
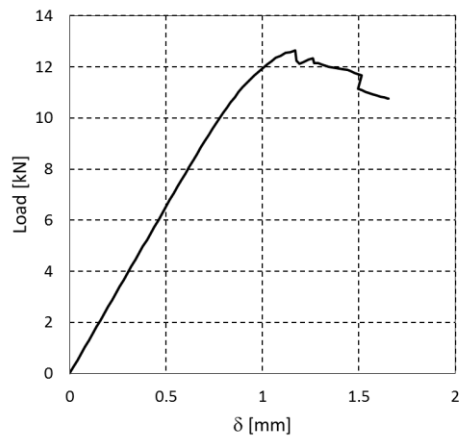
(b) Load vs. δ curve for the loaded corner

Figure 79 Displacement of UNR specimen.

Referring to the color map of the displacement, it is possible to see the sliding failure mode of the unreinforced masonry wall along the second upper mortar joint as it has seen in the experimental test. From the load displacement curve, the brittle behavior of the specimen after having reached the maximum load is confirmed. In Figure 80a, the principal stresses S1 are plotted, while in Figure 80b, the tangential stresses along the joints are plotted at the end of the test.
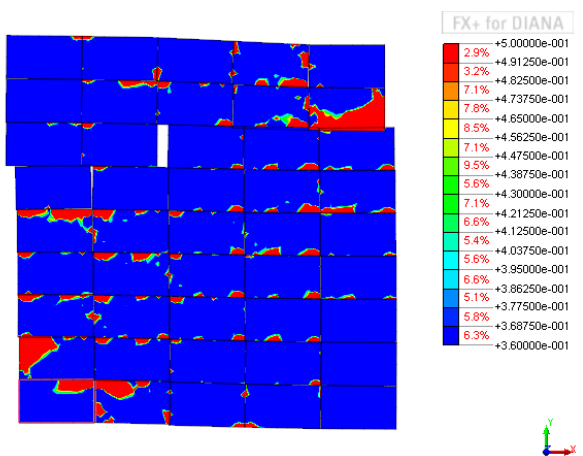
(a) Principal stresses S1
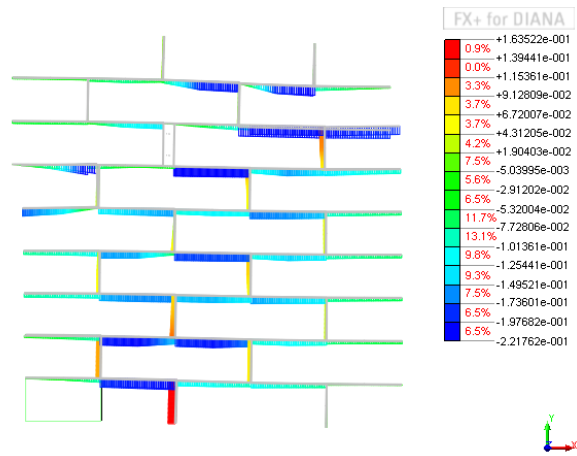
(b) Tangential stresses St_x of the joints

Figure 80 Principal normal and tangential stresses of UNR specimen.

Referring to the tensile stresses S1, the sliding of the mortar joints starts from the second upper joints where there is a concentration of higher values of tensile stresses. In Figure 80b, the shear stress along the mortar joints, that have not linear constitutive behavior, magnifies the sliding failure mode of the specimen at the end of the test.

4.10.3. Modeling strategy for RF specimens

The specimen strengthened by FRCM system on one side is modelled considering the Total Strain crack model, in which it is necessary to define the uniaxial stress – strain curve and then the principal stresses and strains are evaluated against this curve.

A macro-modelling strategy is used for the masonry wall that is more practice oriented due to the reduced time and memory requirements as well as a user-friendly mesh generation. This type of modeling is most valuable when a compromise between accuracy and efficiency is needed.

In order to model the reinforcement, a 3D interface with very high stiffness is used to simulate the perfect bond between the masonry substrate and the FRCM system. The mortar layer, attached to the homogenized masonry specimen, simulate the structural mortar used for the application of FRCM system. Inside it, a reinforcement grid is embedded to reproduce the glass fibre square mesh. In this way, the failure modes considered by the numerical model are: cracking of the mortar, failure of the fibers due to reaching of the tensile strength and slipping of the fibers. The sliding failure of the mortar joints in the masonry substrate is not considered in the modeling of the specimen strengthened by using FRCM system, because from the experimental results, diagonal tension failure occurred for all the specimens.

4.10.3.1. Models and numerical results

4.10.3.1.1. Finite element and constitutive behavior

A 2D finite element model was developed using Midas FX+ for DIANA. The model is made of: masonry substrate, perfect bond interface, structural mortar and embedded the reinforcement grid.

Masonry

Masonry was modeled by using 2D curved shell CQ40S elements (mesh size 15 x 15 mm) characterized by total strain based crack model as non linear behavior with an equivalent elastic modulus, E_b, equal to 2300 MPa and an equivalent Poisson's ratio, v, of 0.15, Figure 81a.

Perfect bond interface

The perfect bond between the FRCM system and the masonry substrate were modeled by using a 2D surface interface CQ48I elements (zero thickness). From the experimental results, no detachment were observed between FRCM and masonry substrate, therefore a linear elastic behavior with dummy stiffness, k_n and k_s, have chosen equal to $10^6 \ N/mm^3$.

Mortar

Structural mortar used for the FRCM strengthening system was modeled by using 2D curved shell CQ40S elements (mesh size 15 x 15 mm) characterized by total strain based crack model as non linear behavior, with an equivalent elastic modulus, E_b, equal to 2300 MPa and an equivalent Poisson's ratio, v, of 0.15, Figure 81a.

Reinforcement

FRCM reinforcements made of glass fibers were modelled as reinforcing grid in the mortar layer. From the experimental results, no failure of the fibers was observed, therefore a linear elastic behavior with an elastic modulus, E_{FRCM}, equal to 72000 MPa is used.

(a) masonry   (b) mortar

Figure 81 Finite element model.
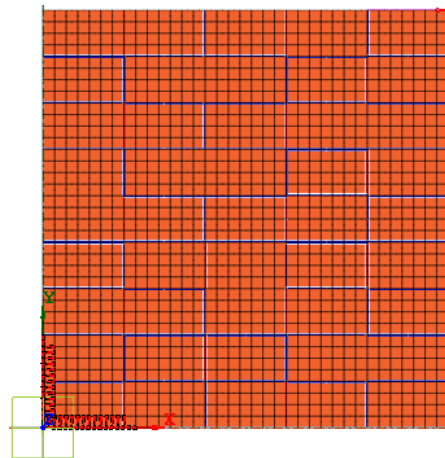
Load

As for unreinforced specimen, one vertical and one horizontal displacements have been applied on the top corner of the masonry specimen. In order to simulate the steel plate used in laboratory, a rigid link has been applied on 7 nodes in the horizontal direction and 7 nodes in the vertical direction, Figure 77a.

Boundary conditions

As for unreinforced specimen, in the bottom corner, 7 nodes in the horizontal direction and 7 nodes in the vertical direction, have been fixed, Figure 77b.

4.10.3.1.2. Calibration of the model

In Table 26, all the parameters used in the model are reported.

Table 26 Numerical values for the total strain crack model.

	Linear material properties			
	Young's modulus	E	2300(calibrated)	*MPa*
	Poisson's ratio	ν	0.15	-
	Total strain crack model			
	Crack orientation: rotating			
Masonry	Tensile curve: exponential			
	Tensile strength	f_t	0.15(calibrated)	*MPa*
	Fracture energy	G_f	0.001	*N/mm*
	Compressive curve: parabolic			
	Compressive strength	f_c	2.0 (calibrated)	*MPa*
	Factor	C_s	3.2 (calibrated)	-
	Linear material properties			
Perfect bond interface	Linear normal stiffness	k_n	$1 \cdot 10^6$	*N/mm³*
	Linear tangential stiffness	k_s	$1 \cdot 10^6$	*N/mm³*
	Linear material properties			
	Young's modulus	E	8000(calibrated)	*MPa*
	Poisson's ratio	ν	0.125	-
	Total strain crack model			
	Crack orientation: rotating			
Mortar	Tensile curve: exponential			
	Tensile strength	f_t	1.5(calibrated)	*MPa*
	Fracture energy	G_f	0.05	*N/mm*
	Compressive curve: parabolic			
	Compressive strength	f_c	10.77 (calibrated)	*MPa*
	Factor	C_s	17.23 (calibrated)	-

As before, it is worth noting that in order to reproduce the results achieved from the experimental campaign, low values of mechanical parameter for the mortar joints compared to the ones achieved from the materials characterization must be used.

The numerical model has been considered "calibrated" when the fictitious LVDTs along the loaded diagonal, evaluated on the numerical model (continuous black line), perfectly matched the experimental one (dashed black line) in the same positions.

4.10.3.1.3. Analysis
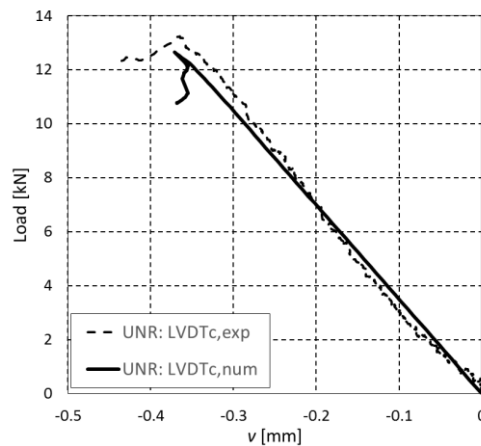
A preliminary linear analysis have been done to check the mesh. After that, a structural non linear analysis have been run. In particular, a Regular Newton-Raphson iterative scheme together with an energy norm criterion (convergence tolerance 10^{-3}) were adopted to solve the non linear equations. Regarding the incremental part of the solution procedures, a regular arc-length control method was used.

4.10.3.1.4. Results

The results are presented in terms of displacement and principal stress in the model. In particular, in Figure 82a, a color map of the global displacement at the end of the test is reported, while in Figure 82b, the principal stresses at the end of the test are presented.
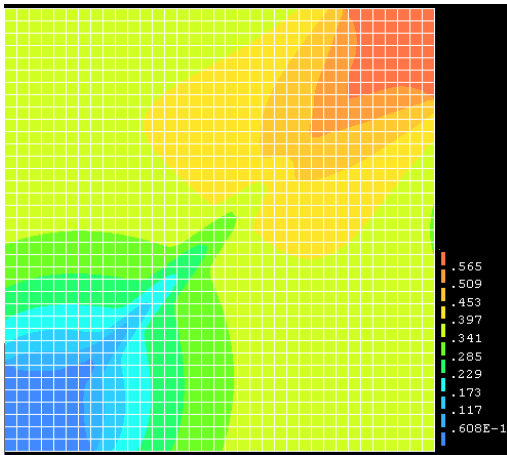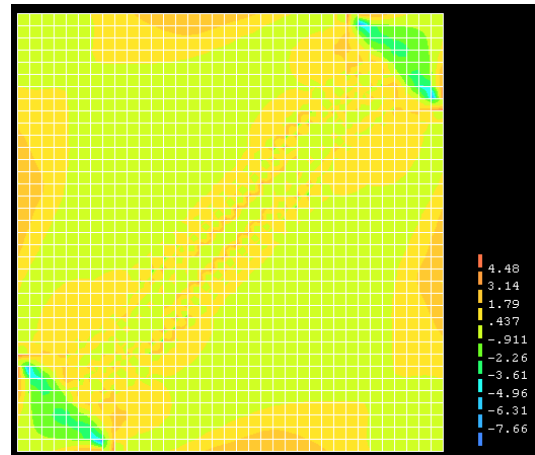
(a) displacement at the end of the test   (b) principal stresses at the end of the test

Figure 82 Displacement and principal stresses for masonry substrate and mortar.

Referring to the color map of the displacement and the principal stresses, remembering that the load is applied only on the masonry and the hypothesis of perfect bond between masonry and structural mortar, it is possible to observe the confinement effect on the sides of the mortar. Furthermore, the presence of reinforcement changes the failure mode from sliding (unreinforced specimen) to diagonal tension (strengthened specimen). In Figure 83, the stresses in x and y directions are plotted, for the reinforcement grid.
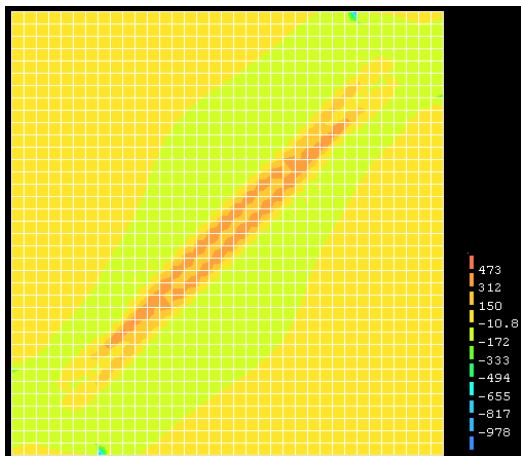
(a) stresses in x direction   (b) stresses in y direction
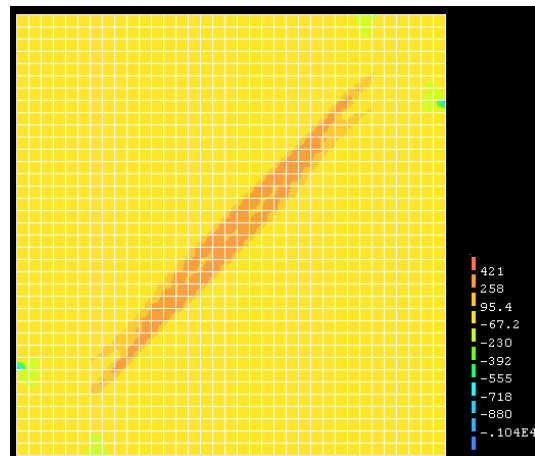
Figure 83 Stresses in x and y directions for reinforcement grid.

From Figure 83, it is possible to conclude that the presence of reinforcement changes the mechanism of failure from brittle to more ductile in addition to increase the peak load of the specimen (close to 60 kN).

4.11. Conclusions

An experimental campaign on diagonal compression tests conducted on masonry specimens strengthened with two different techniques is presented. In particular, the strengthening systems investigated were: structural repointing by inserting basalt bars in two mortar joints in a symmetric and asymmetric configuration and FRCM system, applying a glass-based mesh grid on one or both sides of the specimens. Diagonal compression test allowed to investigate the load capacity as well as the ductility of the tested specimens. In particular, for both the retrofitting solutions an increase in maximum load, shear stiffness and ductility proportionally to the reinforcement ratio was registered. However, in the case of repointing the mode of failure was sliding along the interface between bricks and mortar, on the other hand in the case of FRCM strengthened specimens the

mode of failure was diagonal cracking. Analytical procedures and numerical modeling have shown to be effective in predicting the shear capacities of both unreinforced and reinforced specimens.

5. Chapter 5: Diagonal Compression test on large masonry specimens

5.1 Introduction

Masonry buildings constitute the greatest part of the building stock in Europe. It is well known that masonry structures suffer of several structural issues. Low tensile strength, low ductility, poor material properties as well as weak connections between structural elements are among the causes of the vulnerability against out-of-plane loads and of the fragile collapses of masonry structures (Oyarzo-Vera & Griffith 2009; Gentilini et al. 2012; Castellazzi et al. 2013; Boscato et al. 2014; Franzoni et al. 2014; Valluzzi et al. 2014; Franzoni et al. 2015).

For these reasons, strengthening interventions are necessary to improve the mechanical performance of masonry structures (Ghiassi et al. 2013; Gattesco & Boem 2015). Innovative materials, as externally bonded textiles (wet lay-up) such as FRP (Fiber Reinforced Polymer) have been helpful for repairing and strengthening both modern and historic constructions and structural components (Valluzzi et al. 2014; Almeida et al. 2015). The composite materials are used to: (*i*) provide tensile strength to masonry elements, (*ii*) modify the structural behavior and the collapse mechanism of the structure, (*iii*) increase the displacement capacity of strengthened composite-to-masonry systems. In the case of masonry façades or elements with facing bricks, the use of externally bonded composites for retrofitting interventions is not a viable solution because violates aesthetic and conservation requirements (Carozzi et al. 2014).

Recently, in order to overcome well-known drawbacks of FRP composites, FRCM (Fiber Reinforced Cementitious Matrix) composites have been introduced. FRCM are a combinations of polymer-modified cementitious matrices and high-strength fibers namely steel, carbon, basalt or glass. The cementitious matrix exhibits significant heat resistance, allows vapor permeability, and can be applied at low temperatures or on wet surfaces.

In such a context, this chapter shows the results of an experimental program that involves large masonry specimens made of hollow-clay bricks and cement-based mortar joints subjected to diagonal compression load. Those specimens, characterized by only horizontal thin mortar layer (approximately 1 mm thick) and hollow bricks, are used for the infill walls. After curing, the specimens are reinforced using FRCM system, a 1-ply basalt and steel-based mesh grid has been applied on the surfaces. Symmetrical configurations without and with connectors that link the two sides are considered. Results are presented in terms of load capacity, shear modulus as well as ductility. In order to compare the results obtained from the tests, a reinforcement ratio is defined. Finally, analytical procedures presented in the codes are followed to predict the shear capacities of the unreinforced specimens. The shear contribution of FRCM system, is calculated following the procedure presented in (ACI 549.4R-13 2013) code.

5.2 Material characterization

5.2.1. Brick

Hollow clay bricks having nominal size 380 x 240 x 180 mm³ were used for manufacturing the specimens. Brick compressive strength in flatwise direction was obtained according to (EN 772-1 2010) on 6 cubic specimens. In Table 27, the mechanical properties of the bricks are reported in terms of percentage of voids, n, elastic modulus E and brick compressive strength f_{cb}.

Table 27 Mechanical properties of the bricks used for the manufacturing of the specimens. Coefficient of variation in parentheses.

Materials	n [%]	E [MPa]	f_{cb} [MPa]
Hollow clay brick	50.15 (5.66)	2874 (180)	40.40 (2.10)

5.2.2. Mortar

Two different types of commercial pre-mixed cement based mortar were used to construct the specimens: the first one called W and the second called L obtained by adding polymers to improve ductile behavior. In particular, two specimens have been constructed by using W mortar and the other two, by using L mortar. From a triplet tests, a shear bond strength between brick and mortar joints is determined: in particular the specimen constructed with W mortar is characterized by a brittle behavior with a value of shear bond strength, τ_0, equal to 0.3 MPa, while the specimen made by L mortar is characterized by a value of shear bond strength, τ_0, equal to 0.6 MPa with a ductile behavior (ductility μ equal to 3). For strengthening operations, a structural mortar, called B, is used to apply FRCM system. Mortar compressive and flexural strengths were obtained according to (EN 1015-11 2007), while the shear strength is obtained according to (EN 1052-3 2007)

In Table 28, the mechanical properties of the mortars are reported in terms of mortar compressive and flexural strength, f_{cm} and f_{fm}, respectively.

Table 28 Mechanical properties of the mortars used for the manufacturing of the specimens.

Materials	f_{cm} [MPa]	f_{fm} [MPa]	τ_0 [MPa]
Mortar W (cement-based mortar)	>10	-	0.3
Mortar L (cement-based mortar)	>5	>3	0.6
Mortar B (structural mortar)	>15	>5	>1

5.2.3. FRCM

FRCM composite used to strengthen the specimens consisted of a square mesh steel and basalt based, characterized by a 17 x 17 mm² mesh size, tensile strength, ($f_{t,FRCM} = 55$ kN/m), modulus of elasticity, E_{FRCM}, equal to 70000 MPa, equivalent thickness of dry fabric equal to 0.032 mm and elongation at failure ε_u, equal to 1.9%.

5.2.4. Connectors

The twisted steel bars (nominal diameter equal to 10 mm and nominal cross sectional area equal to 12.80 mm^2) are used to link the two side of the specimen in the case of one or multiple leaves, without and with reinforcement, Figure 84.

Figure 84 Twisted steel bar.

In order to check the mechanical properties of the steel bars, direct tensile tests were performed. The procedure used was the same adopted for the steel bars diameter 6 mm (paragraph 3.5.1.2). Based on preliminary tests, it was determined that 150 mm anchor length could offer adequate restraint. The dimension of the specimens has been obtained according to (BS EN ISO 6892-1:2009 2015). The specimens, with a total length (L_p) of 800 mm, are provided with two anchoring systems (one for every end), with a length (L_a) of 150 mm, leaving an effective length (L_u) of 500 mm.

A universal testing machine, Metrocom 600 kN, has been used for the tests. The load has been applied through a constant speed of 2 mm/min until the failure of the specimen. It is notably that specimens rupture occurred at a time between one and ten minutes, according to (BS EN 845-1:2013 2003; BS EN 846-7:2012 2015). Each specimen was provided by a deformometer placed in a central position in the bar to record for the elongation. A LVDT measured the displacement of the machine head (Figure 85). To check if the anchoring system could affect the test, also the position on the sample where the break occurs has been recorded.

(a)   (b)

Figure 85 Tensile test on the steel bar: a) specimen at the beginning of the test; b) specimen at the end of the test.

Results in terms of breaking force (P_{max}), maximum tensile stress (σ_{max}), breaking elongation (ε_u) as well as elastic modulus are collected in Table 29. The values were obtained as the mean on three samples. In Figure 86, σ-ε curve for one steel bar is reported.

Table 29 Mechanical properties of the steel bars. Values averaged on five samples. Standard deviation in parentheses.

Material	E [MPa]	P_{max} [kN]	σ_{max} [MPa]	ε_u [%]
Bar 1	140912	16.02	1251.56	3.80
Bar 2	141838	16.02	1251.56	3.92
Bar 3	119901	16.21	1266.41	3.13
Mean	134217 (12407)	16.08 (0.11)	1256.51 (8.57)	3.62 (0.43)
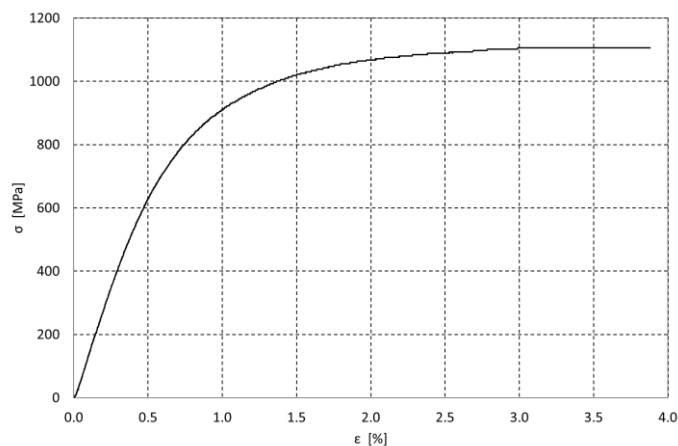
Figure 86 Stress-strain curve for steel bar.

5.2.4.1. Further insight on the connectors

The connectors are drilled inside the masonry panel (Figure 87a) and, at the two free ends are bended on the surface of the specimen (Figure 87b).

(a)   (b)

Figure 87 Application of the steel bars as connectors to link the two strengthened side of the specimen.

In this way, at the end of the strengthening procedure, the bending of the connectors are clearly visible on the surface of the specimen.

For this reason, a new system is "ongoing", Figure 88, characterized by the fact that the bar is drilled inside it and is not yet necessary to bend the bar; in this phase only preliminary results have been presented.

Figure 88 New sleeve system.

In order to test this system, the steel bar is drilled inside the sleeve on one side and on the other side is fixed on the top jaw of the machine. The sleeve is positioned between two steel plates and fixed at the bottom of the machine, (Figure 89a). The load has been applied through a constant speed of 2mm/min until the failure of the sleeve Figure 89b.

(a) Test set-up   (b) Specimen at the end of the test

Figure 89 Tensile test on the sleeve.

Results in terms of breaking force (P_{max}) are collected in Table 30. The values were obtained as the mean on five samples. In Figure 90, load - displacement curve for one sleeve is reported.

Table 30 Maximum load of sleeves. Values averaged on five samples. Standard deviation in parentheses.

Material	P_{max} [kN]
Sleeve 1	1.48
Sleeve 2	1.38
Sleeve 3	1.56
Sleeve 4	1.40
Sleeve 5	1.70
Mean	1.51 (0.13)
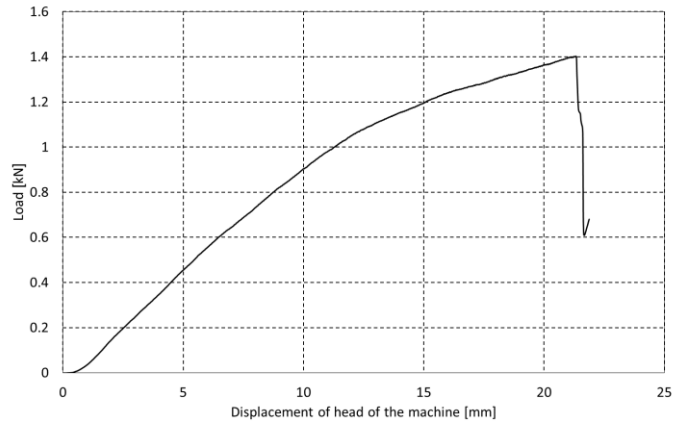
Figure 90 Stress-displacement curve for the sleeve.

5.3 Specimens

Each specimen was built with six courses of bricks and five 1 mm thick mortar layers only along the bed joints (no vertical joints), and had a nominal total size equal to 1200 x 1200 x 380 mm^3 (Figure 91b).

In particular, four types of specimens were constructed:

i) reference specimens hereinafter denoted with UNR-W – Unreinforced with mortar W, Figure 91a;

ii) reference specimens hereinafter denoted with UNR-L – Unreinforced with mortar L, Figure 91a;

iii) specimens realized by using mortar L, with symmetric FRCM obtained applying a 1-ply basalt and steel-based grid mesh on both sides of the specimen, hereinafter denoted with RF-L - Reinforced FRCM and mortar L, Figure 91c;

iv) specimens realized by using mortar W, with symmetric FRCM obtained applying a 1-ply basalt and steel-based grid mesh on both sides of the specimen, hereinafter denoted with RF-WC - Reinforced FRCM, mortar W and four connectors in the corners, Figure 91d.

The specimens were strengthened after the maturation of 28 days.

As FRCM system, the main phases of the application were: wet the surface of the specimen, application of the first layer of structural mortar with a thickness of 5 mm, positioning of the fiber mesh, application of a second layer of structural mortar.

For the connectors, four holes were drilled in the four corner of the specimen. Then the connectors have been inserted inside the holes and bend at the free end over the surface of the wall.

In Table 31, the tested specimens are summarized. One specimen for type has been tested.
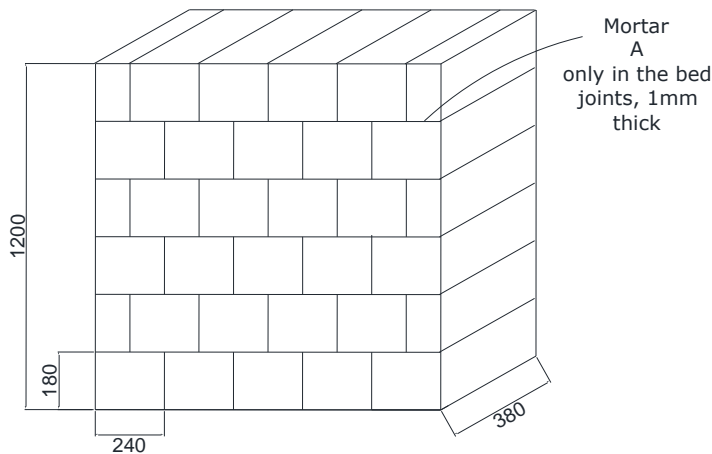
(a) UNR specimen

(b) UNR specimen
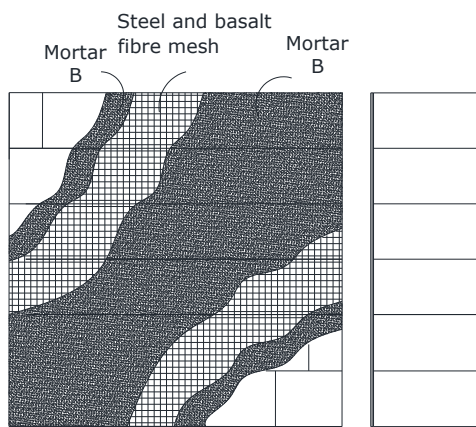
(c) LF specimen
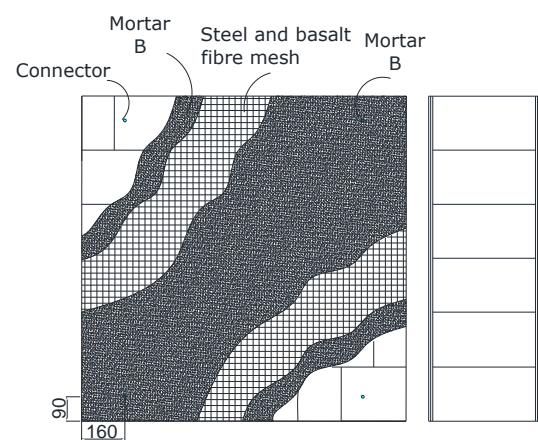
(d) WFC specimen

Figure 91 Specimens tested in the experimental program. Dimensions in mm.

Table 31 Specimen label and description.

Specimen label	Number of each specimens	Description
UNR-W	1	Specimen realized with mortar W without reinforcement (Figure 91a)
UNR-L	1	Specimen realized with mortar W without reinforcement (Figure 91a)
RF-L	1	Specimen realized with mortar L with reinforcement: 1-ply basalt and steel based on both side of the specimen (Figure 91c)
RF-WC	1	Specimen realized with mortar W with reinforcement: 1-ply basalt and steel based on both side of the specimen with connectors in the corners (Figure 91d)

5.4 Test set up and instrumentation

After curing, all the specimens were subjected to a diagonal compression test in a standard configuration normalized by (ASTM E 519 2002) and (RILEM 1991), Figure 92. The load is applied through a steel shoe

with inner dimensions 240 x 240 x 20 mm^3 placed at the top corner. All the specimens were tested in a universal testing machine Losenhausen 6000 kN operating in displacement control at a rate equal to 0.001 mm/s.

Figure 92 Test set-up.

In Figure 93, the instrumentation of the specimens is shown. During the test, the values of the applied load and the diagonal displacements were recorded (Mojsilovic & Salmanpour 2016). The displacements were measured by four linear variable displacement transducers: two on the front face (LVDTc,f and LVDTt,f), and two on the back face, (LVDTc,b and LVDTt,b). In particular, LVDTc,f and LVDTc,b were vertically oriented along the force line to measure the wall shortening, while LVDTt,f and LVDTt,b were placed horizontally, perpendicular to the force line to record the crack opening. A load cell was used to measure the force along the loaded diagonal.

| (a) Specimen front face | b) Specimen back face |

Figure 93 Instrumentation of the specimens.

In Figure 94, the load pattern is presented. In particular, six cycles of loading and unloading (three until 10 kN of load and three until 50 kN of load) have been done before get the specimen up to failure.
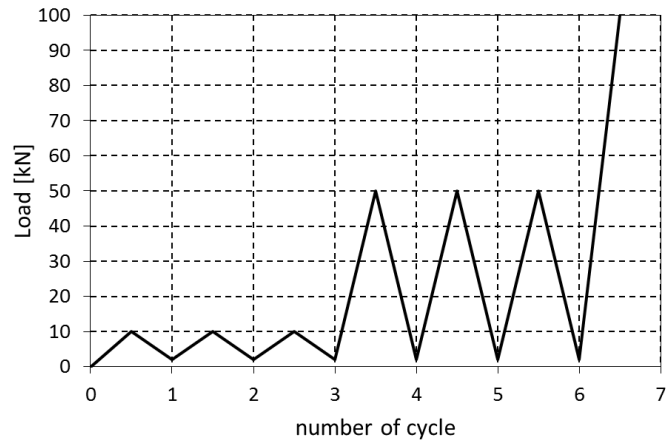
Figure 94 Load protocol of the test.

5.5 Results

In the following, results obtained from the tests conducted on the specimens are presented. In particular, results are given in terms of load versus vertical displacement (load - v curves) and load versus horizontal displacement (load – u curves). It is worth noting that negative signal of the LVDTs means shortening, while positive signal means elongation.

5.5.1. UNR specimens

In Figure 95, for negative abscissa, the load - v curves (black lines) for the two UNR specimens are represented: the continuous lines are referred to specimen constructed by using W mortar, while the dashed lines corresponding to the specimen made by L mortar. Each curve is obtained as the average of the signals from the two vertical LVDTc (LVDTc,f and LVDTc,b in Figure 93). For positive abscissa, the corresponding load - u curves for the UNR specimens are shown. Each curve is obtained as the average of the signals from the two horizontal LVDTt (LVDTt,f and LVDTt,b in Figure 93).

In Figure 96a and Figure 96b, UNR-W and UNR-L specimens at the end of the test are shown, respectively.
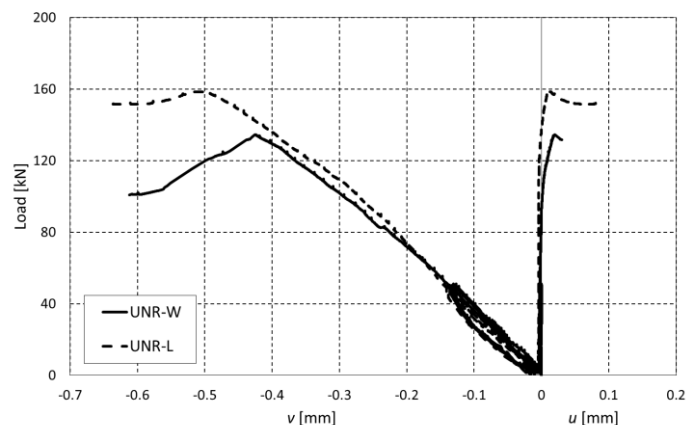
Figure 95 Load-vertical and load-horizontal displacement curves for UNR-W and UNR-L specimens.
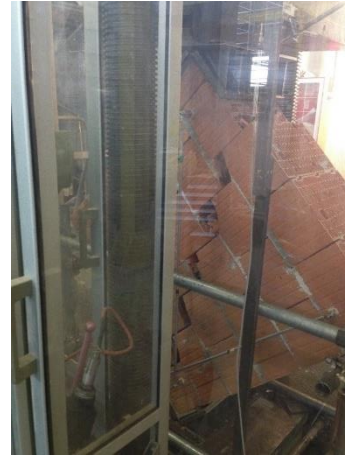
| (a) UNR-W specimen | (b) UNR-L specimen |

Figure 96 UNR specimens: failure mode.

Referring to load - v curve and load - u curve in Figure 95, UNR-W and UNR-L specimens exhibited a linear behavior until the end of the test, with the same initial stiffness although the different type of mortar used in the construction phase. After the peak load (P_{max}) is reached (around 130 kN for UNR-W and 160 kN for UNR-L), corresponding to a vertical shortening equal to 0.4 mm for UNR-W and 0.5 mm for UNR-L, and a horizontal elongation equal to 0.01 mm, the specimens collapsed in a brittle way in which a main crack developed within the mortar joints, Figure 96. From Figure 96a, UNR-W that is made using a brittle mortar, fails due to sliding at the brick/mortar interface while, UNR-L that is made by using a ductile mortar fails due to the propagation of a "stepped crack" along the bed and head joints (Figure 96b).

5.5.2 RF-L and RF-WC specimens

In Figure 97, for negative abscissa, the load - v curves (grey lines) for RF-L and RF-WC specimens retrofitted with FRCM system (RF specimens) are represented. Each curve is obtained as the average of the signals from the two vertical LVDTc (LVDTc,f and LVDTc,b in Figure 93). For positive abscissa, the corresponding load - u curves for the RF specimens are shown. Each curve is obtained as the average of the signals from the two horizontal LVDTt (LVDTt,f and LVDTt,b in Figure 93). For comparison purposes, the curves of the UNR-W and UNR-L specimen are reported on the same figure.

In Figure 98, RF-L and RF-WC specimens at the end of the test are shown, respectively.
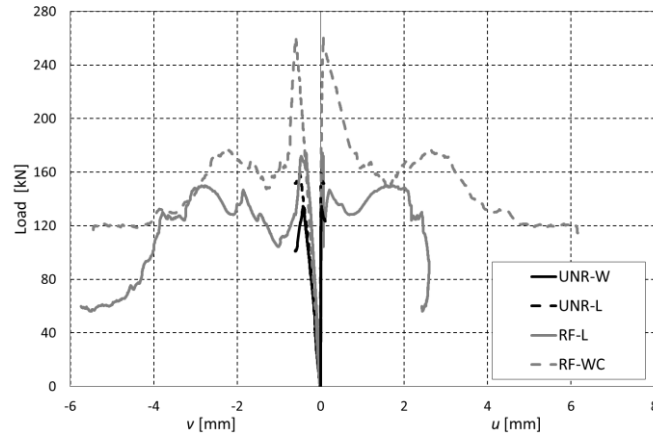
Figure 97 Load-vertical and load-horizontal displacement curves for RF-L (continuous grey line) and RF-WC (dashed grey line) specimens.

(a) RF-L specimen

(b) RF-WC specimen

Figure 98 RF specimens: failure mode.

Referring to load - v curves, RF specimens exhibited a linear behavior until the maximum load, Figure 97. After the peak load is attained (around 170 kN for RF-L and 260 kN for RF-WC), a softening branch is registered.

Comparing the load - v black curve related to the unreinforced specimen with the grey ones of RF specimens, it might be noted that from the initial part of the diagram, the stiffness of RF is the same than that of UNR. As expected, reinforced specimens reach a higher peak load (P_{max}) with respect to UNR, and after the peak load is attained, the softening branch is longer with respect to the unreinforced specimen, showing a more ductile behavior.

Referring to the failure mode of RF-L specimens, Figure 98a, after the peak load is attained, vertical cracks started to appear in the mid area of the specimen body, involving both the bed joints and the bricks. The cracks kept evolving in the mid vertical position until the bottom corner, leaving the top corner unaffected. The specimens failed due to toe crushing and, at the same time, FRCM debonded from the masonry substrate to which it was applied.

Referring to the failure mode of RF-WC specimen, Figure 97, after the peak value of the compression load is reached, vertical cracks started to appear in the mid part of the specimen body. The cracking pattern developed

within the two loading shoes, leaving the outer corners unaffected, and a diagonal tension failure occurred in the specimen. The change in the failure mechanism can be attributed to the presence of the connectors that avoids the toe crushing of the corner. On both sides, the FRCM layers began to debond from the masonry underneath.

5.6 Summary

A summary of the relevant mechanical parameters obtained from the diagonal compression test for all the specimens in terms of mean values and standard deviations is given in Table 32. The average peak load values ($\bar{P}_{max}$) are listed. Parameter Δ, representing the structural enhancement achieved in terms of $\bar{P}_{max}$ by using reinforcements, is calculated by using Eq.(32).

The maximum shear stress (τ_{max}) is computed following (ASTM E 519 2002) by using Eq.(42), considering the net area of the specimen and assuming that the shear stress τ is equal to both tensile and compressive principal stresses, representing a pure shear stress state in masonry (Brignola et al. 2008; Calderini et al. 2010). Also, τ_{max} is calculated considering the gross area of the wall and this value is used in the calculation of the shear modulus.

The elastic shear modulus is derived by using Eq.(48), and the μ parameter that allows to quantify the benefit in terms of ductility of the considered retrofitting solutions is calculated from Eq.(50).

Finally, in order to compare the two retrofitting solutions, a parameter ω_f representing the calibrated reinforcement ratio (Babaeidarabad et al. 2014), is defined by using Eq.(34).

Table 32 Summary of the results of the experimental investigation.

Specimen label	$\bar{P}_{max}$ [kN]	Δ_1 [%]	$\bar{\tau}_{max}(A_{gross})$ [MPa]	$\bar{\tau}_{max}(A_{net})$ [MPa]	$\bar{G}$ [MPa]	μ	ω_f [%]	Failure mode
UNR-W	134.55	-	0.22	0.44	705.35	-	-	sliding
UNR-L	159.10	-	0.26	0.52	710.01	-	-	shear friction
RF-L	174.21	9.50	0.27	0.54	956.88	15	0.82	toe crushing
RF-WC	260.07	93.29	0.40	0.80	799.32	9.24	0.82	diagonal tension

5.7 Discussion of the results

From Table 32, comparing the results for UNR-W and RF-WC specimens in terms of peak load, the increment is around 93% $\Delta_1 = 93.29\%$), whereas between UNR-L and RF-L the load capacity increment is around 9% ($\Delta_1 = 9.50\%$). Moreover, an increment in the shear modulus, $\bar{G}$, is registered moving from UNR specimens to RF. In terms of ductility, it is worth noting that μ parameter is lower for RF-WC with respect to RF-L.

The presence of FRCM avoids sliding failure but a toe crushing failure can occur in the bottom corner of the specimen. The steel bars, inserted in the corners of the specimen as connectors between the two side of the specimen, change the mechanism of failure from toe crushing to diagonal tension.

Furthermore, the maximum load, $\bar{P}_{max}$, increases as reinforcement ratio, ω_f, increases.

5.8 Analytical investigation

In this section, the analytical procedure presented in the code (ACI 549.4R-13 2013), to predict the nominal shear capacities of masonry walls is followed and finally compared to the ones obtained from the experimental tests. The procedure has been explained in paragraph 4.9; for this reason only the main formula and the final results are reported. It is worth noting that the analytical approach does not take into account the presence of the connectors.

Considering a masonry panel of width equal to W, height equal to H and thickness equal to T, subjected to a compression load equal to P, it is possible to compute the nominal shear capacity of the specimen, V_n, as the sum of two contributions:

$$V_n = V_m + V_f \tag{96}$$

where V_m and V_f are the contributions of the masonry wall and the reinforcement, respectively.

All the calculations are given in Appendix D for determining the shear capacities of the unreinforced and reinforced walls tested.

In Table 33, a comparison between the experimental and the analytical results is reported in terms of nominal shear capacity. A ratio between the results is also calculated.

Table 33 Comparison between experimental and analytical results.

	UNR-W	UNR-L	RF-L	RF-WC
	[kN]	[kN]	[kN]	[kN]
Experimental	$V_n = P_{max}cos(\theta)$	$V_n = P_{max}cos(\theta)$	$V_n = P_{max}cos(\theta)$	$V_n = P_{max}cos(\theta)$
	95.14	112.50	123.18	183.90
Analytical	$V_n = V_m$	$V_n = V_m$	$V_n = V_m + V_f$	$V_n = V_m + V_f$
	97.70	83.0	126	140.7
Ratio experimental/analytical	0.97	1.35	0.98	1.31

5.8.1. Discussion of the results

From Table 33, it is possible to observe that analytical results give a good prediction of the shear capacity for both unreinforced specimens and specimens strengthened by using FRCM system reinforcement. Infact, the ratio between the experimental and analytical values in all cases is close to 1.

5.9 Conclusions

An experimental campaign on diagonal compression tests conducted on large masonry specimens strengthened with FRCM system is presented. Four different specimens have been tested. As unstregthened samples, two types of mortar were used in the construction phase: one brittle and the other more ductile. As strengthened samples, for both specimens, an FRCM steel and basalt based was applied on the surfaces of the specimens; in addition in order to link the two sides, four connectors in the corner were applied on one strengthened specimen. A load protocol with several loading and unloading cycle was used to get the specimens up to failure. As expected, the unstrenghtened specimens fail in sliding or shear friction mode. The presence of FRCM avoids sliding failure but a toe crushing failure can occur in the bottom corner of the specimen. The steel bars,

inserted in the corners of the specimen as connectors between the two side of the specimen, change the mechanism of failure from toe crushing to diagonal tension.

The structural enhancements achieved by using FRCM system are: *i*) increment in shear capacity, *ii*) increment in displacement capacity, *iii*) more stable behavior compared to the unreinforced specimens and *iv*) change in failure mode.

6. Chapter 6: Evaluation of collapse mechanisms in masonry buildings: application of structural repointing and plating system

6.1 Introduction

Historic masonry buildings are characterized by a high seismic vulnerability and it is difficult to find the best analytical model to capture the behavior of these structures under earthquake excitation. One of the most commonly used approach is based on the evaluation of the potential local mechanisms. The assumptions at the base of this method are (Heyman 1992): *i*) compressive strength of the masonry is infinite, *ii*) tensile strength of masonry is close to zero, *iii*) elastic strains are negligible and *iv*) no sliding between blocks can occur. Those hypotheses work properly in case of rigid block mechanisms, means single leaf instead of multiple leaves masonry, and they are extensively accepted when local failures are involved. When rigid collapsing modes occur, the Italian Standard (D.M. 14 Gennaio 2008; Circolare 2 febbraio n 617 2009) states to proceed with a limit analysis, using a kinematic approach; then, both linear and non linear kinematic analysis are requested to be fulfilled in the verification process. With the limit analysis, it is possible to study the trend of the horizontal action the macroelement is submitted whilst has to bear whilst collapsing. Given a load configuration, proportional to α - multiplier, it is possible to calculate its maximum value, corresponding to a limit condition, and beyond which the structure undergoes a local collapse. On a specific macroelement the mechanisms that are likely to occur are highlighted, taking into consideration also the specific vulnerabilities of the structure (i.e. the presence of aligned windows on the wall, thickenings/narrowings of the section) verifying that they are also kinematically admissible. Then the lowest α - multiplier is found by using kinematic theorem, corresponding to a specific collapse mechanism. Then the Principle of Virtual Works (PVW) can be applied to the aforementioned movement, taking the rigid body motions as a sequence of rigid movements in which the rotation angle varies of an infinitesimal step $d\phi$, bringing the macroelement gradually to collapse. With this step by step procedure, it is possible to draw the trend of the α - multiplier in relationship with a control point displacement dk, placed on the overturning macroblock (Acito et al. 2014).

A preliminary requirement to be done in order to take the limit analysis as a proper evaluation tool is to guarantee a minimum value of the Masonry Quality Index (IQM). A minimum value has to be taken in order to ensure that the considered mechanism is rigid and the masonry crumbling is avoided (Borri, Corradi, et al. 2015). The infinite compressibility assumption is taken into account by moving the instantaneous rotation hinge from the external face to the point in which the stress is less than the design value, f_{cd} that is defined as Eq.(97), (Circolare 2 febbraio n 617 2009)

$$f_{cd} = \frac{f_c c_{ct}}{FC \gamma_m} \tag{97}$$

with f_c is the average compressive stress, c_{ct} is a corrective factor, FC is the confidence factor, γ_m is the material security factor.

After the macroblock capability to collapse following a rigid body motion is ensured, all the acting forces are underlined, and the kinematic chain is evaluated to PVW

$$\alpha_0 \left(\sum_{i=1}^{n} P_i \delta_{x,i} + \sum_{i=1}^{n+m} P_j \delta_{x,j} \right) - \sum_{i=1}^{n} P_i \delta_{y,i} - \sum_{h=1}^{o} F_h \delta_h = L_{fi} \tag{98}$$

where:

P_i is a generic weight force directly applied to the centroids of the different blocks concurring in the mechanism;

P_j is a generic weight forces not directly applied to the centroids of the blocks which mass during the seismic action lead to an horizontal action on the blocks involved in the mechanism;

F_h is a generic external force acting on the blocks;

n, m and o are the numbers of P_i, P_j, and F_h, respectively;

L_{fi} is the inner work generated by internal forces (e.g. block friction, interlocking forces);

$\delta_{x,i}$ is the virtual horizontal displacement of the application point of the i-th weight force P_i acting on the mechanism;

$\delta_{y,i}$ is the virtual vertical displacement of the application point of the j-th weight force P_i acting on the mechanism;

$\delta_{x,j}$ is the virtual horizontal displacement of the application point of the j-th force P_j;

δ_h is the virtual horizontal displacement of the application point of the h-th force F_h.

The control point, CP, should be representative of all the mechanisms analyzed and, generally is located on the top floor of the structure or in the floor where there is a higher concentration of mass with relevant displacements. Once defined a control point onto the macroblock, it is possible to define the α - multiplier trend from the activation point, α_0, up to the complete failure (i.e. $\alpha = 0$) over the control point displacement, since the virtual displacements depend on the rotational variable $d\phi$.

To compare the mechanism with the seismic displacement spectrum, a spectral counterpart have to be evaluated, simplifying any complex movement by considering its equivalent single degree of freedom oscillator. In order to do that, the participating mass during the mechanism, M^* has to be evaluated, along with the spectral acceleration of the SDOF, a^*, and its corresponding spectral displacement, d^*:

$$M^* = \frac{\left(\sum_{i=1}^{n+m} P_i \delta_{x,i} \right)^2}{g \sum_{i=1}^{n+m} P_i \delta_{x,i}^2} \tag{99}$$

$$a^* = \frac{\alpha_0 \sum_{i=1}^{n+m} P_i}{M^* FC} \tag{100}$$

$$d^* = \frac{\sum_{i=1}^{n+m} P_i \delta_{x,i}^2}{FC \, \delta_{x,k} \sum_{i=1}^{n+m} P_i \delta_{x,i}} \tag{101}$$

where $\delta_{x,k}$ is the normalized horizontal virtual displacement of the control point.

The plot coming out from the spectral acceleration over the displacement defines the capacity curve of the system. It represents the displacement of a discrete number of rigid bodies relatively moving, simplifying the problem to a single mass M^* placed on a vertical beam, oscillating with a defined flexural stiffness because of a seismic input.

6.2 Kinematic analysis: linear and non linear approach

The kinematic approach, that can be linear and non linear, is based on the determination of the horizontal action that the structure can sustain during the evolution of the collapse mechanism. The difference between linear and non linear can have influence on the verification of the results: in the linear approach the verification is made in terms of spectral acceleration while, in the non linear analysis is in terms of displacement.

In other words, the linear kinematic analysis is based on the determination of the resistance of the system with regard to the horizontal acceleration that activates the local mechanism. This approach is in terms of force and a behavior factor $q > 1$ is introduced (Circolare 2 febbraio n 617 2009) to decrease the demand in dependency to estimated ductility effects of the masonry structure. The coefficient q is recommended by standards but is dependent on the geometry and material consistency of the structure.

The non linear kinematic approach is in terms of displacement and is based on a comparison between the ultimate displacement capacity of the structure, d_u^*, and the displacement demand of the earthquake, Δ_d (Fajfar 1999; Fajfar 2000).

The verification is done with seismic spectra corresponding to specific limit states, and in particular: *i)* for the Damage Limit State, (SLD), in which the spectral acceleration that activates the damage mechanism, a_0^*, is considered and *ii)* for the Life Safety Limit State (SLV), in which the spectral displacement, d_u^*, that brings the SDOF up to collapse is considered and evaluated as the minimum value between the 40% of the displacement for which the spectral acceleration becomes null and the displacement corresponding to locally incompatible situations, according to the stability of the elements.

6.2.1. Linear kinematic analysis

The verification by using linear kinematic analysis consists in verify that the acceleration that activates the collapse mechanism is higher than the peak seismic acceleration demand (Circolare 2 febbraio n 617 2009). For this verification, both the SLS and ULS have to be taken into account.

6.2.1.1. Damage Limit State

If the collapsing macroblock is imposed on the ground surface, the verification is satisfied if

$$a_o^* \geq a_g\left(P_{V_r}\right)S \tag{102}$$

where $a_g\left(P_{V_r}\right)$ is the peak ground acceleration, evaluated on the exceedance probability of the chosen limit state and S is the soil coefficient.

If the collapsing macroblock is imposed at height *h* different from zero, the verification is satisfied if

$$a_o^* \geq S_e(T_1)\,\psi(z)\gamma \tag{103}$$

where $S_e(T_1)$ is the elastic spectrum calculated for the period T_1, and it is associated with the first modal shape of the structure, $\psi(z) = z/H$ is the approximated first modal shape of the structure on the considered vibration direction, normalized over the top storey (*z* is the height from the foundation of the centroid of the restraints and *H* is the height of the collapsing resultant from the foundation) and *γ* is the modal participation factor relate to the approximated first modal shape, taken as *3N/(2N+1)*, where *N* in the number of storey of the structure.

6.2.1.2. Life Safety Limit State

It is a simplified verification in which it is more restrictive due to the use of a behavior factor, q.

If the collapsing macroblock is imposed on the ground surface, the verification is satisfied if:

$$a_o^* \geq \frac{a_g(P_{V_r})S}{q} \tag{104}$$

If the collapsing macroblock is imposed at height, *h*, different from zero, the verification is satisfied if:

$$a_o^* \geq \frac{a_g(P_{V_r})\psi(z)\gamma}{q} \tag{105}$$

The behavior factor, *q*, can be assumed equal to 2 (Circolare 2 febbraio n 617 2009).

6.2.2. Non linear kinematic analysis

In this case the verification takes into account the spectral displacements that the structure can withstand before collapsing, considering only the life safety limit state; the verification will then be satisfied if the displacement capacity of the structure is higher than the ultimate displacement demand coming from the seismic input (Circolare 2 febbraio n 617 2009). For this particular verification, two different capacity curves have to be defined: in one instance, all the forces acting on the macroblock, even if not persistent until the collapse (e.g. pushing rafters, unknown stresses of tie-rods, curve (a) Figure 99), in the other case all the acting and persistent forces (block self weight, constant weights, curve (b) Figure 99).
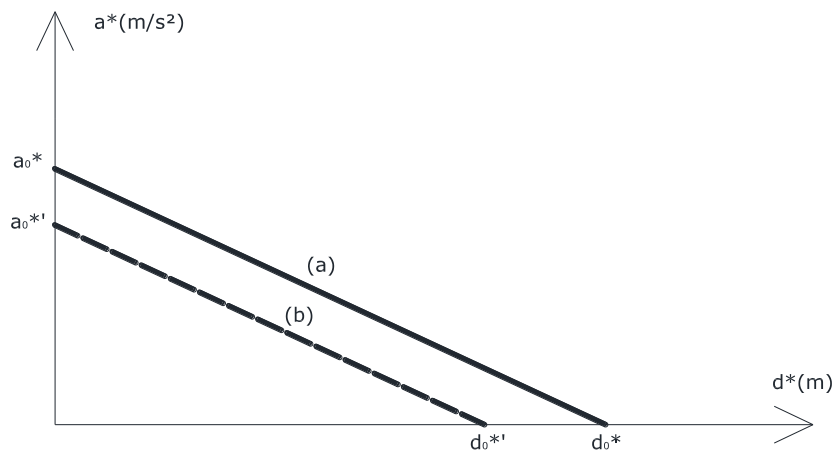
Figure 99 Capacity curve.

On the capacity curve of the persistent forces, the ultimate displacement d_u^* is evaluated as the displacement corresponding to a null spectral acceleration. From this, the capacity of the system is defined as the 40% of the ultimate displacement:

$$d_u^* = 0.40 d_0^* \tag{106}$$

This value is taken as the maximum displacement the rigid block can withstand keeping an equilibrium configuration in a near collapse condition. The displacement demand is obtained from the Acceleration Response Spectrum (ADRS), in correspondence to the so-called secant period T_s, to which coincides a secant displacement d_s. According to statistical considerations conducted on non linear dynamic analyses of masonry elements subjected to different accelerograms (Lagomarsino & Magenes 2009), this secant displacement has

seen to be approximately the 50% of the system capacity. The (Circolare 2 febbraio n 617 2009) valuates that as

$$d_s^* = 0.40 d_u^*$$ (107)

Once these parameters are defined, the secant period is given as

$$T_s = 2\pi\sqrt{d_s^*/a_s^*}$$ (108)

where $a_s^* = a(d_s^*)$ is the acceleration corresponding to d_s^* on the ADRS spectrum. In Figure 100, a graphical sketch of how the non linear verification is made is reported, with the comparison between the elastic spectrum and the capacity curve.
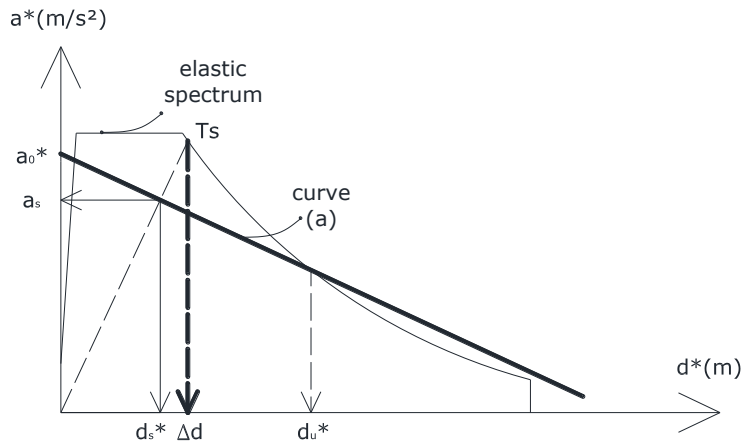
Figure 100 Non linear kinematic verification of a collapse mechanism.

If the collapsing macroblock is imposed on the ground surface, the verification is satisfied if

$$d_u^* = S_{D_e}(T_s)$$ (109)

where $S_{D_e}(T_s)$ is the elastic response spectra in terms of displacement ADRS, evaluated as the secant period.

If the collapsing macroblock is imposed at height different from zero, the verification is satisfied if

$$d_u^* \geq S_{D_e}\psi(z)\gamma \frac{(T_s/T_1)^2}{\sqrt{\left(1 - \frac{T_s}{T_1}\right)^2 + 0.02\frac{T_s}{T_1}}}$$ (110)

where $T_1 \cong 0.05H^{3/4}$ is the approximated period of the first modal shape of the structure.

6.3 Case study: design of strengthening interventions

The design of strengthening interventions have been made for two different historical masonry buildings both located in Modena: San Barnaba Church and Luciano Pavarotti Theatre.

6.3.1. Mechanical properties of the components

6.3.1.1. Masonry

The mechanical characteristics of masonry are obtained from several surveys performed on the buildings according to (Circolare 2 febbraio n 617 2009) and reported in Table 34 (f_c is the mean compressive strength, f_t is the mean tensile strength, τ is the mean shear strength, E is the elastic modulus, μ_0 is the friction coefficient,

153

γ_w is the specific weight, f_{cd} is the design compressive strength, τ_d is the design shear strength and μ_d is the design friction coefficient considering a confidence factor, *FC*, equal to 1.35).

Table 34 Mechanical characteristics of masonry.

f_c	[MPa]	$2.4 \div 4.0$
f_t	[MPa]	0.3
τ	[MPa]	0.06
E	[MPa]	3000
μ_0	[-]	0.4
γ_w	[kN/m^3]	18
$f_{cd} = \dfrac{f_m}{FC}$	[MPa]	3
$\tau_d = \dfrac{\tau}{FC}$	[MPa]	0.05
$\mu_d = \dfrac{\mu_m}{FC}$	[-]	0.30

In order to take into account the presence of some voids (in italian "false aperture"), the weight of the wall is evaluated according to Eq.(111)

$$P_{eff} = A_{projected}\gamma_m T \tag{111}$$

where P_{eff} is the effective weight of the wall, $A_{projected}$ is the projected area, γ_m is the specific weight and *T* is the nominal thickness of the wall assumed equal to 0.6MPa.

6.3.1.2. Soil of foundation

The soil of Piazza Grande in Modena belongs to C category and is characterized by a limit pressure in undrained conditions equal to

$$p_{lim,und} = 0.714 \, MPa \tag{112}$$

6.3.1.3. Strengthening materials

6.3.1.3.1. Stainless Steel flat product

The stainless steel AISI 304 is used and has the geometric and mechanical properties reported in Table 35 (t_s is the thickness of the steel lamina, f_y is the yield strength, f_t is the tensile strength and f_{yd} design yielding strength).

Table 35 Geometric and mechanical properties of the stainless steel flat product.

t_s	[mm]	4
f_y	[MPa]	230
f_t	[MPa]	540
$f_{yd} = 0.8f_y$	[MPa]	184

6.3.1.3.2. FRCM (Fabric Reinforced Cementitious Matrix)

Two different types of FRCM have been used in the design of the strengthening interventions: the fabric GeoSteel G600 with GeoCalce as epoxy resin or GeoSteel G2000 with Geolite as resin.

The geometric and mechanical properties of the fabric is reported in Table 36 (t_f is equivalent thickness of the fabric, f_t is the tensile strength, *E* is the elastic modulus and ε_u is the ultimate elongation).

Table 36 Geometric and mechanical properties of the fabric.

		G600	G2000
t_f	[mm]	0.084	0.254
f_t	[MPa]	>2800	>2800
E	[GPa]	>190	>190
ε_u	[%]	>1.5	>1.5

In order to ensure the connection between the FRCM system and the masonry substrate, connectors (in Italian connettore a fiocco) have been used.

In Table 37, the maximum load carried out by connectors from technical sheet, *T*, is reported.

Table 37 Mechanical properties of the connectors.

		G600	G2000
T	[kN]	>35	>70

Debonding force

The debonding force of the FRCM from the masonry substrate considering the presence of the connectors can be calculated by using Eq.(113)

$$F'_{max} = \sqrt{N_0^2 + F'_{0max}}$$ (113)

with N_0 is the maximum pull - out force of the connector evaluated by using Eq.(114) and F'_{omax} is the contribution of the fabric.

$$N_0 = A_{eff} E \frac{\varepsilon_u}{c_{ct}}$$ (114)

where A_{eff}, E, ε_u are the effective area, the elastic modulus and the breaking elongation of the connector, respectively and c_{ct} is the reduction factor due to bending of the wires composing the connector.

The effective area is defined as the 30% or 40% of the area of the connector in order to exclude the overlapping area of the textile. Assuming a width of the fabric wrapped equal between 100 and 150mm and considering that the connector is made of GeoSteel G600 or GeoSteel G2000, substituting the numerical values, it is possible to evaluate maximum pull – out force:

$$A_{eff,G600} = 0.30 \cdot 150 \cdot 0.084 = 12.6 \; mm^2$$ (115)

$$N_{0,G600} = 12.6 \cdot 190000 \frac{0.015}{1.50} = 7220 \; N \cong 7 \; kN$$ (116)

$$A_{eff,G2000} = 0.40 \cdot 100 \cdot 0.254 = 25.4 \; mm^2$$ (117)

$$N_{0,G2000} = 25.4 \cdot 190000 \frac{0.015}{1.50} = 18821 \; N \cong 19 \; kN$$ (118)

The debonding force of the FRCM from the masonry substrate without connectors can be estimated by using the formula presented in (Consiglio Nazionale delle Ricerche 2013), Eq.(119)

$$F'_{0max} = \sqrt{2b_f^2 E_f t_f G_f}$$ (119)

where b_f is the width (assumed equal to 300 mm), E_f is the elastic modulus, t_f is the equivalent thickness of the fabric, respectively and G_f is the specific fracture energy of the brick assumed equal to 0.024 Nmm^{-1}. Substituting the numerical values

$$F'_{0max,G600} = b_f\sqrt{2E_f t_f G_f} = 300\sqrt{2 \cdot 190000 \cdot 0.084 \cdot 0.024} = \sqrt{68947200} = 8300 \ N \qquad (120)$$

$$F'_{0max,G2000} = b_f\sqrt{2E_f t_f G_f} = 300\sqrt{2 \cdot 190000 \cdot 0.254 \cdot 0.024} = \sqrt{208200000} = 14438 \ N \qquad (121)$$

Considering the presence of both fabric and connectors, Eq.(113) can be applied

$$F'_{max,G600} = \sqrt{7220^2 + 68947200} = 11000 \ N = 11 \ kN \qquad (122)$$

$$F'_{max,G2000} = \sqrt{18821^2 + 208200000} = 23715 \ N = 20 \ kN \qquad (123)$$

Effective length

The effective length of GeoSteel G 600 is calculated using the Eq.(124)

$$L_{eff} = \sqrt{\frac{E_f \cdot t_f \cdot 1(mm)}{2 \cdot f_t}} \qquad (124)$$

with f_t mean tensile strength of the substrate (considering 1/10 of mean design compressive strength of masonry). Substituting the numerical values:

$$L_{eff,G600} = \sqrt{\frac{190000 \cdot 0.084 \cdot 1}{2 \cdot 0.3}} \cong 163 \ mm \cong 16 \ cm \qquad (125)$$

$$L_{eff,G2000} = \sqrt{\frac{190000 \cdot 0.254 \cdot 1}{2 \cdot 0.3}} \cong 280 \ mm \cong 28 \ cm \qquad (126)$$

6.3.1.3. Evaluation of the demand

According to (D.M. 14 Gennaio 2008), the seismic design action for the life safety limit state is evaluated. The design spectrum is defined as

$$S_d(T) = \begin{cases} \frac{a_g S F_0}{q}\left[\frac{T}{T_B} + \frac{q}{F_0}\left(1 - \frac{T}{T_B}\right)\right] & if \ 0 \leq T < T_B \\ a_g S \frac{1}{q} F_0 & if \ T_B \leq T < T_C \\ a_g S \frac{1}{q} F_0 \frac{T_C}{T} & if \ T_C \leq T < T_D \\ a_g S \frac{1}{q} F_0 \frac{T_C T_D}{T^2} & if \ T_D \leq T \end{cases} \qquad (127)$$

where

$a_g = 0.190g$ is the design ground acceleration, relatively to an exceedance probability of 10% in the reference period of the limit state considered;

S is the soil factor;

$F_0 = 2.437$ is the amplification factor, relatively to an exceedance probability of 10% in the reference period of the limit state considered;

156

$q = 2.25$ is the behavior factor for masonry structure made by bricks without reinforcement. For the reinforced masonry structure by using steel wires, the behavior factor can be increased until 2.70, according to (D.M. 14 Gennaio 2008);

T_B is the lower limit of the period of the constant spectral acceleration branch;

T_C is the upper limit of the period of the constant spectral acceleration branch;

T_D is the value defining the beginning of the constant displacement response range of the spectrum.

The reference period is defined as

$$V_R = V_N C_U = 50 \cdot 1.5 = 75 \; years \tag{128}$$

where:

$V_N = 50 \; years$ the nominal life of the structure;

$C_U = 1.5$ in italian "coefficiente d'uso (classe IIII: affollamenti significativi)".

The return period associated to an exceedance probability of 10% in 75 years is

$$T_R = 9.5 \cdot V_R = 712 \; years \tag{129}$$

that corresponds to a peak ground acceleration (considering as a site Modena, Piazza Grande, latitude: 44°.64601580, longitude: 10°.92584520)

$$a_g = 0.190g \tag{130}$$

Considering that the soil belongs to a C category, the site response parameter is calculated as

$$S = S_S S_T \tag{131}$$

where

$S_S = 1 \leq 1.7 - 0.6\dfrac{F_0}{a_g} \leq 1.5 = 1.422$ is the stratigraphic coefficient;

$S_T = 1$ is the topographic coefficient.

The period T_c is defined as

$$T_C = C_C T_C^* = 0.457 \; s \tag{132}$$

with

$$T_C^* = 0.289 \; s$$

$$C_C = 1.05 T_C^{*-0.33} = 1.582$$

The period T_B is defined as

$$T_B = \frac{T_C}{3} = 0.152 \; s \tag{133}$$

The period T_D is defined as

$$T_D = 1.6 + 4\frac{a_g}{g} = 2.361 \; s \tag{134}$$

In Figure 101, the elastic response spectrum (Figure 101a) and the design response spectrum calculated by using behavior factor $q = 2.25$ (Figure 101b) are reported.
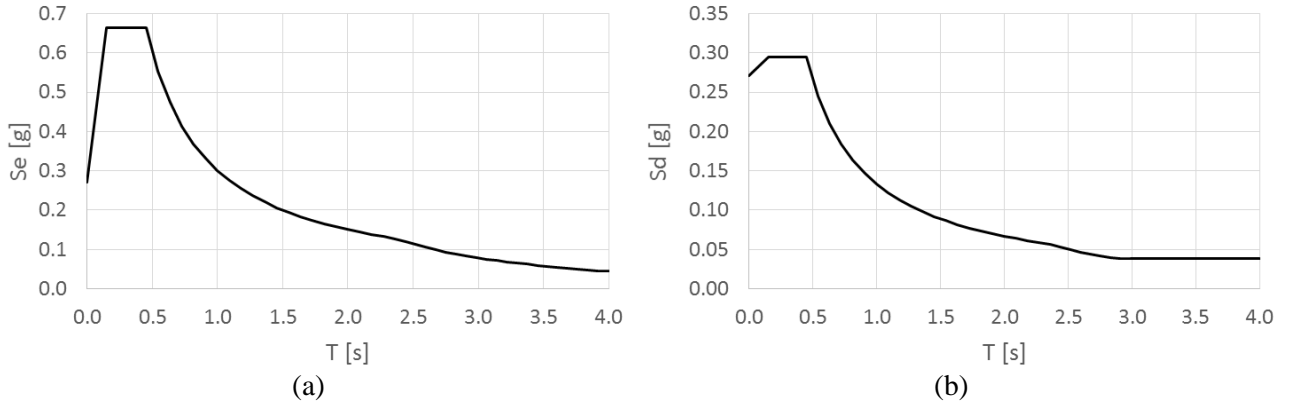
Figure 101 a) Elastic response and b) design response spectra.

Summarizing, the main steps for the calculation of the demand for a specific site are: (*i*) calculation of the elastic response spectrum (q = 1), (*ii*) calculation of the design response spectrum considering a behavior factor q = 2.25 for the unreinforced structure and q = 2.70 for the reinforced structure, (*iii*) magnification of 10% of the peak ground acceleration corresponding to the first period of vibration.

$$a_D^* = 1.1 S_D(T_1, 2.25) = 0.322 \, g \tag{135}$$

In the case of strengthened masonry

$$a_D^* = 1.1 S_D(T_1, 2.70) = 0.268 \, g \tag{136}$$

In the following, six different partial local mechanisms have been studied.

6.3.1.4 Evaluation of the capacity

During the evolution of the collapse mechanism, the macro – element is considered made of several rigid blocks separated one from each other by cylindrical hinges. At each block, the following forces are applied: *i*) weight load, and ii) horizontal load proportional of the weight load through the λ multiplier. The expression of the λ multiplier can be written as

$$\lambda = -\frac{\sum_{i=1}^{n} P_i \eta_i}{\sum_{i=1}^{n} P_i \delta_i} \tag{137}$$

with

n is the number of vertical forces applied;

P_i is the *i*-th vertical force;

η_i is the virtual vertical displacement of the application point of P_i as regard to the collapse mechanism under consideration;

δ_i is the virtual horizontal displacement of the application point of P_i as regard to the collapse mechanism under consideration.

The effective multiplier of the load, λ_c, is the minimum between all the possible ones. At this point, the spectral acceleration that activates the mechanism can be calculated as

$$a_0^* = \frac{\lambda_c g}{e^* FC} \tag{138}$$

where *FC* is the confidence factor, equal to 1.35 for masonry characterized by an infinite compressive strength, and e^* is the fraction of participating mass calculated as

158

$$e^* = \frac{gM^*}{P_{tot}} \qquad M^* = \frac{1}{g\sum_{i=1}^{n} P_i \delta_i^2}\left(\sum_{i=1}^{n} P_i \delta_i\right)^2 \tag{139}$$

with M^* the participating mass to the mechanism and P_{tot} the total weight of the masses involved in the collapse mechanism.

Eq.(138), can be used by putting FC equal to 1 in the case of masonry with finite compressive strength.

6.3.2. San Barnaba Church in Modena

In Figure 102, a picture of the church is reported.

Figure 102 San Barnaba Church in Modena.

6.3.2.1. Geometric scheme

In Figure 103, the geometric scheme of the San Barnaba Church is reported.
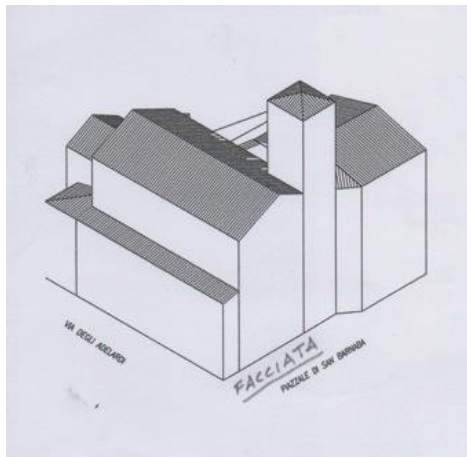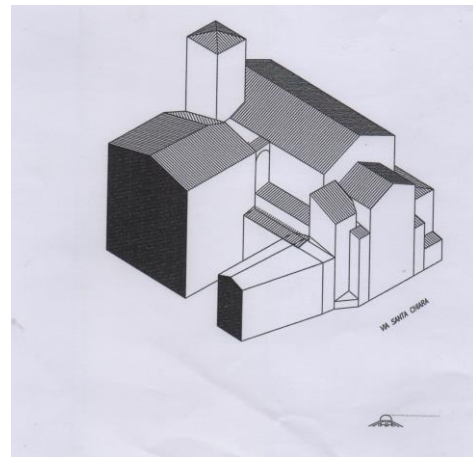
(a) Front side   (b) Rear side

Figure 103 Geometric scheme of San Barnaba Church in Modena.

6.3.2.2. Collapse mechanisms analyzed

For each macro – element considered, two collapse mechanisms have been studied: the first one "in plane" and the second one "out of plane".

6.3.2.2.1. Macro - element: lateral wall

Mechanism 1 (out of plane)

The mechanism analyzed (Figure 104a) is an out of plane mechanism that involves the lateral wall of the church. The vertical cylindrical hinges involved in the mechanism are three: two in the correspondence of the

159

pilasters (in Italian paraste) and one in the middle along the axis of the window. The centroids of the participating masses are positioned at 15 m height from the soil and the thickness of the wall is approximated equal to 0.6m.
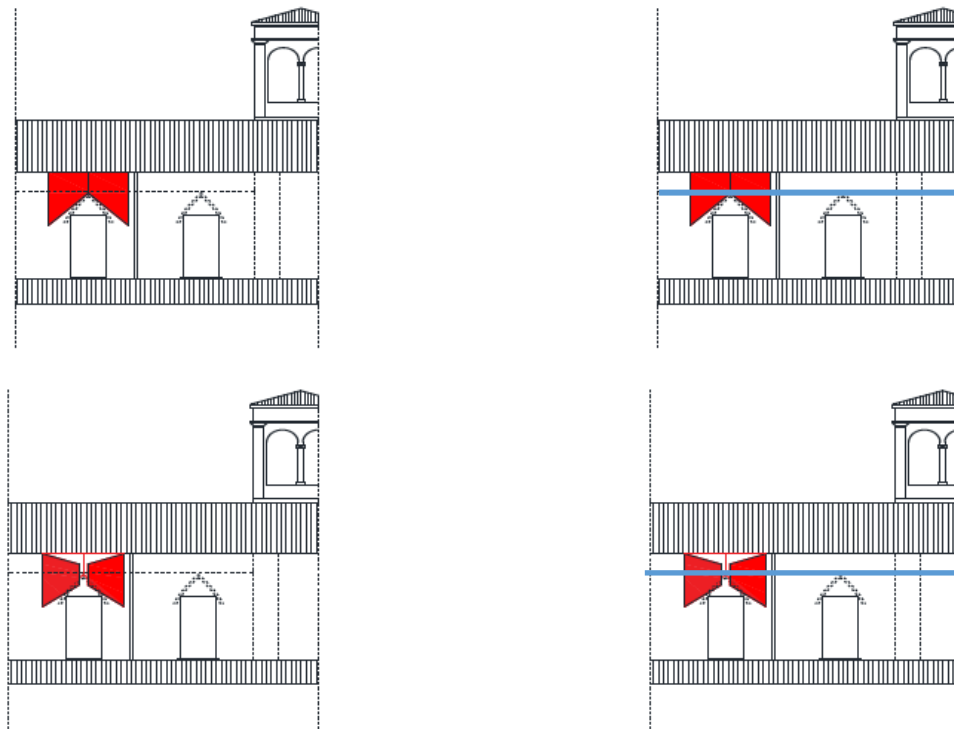
| (a) Mechanism analyzed | (b) Strengthening interventions |

Figure 104 Lateral wall: mechanism 1 (out of plane).

By using Eq.(137), the value of the λ_1 multiplier of the unstrengthened wall is equal to 0.296 and the ratio between the capacity and the demand, R, is 0.68 means unsafety. For this reason, a strengthening intervention has been designed. In particular a folded - steel beam (AISI 304) with a "L" shape 200 x 200 mm with a thickness of 5 mm positioned in the internal side of the wall, (Figure 104b). After the strengthening intervention, the value of the λ_1 multiplier increases, and the value of the capacity/demand ratio, R', becomes 2.62 means safe condition.

Mechanism 2 (in plane)

The mechanism analyzed (Figure 105a) is an in plane mechanism that involves the lateral wall of the church. The inclined crack considered starts from the roof and arrives until the upper part of the window. As before, the thickness of the wall is approximated equal to 0.6m.

(a) Mechanism analyzed   (b) Strengthening interventions

Figure 105 Lateral wall: mechanism 2 (in plane).

By using Eq.(137), the value of the λ_2 multiplier of the unstrengthened wall is equal to 1.87 and the ratio between the capacity and the demand, R, is 4.44 means safety. Due to the presence of a folded - steel beam (AISI 304) designed for the mechanism (Figure 105b), the value of the λ_2 multiplier increases, and the value of the capacity/demand ratio, R', becomes 33.5.

6.3.2.2.2. Macro - element: façade

Mechanism 3 (out of plane)

The mechanism analyzed (Figure 106) is an out of plane mechanism that involves the tympanum of the façade of the church. Due to the fact that in the past one lateral side of the tympanum has been connected to one lateral side of the bell tower, the a right triangle has been considered as geometric scheme for the calculation. As before, the thickness of the wall is approximated equal to 0.6m.
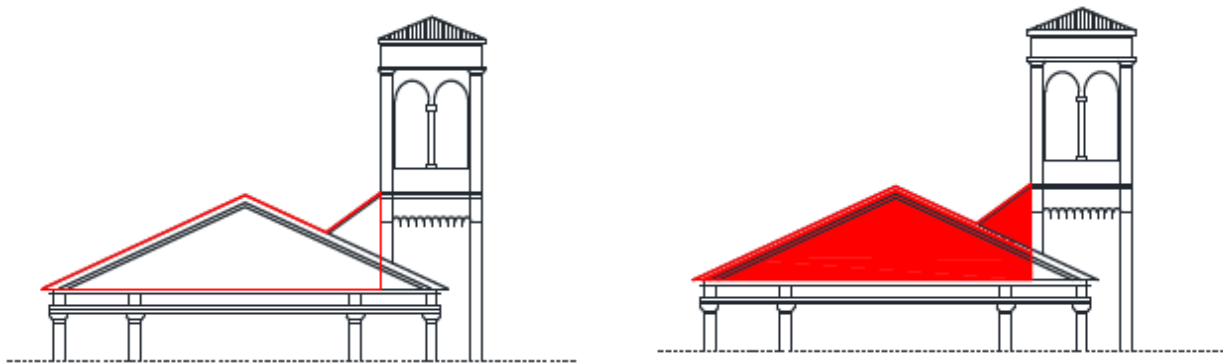
Figure 106 Façade: mechanism 3 (out of plane).
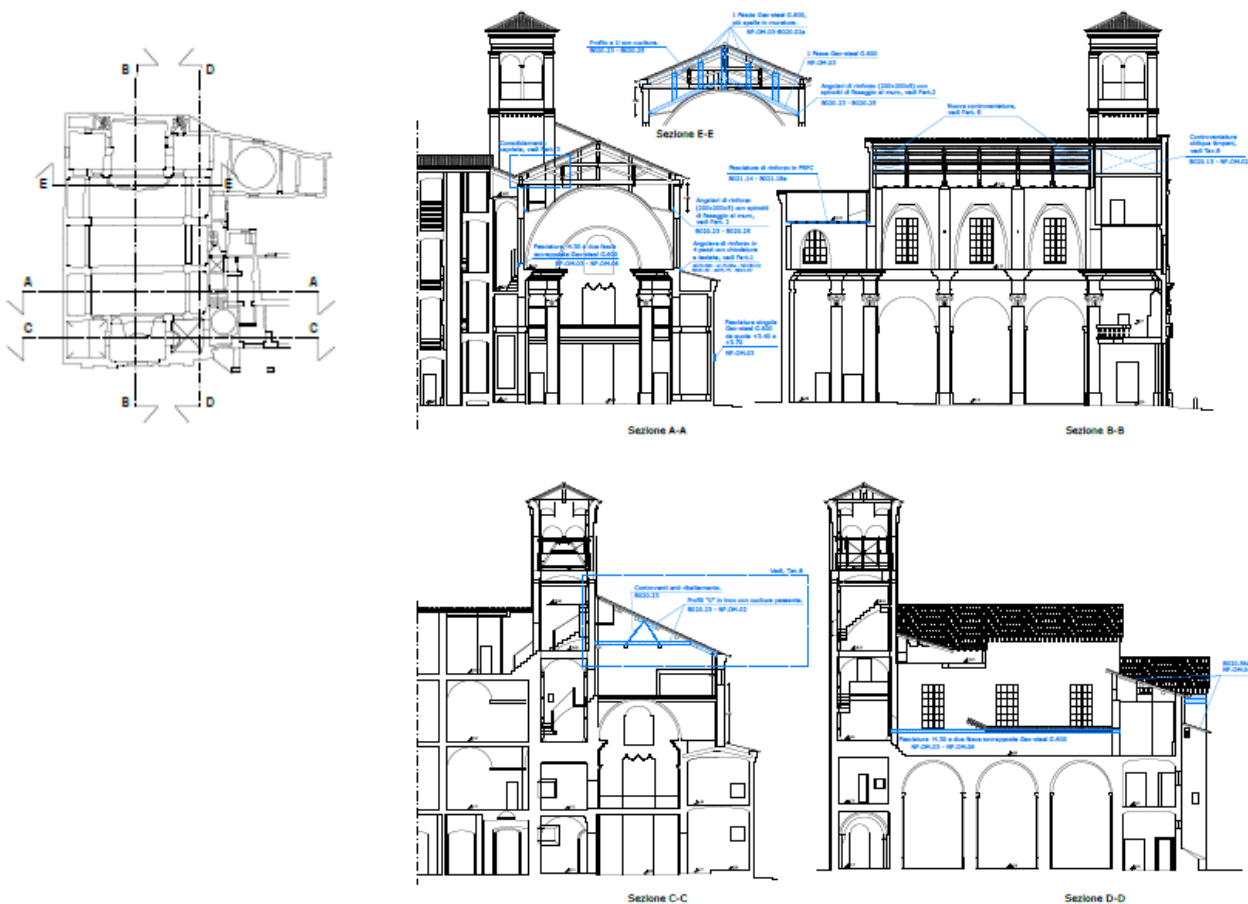
Figure 107 Façade: mechanism 3 (out of plane): strengthening intervention.

By using Eq.(137), the value of the λ_3 multiplier of the unstrengthened wall is equal to 0.257 and the ratio between the capacity and the demand, R, is 0.84 means unsafety. For this reason, a strengthening intervention has been designed. In particular one lateral bracing system and one horizontal bracing system are applied on the tympanum together with G600 steel strip (Figure 107). After the strengthening intervention, the value of the λ_3 multiplier increases, and the value of the capacity/demand ratio, R', becomes 2.84 means safe condition.

Mechanism 4 (in plane)

The mechanism analyzed (Figure 108a) is an in plane mechanism that involves the façade of the church. The inclined crack considered starts from the top right corner of the window positioned and goes to the top left corner of the main door. As before, the thickness of the wall is approximated equal to 0.6m.
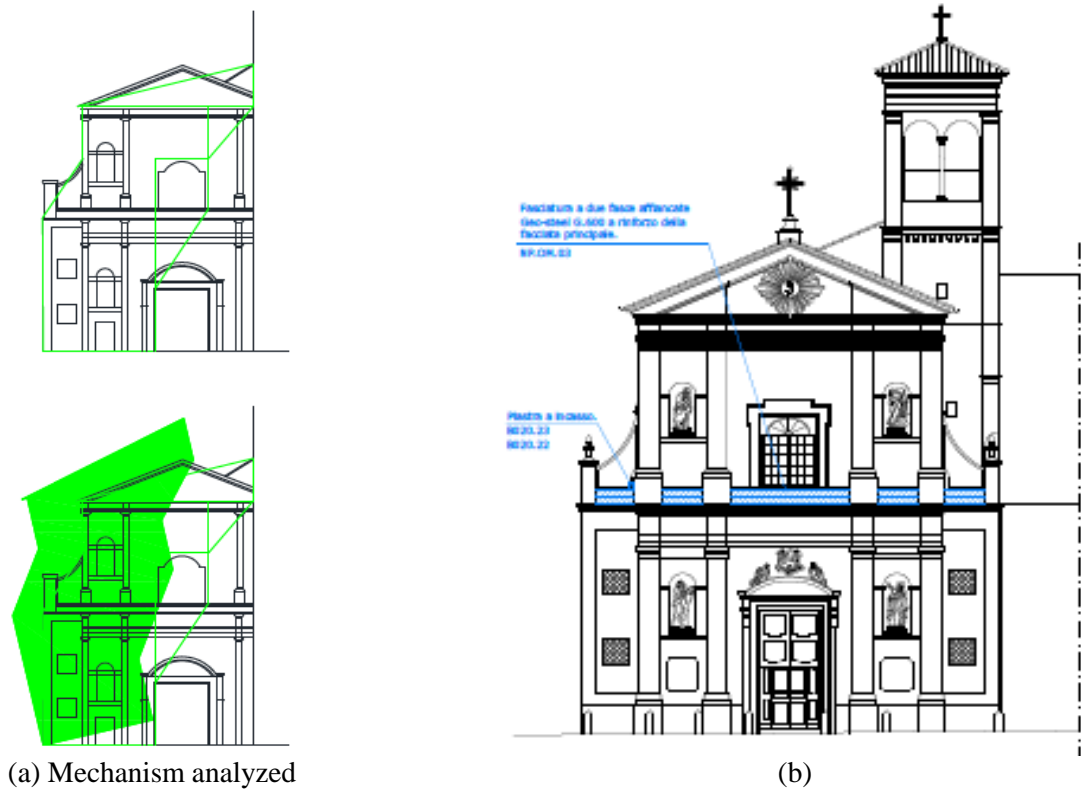
<table>
<tr><td>(a) Mechanism analyzed</td><td>(b)</td></tr>
</table>

Figure 108 Façade: mechanism 4 (in plane).

By using Eq.(137), the value of the λ_4 multiplier of the unstrengthened wall is equal to 0.55 and the ratio between the capacity and the demand, R, is 1.675 means safety. Due to the presence of three G600 steel strips, one below the tympanum and two at the base of the window (Figure 108b), the value of the λ_4 multiplier increases, and the value of the capacity/demand ratio, R', becomes 2.102.

6.3.2.2.3. Macro - element: rear wall of the apse

Mechanism 5 (out of plane)

The mechanism analyzed (Figure 109a) is an out of plane mechanism that involves the overturning of the rear wall of the apse and, consequently, the lateral walls of the church. For safety reasons, the action of the roof, that is stabilizing, is not considered in the calculation As before, the thickness of the wall is approximated equal to 0.6m.
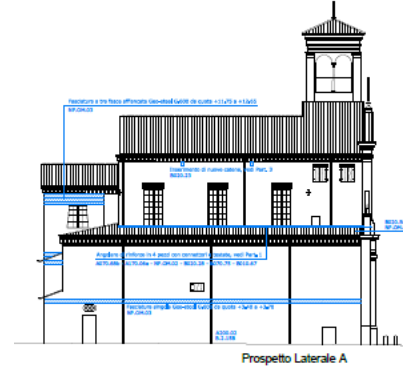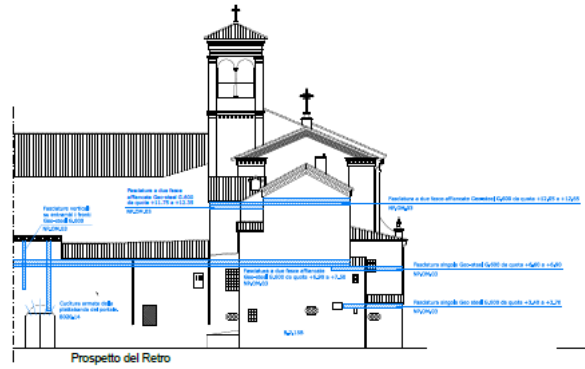
| (a) Mechanism analyzed | (b) Strengthening interventions |

Figure 109 Rear wall of the apse: mechanism 5 (out of plane).

By using Eq.(137), the value of the λ_5 multiplier of the unstrengthened wall is equal to 0.129 and the ratio between the capacity and the demand, R, is 0.33 means unsafety. For this reason, a strengthening intervention has been designed. In particular three G600 steel strips for each side means six strips are applied on the rear wall of the church (Figure 109b). After the strengthening intervention, the value of the λ_5 multiplier increases, and the value of the capacity/demand ratio, R', becomes 1.062 means safe condition.

Mechanism 6 (in plane)

The mechanism analyzed (Figure 110a) is an in plane mechanism that involves the rear wall of the apse. The inclined crack considered starts from the right corner positioned in the upper part and arrives until the first slab in the lateral side. As before, the thickness of the wall is approximated equal to 0.6m.

(a) Mechanism analyzed

(b) Strengthening interventions

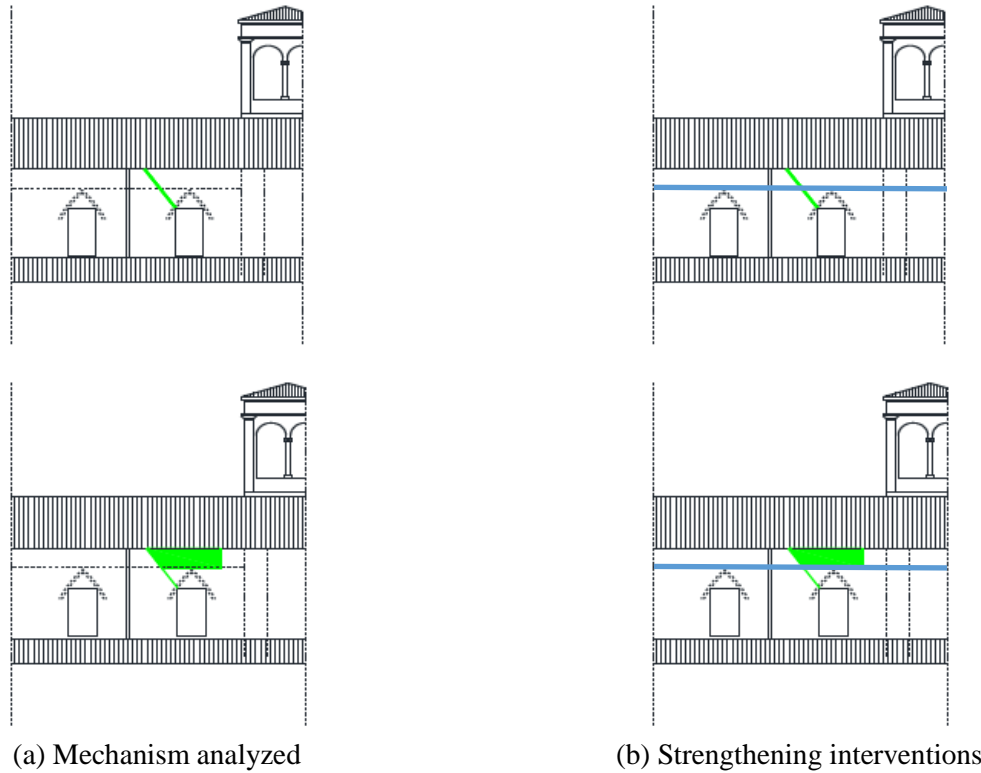Figure 110 Rear wall of the apse: mechanism 6 (in plane).

By using Eq.(137), the value of the λ_6 multiplier of the unstrengthened wall is equal to 0.598 and the ratio between the capacity and the demand, R, is 1.375 means safety. Due to the presence of three G600 steel strips, (Figure 110b), the value of the λ_6 multiplier increases, and the value of the capacity/demand ratio, R', becomes 2.155.

6.3.3. Luciano Pavarotti Theatre in Modena

In Figure 111, a picture of the theatre is reported.

Figure 111 Luciano Pavarotti Theatre in Modena.

6.3.3.1. Geometric scheme

In Figure 112, the geometric scheme of the Luciano Pavarotti Theatre is reported.

165

(a) Front side   (b) Rear side

Figure 112 Geometric scheme of San Barnaba Church in Modena.

6.3.3.2. Collapse mechanisms analyzed

For each macro – element considered, two collapse mechanisms have been studied: the first one "in plane" and the second one "out of plane".

6.3.3.2.1. Mechanism 1 (out of plane)

The mechanism analyzed (Figure 113a) is an out of plane mechanism that involves the rear wall of the theatre. A vertical crack crosses the wall and the opening of the two side occurs.
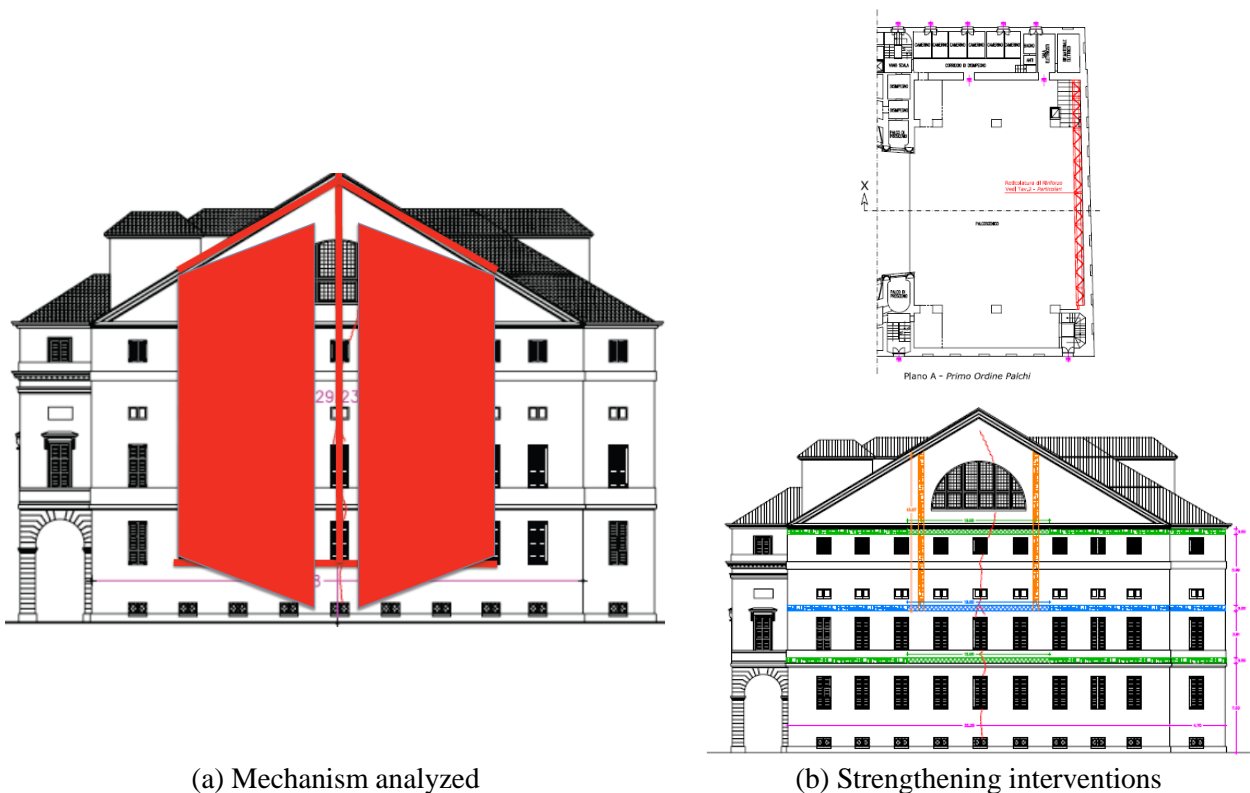
(a) Mechanism analyzed   (b) Strengthening interventions

Figure 113 Mechanism 1 (out of plane).

By using Eq.(137), the value of the λ_1 multiplier of the unstrengthened wall is equal to 0.30 and the ratio between the capacity and the demand, R, is 0.68 means unsafety. For this reason, a strengthening intervention has been designed. In particular, a steel beam (IPE 400) is positioned in the internal side of the wall, (Figure 113b), in combination with 12 FRCM G2000 external strips and 9 FRCM G2000 internal strips. After the

166

strengthening intervention, the value of the λ_1 multiplier increases, and the value of the capacity/demand ratio, *R'*, becomes 0.933.

6.3.3.2.2. Mechanism 2 (out of plane)

The mechanism analyzed (Figure 114a) is an out of plane mechanism that involves the overturning of the tympanum along a horizontal cylindrical hinge at the base of the semicircular window.

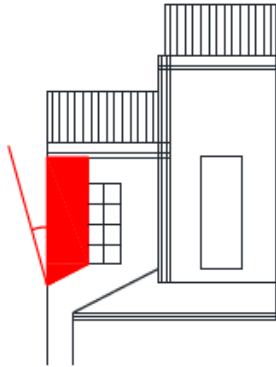(a) Mechanism analyzed   (b)) Strengthening interventions
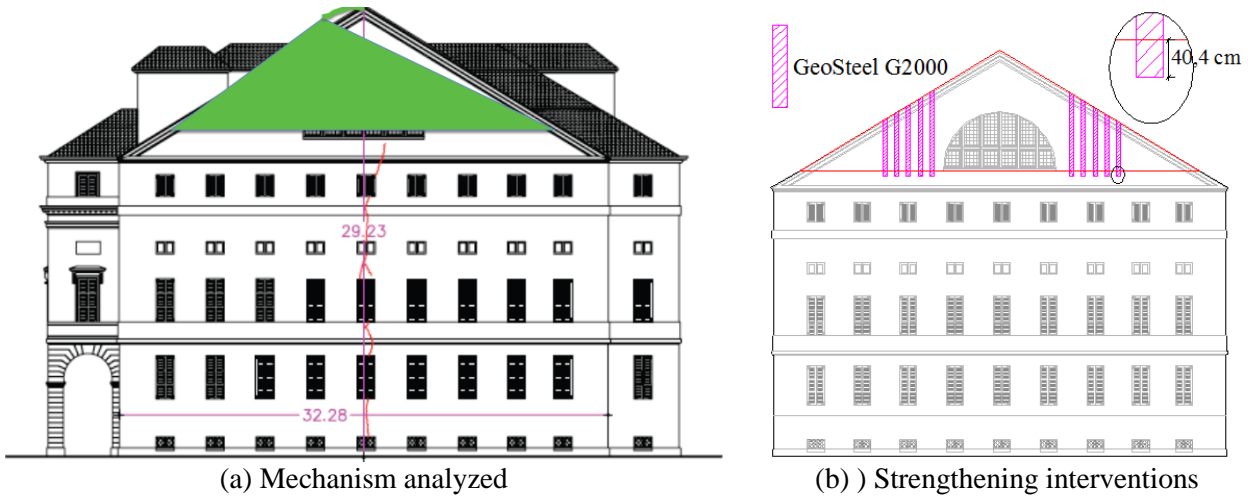
Figure 114 Mechanism 2 (out of plane).

By using Eq.(137), the value of the λ_2 multiplier of the unstrengthened wall is equal to 0.121 and the ratio between the capacity and the demand, *R*, is 0.279 means unsafety. For this reason, a strengthening intervention has been designed. In particular, 10 FRCM G2000 external strips are applied on the wall. After the strengthening intervention, the value of the λ_1 multiplier increases, and the value of the capacity/demand ratio, *R'*, becomes 0.407.

6.3.3.2.3. Mechanism 3 (out of plane)

The mechanism analyzed (Figure 115a) is an out of plane mechanism that involves the overturning along a horizontal hinge of a reduced area of the wall.

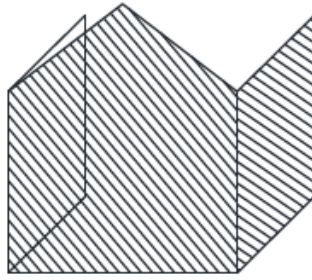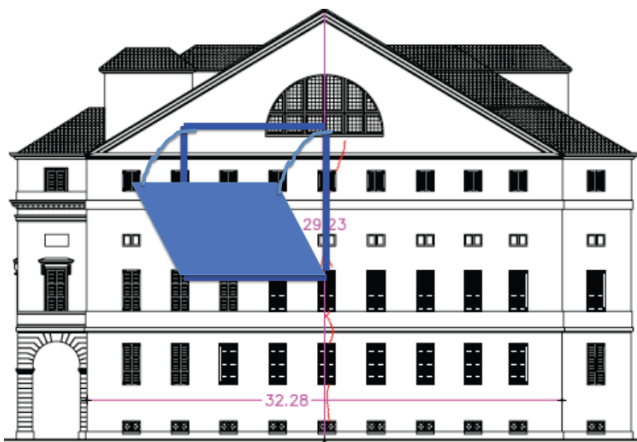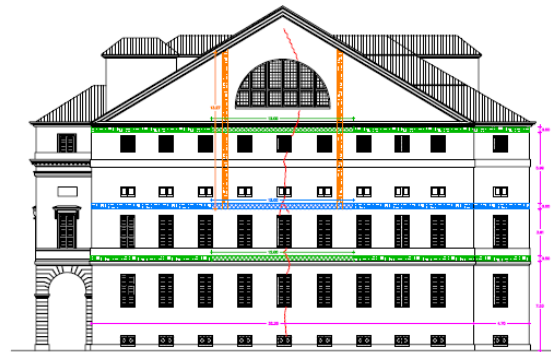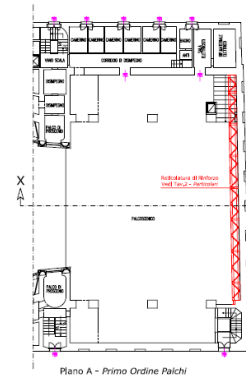(a) Mechanism analyzed   (b) Strengthening interventions

Figure 115 Mechanism 3 (out of plane).

By using Eq.(137), the value of the λ_3 multiplier of the unstrengthened wall is equal to 0.139 and the ratio between the capacity and the demand, R, is 0.485 means unsafety. For this reason, a strengthening intervention has been designed and is the same used to contrast the mechanism 1. After the strengthening intervention, the value of the λ_1 multiplier increases, and the value of the capacity/demand ratio, R', becomes 2.24.

6.4 Conclusions

In this Chapter the vulnerability of existing monuments is evaluated by using the local mechanism approach. From national and international codes, there are different procedures that can be used and that give different responses. This is mainly due to the use of several not objective coefficients (such as, confidence factor, behavior factor), that drive to a not unique answer in terms of safety evaluation.

Regarding the procedure via local mechanisms, the main aspect that has to be taken into account is the interaction of the blocks with surroundings structures that are difficult to evaluate (for example interaction between the main structure and the roof). Also, in the analytical evaluation of the mechanism, sometimes its evolution is not clear.

The application of FRCM to contrast the local mechanisms is effective but this topic is not completely covered by the codes or by the standard formulation. For example, if a Mode II mechanism occurs, the contrast can be done essentially by applying strip with mechanical connectors and the evaluation of their mode of operation and analytical modelling is not covered by standard formulation.

7. Chapter 7: Conclusions

In this work, an extended experimental campaign on masonry specimens reinforced by using repointing technique and FRCM system have been performed. In addition to experimental results, analytical and numerical models have been used to predict the behavior of strengthened masonry and, therefore, to develop simplify design tools. The repointing technique has been applied in the mortar joints of pre-cracked masonry specimens tested in compression while FRCM technology has been used for diagonal test set-up. As repointing materials, carbon wires and steel bars have been studied and no changes in the overall behavior of the samples have been observed. Two different FRCM systems have been used: one glass based and the second steel and basalt based. Two different test setups have been analyzed: a non uniform compression test for small masonry specimens made of clay bricks and a diagonal compression test for both small and large specimens constructed with clay bricks and hollow clay bricks. The novel aspect for the small specimens test is the presence of a pre-crack in the middle to simulate damage masonry wall. Instead, large specimens made of hollow clay bricks are characterized by the presence of only horizontal bed joints (no vertical head joints).

From the experimental campaign, it is possible to conclude that reinforcements produce advantages in terms of crack arrestors, ductility, load and displacement capacity. At the same time, a symmetric configuration of the strengthening system maximizes the structural performance of the specimens compared to asymmetric one. Repointing system is more effective in compression instead of diagonal configuration for which FRCM plating system is more effective. In addition, the presence of reinforcement modifies the mechanism of failure from brittle (without reinforcement) to ductile (with reinforcement).

8. Acknowledgments

9. References

ACI 549.4R-13, 2013. *Guide to Design and Construction of Externally Bonded Fabric-Reinforced Cementitious Matrix (FRCM) Systems for Repair and Strengthening Concrete and Masonry Structures*,

Acito, M. et al., 2014. Collapse of the clock tower in Finale Emilia after the May 2012 Emilia Romagna earthquake sequence: Numerical insight. *Engineering Structures*, 72(May 2012), pp.70–91. Available at: http://www.sciencedirect.com/science/article/pii/S0141029614002399.

Akhaveissy, A.H. & Milani, G., 2013. A numerical model for the analysis of masonry walls in-plane loaded and strengthened with steel bars. *International Journal of Mechanical Sciences*, 72, pp.13–27. Available at: http://www.sciencedirect.com/science/article/pii/S0020740313000787.

Almeida, J.A.P.P., Pereira, E.B. & Barros, J.A.O., 2015. Assessment of overlay masonry strengthening system under in-plane monotonic and cyclic loading using the diagonal tensile test. *Construction and Building Materials*, 94, pp.851–865. Available at: http://www.sciencedirect.com/science/article/pii/S0950061815300635.

ASTM D 7205, 2011. Standard Test Method for Tensile Properties of Fiber Reinforced Polymer Matrix Composite Bars. , 6.

ASTM E 519, 2002. Standard test method for diagonal tension (shear) in masonry addemblages. *ASTM International*, p.5.

Babaeidarabad, S., 2013. Masonry Walls Strengthened with Fabric- Reinforced Cementitious Matrix Composite Subjected to In-Plane and Out-of-Plane Load. , p.147. Available at: http://scholarlyrepository.miami.edu/oa_dissertations Recommended.

Babaeidarabad, S. et al., 2014. Out-of-Plane Behavior of URM Walls Strengthened with Fabric-Reinforced Cementitious Matrix Composite. *Asce*, 549(2013), pp.1–11.

Bednarz, Ł.J. et al., 2014. Strengthening and long-term monitoring of the structure of an historical church presbytery. *Engineering Structures*, 81, pp.62–75.

Bernat, E. et al., 2013. Experimental and analytical study of TRM strengthened brickwork walls under eccentric compressive loading. *Construction and Building Materials*, 44, pp.35–47. Available at: http://linkinghub.elsevier.com/retrieve/pii/S0950061813002079.

Binda, L. et al., 2006. Vulnerability analysis of the historical buildings in seismic area by a multilevel approach. *Asian Journal of Civil Engineering (Building and Housing)*, 7(4), pp.343–357.

Borri, A., Corradi, M., et al., 2015. A method for the analysis and classification of historic masonry. *Bulletin of Earthquake Engineering*, 13(9), pp.2647–2665.

Borri, A. et al., 2011. Shear behavior of unreinforced and reinforced masonry panels subjected to in situ diagonal compression tests. *Construction and Building Materials*, 25(12), pp.4403–4414. Available at: http://linkinghub.elsevier.com/retrieve/pii/S0950061811000237.

Borri, A., Castori, G. & Marco, C., 2015. Behavior of masonry columns repaired using small diameter cords. *Key Engineering Materials*, 624, pp.254–265.

Boscato, G. et al., 2014. Seismic Behavior of a Complex Historical Church in L'Aquila. *International Journal of Architectural Heritage*, 8(5), pp.718–757. Available at: http://www.scopus.com/inward/record.url?eid=2-s2.0-84894212839&partnerID=tZOtx3y1.

Brignola, A. et al., 2008. Identification of Shear Parameters of Masonry Panels Through the In-Situ Diagonal Compression Test. *International Journal of Architectural Heritage*, 3(March 2015), pp.52–73.

BS EN 845-1:2013, 2003. Specification for ancillary components for masonry — Part 1: Wall ties, tension straps, hangers and brackets. *Strategy*, 3(September 2013).

BS EN 846-7:2012, 2015. Methods of test for ancillary components for masonry. Part 7 : Determination of shear load capacity and load displacement characteristics of shear ties and slip ties (couplet test for mortar

joint connections).

BS EN ISO 6892-1:2009, 2015. Metallic materials — Tensile testing Part 1 : Method of test at ambient temperature.

Calderini, C., Cattari, S. & Lagomarsino, S., 2010. The use of the diagonal compression test to identify the shear mechanical parameters of masonry. *Construction and Building Materials*, 24(5), pp.677–685. Available at: http://dx.doi.org/10.1016/j.conbuildmat.2009.11.001.

Carozzi, F.G., Milani, G. & Poggi, C., 2015. Mechanical properties and numerical modeling of Fabric Reinforced Cementitious Matrix (FRCM) systems for strengthening of masonry structures. *Composite Structures*, 70, pp.215–230. Available at: http://dx.doi.org/10.1016/j.compstruct.2013.08.026.

Carozzi, F.G., Milani, G. & Poggi, C., 2014. Mechanical properties and numerical modeling of Fabric Reinforced Cementitious Matrix (FRCM) systems for strengthening of masonry structures. *Composite Structures*, 107, pp.711–725. Available at: http://linkinghub.elsevier.com/retrieve/pii/S0263822313004236.

Casacci, S., Angelo, D.T. & Gentilini, C., 2014. Reinforced Repointing Technique to Strengthen Masonry. In *Proceeding of the 2nd International Conference on Protection of Historical Constructions*. pp. 67–73.

Casacci, S., di Tommaso, A. & Gentilini, C., 2015. Crack Propagation in Compression and Mounted Arrestors. *Key Engineering Materials*, 624, pp.595–602. Available at: http://www.scientific.net/KEM.624.595.

Casacci, S., Di Tommaso, A. & Gentilini, C., 2016. Experimental investigation on pre-cracked masonry specimens repaired by bed joints structural repointing. In *Brick and Block masonry - Trends, Innovations and Challenges*. pp. 2047–2054.

Castellazzi, G., Gentilini, C. & Nobile, L., 2013. Seismic Vulnerability Assessment of a Historical Church : Limit Analysis and Nonlinear Finite Element Analysis. *Advances in Civil Engineering*.

Chamis, C.C., 1986. DESIGN CONCEPTS/PARAMETERS ASSESSMENT AND SENSITIVITY ANALYSES OF SELECT COMPOSITE STRUCTURAL COMPONENTS. *International Journal of Materials and Product Technology*, 1(2).

Circolare 2 febbraio n 617, 2009. *Istruzioni per l'applicazione delle "Nuove norme tecniche per le costruzioni" di cui al D.M. 14 Gennaio 2008*,

Consiglio Nazionale delle Ricerche, 2013. DT-200/2013 - Istruzioni per la progettazione, l'esecuzione ed il controllo di interventi di consolidamento statico mediante l'utilizzo di compositi fibrorinforzati.

Corradi, M. et al., 2008. Experimental evaluation of shear and compression strength of masonry wall before and after reinforcement: Deep repointing. *Construction and Building Materials*, 22(4), pp.463–472.

Cosenza, E. & Iervolino, I., 1997. SEISMIC PERFORMANCE IMPROVEMENT OF THE BELL TOWER IN SERRA S . QUIRICO BY COMPOSITES.

D.M. 14 Gennaio, 2008. *Norme Tecniche per le Costruzioni*,

D'Ambrisi, A., Focacci, F. & Caporale, A., 2013. Strengthening of masonry-unreinforced concrete railway bridges with PBO-FRCM materials. *Composite Structures*, 102, pp.193–204. Available at: http://dx.doi.org/10.1016/j.compstruct.2013.03.002.

D'Antino, T. et al., 2015. Experimental analysis of the bond behavior of glass , carbon , and steel FRCM composites. *Key Engineering Materials*, 624, pp.371–378.

Derkowski, W., 2015. Opportunities and Risks Arising from the Properties of FRP Materials Used for Structural Strengthening. *Procedia Engineering*, 108, pp.371–379. Available at: http://www.sciencedirect.com/science/article/pii/S1877705815011145.

EN 1015-11, 2007. Metodi di prova per malte per opere murarie Parte 11 : Determinazione della resistenza a flessione e a compressione della malta indurita.

EN 1052-3, 2007. Metodi di prova per muratura - Determinazione della resistenza iniziale a taglio.

EN 14580, 2013. Metodi di prova per pietre naturali. Detemrinazione del modulo elastico statico. , 44(0).

EN 196-1, 2011. Metodi di prova dei cementi Parte 1 : Determinazione delle resistenze meccaniche.

EN 1998-1, 2004. European Standard.

EN 772-1, 2010. Metodi di prova per muratura. , 4.

Fajfar, P., 2000. A Nonlinear Analysis Method for Performance - based Seismic Design. , pp.573–592.

Fajfar, P., 1999. Capacity spectrum method based on inelastic demand spectra. *Earthquake Engineering and Structural Dynamics*, 28(February), pp.979–993.

Foraboschi, P., 2004. Strengthening of Masonry Arches With Fiber Reinforced Polymer Strips. *Journal of Composites for Construction*, 8(3), pp.191–202.

Franzoni, E. et al., 2015. Compressive behaviour of brick masonry triplets in wet and dry conditions. *Construction and Building Materials*, 82, pp.45–52. Available at: http://linkinghub.elsevier.com/retrieve/pii/S0950061815001993.

Franzoni, E. et al., 2014. Towards the assessment of the shear behaviour of masonry in on-site conditions: A study on dry and salt/water conditiones brick masonry triplets. *Construction and Building Materials*, 65, pp.405–416. Available at: http://linkinghub.elsevier.com/retrieve/pii/S0950061815001993.

Garbin, E. et al., 2009. Compressive Behaviour of Brick Masonry Panels Strengthened With CFRP Bed Joints Reinforcement. *11th Canadian Masonry Symposium, Toronto, Ontario*.

Gattesco, N. & Boem, I., 2015. Experimental and analytical study to evaluate the effectiveness of an in-plane reinforcement for masonry walls using GFRP meshes. *Construction and Building Materials*, 88, pp.94–104. Available at: http://linkinghub.elsevier.com/retrieve/pii/S0950061815004481.

Gentilini, C. et al., 2012. Effect of salt crystallisation on the shear behaviour of masonry walls: An experimental study. *Construction and Building Materials*, 37, pp.181–189. Available at: http://dx.doi.org/10.1016/j.conbuildmat.2012.07.086.

Ghiassi, B. et al., 2013. Application of digital image correlation in investigating the bond between FRP and masonry. *Composite Structures*, 106, pp.340–349. Available at: http://dx.doi.org/10.1016/j.compstruct.2013.06.024.

Greszczuk, L.B., 1975. CONSIDERATION OF FAILURE MODES IN THE DESIGN OF COMPOSITE STRUCTURES. *AGARD Conf Proc*, (16).

Hashin, Z., 1972. THEORY OF FIBER REINFORCED MATERIALS. *NASA Contractor Reports*, (CR-1974).

Heyman, J., 1992. Leaning Towers.

Hillerborg, A., 1991. Application of the fictitious crack model to different types of materials. *International Journal of Fracture*, 51(2), pp.95–102.

Ismail, N. et al., 2011. Diagonal shear behaviour of unreinforced masonry wallettes strengthened using twisted steel bars. *Construction and Building Materials*, 25(12), pp.4386–4393. Available at: http://dx.doi.org/10.1016/j.conbuildmat.2011.04.063.

Ismail, N. & Ingham, J.M., 2012. In-situ and laboratory based out-of-plane testing of unreinforced clay brick masonry walls strengthened using near surface mounted twisted steel bars. *Construction and Building Materials*, 36, pp.119–128. Available at: http://linkinghub.elsevier.com/retrieve/pii/S0950061812002899.

Lagomarsino, S. & Magenes, G., 2009. *Evaluation and Reduction of the Vulnerability of Masonry Buildings*,

Li, T. et al., 2005. Analysis of unreinforced masonry concrete walls strengthend with glass fiber-reinforced polymer bars.

De Lorenzis, L., Dimitri, R. & La Tegola, A., 2007. Reduction of the lateral thrust of masonry arches and vaults with FRP composites. *Construction and Building Materials*, 21(7), pp.1415–1430. Available at:

http://linkinghub.elsevier.com/retrieve/pii/S0950061806001589.

De Lorenzis, L. & Nanni, A., 2001. Shear strengthening of reinforced concrete beams with near-surface mounted fiber-reinforced polymer rods. *ACI Structural Journal*, 98(1), pp.60–68.

De Lorenzis, L., Nanni, A. & Circle, M., 2004. INTERNATIONAL WORKSHOP ON PRESERVATION OF Final Report Submitted to : National Science Foundation (NSF) Submitted by : University of Lecce. , (July).

De Lorenzis, L. & Teng, J.G., 2007. Near-surface mounted FRP reinforcement: An emerging technique for strengthening structures. *Composites Part B: Engineering*, 38(2), pp.119–143.

Lourenço, P.B., 1996. *Computational strategies for masonry structures*, Available at: http://www.narcis.nl/publication/RecordID/oai:tudelft.nl:uuid:4f5a2c6c-d5b7-4043-9d06-8c0b7b9f1f6f.

Lourenco, P.B. & Rots, J.G., 1997. Multisurface interface model for analysis of masonry structures. *Journal of Engineering Mechanics*, 123(7), pp.660–668.

Magenes, G. & Calvi, G.M., 1997. In-plane seismic response of brick masonry walls. *Earthquake Engineering Structural Dynamics*, 26(11), pp.1091–1112. Available at: http://doi.wiley.com/10.1002/(SICI)1096-9845(199711)26:11%3C1091::AID-EQE693%3E3.0.CO;2-6.

Maragna, M., Casacci, S. & Gentilini, C., 2016. In-plane shear behaviour of masonry wall panels strengthened by structural repointing. , 1(3), pp.253–276.

Meier, U., 1995. Strengthening of structures using carbon fibre / epoxy composites. *Construction and Building Materials*, 9(6), pp.341–351.

Modena, C. et al., 2011. Structural aspects of the conservation of historic masonry constructions in seismic areas: Remedial measures and emergency actions. *International Journal of Architectural Heritage*, 5(November), pp.539–558.

Mojsilovic, N. & Salmanpour, A.H., 2016. Masonry walls subjected to in-plane cyclic loading : application of digital image correlation for deformation field measurement Nebojša Mojsilović * and Amir Hosein Salmanpour. *Int. J. Research and Innovation*, X(2), pp.165–187.

Oliveira, D. V. et al., 2012. Strengthening of three-leaf stone masonry walls: an experimental research. *Materials and Structures*, 45(8), pp.1259–1276. Available at: http://www.springerlink.com/index/10.1617/s11527-012-9832-3.

Oyarzo-Vera, C. & Griffith, M., 2009. The Mw 6.3 Abruzzo (Italy) earthquake of April 6th, 2009: on site observations. , 42(4), pp.302–307.

Papanicolaou, C.G. et al., 2007. Textile reinforced mortar (TRM) versus FRP as strengthening material of URM walls: out-of-plane cyclic loading. *Materials and Structures*, 41(1), pp.143–157.

Petersen, R.B., Ismail, NajifMasia, M.J. & Ingham, J.M., 2012. Finite element modelling of unreinforced masonry shear wallettes strengthened using twisted steel bars. *Construction and Building Materials*, 33, pp.14–24. Available at: http://dx.doi.org/10.1016/j.conbuildmat.2012.01.016.

Petzet, M., 1964. Principles of preservation. In pp. 7–29.

Quagliarini, E. et al., 2012. Tensile characterization of basalt fiber rods and ropes: A first contribution. *Construction and Building Materials*, 34, pp.372–380. Available at: http://dx.doi.org/10.1016/j.conbuildmat.2012.02.080.

Razavizadeh, A., Ghiassi, B. & Oliveira, D. V., 2014. Bond behavior of SRG-strengthened masonry units: Testing and numerical modeling. *Construction and Building Materials*, 64, pp.387–397. Available at: http://www.sciencedirect.com/science/article/pii/S0950061814003870.

RILEM, 1991. Diagonal tensile strength tests of small wall specimens.

Shrive, N.G., 2006. The use of fibre reinforced polymers to improve seismic resistance of masonry.

Construction and Building Materials, 20(4), pp.269–277.

Tetta, Z.C., Koutas, L.N. & Bournas, D.A., 2015. Textile-reinforced mortar (TRM) versus fiber-reinforced polymers (FRP) in shear strengthening of concrete beams. *Composites Part B: Engineering*, 77, pp.338–348. Available at: http://linkinghub.elsevier.com/retrieve/pii/S1359836815001742.

Tinazzi, D., Modena, C. & Nanni, A., 2000. Strengthening of masonry assemblages with FRP rods and laminates. In *International Meeting on Composite Materials, PLAST*. pp. 411–418.

Turco, V. et al., 2006. Flexural and shear strengthening of un-reinforced masonry with FRP bars. *Composites Science and Technology*, 66(2), pp.289–296.

Valluzzi, M., Modena, C. & de Felice, G., 2014. Current practice and open issues in strengthening historical buildings with composites. *Materials and Structures*, 47(12), pp.1971–1985. Available at: http://dx.doi.org/10.1617/s11527-014-0359-7.

Valluzzi, M.R., Binda, L. & Modena, C., 2005. Mechanical behaviour of historic masonry structures strengthened by bed joints structural repointing. *Construction and Building Materials*, 19(1), pp.63–73. Available at: http://www.sciencedirect.com/science/article/pii/S0950061804000546.

Valluzzi, M.R., Tinazzi, D. & Modena, C., 2002. Shear behavior of masonry panels strengthened by FRP laminates. *Construction and Building Materials*, 16(7), pp.409–416.

Van Zijl, G.P.A.G., 2000. *Computational modelling of masonry creep and shrinkage*.

10. Appendix

10.1 Appendix A

10.1.1. Orthotropic linear elastic constitutive equations

σ - ε relation

$$
\begin{bmatrix} \sigma_{11} \\ \sigma_{22} \\ \sigma_{33} \\ \sigma_{12} \\ \sigma_{13} \\ \sigma_{21} \\ \sigma_{23} \\ \sigma_{31} \\ \sigma_{32} \end{bmatrix} = \begin{bmatrix} E_{1111} & E_{1122} & E_{1133} & E_{1112} & E_{1113} & E_{1121} & E_{1123} & E_{1131} & E_{1132} \\ E_{2211} & E_{2222} & E_{2233} & E_{2212} & E_{2213} & E_{2221} & E_{2223} & E_{2231} & E_{2232} \\ E_{3311} & E_{3322} & E_{3333} & E_{3312} & E_{3313} & E_{3321} & E_{3323} & E_{3331} & E_{3332} \\ E_{1211} & E_{1222} & E_{1233} & E_{1212} & E_{1213} & E_{1221} & E_{1223} & E_{1231} & E_{1232} \\ E_{1311} & E_{1322} & E_{1333} & E_{1312} & E_{1313} & E_{1321} & E_{1323} & E_{1331} & E_{1332} \\ E_{2111} & E_{2122} & E_{2133} & E_{2112} & E_{2113} & E_{2121} & E_{2123} & E_{2131} & E_{2132} \\ E_{2311} & E_{2322} & E_{2333} & E_{2312} & E_{2313} & E_{2321} & E_{2323} & E_{2331} & E_{2332} \\ E_{3111} & E_{3122} & E_{3133} & E_{3112} & E_{3113} & E_{3121} & E_{3123} & E_{3131} & E_{3132} \\ E_{3211} & E_{3222} & E_{3233} & E_{3212} & E_{3213} & E_{3221} & E_{3223} & E_{3231} & E_{3232} \end{bmatrix} \begin{bmatrix} \varepsilon_{11} \\ \varepsilon_{22} \\ \varepsilon_{33} \\ \varepsilon_{12} \\ \varepsilon_{13} \\ \varepsilon_{21} \\ \varepsilon_{23} \\ \varepsilon_{31} \\ \varepsilon_{32} \end{bmatrix}
\tag{140}
$$

Due to the symmetry of stress – strain tensor ($\sigma_{ij} = \sigma_{ji}, \varepsilon_{ij} = \varepsilon_{ji} \quad i \neq j$), the Eq.(140) can be written as

$$
\begin{bmatrix} \sigma_{11} \\ \sigma_{22} \\ \sigma_{33} \\ \sigma_{12} \\ \sigma_{13} \\ \sigma_{23} \end{bmatrix} = \begin{bmatrix} E_{1111} & E_{1122} & E_{1133} & E_{1112} & E_{1113} & E_{1123} \\ E_{2211} & E_{2222} & E_{2233} & E_{2212} & E_{2213} & E_{2223} \\ E_{3311} & E_{3322} & E_{3333} & E_{3312} & E_{3313} & E_{3323} \\ E_{1211} & E_{1222} & E_{1233} & E_{1212} & E_{1213} & E_{1223} \\ E_{1311} & E_{1322} & E_{1333} & E_{1312} & E_{1313} & E_{1323} \\ E_{2311} & E_{2322} & E_{2333} & E_{2312} & E_{2313} & E_{2323} \end{bmatrix} \begin{bmatrix} \varepsilon_{11} \\ \varepsilon_{22} \\ \varepsilon_{33} \\ \varepsilon_{12} \\ \varepsilon_{13} \\ \varepsilon_{23} \end{bmatrix}
\tag{141}
$$

Assuming that the strain energy is independent from the strain path:

$$
L = \int \sum_{i,j=1}^{3} \sigma_{ij} d\varepsilon_{ij} = \sum_{i,j=1}^{3} \int \sigma_{ij} d\varepsilon_{ij} = U
\tag{142}
$$

the derivative of the strain energy respect to the generic component of the strain, ε_{ij}, is equal to the generic component of the stress, σ_{ij} and by using Eq.(141) it is possible to write

$$
\frac{\partial U}{\partial \varepsilon_{ij}} = \sigma_{ij} = \sum_{k,l=1}^{3} E_{ijkl} \varepsilon_{kl}
\tag{143}
$$

and the second derivative of the strain energy respect to the generic component of the strain, ε_{kl}, by using Eq.(141) is

$$
\frac{\partial \sigma_{ij}}{\partial \varepsilon_{kl}} = \frac{\partial^2 U}{\partial \varepsilon_{kl} \partial \varepsilon_{ij}} = \frac{\partial}{\partial \varepsilon_{kl}} \sum_{k,l=1}^{3} E_{ijkl} \varepsilon_{kl} = E_{ijkl}
\tag{144}
$$

Changing the order of derivative

$$
\frac{\partial U}{\partial \varepsilon_{kl}} = \sigma_{kl} = \sum_{i,j=1}^{3} E_{klij} \varepsilon_{ij}
\tag{145}
$$

$$
\frac{\partial \sigma_{kl}}{\partial \varepsilon_{ij}} = \frac{\partial^2 U}{\partial \varepsilon_{ij} \partial \varepsilon_{kl}} = \frac{\partial}{\partial \varepsilon_{ij}} \sum_{k,l=1}^{3} E_{klij} \varepsilon_{ij} = E_{klij}
\tag{146}
$$

Being the strain energy of class C^2 respect to the strains, the Schwarz theorem can be applied

179

$$\frac{\partial^2 U}{\partial \varepsilon_{ij} \partial \varepsilon_{kl}} = \frac{\partial^2 U}{\partial \varepsilon_{kl} \partial \varepsilon_{ij}} = E_{ijkl} = E_{klij} \tag{147}$$

The stiffness matrix is symmetric so the constants become 21

$$\begin{bmatrix} \sigma_{11} \\ \sigma_{22} \\ \sigma_{33} \\ \sigma_{12} \\ \sigma_{13} \\ \sigma_{23} \end{bmatrix} = \begin{bmatrix} E_{1111} & E_{1122} & E_{1133} & E_{1112} & E_{1113} & E_{1123} \\ E_{1122} & E_{2222} & E_{2233} & E_{2212} & E_{2213} & E_{2223} \\ E_{1133} & E_{2233} & E_{3333} & E_{3312} & E_{3313} & E_{3323} \\ E_{1112} & E_{2212} & E_{3312} & E_{1212} & E_{1213} & E_{1223} \\ E_{1113} & E_{2213} & E_{3313} & E_{1213} & E_{1313} & E_{1323} \\ E_{1123} & E_{2223} & E_{3323} & E_{1223} & E_{1323} & E_{2323} \end{bmatrix} \begin{bmatrix} \varepsilon_{11} \\ \varepsilon_{22} \\ \varepsilon_{33} \\ \varepsilon_{12} \\ \varepsilon_{13} \\ \varepsilon_{23} \end{bmatrix} \tag{148}$$

Orthotropic material implies that there are three symmetry planes mutually orthogonal, on which the stress σ_{ii} produces linear strains such as ε_{jj} ($j = 1, 2, 3$) while the shear strains ε_{jk} ($j \neq k$) are equal to 0: this means that E_{ijkl} are equal to 0. Moreover, due to symmetry, the tangential stress σ_{ij} ($i \neq j$) produces a distorsion ε_{ij} being the other null. The Eq.(148) can be written as

$$\begin{bmatrix} \sigma_{11} \\ \sigma_{22} \\ \sigma_{33} \\ \sigma_{12} \\ \sigma_{13} \\ \sigma_{23} \end{bmatrix} = \begin{bmatrix} E_{1111} & E_{1122} & E_{1133} & 0 & 0 & 0 \\ E_{1122} & E_{2222} & E_{2233} & 0 & 0 & 0 \\ E_{1133} & E_{2233} & E_{3333} & 0 & 0 & 0 \\ 0 & 0 & 0 & E_{1212} & 0 & 0 \\ 0 & 0 & 0 & 0 & E_{1313} & 0 \\ 0 & 0 & 0 & 0 & 0 & E_{2323} \end{bmatrix} \begin{bmatrix} \varepsilon_{11} \\ \varepsilon_{22} \\ \varepsilon_{33} \\ \varepsilon_{12} \\ \varepsilon_{13} \\ \varepsilon_{23} \end{bmatrix} \tag{149}$$

In the end, the elastic constants are 9.

In the case of composite lamina, the stress state is plane so the relation between the non null component of stress and the corresponding strains can be derived

$$\begin{bmatrix} \sigma_{11} \\ \sigma_{22} \\ 0 \\ \sigma_{12} \\ 0 \\ 0 \end{bmatrix} = \begin{bmatrix} E_{1111} & E_{1122} & E_{1133} & 0 & 0 & 0 \\ E_{1122} & E_{2222} & E_{2233} & 0 & 0 & 0 \\ E_{1133} & E_{2233} & E_{3333} & 0 & 0 & 0 \\ 0 & 0 & 0 & E_{1212} & 0 & 0 \\ 0 & 0 & 0 & 0 & E_{1313} & 0 \\ 0 & 0 & 0 & 0 & 0 & E_{2323} \end{bmatrix} \begin{bmatrix} \varepsilon_{11} \\ \varepsilon_{22} \\ \varepsilon_{33} \\ \varepsilon_{12} \\ 0 \\ 0 \end{bmatrix}$$

$$\begin{cases} \sigma_{11} = E_{1111}\varepsilon_{11} + E_{1122}\varepsilon_{22} + E_{1133}\varepsilon_{33} \\ \sigma_{22} = E_{1122}\varepsilon_{11} + E_{2222}\varepsilon_{22} + E_{2233}\varepsilon_{33} \\ 0 = E_{1133}\varepsilon_{11} + E_{2233}\varepsilon_{22} + E_{3333}\varepsilon_{33} \\ \sigma_{12} = E_{1212}\varepsilon_{12} \end{cases}$$

$$\begin{cases} \sigma_{11} = E_{1111}\varepsilon_{11} + E_{1122}\varepsilon_{22} + E_{1133}\left(-\frac{E_{1133}}{E_{3333}}\varepsilon_{11} - \frac{E_{2233}}{E_{3333}}\varepsilon_{22}\right) \\ \sigma_{22} = E_{1122}\varepsilon_{11} + E_{2222}\varepsilon_{22} + E_{2233}\left(-\frac{E_{1133}}{E_{3333}}\varepsilon_{11} - \frac{E_{2233}}{E_{3333}}\varepsilon_{22}\right) \\ \varepsilon_{33} = -\frac{E_{1133}}{E_{3333}}\varepsilon_{11} - \frac{E_{2233}}{E_{3333}}\varepsilon_{22} \\ \sigma_{12} = E_{1212}\varepsilon_{12} \end{cases}$$

$$\begin{cases} \sigma_{11} = \left(E_{1111} - \frac{E_{1133}^2}{E_{3333}}\right)\varepsilon_{11} + \left(E_{1122} - \frac{E_{1133}E_{2233}}{E_{3333}}\right)\varepsilon_{22} \\ \sigma_{22} = \left(E_{1122} - \frac{E_{1133}E_{2233}}{E_{3333}}\right)\varepsilon_{11} + \left(E_{2222} - \frac{E_{2233}^2}{E_{3333}}\right)\varepsilon_{22} \\ \sigma_{12} = E_{1212}\varepsilon_{12} \end{cases}$$

In matrix form

180

$$\begin{bmatrix} \sigma_{11} \\ \sigma_{22} \\ \sigma_{12} \end{bmatrix} = \begin{bmatrix} E_{1111} & E_{1122} & 0 \\ E_{1122} & E_{2222} & 0 \\ 0 & 0 & E_{1212} \end{bmatrix} \begin{bmatrix} \varepsilon_{11} \\ \varepsilon_{22} \\ \varepsilon_{12} \end{bmatrix} \tag{150}$$

By using different symbols, the Eq.(150) becomes

$$\begin{bmatrix} \sigma_1 \\ \sigma_2 \\ \tau_{12} \end{bmatrix} = \begin{bmatrix} E_{11} & E_{12} & 0 \\ E_{12} & E_{22} & 0 \\ 0 & 0 & E_{33} \end{bmatrix} \begin{bmatrix} \varepsilon_1 \\ \varepsilon_2 \\ \gamma_{12} \end{bmatrix} \tag{151}$$

At this stage, it is possible to define the compliance matrix as the inverse of the latter matrix

$$\begin{bmatrix} \varepsilon_T \\ \varepsilon_L \\ \gamma_{LT} \end{bmatrix} = \begin{bmatrix} \dfrac{1}{E_L} & -\dfrac{v_{LT}}{E_L} & 0 \\ -\dfrac{v_{LT}}{E_L} & \dfrac{1}{E_T} & 0 \\ 0 & 0 & \dfrac{1}{G_{LT}} \end{bmatrix} \begin{bmatrix} \sigma_L \\ \sigma_T \\ \tau_{LT} \end{bmatrix} \tag{152}$$

with $\dfrac{v_{LT}}{E_L} = \dfrac{v_{TL}}{E_T}$.

After some analytical passages, it is possible to derive the coefficients of the stiffness matrix

$$\begin{bmatrix} \dfrac{1}{E_L} & -\dfrac{v_{LT}}{E_L} & 0 \\ -\dfrac{v_{LT}}{E_L} & \dfrac{1}{E_T} & 0 \\ 0 & 0 & \dfrac{1}{G_{LT}} \end{bmatrix}^{-1} = \dfrac{1}{\dfrac{1}{G_{LT}}\left(\dfrac{1}{E_L E_T} - \dfrac{v_{LT}v_{TL}}{E_L E_T}\right)} \begin{bmatrix} \dfrac{1}{G_{LT}E_T} & -\dfrac{v_{LT}}{G_{LT}E_L} & 0 \\ -\dfrac{v_{LT}}{G_{LT}E_L} & \dfrac{1}{G_{LT}E_L} & 0 \\ 0 & 0 & \dfrac{1}{E_L E_T} - \dfrac{v_{LT}v_{TL}}{E_L E_T} \end{bmatrix} =$$

$$= \dfrac{G_{LT}E_L E_T}{1 - v_{LT}v_{TL}} \begin{bmatrix} \dfrac{1}{G_{LT}E_T} & \dfrac{v_{LT}}{G_{LT}E_L} & 0 \\ -\dfrac{v_{LT}}{G_{LT}E_L} & \dfrac{1}{G_{LT}E_L} & 0 \\ 0 & 0 & \dfrac{1}{E_L E_T} - \dfrac{v_{LT}v_{TL}}{E_L E_T} \end{bmatrix} = \begin{bmatrix} \dfrac{E_L}{1 - v_{LT}v_{TL}} & \dfrac{E_L v_{LT}}{1 - v_{LT}v_{TL}} & 0 \\ \dfrac{E_T v_{LT}}{1 - v_{LT}v_{TL}} & \dfrac{E_T}{1 - v_{LT}v_{TL}} & 0 \\ 0 & 0 & G_{LT} \end{bmatrix}$$

In the end

$$\begin{bmatrix} \sigma_1 \\ \sigma_2 \\ \tau_{12} \end{bmatrix} = \begin{bmatrix} \dfrac{E_L}{1 - v_{LT}v_{TL}} & \dfrac{E_L v_{LT}}{1 - v_{LT}v_{TL}} & 0 \\ \dfrac{E_T v_{LT}}{1 - v_{LT}v_{TL}} & \dfrac{E_T}{1 - v_{LT}v_{TL}} & 0 \\ 0 & 0 & G_{LT} \end{bmatrix} \begin{bmatrix} \varepsilon_1 \\ \varepsilon_2 \\ \gamma_{12} \end{bmatrix} \tag{153}$$

10.1.2. Elastic constants for composite lamina

The elastic constants inside contained in both stiffness and compliance matrices depend on the type of fibers and the resin, respectively. The analytical model developed from here onward is different for the longitudinal and transversal direction.

10.1.2.1. Longitudinal direction

The hypothesis at the base of the model are: *i*) the fibers are geometrically equal and with the same mechanical properties, *ii*) the fibers are parallel one to each other and *iii*) perfect bond between the fibers and the matrix. In Figure 116, a schematization of the composite lamina is reported.
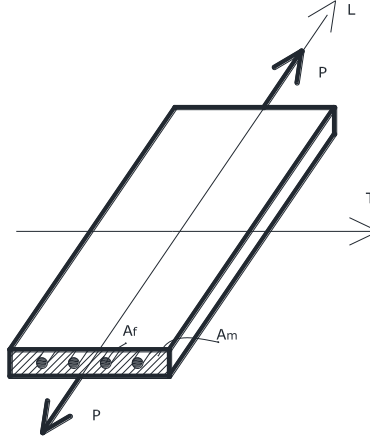
Figure 116 Composite lamina.

Due to the hypotheses of perfect bond between fibers and resin, it is possible to write

$$
\begin{cases}
\varepsilon_f = \dfrac{\sigma_f}{E_f} \\
\varepsilon_m = \dfrac{\sigma_m}{E_m} \xrightarrow{\varepsilon_f = \varepsilon_m = \varepsilon_L} \dfrac{\sigma_f}{E_f} = \dfrac{\sigma_m}{E_m} \rightarrow \dfrac{\sigma_f}{\sigma_m} = \dfrac{E_f}{E_m} \\
\varepsilon_L = \dfrac{\sigma_L}{E_L}
\end{cases}
\tag{154}
$$

with pedex f and m related to fibers and matrix, respectively and pedex L is referred to the longitudinal direction.

10.1.2.1.1. Elastic modulus

The tensile force on the lamina, P, can be written as

$$
P = P_f + P_m \rightarrow \sigma_L A = \sigma_f A_f + \sigma_m A_m
\tag{155}
$$

Substituting Eq.(154) in Eq.(155) the following relation is obtained

$$
\varepsilon_L E_L A = \varepsilon_f E_f A_f + \varepsilon_m E_m A_m \rightarrow E_L A = E_f A_f + E_m A_m \rightarrow E_L = E_f \frac{A_f}{A} + E_m \frac{A_m}{A}
$$

$$
E_L = E_f V_f + E_m V_m
\tag{156}
$$

with V_m and V_f represent the volume of matrix and fibers, respectively.

Knowing the elastic moduli of fibers and matrix, it is possible to evaluate the elastic modulus of composite by using Eq. (156)

$$
E_L = E_f V_f + E_m V_m = E_f (1 - V_m) + E_m V_m
$$

$$
E_L = E_f V_f + E_m (1 - V_f)
\tag{157}
$$

10.1.2.1.2. Tensile strength

Under the hypothesis that the failure of the composite is due to the damage of the fibers (the deformation of the matrix is higher than that of the fibers), it is possible to evaluate the ultimate tensile strength of the composite by using Eq.(155)

$$
\varepsilon_{fu} = \frac{\sigma_{fu}}{E_f}
\tag{158}
$$

ith pedex u that identifies the ultimate conditions.

the From Eq.(155) and Eq.(157)

$$\sigma_{Lu} = \sigma_{fu}V_f + E_m\varepsilon_{fu}V_m = \varepsilon_{fu}\big(E_fV_f + E_mV_m\big)$$

$$\sigma_{Lu} = \varepsilon_{fu}E_L$$

(159)

10.1.2.2. Transversal direction

10.1.2.2.1. Elastic modulus

Considering the fibers and the matrix as element in series, referring to Figure 116, the elongations, ΔL, can be written

$$\begin{cases} \Delta L_T = \Delta L_f + \Delta L_m \\ \quad \Delta L_f = \varepsilon_f L_f \\ \quad \Delta L_m = \varepsilon_m L_m \\ \quad \Delta L_T = \varepsilon_T L_T \end{cases}$$

(160)

After some analytical passages

$$\varepsilon_T L_T = \varepsilon_f L_f + \varepsilon_m L_m \xrightarrow[\substack{V_m=L_m/L_T}]{V_f=L_f/L_T} \varepsilon_T = \varepsilon_f V_f + \varepsilon_m L_m$$

(161)

In the linear elastic case, considering the element in series means that the state of stress is equal in each element

$$\frac{\sigma_T}{E_T} = \frac{\sigma_f}{E_f}V_f + \frac{\sigma_m}{E_m}V_m$$

$$\frac{1}{E_T} = \frac{V_f}{E_f} + \frac{V_m}{E_m}$$

(162)

In order to consider also the Poisson coefficients, Eq.(162) (Hashin 1972)can be used

$$\frac{1}{E_T} = \left(\frac{V_f}{E_f}\right)\frac{1}{V_f + V_m} - V_fV_m\frac{\left(\frac{E_f v_m}{2} - E_m v_f\right)\left(\frac{v_m}{E_m} - \frac{v_f}{E_f}\right)}{\left(V_fE_f + V_mE_m\right)\left(V_f + \frac{V_m}{2}\right)}$$

$$\frac{1}{E_T} = \frac{V_f}{E_f} - V_fV_m\frac{\left(\frac{E_f v_m}{2} - E_m v_f\right)\left(\frac{v_m}{E_m} - \frac{v_f}{E_f}\right)}{E_L\left(V_f + \frac{V_m}{2}\right)}$$

(163)

10.1.2.2.2. Tensile strength

The presence of the fibers produce a concentration of stress and, consequently, cause a strong reduction in the tensile strength of the matrix. Considering a model in series, this represent the mechanism of failure.

$$\sigma_{rt} = \frac{\sigma_{rm}}{k}$$

(164)

where k is a constant higher than 1 that represents a decrease in strength due to the percentage of fibers, V_f, the presence of voids, defects of fabrication, debonding between fibers and matrix.

Greszczuk (Greszczuk 1975) proposed the Eq.(165) to evaluate the stress concentration coefficient

$$FCS = \frac{1 - V_f\left(1 - \frac{E_m}{E_f}\right)}{1 - \left(\frac{4V_f}{\pi}\right)^{1/2}\left(1 - \frac{E_m}{E_f}\right)}$$

(165)

Putting $k = FCS$, from Eq.(164) it is possible to calculate

$$\sigma_{rt} = \frac{\sigma_{rm}}{FCS}$$

(166)

In order to take into account of defects of fabrication or the presence of voids, the Eq.(165) is modified (Chamis 1986)

$$k = FCS\frac{\beta_v}{\beta_t}$$

(167)

with $\beta_v > 1$ and $\beta_t < 1$ take into account the presence of voids and defects due to the fabrication process, respectively. β_t is obtained experimentally and assumes a values in the range of $0.5 - 0.7$ (Greszczuk 1975), while $\beta_v = \frac{1}{1 - \left(\frac{4V_v}{\pi V_m}\right)^{1/2}}$. Substituting in Eq.(164)

$$\sigma_{rt} = \frac{\beta_t}{\beta_v}\frac{\sigma_{rm}}{FCS}$$

(168)

10.1.2.3. Shear modulus

Considering a tangential stress, τ_{LT}, the point moves from A to A', (Figure 117)

$$AA' = \gamma_{LT}\left(L_f + L_m\right) = \gamma_f L_f + \gamma_m L_m$$

(169)
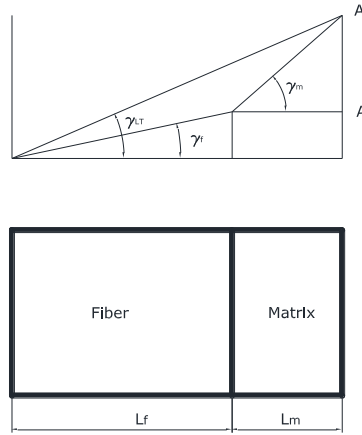
Figure 117 Composite material: shear stress.

Considering matrix and fibers as series system means that the shear stress is equal for all the elements, from Eq.(168), remembering Eq.(161)

$$\gamma_{LT} = \frac{\gamma_f L_f + \gamma_m L_m}{L_f + L_m} = \gamma_f V_f + \gamma_m V_m \xrightarrow[\tau_m = G_m/\gamma_m]{\substack{\tau_{LT}=G_{LT}/\gamma_{LT} \\ \tau_f = \frac{G_f}{\gamma_f}}} \frac{\tau_{LT}}{G_{LT}} = \frac{\tau_f}{G_f}V_f + \frac{\tau_m}{G_m}V_m \xrightarrow{\tau_{LT}=\tau_f=\tau_m} \frac{1}{G_{LT}}$$

$$= \frac{V_f}{G_f} + \frac{V_m}{G_m}$$

(170)

A more realistic formula is (Hashin 1972)

$$\frac{1}{G_{LT}} = \left(\frac{V_f}{G_f} + \frac{\eta_c V_m}{G_m}\right)\frac{1}{V_f + \eta_c V_m} \tag{171}$$

with η_c corrective coefficient determined experimentally and assumes a value in the range of 0.4 - 0.5.

10.1.2.3. Poisson coefficient

From Eq.(152), due to symmetry of the compliance matrix

$$\frac{v_{LT}}{E_L} = \frac{v_{TL}}{E_T} \tag{172}$$

Poisson coefficient is proportional to the elastic modulus so

$$E_L \gg E_T \rightarrow v_{LT} \gg v_{TL} \tag{173}$$
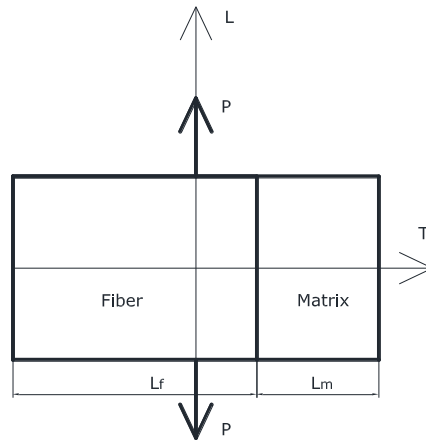
Figure 118 Composite material: Poisson coefficient.

The Poisson coefficient is defined as

$$v_{LT} = -\frac{\varepsilon_T}{\varepsilon_l} \tag{174}$$

From Figure 118, imposing a deformation ε_L to the lamina, calling $\varDelta L_f$ and $\varDelta L_m$ the dimensional variation in the transversal direction it can be derived that

$$\varepsilon_T = \frac{\varDelta L_f + \varDelta L_m}{L_f + L_m} \tag{175}$$

Under the hypothesis of equal deformation in the longitudinal direction between fibers and matrix and assuming both the materials as isotropic

$$\varepsilon_T = -\frac{v_f \varepsilon_L L_f + v_m \varepsilon_f L_m}{L_f + L_m} \tag{176}$$

Substituting Eq.(176) in Eq.(175) and remembering Eq.(161)

$$v_{LT} = -\frac{v_f L_f + v_m L_m}{L_f + L_m} = v_f V_f + v_m V_m \tag{177}$$

10.1.3. Ideal model made by one isotropic component and the other orthotropic

The stress – strain relation can be written as

$$
\begin{bmatrix} \varepsilon_x \\ \varepsilon_y \\ \varepsilon_z \end{bmatrix} = \begin{bmatrix} \dfrac{1}{E_x} & -\dfrac{v_{yx}}{E_y} & -\dfrac{v_{zx}}{E_z} \\[2mm] -\dfrac{v_{xy}}{E_x} & \dfrac{1}{E_y} & -\dfrac{v_{zy}}{E_z} \\[2mm] -\dfrac{v_{xz}}{E_x} & -\dfrac{v_{yz}}{E_y} & \dfrac{1}{E_z} \end{bmatrix} \begin{bmatrix} \sigma_x \\ \sigma_y \\ \sigma_z \end{bmatrix}
\tag{178}
$$

The matrix that links stress and strain is symmetric means that

$$
\frac{v_{yx}}{E_y} = \frac{v_{xy}}{E_x}, \qquad \frac{v_{zx}}{E_z} = \frac{v_{xz}}{E_x}, \qquad \frac{v_{zy}}{E_z} = \frac{v_{yz}}{E_y},
$$

$$
\begin{bmatrix} \varepsilon_x \\ \varepsilon_y \\ \varepsilon_z \end{bmatrix} = \begin{bmatrix} \dfrac{1}{E_x} & -\dfrac{v_{xy}}{E_x} & -\dfrac{v_{xz}}{E_x} \\[2mm] -\dfrac{v_{xy}}{E_x} & \dfrac{1}{E_y} & -\dfrac{v_{zy}}{E_z} \\[2mm] -\dfrac{v_{xz}}{E_x} & -\dfrac{v_{zy}}{E_z} & \dfrac{1}{E_z} \end{bmatrix} \begin{bmatrix} \sigma_x \\ \sigma_y \\ \sigma_z \end{bmatrix}
\tag{179}
$$

Reference is made to an ideal linear elastic model (Figure 5) made by superimposed bricks and joints. The bricks are considered isotropic, while the joints, are orthotropic and isotropic in the transversal direction, simulating a reinforcing material made by fibers. Calling the two materials with pedex b and o, and assuming fibers located in the y direction:

$$
\begin{aligned}
E_{oy} &= E_{oL} \\
E_{ox} &= E_{oz} = E_{oT} \\
v_{xy} &= v_{zy} = v_{oTL} \\
v_{xz} &= v_{oTT}
\end{aligned}
\tag{180}
$$

In particular for the element b becomes:

$$
\begin{bmatrix} \varepsilon_{bx} \\ \varepsilon_{by} \\ \varepsilon_{bz} \end{bmatrix} = \begin{bmatrix} \dfrac{1}{E_b} & -\dfrac{v_b}{E_b} & -\dfrac{v_b}{E_b} \\[2mm] -\dfrac{v_b}{E_b} & \dfrac{1}{E_b} & -\dfrac{v_b}{E_b} \\[2mm] -\dfrac{v_b}{E_b} & -\dfrac{v_b}{E_b} & \dfrac{1}{E_b} \end{bmatrix} \begin{bmatrix} \sigma_{bx} \\ \sigma_{by} \\ \sigma_{bz} \end{bmatrix}
\tag{181}
$$

while for the element o becomes:

$$
\begin{bmatrix} \varepsilon_{ox} \\ \varepsilon_{oy} \\ \varepsilon_{oz} \end{bmatrix} = \begin{bmatrix} \dfrac{1}{E_{oT}} & -\dfrac{v_{oTL}}{E_{oT}} & -\dfrac{v_{oTT}}{E_{oT}} \\[2mm] -\dfrac{v_{oTL}}{E_{oT}} & \dfrac{1}{E_{oL}} & -\dfrac{v_{oTL}}{E_{oT}} \\[2mm] -\dfrac{v_{oTT}}{E_{oT}} & -\dfrac{v_{oTL}}{E_{oT}} & \dfrac{1}{E_{oT}} \end{bmatrix} \begin{bmatrix} \sigma_{ox} \\ \sigma_{oy} \\ \sigma_{oz} \end{bmatrix}
\tag{182}
$$

For the translational equilibrium along z direction

$$
\sigma_{bz} = \sigma_{cz} = \sigma_z
\tag{183}
$$

Calling t_b and t_o the thickness of the two materials, respectively, by imposing the equilibrium along x and y directions, the following relations are obtained:

186

$$\sigma_{bx}t_b + \sigma_{ox}t_o = 0 \rightarrow \sigma_{bx} = -\sigma_{ox}\frac{t_o}{t_b} = -\alpha\sigma_{ox} \qquad eq.\ along\ x$$

$$\sigma_{by}t_b + \sigma_{oy}t_o = 0 \rightarrow \sigma_{by} = -\sigma_{oy}\frac{t_o}{t_b} = -\alpha\sigma_{oy} \qquad eq.\ along\ y \tag{184}$$

with $\alpha = t_o/t_b$.

The compatibility along x and y directions is expressed by:

$$\varepsilon_{bx} = \varepsilon_{ox} = \varepsilon_x$$
$$\varepsilon_{by} = \varepsilon_{oy} = \varepsilon_y \tag{185}$$

Substituting Eq.(184) and Eq.(185) in Eq.(181) and Eq.(182), the stress - strain relations for the two materials can be written in a different manner. In particular for the element b becomes:

$$\begin{bmatrix} \varepsilon_x \\ \varepsilon_y \\ \varepsilon_{bz} \end{bmatrix} = \begin{bmatrix} \dfrac{1}{E_b} & -\dfrac{v_b}{E_b} & -\dfrac{v_b}{E_b} \\ -\dfrac{v_b}{E_b} & \dfrac{1}{E_b} & -\dfrac{v_b}{E_b} \\ -\dfrac{v_b}{E_b} & -\dfrac{v_b}{E_b} & \dfrac{1}{E_b} \end{bmatrix} \begin{bmatrix} -\alpha\sigma_{ox} \\ -\alpha\sigma_{oy} \\ \sigma_z \end{bmatrix} = \begin{bmatrix} \dfrac{1}{E_b} & -\dfrac{v_b}{E_b} & \dfrac{v_b}{E_b} \\ -\dfrac{v_b}{E_b} & \dfrac{1}{E_b} & -\dfrac{v_b}{E_b} \\ -\dfrac{v_b}{E_b} & -\dfrac{v_b}{E_b} & \dfrac{1}{E_b} \end{bmatrix} \begin{bmatrix} -\alpha\phi_x \\ -\alpha\phi_y \\ 1 \end{bmatrix} \sigma_z \tag{186}$$

$$\begin{bmatrix} \varepsilon_x \\ \varepsilon_y \\ \varepsilon_{oz} \end{bmatrix} = \begin{bmatrix} \dfrac{1}{E_{oT}} & -\dfrac{v_{oTL}}{E_{oT}} & -\dfrac{v_{oTT}}{E_{oT}} \\ -\dfrac{v_{oTL}}{E_{oT}} & \dfrac{1}{E_{oL}} & -\dfrac{v_{oTL}}{E_{oT}} \\ -\dfrac{v_{oTT}}{E_{oT}} & -\dfrac{v_{oTL}}{E_{oT}} & \dfrac{1}{E_{oT}} \end{bmatrix} \begin{bmatrix} \sigma_{ox} \\ \sigma_{oy} \\ \sigma_z \end{bmatrix} = \begin{bmatrix} \dfrac{1}{E_{oT}} & -\dfrac{v_{oTL}}{E_{oT}} & -\dfrac{v_{oTT}}{E_{oT}} \\ -\dfrac{v_{oTL}}{E_{oT}} & \dfrac{1}{E_{oL}} & -\dfrac{v_{oTL}}{E_{oT}} \\ -\dfrac{v_{oTT}}{E_{oT}} & -\dfrac{v_{oTL}}{E_{oT}} & \dfrac{1}{E_{oT}} \end{bmatrix} \begin{bmatrix} \phi_x \\ \phi_y \\ 1 \end{bmatrix} \sigma_z \tag{187}$$

with $\phi_x = \sigma_{ox}/\sigma_z$ and $\phi_y = \sigma_{oy}/\sigma_z$.

Subtracting Eq.(187) to Eq.(186)

$$\begin{bmatrix} 0 \\ 0 \\ \varepsilon_{bz} - \varepsilon_{cz} \end{bmatrix} = \left\{ \begin{bmatrix} \dfrac{1}{E_b} & -\dfrac{v_b}{E_b} & -\dfrac{v_b}{E_b} \\ -\dfrac{v_b}{E_b} & \dfrac{1}{E_b} & -\dfrac{v_b}{E_b} \\ -\dfrac{v_b}{E_b} & -\dfrac{v_b}{E_b} & \dfrac{1}{E_b} \end{bmatrix} \begin{bmatrix} -\alpha\phi_x \\ -\alpha\phi_y \\ 1 \end{bmatrix} - \begin{bmatrix} \dfrac{1}{E_{oT}} & -\dfrac{v_{oTL}}{E_{oT}} & -\dfrac{v_{oTT}}{E_{oT}} \\ -\dfrac{v_{oTL}}{E_{oT}} & \dfrac{1}{E_{oL}} & -\dfrac{v_{oTL}}{E_{oT}} \\ -\dfrac{v_{oTT}}{E_{oT}} & -\dfrac{v_{oTL}}{E_{oT}} & \dfrac{1}{E_{oT}} \end{bmatrix} \begin{bmatrix} \phi_x \\ \phi_y \\ 1 \end{bmatrix} \right\} \sigma_z$$

$$\begin{bmatrix} 0 \\ 0 \\ \varepsilon_{bz} - \varepsilon_{cz} \end{bmatrix} = \left\{ \begin{bmatrix} \dfrac{1}{E_b} & -\dfrac{v_b}{E_b} & \dfrac{v_b}{\alpha E_b} \\ -\dfrac{v_b}{E_b} & \dfrac{1}{E_b} & \dfrac{v_b}{\alpha E_b} \\ -\dfrac{v_b}{E_b} & -\dfrac{v_b}{E_b} & -\dfrac{1}{\alpha E_b} \end{bmatrix} \begin{bmatrix} -\alpha\phi_x \\ -\alpha\phi_y \\ -\alpha \end{bmatrix} - \begin{bmatrix} \dfrac{1}{E_{oT}} & -\dfrac{v_{oTL}}{E_{oT}} & -\dfrac{v_{oTT}}{E_{oT}} \\ -\dfrac{v_{oTL}}{E_{oT}} & \dfrac{1}{E_{oL}} & -\dfrac{v_{oTL}}{E_{oT}} \\ -\dfrac{v_{oTT}}{E_{oT}} & -\dfrac{v_{oTL}}{E_{oT}} & \dfrac{1}{E_{oT}} \end{bmatrix} \begin{bmatrix} \phi_x \\ \phi_y \\ 1 \end{bmatrix} \right\} \sigma_z \tag{188}$$

$$\begin{bmatrix} 0 \\ 0 \\ \varepsilon_{bz} - \varepsilon_{cz} \end{bmatrix} = -\left\{ \alpha^3 \begin{bmatrix} \dfrac{1}{E_b} & -\dfrac{v_b}{E_b} & \dfrac{v_b}{\alpha E_b} \\ -\dfrac{v_b}{E_b} & \dfrac{1}{E_b} & \dfrac{v_b}{\alpha E_b} \\ -\dfrac{v_b}{E_b} & -\dfrac{v_b}{E_b} & -\dfrac{1}{\alpha E_b} \end{bmatrix} + \begin{bmatrix} \dfrac{1}{E_{oT}} & -\dfrac{v_{oTL}}{E_{oT}} & -\dfrac{v_{oTT}}{E_{oT}} \\ -\dfrac{v_{oTL}}{E_{oT}} & \dfrac{1}{E_{oL}} & -\dfrac{v_{oTL}}{E_{oT}} \\ -\dfrac{v_{oTT}}{E_{oT}} & -\dfrac{v_{oTL}}{E_{oT}} & \dfrac{1}{E_{oT}} \end{bmatrix} \right\} \begin{bmatrix} \phi_x \\ \phi_y \\ 1 \end{bmatrix} \sigma_z$$

187

$$\begin{bmatrix} 0 \\ 0 \\ \varepsilon_{bz} - \varepsilon_{cz} \end{bmatrix} = \left\{ \begin{bmatrix} -\dfrac{\alpha}{E_b} - \dfrac{1}{E_{oT}} & \dfrac{\alpha v_b}{E_b} + \dfrac{v_{oTL}}{E_{oT}} & -\dfrac{v_b}{E_b} + \dfrac{v_{oTT}}{E_{oT}} \\ \dfrac{\alpha v_b}{E_b} + \dfrac{v_{oTL}}{E_{oT}} & -\dfrac{\alpha}{E_b} - \dfrac{1}{E_{oL}} & -\dfrac{v_b}{E_b} + \dfrac{v_{oTL}}{E_{oT}} \\ \dfrac{\alpha v_b}{E_b} + \dfrac{v_{oTT}}{E_{oT}} & \dfrac{\alpha v_b}{E_b} + \dfrac{v_{oTL}}{E_{oT}} & \dfrac{1}{E_b} - \dfrac{1}{E_{oT}} \end{bmatrix} \right\} \begin{bmatrix} \phi_x \\ \phi_y \\ 1 \end{bmatrix} \sigma_z$$

Making the following positions

$$\beta_L = E_{oL}/E_b \rightarrow E_{oL} = \beta_L E_b$$
$$\beta_T = E_{oT}/E_b \rightarrow E_{oT} = \beta_T E_b$$

(189)

the Eq.(188) becomes

$$\begin{bmatrix} 0 \\ 0 \\ \varepsilon_{bz} - \varepsilon_{cz} \end{bmatrix} = \left\{ \begin{bmatrix} -\dfrac{\alpha}{E_b} - \dfrac{1}{\beta_T E_b} & \dfrac{\alpha v_b}{E_b} + \dfrac{v_{oTL}}{\beta_T E_b} & -\dfrac{v_b}{E_b} + \dfrac{v_{oTT}}{\beta_T E_b} \\ \dfrac{\alpha v_b}{E_b} + \dfrac{v_{oTL}}{\beta_T E_b} & -\dfrac{\alpha}{E_b} - \dfrac{1}{\beta_L E_b} & -\dfrac{v_b}{E_b} + \dfrac{v_{oTL}}{\beta_T E_b} \\ \dfrac{\alpha v_b}{E_b} + \dfrac{v_{oTT}}{\beta_T E_b} & \dfrac{\alpha v_b}{E_b} + \dfrac{v_{oTL}}{\beta_T E_b} & \dfrac{1}{E_b} - \dfrac{1}{\beta_T E_b} \end{bmatrix} \right\} \begin{bmatrix} \phi_x \\ \phi_y \\ 1 \end{bmatrix} \sigma_z$$

$$\begin{bmatrix} 0 \\ 0 \\ \varepsilon_{bz} - \varepsilon_{cz} \end{bmatrix} = \dfrac{1}{E_b^3} \left\{ \begin{bmatrix} -\alpha - \dfrac{1}{\beta_T} & \alpha v_b + \dfrac{v_{oTL}}{\beta_T} & -v_b + \dfrac{v_{oTT}}{\beta_T} \\ \alpha v_b + \dfrac{v_{oTL}}{\beta_T} & -\alpha - \dfrac{1}{\beta_L} & -v_b + \dfrac{v_{oTL}}{\beta_T} \\ \alpha v_b + \dfrac{v_{oTT}}{\beta_T} & \alpha v_b + \dfrac{v_{oTL}}{\beta_T} & 1 - \dfrac{1}{\beta_T} \end{bmatrix} \right\} \begin{bmatrix} \phi_x \\ \phi_y \\ 1 \end{bmatrix} \sigma_z$$

$$\begin{bmatrix} 0 \\ 0 \end{bmatrix} = \dfrac{1}{E_b^2} \begin{bmatrix} -\alpha - \dfrac{1}{\beta_T} & \alpha v_b + \dfrac{v_{oTL}}{\beta_T} & -v_b + \dfrac{v_{oTT}}{\beta_T} \\ \alpha v_b + \dfrac{v_{oTL}}{\beta_T} & -\alpha - \dfrac{1}{\beta_L} & -v_b + \dfrac{v_{oTL}}{\beta_T} \end{bmatrix} \begin{bmatrix} \phi_x \\ \phi_y \\ 1 \end{bmatrix} \sigma_z$$

$$\begin{bmatrix} 0 \\ 0 \end{bmatrix} = \begin{bmatrix} -\alpha - \dfrac{1}{\beta_T} & \alpha v_b + \dfrac{v_{oTL}}{\beta_T} & -v_b + \dfrac{v_{oTT}}{\beta_T} \\ \alpha v_b + \dfrac{v_{oTL}}{\beta_T} & -\alpha - \dfrac{1}{\beta_L} & -v_b + \dfrac{v_{oTL}}{\beta_T} \end{bmatrix} \begin{bmatrix} \phi_x \\ \phi_y \\ 1 \end{bmatrix}$$

(190)

$$\begin{bmatrix} 0 \\ 0 \end{bmatrix} = \begin{bmatrix} \left(\alpha v_b + \dfrac{v_{oTL}}{\beta_T}\right)\left(-\alpha - \dfrac{1}{\beta_T}\right) & \left(\alpha v_b + \dfrac{v_{oTL}}{\beta_T}\right)\left(\alpha v_b + \dfrac{v_{oTL}}{\beta_T}\right) & \left(\alpha v_b + \dfrac{v_{oTL}}{\beta_T}\right)\left(-v_b + \dfrac{v_{oTT}}{\beta_T}\right) \\ \left(-\alpha - \dfrac{1}{\beta_T}\right)\left(\alpha v_b + \dfrac{v_{oTL}}{\beta_T}\right) & \left(-\alpha - \dfrac{1}{\beta_T}\right)\left(-\alpha - \dfrac{1}{\beta_L}\right) & \left(-\alpha - \dfrac{1}{\beta_T}\right)\left(-v_b + \dfrac{v_{oTL}}{\beta_T}\right) \end{bmatrix} \begin{bmatrix} \phi_x \\ \phi_y \\ 1 \end{bmatrix}$$

$$\begin{bmatrix} 0 \\ 0 \end{bmatrix}$$
$$= \begin{bmatrix} 0 & \left(\alpha v_b + \dfrac{v_{oTL}}{\beta_T}\right)^2 - \left(\alpha - \dfrac{1}{\beta_T}\right)\left(-\alpha - \dfrac{1}{\beta_L}\right) & \left[\left(\alpha v_b + \dfrac{v_{oTL}}{\beta_T}\right)\left(-v_b + \dfrac{v_{oTT}}{\beta_T}\right)\right] - \left[\left(-\alpha - \dfrac{1}{\beta_T}\right)\left(-v_b + \dfrac{v_{oTL}}{\beta_T}\right)\right] \\ \left(\alpha v_b + \dfrac{v_{oTL}}{\beta_T}\right) & \left(-\alpha - \dfrac{1}{\beta_L}\right) & \left(-v_b + \dfrac{v_{oTL}}{\beta_T}\right) \end{bmatrix} \begin{bmatrix} \phi_x \\ \phi_y \\ 1 \end{bmatrix}$$

$$\left[\left(\alpha v_b + \dfrac{v_{oTL}}{\beta_T}\right)^2 - \left(-\alpha - \dfrac{1}{\beta_T}\right)\left(-\alpha - \dfrac{1}{\beta_L}\right)\right]\phi_y + \left[\left(\alpha v_b + \dfrac{v_{oTL}}{\beta_T}\right)\left(-v_b + \dfrac{v_{oTT}}{\beta_T}\right) - \left(-\alpha - \dfrac{1}{\beta_T}\right)\left(v_b + \dfrac{v_{oTL}}{\beta_T}\right)\right] = 0$$

$$\phi_y = \dfrac{\left[\left(\alpha v_b + \dfrac{v_{oTL}}{\beta_T}\right)\left(-v_b + \dfrac{v_{oTT}}{\beta_T}\right) - \left(-\alpha - \dfrac{1}{\beta_T}\right)\left(v_b + \dfrac{v_{oTL}}{\beta_T}\right)\right]}{\left(\alpha v_b + \dfrac{v_{oTL}}{\beta_T}\right)^2 - \left(-\alpha - \dfrac{1}{\beta_T}\right)\left(-\alpha - \dfrac{1}{\beta_L}\right)}$$

$$\phi_y = \frac{[(\alpha\beta_T\nu_b + \nu_{oTL})(-\nu_b\beta_T + \nu_{oTT}) - (-\alpha\beta_T - 1)(\nu_b\beta_T + \nu_{oTL})]}{(\alpha\beta_T\nu_b + \nu_{oTL})^2 - (-\alpha\beta_T - 1)\left(-\alpha\beta_L - \frac{\beta_T}{\beta_L}\right)}$$

$$\begin{bmatrix} 0 \\ 0 \end{bmatrix} = \begin{bmatrix} \left(-\alpha - \frac{1}{\beta_T}\right)\left(-\alpha - \frac{1}{\beta_L}\right) & \left(\alpha\nu_b + \frac{\nu_{oTL}}{\beta_T}\right) - \left(-\alpha - \frac{1}{\beta_L}\right) & \left(-\nu_b + \frac{\nu_{oTT}}{\beta_T}\right)\left(-\alpha - \frac{1}{\beta_L}\right) \\ \left(\alpha\nu_b + \frac{\nu_{oTL}}{\beta_T}\right)\left(\alpha\nu_b + \frac{\nu_{oTL}}{\beta_T}\right) & \left(-\alpha - \frac{1}{\beta_L}\right)\left(\alpha\nu_b + \frac{\nu_{oTL}}{\beta_T}\right) & \left(-\nu_b + \frac{\nu_{oTL}}{\beta_T}\right)\left(\alpha\nu_b + \frac{\nu_{oTL}}{\beta_T}\right) \end{bmatrix}\begin{bmatrix} \phi_x \\ \phi_y \\ 1 \end{bmatrix}$$

$$\begin{bmatrix} 0 \\ 0 \end{bmatrix} = \begin{bmatrix} \left(-\alpha - \frac{1}{\beta_T}\right)\left(-\alpha - \frac{1}{\beta_L}\right) - \left(\alpha\nu_b + \frac{\nu_{oTL}}{\beta_T}\right)\left(\alpha\nu_b + \frac{\nu_{oTL}}{\beta_T}\right) & 0 & \left(-\nu_b + \frac{\nu_{oTT}}{\beta_T}\right)\left(-\alpha - \frac{1}{\beta_L}\right) - \left(-\nu_b + \frac{\nu_{oTL}}{\beta_T}\right)\left(\alpha\nu_b + \frac{\nu_{oTL}}{\beta_T}\right) \\ \left(\alpha\nu_b + \frac{\nu_{oTL}}{\beta_T}\right) & \left(-\alpha - \frac{1}{\beta_L}\right) & \left(-\nu_b + \frac{\nu_{oTL}}{\beta_T}\right) \end{bmatrix}\begin{bmatrix} \phi_x \\ \phi_y \\ 1 \end{bmatrix}$$

$$\left[\left(-\alpha - \frac{1}{\beta_T}\right)\left(-\alpha - \frac{1}{\beta_L}\right) - \left(\alpha\nu_b + \frac{\nu_{oTL}}{\beta_T}\right)^2\right]\phi_x + \left[\left(-\nu_b + \frac{\nu_{oTT}}{\beta_T}\right)\left(-\alpha - \frac{1}{\beta_L}\right)\right] - \left[\left(-\nu_b + \frac{\nu_{oTL}}{\beta_T}\right)\left(\alpha\nu_b + \frac{\nu_{oTL}}{\beta_T}\right)\right] = 0$$

$$\phi_x = \frac{\left(-\nu_b + \frac{\nu_{oTT}}{\beta_T}\right)\left(-\alpha - \frac{1}{\beta_L}\right) - \left(-\nu_b + \frac{\nu_{oTL}}{\beta_T}\right)\left(\alpha\nu_b + \frac{\nu_{oTL}}{\beta_T}\right)}{\left[\left(-\alpha - \frac{1}{\beta_T}\right)\left(-\alpha - \frac{1}{\beta_L}\right) - \left(\alpha\nu_b + \frac{\nu_{oTL}}{\beta_T}\right)^2\right]}$$

$$\phi_x = \frac{\left(-\nu_b\beta_T + \nu_{oTT}\right)\left(-\alpha\beta_T - \frac{\beta_T}{\beta_L}\right) - (-\nu_b\beta_T + \nu_{oTL})(\alpha\beta_T\nu_b + \nu_{oTL})}{\left[(-\alpha\beta_T - 1)\left(-\alpha\beta_T - \frac{\beta_T}{\beta_L}\right)\right] - (\alpha\beta_T\nu_b + \nu_{oTL})^2}$$

$$\phi_x = \frac{\left(-\nu_b\beta_T + \nu_{oTT}\right)\left(-\alpha\beta_T - \frac{\beta_T}{\beta_L}\right) - (-\nu_b\beta_T + \nu_{oTL})(\alpha\nu_b\beta_T + \nu_{oTL})}{(\alpha\beta_T\nu_b + \nu_{oTL})^2 - (-\alpha\beta_T - 1)\left(-\alpha\beta_T - \frac{\beta_T}{\beta_L}\right)}$$

$$\phi_y = \frac{(-\alpha\beta_T - 1)(-\nu_b\beta_T + \nu_{oTL}) - (-\nu_b\beta_T + \nu_{oTT})(\alpha\beta_T\nu_b + \nu_{oTL})}{(\alpha\beta_T\nu_b + \nu_{oTL})^2 - (-\alpha\beta_T - 1)\left(-\alpha\beta_T - \frac{\beta_T}{\beta_L}\right)}$$

Isotropic case applied to ϕ_x

$$\phi = \frac{(-\alpha\beta - 1)(-\nu_b\beta + \nu_o) - (-\nu_b\beta + \nu_o)(\alpha\beta\nu_b + \nu_o)}{(\alpha\beta\nu_b + \nu_o)^2 - (-\alpha\beta - 1)(-\alpha\beta - 1)}$$

$$\phi = \frac{(\nu_o - \beta\nu_b)[(-\alpha\beta - 1)(\alpha\beta\nu_b + \nu_o)]}{[(\alpha\beta\nu_b + \nu_o) + (-\alpha\beta - 1)][(\alpha\beta\nu_b + \nu_o) - (-\alpha\beta - 1)]}$$

$$\phi = \frac{(-\nu_o + \beta\nu_b)[(\alpha\beta\nu_b + \nu_o) - (-\alpha\beta - 1)]}{[(\alpha\beta\nu_b + \nu_o) + (-\alpha\beta - 1)][(\alpha\beta\nu_b + \nu_o) - (-\alpha\beta - 1)]}$$

$$\phi = \frac{-\nu_o + \beta\nu_b}{\nu_o + \alpha\beta\nu_b - (1 + \alpha\beta)}$$

(191)

Isotropic case applied to ϕ_y

$$\phi = \frac{(-\alpha\beta - 1)(-\nu_b\beta + \nu_o) - (-\nu_b\beta + \nu_o)(\alpha\beta\nu_b + \nu_o)}{(\alpha\beta\nu_b + \nu_o)^2 - (-\alpha\beta - 1)(-\alpha\beta - 1)}$$

$$\phi = \frac{(\nu_o - \beta\nu_b)[(-\alpha\beta - 1)(\alpha\beta\nu_b + \nu_o)]}{[(\alpha\beta\nu_b + \nu_o) + (-\alpha\beta - 1)][(\alpha\beta\nu_b + \nu_o) - (-\alpha\beta - 1)]}$$

$$\phi = \frac{(-\nu_o + \beta\nu_b)[(\alpha\beta\nu_b + \nu_o) - (-\alpha\beta - 1)]}{[(\alpha\beta\nu_b + \nu_o) + (-\alpha\beta - 1)][(\alpha\beta\nu_b + \nu_o) - (-\alpha\beta - 1)]}$$

(192)

$$\phi = \frac{-v_o + \beta v_b}{v_o + \alpha\beta v_b - (1 + \alpha\beta)}$$

It is possible to observe that in the isotropic case, the two expressions are equal.

$$\phi = \frac{-v_o + \beta v_b}{v_o + \alpha\beta v_b - (1 + \alpha\beta)}$$

10.2 Appendix B

10.2.1. Carbon bundles

Compressive strength of brick: f_{cb} = 20 MPa

Compressive strength of mortar: f_{cm} = 13.57 MPa

Height of the specimen: H = 315 mm

Thickness of the specimen: T = 120 mm

Net area of the specimen: A_n = 37800 mm^2

Compressive strength of masonry: $f'_m = K f_{cb}^{0.7} f_{cm}^{0.3}$ = 9.79 MPa (according to (EN 1998-1 2004) assuming masonry made by general purpose mortar)

Elastic modulus of masonry: $E_M = 1000 f'_m$ = 9791 MPa (D.M. 14 Gennaio 2008)

Diameter of the bar: ϕ_{BAR} = 6mm

Cross-sectional area of the bar: A_{BAR} = 28.27 mm^2

Elastic modulus of the bar: E_{BAR} = 240000 MPa

Reinforcement ratio: $\omega_f (LC8)$ = 0.015

Reinforcement ratio: $\omega_f (SC4)$ = 0.073

10.2.2. Steel bars

Compressive strength of brick: f_{cb} = 20 MPa

Compressive strength of mortar: f_{cm} = 5 MPa

Height of the specimen: H = 315 mm

Thickness of the specimen: T = 120 mm

Net area of the specimen: A_n = 37800 mm^2

Compressive strength of masonry: $f'_m = K f_{cb}^{0.7} f_{cm}^{0.3}$ = 7.26 MPa (according to (EN 1998-1 2004) assuming masonry made by general purpose mortar)

Elastic modulus of masonry: $E_M = 1000 f'_m$ = 7257 MPa (D.M. 14 Gennaio 2008)

Diameter of the bar: ϕ_{BAR} = 6mm

Cross-sectional area of the bar: A_{BAR} = 8 mm^2

Elastic modulus of the bar: E_{BAR} = 139261 MPa

Reinforcement ratio: $\omega_f (LC4)$ = 0.016

Reinforcement ratio: $\omega_f (LC8)$ = 0.032

Reinforcement ratio: $\omega_f (SC4)$ = 0.016

10.3 Appendix C

10.3.1. Masonry properties

Width of the brick: $w = 200$ mm

Height of the brick: $h = 50$ mm

Thickness of the brick $t = 100$ mm

Compressive strength of brick: $f_{cb} = 14.3$ MPa

Compressive strength of mortar: $f_{cm} = 8.82$ MPa

Width of the specimen: $W = 520$ mm

Height of the specimen: $H = 530$ mm

Thickness of the specimen: $T = 100$ mm

Thickness of the mortar joint: $t_m = 10$ mm

Net area of the specimen: $A_n = 52500$ mm^2

Compressive strength of masonry: $f'_m = K f_{cb}^{0.7} f_{cm}^{0.3} = 0.55 \cdot 14.3^{0.7} \cdot 8.82^{0.3} = 6.80$ MPa (according to (EN 1998-1 2004) assuming masonry made by general purpose mortar)

Tensile strength of masonry: $f'_t = 0.67 \sqrt{f'_m} = 1.75$ MPa

Elastic modulus of masonry: $E_M = 1000 f'_m = 6800$ MPa (D.M. 14 Gennaio 2008)

Shear bond strength of mortar joint: $\tau_0 = 3\% \ f'_m = 0.204$ MPa (Babaeidarabad 2013)

Coefficient of internal shear friction in mortar joints: $\mu_0 = 0.30$ (Babaeidarabad 2013)

Modified shear bond strength of mortar joint: $\tau_{0,m} = 0.166$ MPa

Modified coefficient of internal shear friction in mortar joints: $\mu_m = 0.270$

Average bond strength between the bar and the structural mortar: $\tau_b = 1.0$ MPa

10.3.2. Basalt bar properties

Diameter of the bar: $\phi_{BAR} = 5$ mm

Cross-sectional area of the bar: $A_f = 19.63$ mm^2

Elastic modulus of the bar: $E_{BAR} = 45000$ MPa

Maximum tensile strength of the bar: $f_{t,BAR} = 1000$ MPa

10.3.3. FRCM properties

Area of FRCM reinforcement by unit width in both directions (horizontal and vertical): $A_{FRCM} = 0.035$ mm^2/mm

Elastic modulus of FRCM: $E_{FRCM} = 72000$ MPa

Elongation at failure: $\varepsilon_u = 0.018$

10.3.4. Masonry contribution (V_m)

10.3.4.1. Shear capacity due to shear sliding failure, V_{ss}:

$$V_{ss} = \frac{\tau_0}{1 - \mu_0 tg\theta} A_n = \frac{0.204}{1 - 0.30 \cdot 1} 52500 = 15300 \text{ N} = 15.3 \text{ kN}$$

10.3.4.2. Shear capacity due to shear friction failure, V_{sf}:

$$V_{sf} = \frac{\tau_{0,m}}{1 - \mu_m tg\theta} A_n = \frac{0.166}{1 - 0.270 \cdot 1} 52500 = 11938.3 \text{ N} = 11.9 \text{ kN}$$

10.3.4.3. Shear capacity due to the diagonal tension failure, V_{dt}:

$$V_{dt} = \frac{tg\theta + \sqrt{21.26 + tg^2\theta}}{10.58} f_t' A_n = \frac{1 + \sqrt{21.26 + 1}}{10.58} 1.75 \cdot 52500 = 49654.62 \text{ N} = 49.65 \text{ kN}$$

10.3.4.4. Shear capacity due to toe crushing failure at the loading end, V_c:

$$V_c = \frac{2wf_m'}{3h + 2wtg\theta} A_m = \frac{2 \cdot 200 \cdot 6.80}{3 \cdot 50 + 2 \cdot 200 \cdot 1} \cdot 100 \cdot 100 = 49454.54 \text{ N} = 49.45 \text{ kN}$$

Finally, UNR shear capacity is calculated by using Eq. (8) as:

$$V_m = min\{V_{ss}, V_{sf}, V_{dt}, V_c\} = min\{15.3 \text{ kN}, 11.9 \text{ kN}, 49.65 \text{ kN}, 49.45 \text{ kN}\} = 11.9 \text{ kN}$$

10.3.5. Bars contribution (V_f)

$$L_e = \frac{f_{t,BAR}R}{2\tau_b} = \frac{1000 \cdot 2.5}{2 \cdot 1} = 1250.0 \text{ mm} = 1.25 \text{ m}$$

$$V_f = \tau_b 2\pi R \sum_{i=1}^{n} L_i \qquad L_i \leq L_e$$

asymmetric reinforcement: $V_f = 1 \cdot 2 \cdot \pi \cdot 2.5 \cdot (200 + 100) = 4.71 \text{ kN}$

symmetric reinforcement: $V_f = 1 \cdot 2 \cdot \pi \cdot 2.5 \cdot (200 \cdot 2 + 100 \cdot 2) = 9.42 \text{ kN}$

10.3.6. FRCM contribution (V_f)

From technical data, the ultimate strain ε_u of FRCM is equal to 1.8% that is higher than 0.4% that represents the admissible value according to (ACI 549.4R-13 2013). As a consequence, ε_u is considered equal to 0.004.

$f_{t,FRCM} = E_{FRCM}\varepsilon_u = 72000 \cdot 0.004 = 288 \text{ MPa}$

$V_f = 2n_{layer}A_{FRCM}Wf_{t,FRCM}$

asymmetric reinforcement: $V_f = 2 \cdot 1 \cdot 0.035 \cdot 520 \cdot 288 = 11007.36 \text{ N} = 11.0 \text{ kN}$

symmetric reinforcement: $V_f = 2 \cdot 2 \cdot 0.035 \cdot 520 \cdot 288 = 22014.72 \text{ N} = 22.0 \text{ kN}$

10.3.7. Limitations

Following (ACI 549.4R-13 2013), the summation of the masonry and FRCM shear contributions should be checked against the substrate toe crushing capacity:

$V_n = min(V_m + V_f; V_c) = min(11.9 + 11; 49.45) = 22.9 \text{ kN}$

10.4   Appendix D

10.4.1. Masonry properties

Width of the brick: $w = 240$ mm

Height of the brick: $h = 180$ mm

Thickness of the brick $t = 380$ mm

Compressive strength of brick: $f_{cb} = 40.40$ MPa

Compressive strength of mortar W: $f_{cm} = 10$ MPa

Compressive strength of mortar L: $f_{cm} = 5$ MPa

Width of the specimen: $W = 1200$ mm

Height of the specimen: $H = 1200$ mm

Thickness of the specimen: $T = 380$ mm

Thickness of the mortar joint: $t_m = 1$ mm

Net area of the specimen: $A_n = 228000$ mm^2

Compressive strength of masonry: $f'_m = K f_{cb}^{0.85} = 0.55 \cdot 40.40^{0.85} = 12.76$ MPa (according to (EN 1998-1 2004) assuming masonry made with thin layer of mortar)

Tensile strength of masonry: $f'_t = 0.67\sqrt{f'_m} = 2.39$ MPa

Elastic modulus of masonry: $E_M = 1000 f'_m = 12760$ MPa (D.M. 14 Gennaio 2008)

Shear bond strength of mortar joint: $\tau_{0,W} = 0.3$ MPa

Shear bond strength of mortar joint: $\tau_{0,L} = 0.6$ MPa

Coefficient of internal shear friction in mortar joints: $\mu_0 = 0.30$ (Babaeidarabad 2013)

Modified shear bond strength of mortar joint: $\tau_{0,m,W} = 0.141$ MPa

Modified shear bond strength of mortar joint: $\tau_{0,m,L} = 0.282$ MPa

Modified coefficient of internal shear friction in mortar joints: $\mu_m = 0.225$

10.4.2. FRCM properties

Area of FRCM reinforcement by unit width in both directions (horizontal and vertical): $A_{FRCM} = 0.032$ mm^2/mm

Elastic modulus of FRCM: $E_{FRCM} = 70000$ MPa

Elongation at failure: $\varepsilon_u = 0.019$

10.4.3. Masonry contribution (V_m)

10.4.3.1. Shear capacity due to shear sliding failure, V_{ss}:

$$V_{ss} = \frac{\tau_{0,W}}{1 - \mu_0 tg\theta} A_n = \frac{0.3}{1 - 0.30 \cdot 1} 228000 = 97714 \text{ N} = 97.7 \text{ kN}$$

$$V_{ss} = \frac{\tau_{0,L}}{1 - \mu_0 tg\theta} A_n = \frac{0.6}{1 - 0.30 \cdot 1} 228000 = 195428 \text{ N} = 195.43 \text{ kN}$$

10.3.3.2. Shear capacity due to shear friction failure, V_{sf}:

$$V_{sf} = \frac{\tau_{0,m,W}}{1 - \mu_m tg\theta} A_n = \frac{0.141}{1 - 0.225 \cdot 1} 228000 = 41481 \text{ N} = 41.4 \text{ kN}$$

$$V_{sf} = \frac{\tau_{0,m,L}}{1 - \mu_m tg\theta} A_n = \frac{0.282}{1 - 0.225 \cdot 1} 228000 = 82962 \text{ N} = 83.0 \text{ kN}$$

10.4.3.3. Shear capacity due to the diagonal tension failure, V_{dt}:

$$V_{dt} = \frac{tg\theta + \sqrt{21.26 + tg^2\theta}}{10.58} f_t' A_n = \frac{1 + \sqrt{21.26 + 1}}{10.58} 2.39 \cdot 228000 = 294507 \text{ N} = 294.51 \text{ kN}$$

10.4.3.4. Shear capacity due to toe crushing failure at the loading end, V_c:

$$V_c = \frac{2wf_m'}{3h + 2wtg\theta} A_m = \frac{2 \cdot 240 \cdot 12.76}{3 \cdot 180 + 2 \cdot 240 \cdot 1} \cdot 240 \cdot 240 \cdot 0.5 = 172936 \text{ N} = 172.94 \text{ kN}$$

Finally, UNR-W shear capacity is calculated as:

$$V_m = min\{V_{SS}, V_{Sf}, V_{dt}, V_c\} = min\{97.7 \text{ kN}, 41.4 \text{ kN}, 294.51 \text{ kN}, 172.94 \text{ kN}\} = 41.4 \text{ kN}$$

while for UNR-L is:

$$V_m = min\{V_{SS}, V_{Sf}, V_{dt}, V_c\} = min\{195.43 \text{ kN}, 83.0 \text{ kN}, 294.51 \text{ kN}, 172.94 \text{ kN}\} = 83.0 \text{ kN}$$

10.4.4. FRCM contribution (V_f)

From technical data, the ultimate strain ε_u of FRCM is equal to 1.9% that is higher than 0.4% that represents the admissible value according to (ACI 549.4R-13 2013). As a consequence, ε_u is considered equal to 0.004.

$$f_{t,FRCM} = E_{FRCM}\varepsilon_u = 70000 \cdot 0.004 = 280 \text{ MPa}$$

$$V_f = 2n_{layer}A_{FRCM}Wf_{t,FRCM} = 2 \cdot 2 \cdot 0.032 \cdot 1200 \cdot 280 = 43008 \text{ N} = 43.0 \text{ kN}$$

10.4.5. Limitations

Following (ACI 549.4R-13 2013), the summation of the masonry and FRCM shear contributions should be checked against the substrate toe crushing capacity. Therefore, for UNR-W:

$$V_n = min(V_m + V_f; V_c) = min(84.4; 172.94) = 84.4 \text{ kN}$$

while, for UNR-L is

$$V_n = min(V_m + V_f; V_c) = min(126.0; 172.94) = 126.0 \text{ kN}$$